The Dissertation Committee for Masatoshi Shoji
certifies that this is the approved version of the following dissertation:

Toward an Understanding of the Large Scale Structure of the Universe with Galaxy Surveys

Committee:

Eiichiro Komatsu, Supervisor

Karl Gebhardt

Gary Hill

Lam Hui

Paul Shapiro

Toward an Understanding of the Large Scale Structure of the Universe with Galaxy Surveys

by

Masatoshi Shoji, B.S.; M.A.

DISSERTATION

Presented to the Faculty of the Graduate School of
The University of Texas at Austin
in Partial Fulfillment
of the Requirements
for the Degree of

DOCTOR OF PHILOSOPHY

THE UNIVERSITY OF TEXAS AT AUSTIN
December 2011

To Akira and Kazuko Shoji

Acknowledgments

First, I would like to express my deepest gratitude to my adviser, Professor Eiichiro Komatsu, for everything he has done for me. His valuable lessons were not merely limited to academics, but enhanced many aspects of my life in Austin, making my Ph.D course work a truly enjoyable experience. He is the most influential and positive person I have ever met.

I am also grateful to my committee members, Professor Paul Shapiro, Professor Karl Gebhardt, Professor Gary Hill, and Professor Lam Hui for their interest in my work, and their many useful comments and wise advice.

I am indebted to my undergraduate adviser, Professor Martin Gaskell, for guiding me into the field of Astronomy, and the care he provided when I started my career in the U.S.

Chapter 5 of this dissertation was accomplished in collaboration with Professor Jounghun Lee at the Seoul National University. I thank Lee-san for teaching and inspiring me in the new field of cosmology. Also, I thank Doctor Caroline Foster for kindly providing her void finding code, which is used in this chapter.

I thank my friends in Japan for always welcoming me upon my return with a shower of beer and sake: Mayo Baker, Aikra Endo, Natsuko Endo,Yoshiaki Hasegawa, Kosuke Niitsu, Keiji Uehara, Kimiko Nezu, Lina

Webb, Sayaka Oku, Takahiro Kasahara and Yukiho Shinagawa with whom I survived undergraduate life in Nebraska together. I thank Hiroshi Aizawa, Hiroyuki Aoki, Katsuyuki Sato, Naoki Kagawa, Shinji Oikawa and Koji Takeuchi for their everlasting friendship.

I deeply appreciate all the warmth Austin provided in making my life here an unforgettable one: I thank my friends in Austin: Kohei Kajimoto, Hyun Seol Park, Anastasiya Travina, and Masayuki Wada, my fellow graduate students; Joshua Adams, John Barentine, Rodolfo Barniol Duran, Amanda Bayless, Guillermo Blanc, Taylor Chonis, Sean Couch, Casey Deen, Bi-Qing For, Candace Gray, Amanda Heiderman, Inh Jee, Myoungwon Jeon, Randi Ludwig, Jeremy Murphy, Hyunbae Park, Rodolfo Santana, Mimi Song, Tim Weinzirl, and Robert Wittenmyer.

I thank Hyo-Jeong Kim: always a cheerful mood maker, drinking coffee, and eating mandarin oranges all the time...

I thank Sehun Hwang, with whom I shared most of my time both outside of my research work and as a fellow graduate student. The “luxurious” road trip to Las Vegas was a great highlight.

I thank Donghui Jeong: my second adviser, who always helped with my research with his great store of knowledge, and as a drinking companion. Our research trip to Japan was amazingly spectacular.

My thanks go to Gordon Orris, the almighty administration staff member of the Astronomy Department. Without his superb help, this work wouldn’t be finished. Going to the shooting range with him was always fun and exciting.

I owe a lot to my graduate coordinators: Stephanie Crouch, Charmarie Burke and Rachel Walker, for understanding my laziness, and helping me successfully fulfill the requirements of my Ph.D. coursework.

I also benefited from the UT cosmology groups members and office mates. I would especially like to thank Kyungjin Ahn, Beth Fernandez, James Hermes, John Jardel, Jun Koda, Yi Mao, Andreas Pawlik, Tanja Rindler-Daller, Yuki Watanabe, and Jun Zhang.

I thank Johnathan Ganc and Chi-Ting Chiang: the past years of sharing an office with you two were always enjoyable, and we probably made the most noise on the 16th floor. Best of luck to your remaining years and future careers.

Finally, last but not least, I cannot express great enough thanks to my parents and sisters, Akira Shoji, Kazuko Shoji, Akina Hayasaka and Eri Shoji for their understanding and kind support of my pursuing a degree in the rich field of Astronomy.

Toward an Understanding of the Large Scale Structure of the Universe with Galaxy Surveys

Masatoshi Shoji, Ph.D.
The University of Texas at Austin, 2011

Supervisor: Eiichiro Komatsu

Large-scale structures we see in the universe, such as galaxies, galaxy clusters and structures beyond the scale of clusters, result from gravitational instability of *almost* isotropic and homogeneous density distribution in the early universe. The degree of the initial anisotropy of the universe and the subsequent growth of gravitational instability, coupled with the expansion rate of the universe, determine the scale and abundance of the structures formed in the universe at later times.

A galaxy survey directly observes a distribution of structures in the sky using galaxies as a tracer of the underlying density distribution, and yields constraints on cosmological models when compared to a physical theory of structure formation based on a given cosmological model. Among many cosmological and astronomical phenomena to be understood from a galaxy survey, the nature of the observed accelerated expansion of the universe is the most profound problem in the modern physics.

Motivated by various planned and on-going galaxy surveys, including our own *Hobby-Ebery Telescope Dark Energy eXperiment* (HETDEX), we show the way to fully exploit the data from a galaxy survey. We improve a model of structure formation to include the effect of baryonic pressure and the free-streaming of massive neutrinos at a mildly non-linear regime. Future galaxy surveys are to reach the level of accuracy, where the effect of massive neutrinos on the observed power spectrum is no longer negligible. Proper understanding of these effects gives a way to measure the absolute masses of neutrinos: one of the most fundamental particles, which, by itself, will be a major development in the field of particle physics.

Yet, most of the space ($\sim 80\%$) observed by galaxy surveys is occupied by voids. An ellipticity probability distribution function of voids offers yet another way of probing cosmology. Especially, a distribution of ellipticities in the redshift space provides a unique way to measure a growth rate of the structure in the universe apart from other cosmological parameters when combined with the galaxy power spectrum.

Table of Contents

List of Tables

List of Figures

Chapter 1

Introduction

Driven by the developments both in theory and observations, past decades have seen the most exciting development of the field of study, *cosmology*: a branch of philosophy in the ancient past has become a serious testable field of science. An observational confirmation of a theory is a core virtue of science, and among various observational techniques available today, galaxy surveys are one of the most fruitful forefront of the observational cosmology.

My research interest lies in the Large Scale Structures (LSS) of the universe, from which we obtain information of an expansion and a structure formation history of the universe. In the coming decades, there will be a prenty of galaxy surveys sufficient to constrain cosmological parameters to the precision, where the currently available cosmological models are well tested against. At the same time, it has become increasingly important to have an accurate model of structure formation to meet the quality standard of available data.

A galaxy survey directly observes a distribution of structures in the sky using galaxies as a tracer of the underlying density distribution at a given redshift. A common statistical tool for studying the distribution of galaxies is a power spectrum of the density contrast,

$$(2\pi)^3 P(\mathbf{k})\delta_D(\mathbf{k}+\mathbf{k}') \equiv \langle \delta(\mathbf{k})\delta(\mathbf{k}') \rangle \,, \tag{1.1}$$

where $\delta(\mathbf{k})$ is a Fourier transform of

$$\delta(\mathbf{x}) = \frac{n(\mathbf{x})}{\bar{n}} - 1. \tag{1.2}$$

In a given power spectrum, we see several characteristic scales encoded at separate historical epochs of the universe, and traces of different ingredients of the universe. Among the characteristic scales in a given power spectrum, two of the most striking features are the scale of the matter radiation equality epoch, $r_H(z_{\rm eq})$, and the scale of the sound horizon at the time of the so called drag epoch, $r_s(z_{\rm drag})$. We see the formar scale as a bent (or a turn over) on the power spectrum, and the latter as a tiny but noticable oscillatory pattern on a power spectrum (a.k.a., Baryon Acoustic Oscillation). With those two characteristic scales as standard rulers, we can put constraints on various cosmological parameters. For example, from the measurements of angular separations of galaxies, one can determine an angular diameter distance, $D_A(z)$, and from the measurements of redshift distributions of galaxies, one can determine a Hubble rate, $H(z)$. These two measurements are tied to cosmological parameters as follows,

$$D_A(z) = \frac{c}{H_0(1+z)} \int_0^z \frac{dz'}{\sqrt{\Omega_m(1+z')^3 + \Omega_{DE} f(z')}}, \tag{1.3}$$

$$H(z) = H_0 \sqrt{\Omega_m(1+z)^3 + \Omega_{DE} f(z)}, \tag{1.4}$$

where

$$f(z) = \exp\left(3\int_0^z \frac{1+w(z')}{1+z'}dz'\right) \tag{1.5}$$

Here, H_0 is a Hubble rate at present ($H_0 = H(z=0)$), and $w(z)$ is an equation of state of dark energy.

Although a power spectrum is a powerful statistical tool to unvail a nature of the universe, the extent to which one can exploit the information contained in the observed power spectrum crusially depends on the accurate analytic understanding of the structure formation.

In chapter 2, we present a method for extracting the angular diameter distances, D_A, and the expansion rates, H, of the universe from the *two-dimensional* Baryon Acoustic Oscillations (BAO) in the galaxy power spectrum. We also show that the full modeling, including the overall shape of the power spectrum and Alcock-Paczynski effect, yields much better determinations of D_A and H, hence the dark energy equation of state parameters such as w_0 and w_a, than the BAO-only analysis by more than a factor of two, provided that non-linear effects are under control.

In chapter 3, we calculate the non-linear matter power spectrum using the 3rd-order perturbation theory without ignoring the pressure gradient term. We consider a semi-realistic system consisting of two matter components with and without pressure, and both are expanded into the 3rd order in perturbations in a self-consistent manner, for the first time. While the pressured component may be identified with baryons or neutrinos, in this paper we mainly explore the physics of the non-linear pressure effect using a toy model in which the Jeans length does not depend on time.

In chapter 4, we study the evolution of linear density fluctuations of free-streaming massive neutrinos at redshift of $z < 1000$, with an explicit justification on the use of a fluid approximation. We solve the collisionless Boltzmann equation in an Einstein de-Sitter (EdS) universe, truncating the Boltzmann hierarchy at $l_{\rm max} = 1$ and 2, and compare the resulting density contrast of neutrinos, $\delta_\nu^{\rm fluid}$, with that of the exact solutions of the Boltzmann equation that we derive in this chapter.

In chapter 5, we study a redshift space ellipticity distribution function of voids. The real space ellipticity distribution function has been studied and known to be a sensitive probe of cosmology via its constraining power on some of the cosmological parameters such as σ_8 and Ω_m. In the redshift space, the redshift space distortion directly change the shape of voids and its ellipticity distribution, making a direct measurement of the growth rate, $f(a) \equiv \frac{d\ln D_+(a)}{d\ln a}$, possible at an arbitrary redshift for a given galaxy survey, when combined with the analysis of a galaxy power spectrum.

Chapter 2

Extracting Angular Diameter Distance and Expansion Rate of the Universe from Two-dimensional Galaxy Power Spectrum at High Redshifts: Baryon Acoustic Oscillation Fitting versus Full Modeling

In this chapter, we present a method for extracting the angular diameter distances, D_A, and the expansion rates, H, of the universe from the *two-dimensional* Baryon Acoustic Oscillations (BAO) in the galaxy power spectrum. We also show that the full modeling, including the overall shape of the power spectrum and Alcock-Paczynski effect, yields much better determinations of D_A and H, hence the dark energy equation of state parameters such as w_0 and w_a, than the BAO-only analysis by more than a factor of two, provided that non-linear effects are under control. [1]

---

[1] A significant part of this chapter was originally published in the Astrophysical Journal by Shoji, M., Jeong, D. & Komatsu, E. Reproduced by permission of the American Astronomical Society.

2.1 Introduction

Dark energy, discovered via the observed luminosity distances out to high-z Type Ia supernovae (Riess et al., 1998; Perlmutter et al., 1999), is the most mysterious element in physics today (see Copeland et al., 2006, for a recent review).

As dark energy primarily affects the expansion rate of the universe, one can gain information on the nature of dark energy by measuring the cosmological distances as well as the expansion rates of the universe accurately.[2]

While the cosmic microwave background (CMB) and the Type Ia supernovae can be used for measuring the angular diameter distance out to $z \simeq 1090$ and the luminosity distances out to $z \lesssim 2$, respectively, the power spectrum of matter distribution in the universe can be used to measure the angular diameter distances *as well as* the expansion rates of the universe out to a wider range of redshifts.

Two length scales are encoded in the matter power spectrum, $P(k)$ (see, e.g., Weinberg, 2008):

- The comoving Hubble horizon size at the matter-radiation equality, $r_H(z_{eq}) = c/[a(z_{eq})H(z_{eq})]$.

---

[2] While dark energy also affects the growth rate of the amplitude of matter fluctuations, which has been seen in the data via the so-called Integrated Sachs–Wolfe (ISW) effect (e.g., Boughn & Crittenden, 2004; Nolta et al., 2004; Afshordi et al., 2004), we do not discuss the effect on the amplitude of fluctuations in this paper.

- The comoving sound horizon size at the so-called drag epoch at which baryons were released from photons, $r_s(z_{drag}) = \int_0^{t(z_{drag})} dt\ c_s(t)/a(t)$, where $c_s(t) = c/\left[\sqrt{3}(1 + a(t)3\Omega_b/(4\Omega_\gamma))\right]$ is the sound speed of photon-baryon fluid.

The former determines the overall shape of the power spectrum of dark matter including the location of the peak of $P(k)$ at $k_{eq} \equiv 1/r_H(z_{eq})$, whereas the latter determines the location of the baryonic features called the Baryon Acoustic Oscillations (BAOs).

These length scales can be predicted from the 5-year data of the Wilkinson Microwave Anisotropy Probe (WMAP) (Hinshaw et al., 2009; Dunkley et al., 2009b; Komatsu et al., 2009)[3]:

$$\begin{aligned} k_{eq} \equiv \frac{1}{r_H(z_{eq})} &= (0.968 \pm 0.046) \times 10^{-2}\ \mathrm{Mpc}^{-1}, && (2.1) \\ r_s(z_{drag}) &= 153.3 \pm 2.0\ \mathrm{Mpc}, && (2.2) \end{aligned}$$

and

$$z_{eq} = 3176^{+151}_{-150}, \qquad z_{drag} = 1020.5 \pm 1.6. \tag{2.3}$$

These lengths can be used as the "standard rulers," which give us the angular diameter distances as well as the expansion rates of the universe (Seo &

---

[3] These predictions assume a flat universe and dark energy being the vacuum energy. For a non-flat universe with dark energy having a constant equation of state, w, the WMAP 5-year data yield $k_{eq} = (0.975^{+0.044}_{-0.045}) \times 10^{-2}\ \mathrm{Mpc}^{-1}$, $r_s(z_{drag}) = 153.4^{+1.9}_{-2.0}$ Mpc, $z_{eq} = 3198^{+145}_{-146}$, and $z_{drag} = 1019.8 \pm 1.5$.

Eisenstein, 2003; Blake & Glazebrook, 2003; Hu & Haiman, 2003).[4]

We, as observers who measure the angular and redshift distribution of galaxies, can measure *four* distance ratios given by

$$\theta_{eq}(z) = \frac{r_H(z_{eq})}{(1+z)D_A(z)} = \frac{1}{k_{eq}(1+z)D_A(z)}, \tag{2.4}$$

$$\theta_s(z) = \frac{r_s(z_{drag})}{(1+z)D_A(z)}, \tag{2.5}$$

$$\delta z_{eq}(z) = \frac{r_H(z_{eq})H(z)}{c} = \frac{H(z)}{k_{eq}c}, \tag{2.6}$$

$$\delta z_s(z) = \frac{r_s(z_{drag})H(z)}{c}, \tag{2.7}$$

where $D_A(z)$ is the proper (i.e., not comoving) angular diameter distance. We measure $\theta_{eq}(z)$ and $\theta_s(z)$ by comparing the predicted lengths with the corresponding observed lengths perpendicular to the line of sight, and $\delta z_{eq}(z)$ and $\delta z_s(z)$ from the lengths parallel to the line of sight.[5]

The BAOs have been detected in the current galaxy redshift survey data from the Sloan Digital Sky Survey (SDSS) and the Two-degree Field Galaxy Redshift Survey (2dFGRS) (Eisenstein et al., 2005; Cole et al., 2005; Hütsi, 2006; Percival et al., 2007). However, the current data are not yet sensitive

---

[4] The matter power spectrum also contains the third distance scale, the Silk damping scale, which can also be used as the standard ruler. The Silk damping scale is the smallest of these three distance scales, and its effect (i.e., the suppression of power below the Silk damping scale) is not as prominent as the effects of the other two distance scales. Nevertheless, the Silk damping must be taken into account when we model the full shape of the power spectrum.

[5] The measured power spectrum in redshift space is a function of the wavenumber parallel to the line of sight, $k_\parallel$, and that perpendicular to the line of sight, $k_\perp$, i.e., $P = P(k_\parallel, k_\perp)$. The angular observables, θ_{eq} and θ_s, are measured from $k_\perp$, while the line-of-sight observables, δz_{eq} and δz_s, are measured from $k_\parallel$.

enough to yield $D_A(z)$ and $H(z)$ separately (Okumura et al., 2008); thus, one can only determine a combined distance scale ratio from the spherically averaged power spectrum. Since two spatial dimensions are available on the sky and one dimension is available along the line of sight, one can measure

$$\left[\theta_s^2(z)\delta z_s(z)\right]^{1/3} = \frac{r_s(z_{drag})}{[(1+z)^2 D_A^2(z) c/H(z)]^{1/3}}. \tag{2.8}$$

Eisenstein et al. (2005) have measured this quantity at $z = 0.35$ from the SDSS Luminous Red Galaxies (LRG), and Percival et al. (2007) have extended their analysis to include more data from the SDSS LRG, as well as the SDSS main galaxy samples and the 2dFGRS galaxies at $z = 0.2$.

Komatsu et al. (2010a) have combined these measurements with the CMB distance ratios determined from the WMAP 5-year data, the "WMAP distance priors," to obtain the constraints on dark energy properties. The analysis performed in Komatsu et al. (2010a) is a proto-type of what one can do in the future. It is clear that we can gain more information if we can measure $D_A(z)$ and $H(z)$ simultaneously at various redshifts. Therefore, in the future we should be able to perform a much more sensitive test of dark energy properties by combining $D_A(z)$ and $H(z)$ from the future galaxy survey data, and the CMB distance priors from the future CMB experiments such as Planck.

Moreover, the BAOs capture only a part of information encoded in the shape of $P(k)$. One would miss another baryonic feature, the Silk damping scale, by only measuring BAOs. A more serious drawback is that one would miss the other prominent standard ruler, k_{eq}, completely, by only measuring BAOs.

Nevertheless, there is one major advantage of using BAOs: the phases (not the amplitude) of BAOs are less sensitive to the distortion of the shape of $P(k)$ due to non-linear matter clustering, non-linear galaxy bias, or non-linear redshift space distortion (Seo & Eisenstein, 2005; Eisenstein et al., 2007; Nishimichi et al., 2007; Smith et al., 2008; Angulo et al., 2008; Sanchez et al., 2008; Seo et al., 2008). As a result, many studies have focused on developing various ways to extract the distance information from BAOs.

Most of the previous work focused only on extracting the BAOs from the spherically averaged $P(k)$ (which gives D_A^2/H) (e.g., Percival et al., 2007). Yamamoto et al. (2005) have studied the monopole and quadrupole moments in the galaxy power spectrum and their implications for determinations of the dark energy equation of state parameter, w, and concluded that even in the worst case scenario (i.e., absence of the BAOs feature on the observed power spectrum), galaxy survey can still provide useful limits on w from a combination of the monopole and quadrupole power spectra. Recently, Padmanabhan & White (2008) have explored an extraction of the quadrupole moment of the two-dimensional power spectrum, $P(k, \mu)$, which gives a different distance combination, $D_A H$.

In this paper, we shall develop a method for extracting D_A and H simultaneously from the two-dimensional BAOs. Since we do not use spherical averaging or truncate the Legendre expansion of BAOs at arbitrary orders, our method uses more information than most of the previous methods. To our knowledge, the full two-dimensional extraction of D_A and H from BAOs has been explored only by Wagner et al. (2008).

This paper is organized as follows. In § 2.2 we give a brief account of the original one-dimensional "fit-and-extract" (FITEX) method, which was developed by Koehler et al. (2007) for extracting BAOs from a spherically averaged one-dimensional $P(k)$. We then extend this method to the two-dimensional FITEX-2d method by including the full two-dimensional information without spherical averaging. In § 2.3 we extract D_A and H from simulated noisy data using the FITEX-2d method, and show that the FITEX-2d yields unbiased estimates of D_A and H. In § 2.4 we repeat the same analysis for a more realistic simulation, using the Millennium Simulation (Springel et al., 2005). In § 2.5 we propagate errors in $H(z)$ and $D_A(z)$ to those in the dark energy equation of state with the parametrization of $w(z) = w_0 + w_a z/(1+z)$. We conclude in § 2.6.

Throughout this paper we shall use the cosmological parameters given by $\Omega_m = 0.277$, $\Omega_\Lambda = 0.723$, $\Omega_b = 0.0459$, $n_s = 0.962$, and $h = 0.702$ (Dunkley et al., 2009a; Komatsu et al., 2010a), which are the maximum likelihood values inferred from the WMAP 5-year data (Hinshaw et al., 2009) combined with the current BAO data (Percival et al., 2007) and Type Ia supernova data (Kowalski et al., 2008).

2.2 FITEX-2d: Methodology

We develop a method for extracting D_A and H simultaneously from the two-dimensional BAOs without spherical averaging.

Our method builds upon the existing "fit-and-extract" (FITEX) method developed by Koehler et al. (2007) for extracting D_A^2/H from a spherically averaged, one-dimensional $P(k)$. The FITEX method extracts BAOs by fitting and removing the non-oscillatory part of $P(k)$, which leaves only the oscillatory component, i.e., BAOs. Koehler et al. (2007) model the non-oscillatory, smooth part by the following functional form:

$$P^{1d}_{smooth}(k) = \left[\frac{A}{1+Bk^{\delta}} e^{(k/k_1)^{\alpha}}\right]^2 k^{n_s}, \tag{2.9}$$

where n_s is the primordial tilt, while A, B, δ, k_1, and α are free parameters. Koehler et al. (2007) have shown that this function is flexible enough to fit out the smooth part of the spherically averaged $P(k)$ measured from the Hubble Volume Simulation (Evrard et al., 2002). They have tested the FITEX method particularly for a large scale, $k < 0.3\ h\ \mathrm{Mpc}^{-1}$, at high redshifts, $1.9 < z < 3.8$, that are relevant to the Hobby Eberly Dark Energy Experiment (HETDEX; Hill et al., 2004).

We make a simple extension of the one-dimensional FITEX method by including angular dependence. We model the two-dimensional smooth power spectrum by

$$\begin{aligned} P^{2d}_{smooth}(k,\mu) &= P^{1d}_{smooth}(k) \\ \times &\left[1 + g^{(2)}(k)P_2(\mu) + g^{(4)}(k)P_4(\mu) + g^{(6)}(k)P_6(\mu)\right], \end{aligned} \tag{2.10}$$

where μ is the cosine of the angle θ between $\mathbf{k}$ and the line of sight, i.e., $\mu = \cos\theta$ and $\tan\theta = k_\perp/k_\parallel$. Therefore, $\mu = 0$ and $\mu = 1$ for $k_\parallel = 0$ and $k_\perp = 0$, respectively.

Here, $P_l(\mu)$ is the Legendre polynomials:

$$\begin{aligned} P_2(\mu) &= \frac{1}{2}\left(3\mu^2 - 1\right), & (2.11) \\ P_4(\mu) &= \frac{1}{8}\left(35\mu^4 - 30\mu^2 + 3\right), & (2.12) \\ P_6(\mu) &= \frac{1}{16}\left(231\mu^6 - 315\mu^4 + 105\mu^2 - 5\right). & (2.13) \end{aligned}$$

The odd multipoles must vanish by symmetry. One may include $l \geq 8$ if necessary, but we find it sufficient to include the terms only up to $l = 6$.

Finally, $g^{(l)}(k)$ is given by the 6th-order polynomials with only even powers of k:

$$g^{(l)}(k) = a_0^{(l)} + a_2^{(l)}k^2 + a_4^{(l)}k^4 + a_6^{(l)}k^6, \tag{2.14}$$

where all of $a_i^{(l)}$'s are varied simultaneously for each l. The odd powers must vanish because they are not analytic in $\mathbf{k}$ (Weinberg, 2008). We include the terms only up to k^6, as we include the multipoles up to $l = 6$. If, for instance, $l = 8$ is included, then k^8 may also be included for consistency.

Aside from the primordial tilt, n_s, the FITEX-2d contains 17 free parameters (5 for $P_{smooth}^{1d}(k)$ plus $4 \times 3 = 12$ for the angular dependence). While it may sound like many, the number of data points available on the *two-dimensional* power spectrum is usually much larger, and thus our fit is well behaved.

It may be instructive to use the conventional model for the redshift space power spectrum to show what these parameters are supposed to capture. The leading order angular distortion is given by the so-called Kaiser effect, which arises from coherent converging velocity flow toward the linear overdensity region (Kaiser, 1987). The linear Kaiser power spectrum is given by

$$\begin{aligned} P^{linear}_{kaiser}(k,\mu) &= b_1^2(1+2\beta\mu^2+\beta^2\mu^4)P^{linear}(k) \\ &= b_1^2\left[\left(1+\frac{2}{3}\beta+\frac{1}{5}\beta^2\right)+\frac{4}{3}\beta\left(1+\frac{3}{7}\beta\right)P_2(\mu)\right. \\ &+ \left.\frac{8}{35}\beta^2P_4(\mu)\right]P^{linear}(k), \end{aligned} \tag{2.15}$$

where $\beta \equiv f/b_1$ is a k-independent function that depends on the linear galaxy bias, b_1, and the cosmological parameters (mainly Ω_m) via

$$f \equiv \frac{d\ln D}{d\ln a}, \tag{2.16}$$

where D is the growth factor of linear density fluctuations. We therefore find

$$a_0^{(0)} = 1 \tag{2.17}$$

$$a_0^{(2)} = \frac{\frac{4}{3}\beta\left(1+\frac{3}{7}\beta\right)}{1+\frac{2}{3}\beta+\frac{1}{5}\beta^2}, \tag{2.18}$$

$$a_0^{(4)} = \frac{\frac{8}{35}\beta^2}{1+\frac{2}{3}\beta+\frac{1}{5}\beta^2}, \tag{2.19}$$

and the other terms are zero.

Another example is the so-called Finger-of-God (FoG) effect, which arises from random motion within virialized halos. When the distribution of the pairwise peculiar velocity within a halo is given by an exponential distribution with the velocity dispersion σ_v^2 (Peebles, 1976; Davis & Peebles, 1983), one finds (Ballinger et al., 1996)

$$P_{FoG}(k,\mu) = \frac{P_{kaiser}^{linear}(k,\mu)}{1+f^2k^2\mu^2\sigma_v^2}. \tag{2.20}$$

While the FoG yields many terms when expanded into the Legendre polynomials, it is still a good approximation to truncate the expansion at $l = 6$ if k is sufficiently smaller than $1/\sigma_v$. Note that the FoG effect yields terms in the form of powers of $(k\mu)^2$; thus, it makes sense to use the same number for the maximum power of k (see Eq. (2.14)) and the maximum multipole (see Eq. (2.10)) of the FITEX-2d fitting function.

In general, neither of these two expressions are adequate. The linear Kaiser formula is valid only on very large scales, while the exponential FoG formula is valid only on very small scales. At the intermediate scales we find more complicated expressions from, e.g., the 3rd-order perturbation theory (Heavens et al., 1998). To account for these complications we have included k-dependent coefficients for the Legendre polynomials.

In Figure 2.1 and 2.2 we show the performance of $P_{smooth}^{2d}(k,\mu)$. In Figure 2.1 we show a simple analytical model[6] for the non-linear galaxy power

---

[6] This model is admittedly too simple to be realistic. We shall test the FITEX-2d method in a more realistic setting using the Millennium Simulation in § 2.4.

spectrum in redshift space given by

$$
\begin{aligned}
P_g(k,\mu) &= b_1^2\left[P_{\delta\delta}(k)+2\beta\mu^2P_{\delta\theta}(k)+\beta^2\mu^4P_{\theta\theta}(k)\right] \\
&\quad\times\frac{1}{1+f^2k^2\mu^2\tilde{\sigma}_v^2},
\end{aligned}
\tag{2.21}
$$

where $P_{\delta\delta}(k)$, $P_{\delta\theta}(k)$, and $P_{\theta\theta}(k)$ are the density-density, density-velocity, and velocity-velocity power spectra computed from the 3rd-order perturbation theory, and they are given by Eq. (63), (64), and (65) in Scoccimarro (2004), respectively. This form is similar to Eq. (71) of Scoccimarro (2004), but we have replaced $\exp(-f^2k^2\mu^2\sigma_v^2)$ and f in his formula by $1/(1+f^2k^2\mu^2\tilde{\sigma}_v^2)$ and β, respectively, where $\tilde{\sigma}_v^2\equiv 0.6\sigma_v^2$ is the 1-d peculiar velocity dispersion with an empirical fudge factor of 0.6 calibrated off our simulations presented in Jeong & Komatsu (2006). Here, σ_v^2 is given by

$$
\sigma_v^2\equiv\frac{1}{3}\int\frac{d^3k}{(2\pi)^3}\frac{P^{linear}(k)}{k^2}=\frac{1}{3}\int\frac{dk}{2\pi^2}P^{linear}(k). \tag{2.22}
$$

We chose $z=2$ and $b_1=2.5$. The contour of power spectrum is anisotropic in Fig. 2.1 due to the redshift space distortion; however, we recover isotropy after subtracting the best-fitting $P^{2d}_{smooth}(k,\mu)$ from the anisotropic data (see Fig. 2.2). We see that the BAOs have been extracted successfully, with isotropy of the oscillation phases recovered well.

2.3 Extraction of D_A and H from noisy data: FITEX-2d vs Full Modeling

In § 2.3.1 we show how well we can estimate D_A and H from the two-dimensional BAOs extracted from noisy data using the FITEX-2d method. In

§ 2.3.2 we compare the BAO results to the accuracy one would obtain from the full modeling of $P(k, \mu)$, including the overall shape. In other words, for the former (BAOs) we only use θ_s and δz_s for measuring D_A and H, while for the latter (full modeling) we can use θ_s, δz_s, θ_{eq}, δz_{eq}, as well as the Silk damping scale for measuring D_A and H, provided that non-linear effects (non-linear matter clustering, non-linear redshift space distortion, and non-linear bias) are under control.

Note that the treatment of non-linear effects in this section is too simple to be realistic. For a more realistic treatment we shall use the galaxy power spectrum from the Millennium Simulation (Springel et al., 2005) in § 2.4.

2.3.1 FITEX-2d

To estimate errors in D_A and H from the FITEX-2d method, we use simple Monte Carlo simulations.

For the underlying spectrum we use the same data as shown in Fig. 2.1, which includes a simplified modeling of non-linear matter clustering and non-linear redshift space distortion as given by Eq. (2.21). As for the galaxy bias, we use a linear bias with $b_1 = 2.5$.

Once the underlying spectrum is specified, it is straightforward to compute the errors in $P_g(k_\parallel, k_\perp)$, σ_{P_g}, provided that the distribution of $P_g(k_\parallel, k_\perp)$ is a Gaussian. We use the standard formula that includes sampling variance as well as shot noise (see, e.g., Jeong & Komatsu, 2009)

$$\frac{\sigma_{P_g}(k_\parallel, k_\perp)}{P_g(k_\parallel, k_\perp)} = 2\pi \sqrt{\frac{1}{V_{survey} k_\perp \Delta k_\perp \Delta k_\parallel}} \frac{1 + n_g P_g(k_\parallel, k_\perp)}{n_g P_g(k_\parallel, k_\perp)}, \tag{2.23}$$

where n_g is the number density of galaxies, V_{survey} is the survey volume, $\Delta k_\perp$ and $\Delta k_\parallel$ are the fundamental wavenumbers, i.e., the resolution in $k_\perp$ and $k_\parallel$. We take these to be $\Delta k_\parallel = \Delta k_\perp = (2\pi)/V_{survey}^{1/3}$.

We use σ_{P_g} from Eq. (2.23) to calculate the r.m.s. error in $P_g(k_\parallel, k_\perp)$, and generate 1000 Monte Carlo realizations. We then apply the FITEX-2d method to remove the smooth component from each realization to extract BAOs. For each realization, we measure D_A and H simultaneously by fitting the phases of extracted two dimensional BAOs to those of the reference BAOs extracted from either (i) the linear power spectrum, or (ii) the non-linear power spectrum given by Eq. (2.21), with known $D_{A,ref}$ and H_{ref}. (Later we find that using the linear spectrum as the reference BAO yields the biased estimates of $D_{A,ref}$ and H_{ref}.) We use a simplex downhill method for χ^2-minimization in the two-dimensional parameter space. The number of free parameters for this analysis is two, i.e., D_A and H, and we do not include the amplitude in the fit. We have checked that including the amplitude does not change the results very much, as the amplitude and the phases of BAOs are nearly uncorrelated (see Appendix A.3.1 for more details). This is true in both real and redshift space. When we apply FITEX-2d to the simulated data, we perform a fit out to $k_{max} = 0.40\ h\ \mathrm{Mpc}^{-1}$.

We choose the survey parameters, V_{survey}, z, and n_g, such that they roughly match those expected for the Hobby-Eberly Dark Energy Experiment (HETDEX) (Hill et al., 2004): $N_g = 0.755 \times 10^6$, and $1.9 \leq z \leq 3.5$ with the sky coverage of 420 deg^2, which yields $V_{survey} \simeq 3.0\ h^{-3}$ Gpc^3.[7]

We find that, when the phases extracted by FITEX-2d are compared with the reference BAOs extracted from the linear power spectrum, the best-fitting values of D_A and H averaged over 1000 simulations disagree with the underlying, "true" values by 0.05% and 0.63% for D_A and H, respectively, due to the phase shift of BAOs caused by non-linearities (including non-linear redshift space distortion). This result extends the previous study by Nishimichi et al. (2007), who studied a spherically averaged 1-d power spectrum and found that the bias was less than 1% in $(D_A^2 H^{-1})^{1/3}$.

On the other hand, when the phases are compared with the reference BAOs extracted from the *non-linear* power spectrum (Eq. (2.21)), the best-fitting values of D_A and H agree with the true values to well within the Monte Carlo sampling error; thus, we confirm that the FITEX-2d method yields unbiased estimates of D_A and H.

In Figure 2.3 we show the projected error ellipses on D_A and H from the BAOs extracted with the FITEX-2d (larger, dotted contours; same in all four panels). We find 1.8% and 2.5% errors on D_A and H, respectively, with the cross-correlation coefficient of $r = 0.44$, from the Monte Carlo simulations. For the same survey parameters, the BAO Fisher matrix proposed by Seo

---

[7] The HETDEX is expected to detect 0.755 million Lyman-α emitting galaxies between $1.9 \leq z \leq 3.5$ over 420 deg^2 in 3 years of observations on the Hobby-Eberly Telescope.

& Eisenstein (2007) yields 1.5% and 2.5% errors on D_A and H, respectively, with $r = 0.41$. Therefore, we conclude that the FITEX-2d method yields the results that nearly saturate the Fisher matrix bound, i.e., it is nearly an optimal method in a sense that it can yield the smallest errorbars one can obtain with the BAO-only analysis.

2.3.2 Full Modeling

To calculate the errors in D_A and H expected from the full modeling of the two-dimensional galaxy power spectrum, $P_g(k, \mu)$, we use the Fisher matrix given by (see, e.g., Eisenstein et al., 1999; Seo & Eisenstein, 2003)

$$F_{ij} = \int_0^{k_{max}} \frac{4\pi k^2 dk}{(2\pi)^3} \int_0^1 d\mu \frac{\partial \ln P_g(k,\mu)}{\partial \theta_i} \frac{\partial \ln P_g(k,\mu)}{\partial \theta_j} w(k,\mu), \tag{2.24}$$

where $\theta_i = (\ln D_A, \ln H, \ln A, \beta, \tilde{\sigma}_v^2, n_s, \alpha_s)$ for i = 1, 2,...,7, respectively, k_{max}=0.40 h Mpc^{-1}, where A is the overall amplitude of the power spectrum, β is the linear redshift distortion parameter, $\tilde{\sigma}_v^2$ is the calibrated 1-d velocity dispersion (see Eq. (2.21)), and n_s and α_s describe the shape of the initial (primordial) power spectrum:

$$P_{ini}(k) \propto k^{n_s + \frac{1}{2}\alpha_s \ln(k/k_{pivot})}. \tag{2.25}$$

Here, the weight function, $w(k, \mu)$, is one half of the so-called "effective volume,"

$$w(k,\mu) \equiv \frac{1}{2}\left[\frac{n_g P_g(k,\mu)}{1 + n_g P_g(k,\mu)}\right] V_{survey} \equiv \frac{1}{2} V_{eff}(k,\mu). \tag{2.26}$$

	none	$\ln A$	β	$\tilde{\sigma}_v^2$	n_s
$\Delta \ln D_A$ (%)	0.279	0.877	0.317	0.282	0.479
$\Delta \ln H$ (%)	0.437	0.786	1.124	0.801	0.509
$r_{D_A,H}$	0.382	-0.720	-0.309	0.082	-0.227
$\Delta \ln R$ (%)	0.187	0.762	0.317	0.259	0.386
	α_s	$\ln A$, β	β, $\tilde{\sigma}_v^2$	$\ln A$, $\tilde{\sigma}_v^2$	
$\Delta \ln D_A$ (%)	0.416	1.100	0.327	0.891	
$\Delta \ln H$ (%)	0.539	1.134	1.457	1.101	
$r_{D_A,H}$	-0.226	0.038	-0.383	-0.632	
$\Delta \ln R$ (%)	0.363	0.775	0.322	0.869	
	$\ln A$, β, $\tilde{\sigma}_v^2$	$\ln A$, n_s, α_s	$\ln A$, β, n_s α_s	$\ln A$, β, $\tilde{\sigma}_v^2$, n_s, α_s	
$\Delta \ln D_A$ (%)	1.101	1.089	1.233	1.250	
$\Delta \ln H$ (%)	1.468	0.984	1.362	1.530	
$r_{D_A,H}$	0.005	-0.820	-0.199	-0.098	
$\Delta \ln R$ (%)	0.879	0.974	1.000	1.014	

Table 2.1: The fractional errors in D_A and H, and their cross-correlation coefficients, $r_{D_A,H}$, and the fractional errors in the combined 1-d distance scale, R (Eq. (2.29)), marginalized ver several combinations of parameters: $\ln A$, β, $\tilde{\sigma}_v^2$, α_s and n_s. The cosmological parameters are taken from Table 1 of the Komatsu et al. (2010a) ("WMAP+BAO+SN ML"). The survey parameters approximate those of HETDEX: the survey area and target redshift are 420 deg^2 and $1.9 < z < 3.5$, respectively, the number of galaxies is $N_g = 0.755 \times 10^6$, and the bias is assumed to be linear with $b_1 = 2.5$.

The effective volume is equal to the actual survey volume, V_{survey}, in the sampling variance dominated regime, $P_g(k,\mu) \gg 1/n_g$, whereas it is small in the shot-noise dominated regime, $P_g(k,\mu) \ll 1/n_g$. In Figure 2.4 we show $n_g P_g(k,\mu)$ for $N_g = 0.755 \times 10^6$ and $b_1 = 2.5$ as a function of z. The factor of 1/2 accounts for symmetry in $\mathbf{k} \to -\mathbf{k}$. The derivatives of $\ln P_g(k,\mu)$ with respect to θ_i are calculated and given in the Appendix A.2.

Unlike for BAOs, which are insensitive to the parameters that affect the overall shape, for the full modeling we need to make sure that we take into account potential degeneracy between D_A and H and any other parameters that affect the overall shape. In this paper we include $\ln A$, β, $\tilde{\sigma_v}^2$, n_s, and α_s. (We shall comment on the effects non-linear bias in § 2.3.3).

We study the effects of marginalization over various parameter combinations by taking the submatrix, $\bar{F}_{ij}$, of the full 7×7 matrix with the index, i, of θ_i running from 1 to 7, such that the submatrix includes the matrix components of desired parameters to be marginalized. In other words, the parameters that are not included in the submatrix are fixed and not marginalized over.

Then, we compute the marginalized errors in $\ln D_A$ and $\ln H$ as

$$\sigma_{\ln D_A} = \sqrt{(\bar{F}^{-1})_{11}}, \tag{2.27}$$

$$\sigma_{\ln H} = \sqrt{(\bar{F}^{-1})_{22}}. \tag{2.28}$$

To simplify the analysis, we fix all the other cosmological parameters, such as $f(z)$, $\Omega_b h^2$, etc. These cosmological parameters will be determined by the future CMB mission, Planck, accurately, and therefore it is a good approximation to simply fix them, and vary only $\ln D_A$, $\ln H$, A, β, $\tilde{\sigma}_v^2$, n_s and α_s. The fiducial value for the bias is set to $b_1 = 2.5$ and $f = d \ln D / d \ln a$ is computed from the fiducial cosmological model.[8] We expect that the analysis

---

[8] One might also wish to marginalize over f for the following reason: while f can be calculated from the cosmological parameters assuming the validity of General Relativity, one might choose to let f free and use it for testing the validity of General Relativity. In this paper we chose to assume the validity of General Relativity, but one can extend our analysis to let f free in a straightforward manner.

of the bispectrum (Fourier transform of three-point function) will give a precise determination of b_1 (as well as non-linear bias parameters such as b_2) (Sefusatti & Komatsu, 2007), and therefore it is also a good approximation to simply fix it. However, we also explore a more conservative case where we do not know what b_1 is, i.e., we marginalize over the overall amplitude as well as β. In the future work we also plan to investigate the effect of marginalization over b_2, using a joint analysis of the power spectrum and bispectrum. Therefore, our calculation presented here will provide the lower limit to the errors in $\ln D_A$ and $\ln H$ expected from the full modeling of the power spectrum measured in a survey like HETDEX. We use the same survey parameters that we have used in § 2.3.1, and we integrate Eq. (2.24) up to $k_{max} = 0.40\ h\ \mathrm{Mpc}^{-1}$.

In Figure 2.3 we show the resulting error ellipses from the full modeling, in the smaller, solid contours, with four choices of marginalization. (We present the results from more choices of marginalization in Table 2.1.) First, for all choices of marginalization we find that the sizes of the errors in both D_A and H are substantially smaller than those from the BAO-only analysis with the FITEX-2d. For example, determinations of both D_A and H are improved by more than a factor of two in the case of the amplitude marginalization. This is expected, as we are able to use more information encoded in the power spectrum; namely, the Hubble horizon at the matter-radiation equality epoch and the Silk damping scale. Second, D_A and H are *anti-correlated* for the amplitude marginalization, with the cross-correlation coefficient of $r = -0.72$ (see top-left panel of Fig. 2.3), as opposed to a positive correlation seen in the BAO-only analysis. This is due to the marginalization over the overall amplitude: if we fixed the overall normalization, then we would still find a positive correlation between D_A and H with $r = 0.38$.

The origin of the negative correlation is the so-called Alcock-Paczynski (AP) test (Alcock & Paczynski, 1979): when the redshift space distortion is known perfectly well, the departure of the power spectrum in redshift space from isotropy, i.e., the dependence of $P(k, \mu)$ on μ, can be used to determine $D_A H$, resulting in $r = -1$ for a power-law power spectrum. The contributions from the departures of $P(k)$ from a pure power-law, i.e., the existence of "standard rulers," such as BAOs, the Hubble horizon at the matter-radiation equality and the Silk damping scale, make r bigger than -1. (See Appendix A.3 for more details.) When $\ln A$ and β are marginalized over simultaneously, the correlation between D_A and H nearly disappears: the AP test no longer works when we marginalize over the linear redshift space distortion. We find $r = 0.038$ (see top-right panel of Fig. 2.3).

When $\ln A$ is marginalized over while the other parameters (β, $\tilde{\sigma}_v^2$, n_s, and α_s) are held fixed, we find 0.88% and 0.79% errors on D_A and H, respectively, with $r = -0.72$. The more parameters we marginalize over, the greater the cross-correlation coefficient between D_A and H as well as the errors on D_A and H become. Note that the increase in the errors does not necessarily imply the decrease in the statistical power in constraining dark energy properties: since the cross-correlation coefficient is also reduced, the error in the combined 1-d distance scale, R, is much less affected by the marginalization (see Table 2.1). The error in $\ln R$ has been computed as (Seo & Eisenstein, 2007):

$$\sigma^2_{\ln R} = \frac{\sigma^2_{\ln D_A}(1-r^2)}{1+2r\sigma_{\ln D_A}/\sigma_{\ln H}+\sigma^2_{\ln D_A}/\sigma^2_{\ln H}}. \tag{2.29}$$

Finally, the errors in D_A, H, and R for various choices of marginalization are: $(\sigma_{\ln D_A}, \sigma_{\ln H}, \sigma_{\ln R})$ = (0.88%, 0.79%, 0.76%), (1.10%, 1.13%, 0.78%), (1.10%, 1.47%, 0.88%), and (1.25%, 1.53%, 1.01%) for the marginalization over $\ln A$, $\ln A$ and β, $\ln A$, β and $\tilde{\sigma}_v^2$, and $\ln A$, β, $\tilde{\sigma}_v^2$, n_s and α_s, respectively (see Table 2.1 for more comprehensive list). This result should be compared with that from the BAO-only analysis: $(\sigma_{\ln D_A}, \sigma_{\ln H}, \sigma_{\ln R})$=(1.76%, 2.47%, 1.08%). It is clear that the full analysis, even with a generous set of marginalization choices, beats the BAO-only analysis with a significant gain in the distance determination accuracies.

2.3.3 Caveat for the full modeling

Our analysis presented in § 2.3.2 is too simplistic and optimistic, as it ignores any systematic errors due to our lack of understanding of the effects of various non-linearities in the power spectrum.

Among the three major non-linearities, non-linear matter clustering is under control, at least for high redshifts, i.e., $z \gtrsim 2$, as one can model non-linear evolution of matter fluctuations almost exactly by the 3rd-order perturbation theory (Jeong & Komatsu, 2006). While the nominal 3rd-order perturbation theory breaks down at lower redshifts, $z \sim 1$, there have been a number of studies aiming at improving upon our ability to compute $P(k)$

at $z \sim 1$ or even lower redshifts (Crocce & Scoccimarro, 2008; Matarrese & Pietroni, 2007; Taruya & Hiramatsu, 2008; Valageas, 2007; Matsubara, 2008; McDonald, 2007). Therefore, it is quite possible that the non-linear matter clustering will be fully under control in the near future, at least for the scales that are relevant to the BAO scales, i.e., $k \lesssim 0.40\ h\ \mathrm{Mpc}^{-1}$.

In a separate paper (Jeong & Komatsu, 2009), we show that non-linear galaxy biasing is also under control in the weakly non-linear regime. One can use the perturbation theory approach combined with the local bias assumption (Fry & Gaztanaga, 1993; McDonald, 2006) to model the galaxy power spectrum with non-linear bias.

The most problematic one is the non-linear redshift space distortion. Our understanding of non-linear redshift space distortion, especially the Finger-of-God (FoG) effect, is limited (Scoccimarro, 2004). Therefore, whether one can achieve the accuracy of D_A and H (H in particular) reported in Fig. 2.3 depends crucially on our ability to correct for the FoG effect. This is work in progress. Note that the marginalization over $\tilde{\sigma}_v^2$ should capture some of the increase in the errors in distance scales due to our ignorance of FoG.

2.4 Extraction of D_A and H from the Millennium Simulation

How realistic is our result for the determinations of D_A and H from the BAO phases using the FITEX-2d method? Since our Monte Carlo simulations used in § 2.3.1 are too simple, in this section we test the FITEX-2d method further by using the Millennium Simulation (Springel et al., 2005).

We use the Millennium Galaxy catalogue, generated by the semi analytical galaxy formation code (Bower et al., 2006; Benson et al., 2003; Cole et al., 2000). We have measured the two-dimensional power spectrum of galaxies in redshift space from the Millennium Simulation, and applied the FITEX-2d method to remove the smooth component. We then find the best-fitting D_A and H from the BAO phases extracted from the FITEX-2d. Again, we use the data up to $k_{max} = 0.40\ h\ \mathrm{Mpc}^{-1}$.

In Figure 2.5 we show the result. The best-fitting value that we find from the Millennium Simulation corresponds to one point at the center of the contours. We find the errors from the Monte Carlo simulations that we described in § 2.3.1 with the survey parameters replaced by those of the Millennium Simulation: $V_{survey} = (0.5\ h^{-1}\ \mathrm{Gpc})^3$, $n_g = 0.138\ h^3\ \mathrm{Mpc}^{-3}$, and $z = 3.06$. (There are 17,238,935 galaxies in the Millennium Simulation at $z = 3.06$.) For the theoretical power spectrum that we use for generating Monte Carlo simulations, we use the best-fitting power spectrum for the galaxy catalogue of the Millennium Simulation found in Jeong & Komatsu (2009).

Since the volume of the Millennium Simulation is $\sim$24 times as small as that would be surveyed by HETDEX, the uncertainties in D_A and H are larger for the Millennium Simulation. (Compare Fig. 2.5 with the larger contours of Fig. 2.3.) We find 5.1% and 6.8% errors on D_A and H, respectively, with the cross-correlation coefficient of $r = 0.43$, from the Monte Carlo simulations. These errors are larger than those from HETDEX Monte-Carlo simulation by a factor of two (rather than $\sqrt{24} \sim 5$) as the shot noise on the power spectrum of the Millennium Simulation is much smaller than that of HETDEX simulation.

The best-fitting values of D_A and H are well within 68% C.L. region, which indicates that the FITEX-2d is able to yield unbiased estimates of the BAO phases from the Millennium Simulation.

These results indicate that the FITEX-2d method that we have developed in this paper can be used for extracting the BAOs and measuring D_A and H safely from the real data. It would be interesting to apply the FITEX-2d method to the two-dimensional power spectrum measured from the SDSS LRG samples (Okumura et al., 2008), and extract D_A and H from them.

2.5 Error Propagation to The Dark Energy Equation of State

In § 2.3 and § 2.4, we have estimated errors in D_A and H from two different approaches, i.e., the BAO fitting using the FITEX-2d method and the full modeling. In this section, we propagate errors in D_A and H to those in the dark energy equation of state parameters. We parametrize $w(z)$ using the linear model, $w(z) = w_0 + w_a z/(1+z)$ (Linder, 2003; Chevallier & Polarski, 2001).

We propagate the errors in D_A and H to those in w_0 and w_a by

$$\tilde{F}_{\alpha\beta} = \sum_{ij} \frac{\partial p_i}{\partial q_\alpha} \frac{\partial p_j}{\partial q_\beta} F_{ij}, \tag{2.30}$$

where $\tilde{F}_{\alpha\beta}$ is the Fisher matrix for the dark energy parameters, F_{ij} is the Fisher matrix for D_A and H, $p_i = (\ln D_A, \ln H)$ for $i = 1$ and 2, and $q_\alpha = (w_0, w_a)$ for $\alpha = 1$ and 2.

Partial derivatives of D_A and H with respect to w_0 and w_a are given by

$$\begin{aligned}
\frac{\partial \ln D_A}{\partial w_0} &= -\frac{3}{2}\Omega_\Lambda \frac{\int_0^z \ln(1+z')f(z')g(z')^{-3/2}dz'}{\int_0^z g(z')^{-1/2}dz'}, & (2.31)\\
\frac{\partial \ln D_A}{\partial w_a} &= -\frac{3}{2}\Omega_\Lambda \frac{\int_0^z [\ln(1+z') - \frac{z'}{1+z'}]f(z')g(z')^{-3/2}dz'}{\int_0^z g(z')^{-1/2}dz'}, & (2.32)\\
\frac{\partial \ln H}{\partial w_0} &= \frac{3}{2}\Omega_\Lambda \ln(1+z)\frac{f(z)}{g(z)}, & (2.33)\\
\frac{\partial \ln H}{\partial w_a} &= \frac{3}{2}\Omega_\Lambda \left[\ln(1+z) - \frac{z}{1+z}\right]\frac{f(z)}{g(z)}, & (2.34)
\end{aligned}$$

where $f(z)$ and $g(z)$ are given by

$$\begin{aligned}
f(z) &= \exp\left(3\int_0^z \frac{1+w_0+w_a\frac{z'}{1+z'}}{1+z'}dz'\right), & (2.35)\\
g(z) &= \Omega_m(1+z)^3 + \Omega_\Lambda f(z). & (2.36)
\end{aligned}$$

Figure 2.6 shows the derivatives as a function of z between $0.5 \le z \le 6.5$ in two different cosmological models, (w_0, w_a)=(-1.0, 0.0) and (-1.1, 0.5). The former is the ΛCDM model, while the latter resembles the maximum likelihood values of w_0 and w_a from the WMAP+BAO+SN+BBN (Komatsu et al., 2010a). The derivatives are similar for these cosmological models, and therefore we use the ΛCDM model as the fiducial model for computing the derivatives.

We add the distance information from CMB as

$$\tilde{F}^{total}_{\alpha\beta}(z) = \tilde{F}^{CMB}_{\alpha\beta} + \tilde{F}^{gal}_{\alpha\beta}(z), \tag{2.37}$$

where we assume that the CMB experiment yields 1% determination of the angular diameter distance out to $z = 1090$, i.e., we use

$$\tilde{F}^{CMB}_{\alpha\beta} = 10^4 \frac{\partial \ln D_A(z=1090)}{\partial q_\alpha} \frac{\partial \ln D_A(z=1090)}{\partial q_\beta}. \tag{2.38}$$

We are interested in how the BAO-only analysis compares with the full modeling. In Fig. 2.7 we show the projected error contours on w_0 and w_a calculated from the BAO-only analysis with the FITEX-2d and those from the full analysis at four redshift bins: $0.5 \le z \le 1.5$, $1.5 \le z \le 2.5$, $2.5 \le z \le 3.5$, and $3.5 \le z \le 4.5$. The survey area and the number of galaxies are 420 deg^2 and $N_g = 2.9 \times 10^6$ for all redshift bins. From the BAO-only analysis we find $(\Delta w_0, \Delta w_a) = (0.29, 1.26)$, $(0.38, 1.39)$, $(0.55, 1.92)$, and $(0.91, 3.18)$, whereas from the full modeling we find $(\Delta w_0, \Delta w_a) = (0.09, 0.27)$, $(0.06, 0.17)$, $(0.09, 0.35)$, and $(0.17, 0.68)$, for $0.5 \le z \le 1.5$, $1.5 \le z \le 2.5$, $2.5 \le z \le 3.5$, and $3.5 \le z \le 4.5$, respectively.

We therefore conclude that the full analysis yields much better constraints on w_0 and w_a than the BAO-only analysis.

2.6 Conclusion

In this paper we have developed a method, called the FITEX-2d method, to extract the two-dimensional phases of BAOs from galaxy power spectra in redshift space. Our model builds on and extends the existing one-dimensional algorithm, called FITEX, developed by Koehler et al. (2007).

Our method removes the smooth, non-oscillating component from the observed galaxy power spectrum in redshift space. The fitting function consists of the smooth one-dimensional spectrum that depends only on k, $P^{1d}_{smooth}(k)$ given by Eq. (2.9), multiplied by the angle-dependent function expanded in the Legendre polynomials with even multipoles. The coefficients of the Legendre polynomials contain even powers of k. The resulting function, given by Eq. (2.10), is able to capture the non-oscillating part of the galaxy power spectrum well.

We have tested the FITEX-2d method using the analytical model without any noise, the Monte Carlo realizations with noise expected from the HETDEX experiment (Hill et al., 2004), and the galaxy catalogue created from the Millennium Simulation (Springel et al., 2005). In all cases the FITEX-2d method yields unbiased estimates of the angular diameter distance, D_A, and the expansion rate, H.

However, the BAOs capture only a part of distance information encoded in the galaxy power spectrum. To exploit the distance information, especially the equality scale, $r_H(z_{eq})$, we have explored the constraints on D_A and H from the full modeling of the galaxy power spectrum in redshift space. Provided that three key non-linearities (non-linear matter clustering, non-linear galaxy bias, and non-linear redshift space distortion) are under control, we find that the full modeling yields the constraints that are better than the BAO-only analysis by more than a factor of two both in D_A and H, and the dark energy parameters such as w_0 and w_a.

While the effects of non-linear matter clustering (Jeong & Komatsu, 2006; Crocce & Scoccimarro, 2008; Matarrese & Pietroni, 2007; Taruya & Hiramatsu, 2008; Valageas, 2007; Matsubara, 2008; McDonald, 2007) and non-linear galaxy bias (Jeong & Komatsu, 2009) are being understood in the weakly non-linear regime that is relevant to the future galaxy surveys, the effects of non-linear redshift space distortion are poorly understood. While the FITEX-2d method that we have developed in this paper are useful for obtaining *robust* constraints on D_A and H, hence the dark energy properties, one must understand non-linear redshift space distortion to fully exploit the full information content of the galaxy power spectrum in redshift space. We would then be able to reduce the errors in D_A and H by more than a factor of two.

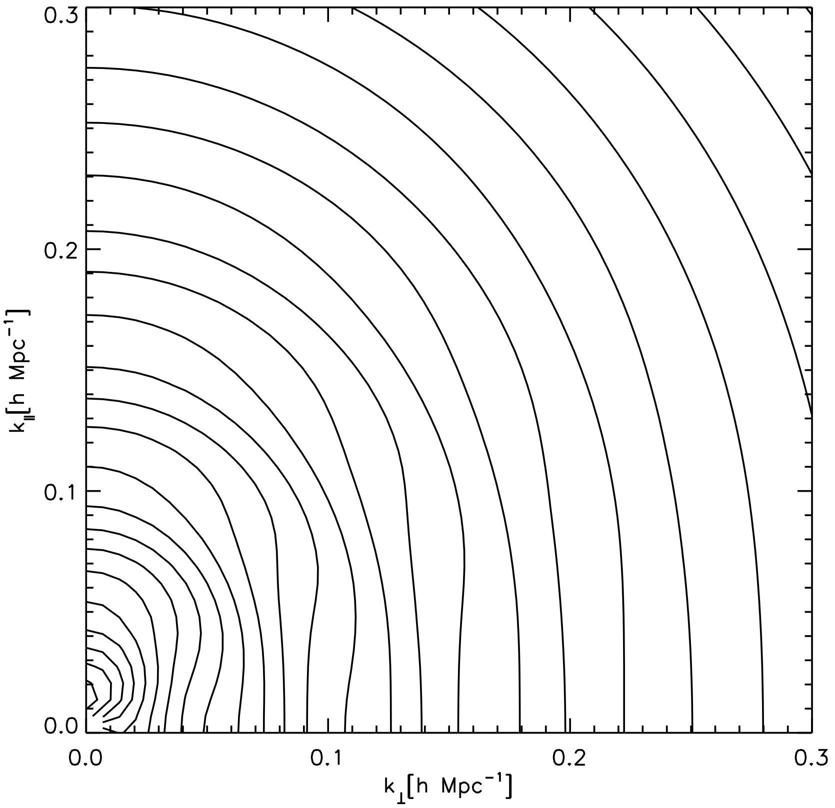

Figure 2.1: Illustration of the FITEX-2d method. This figure shows an anisotropic non-linear galaxy power spectrum before we apply FITEX-2d. The contours show $\ln[P(k_{\parallel}, k_{\perp})]$ at $z = 2$, where we have computed $P(k_{\parallel}, k_{\perp})$ from Eq. (2.21). Anisotropic distribution of power due to redshift space distortion is apparent.

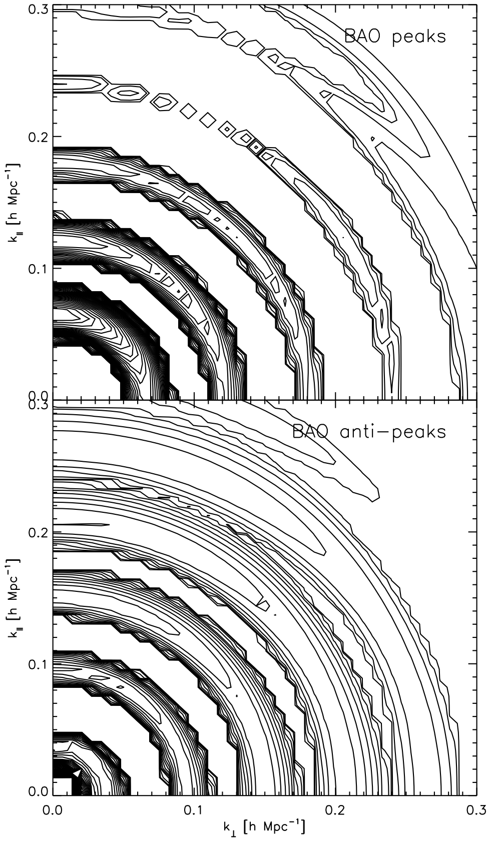

Figure 2.2: Illustration of the FITEX-2d method. This figure shows the power spectrum shown in Fig. 2.1 minus the best-fitting two-dimensional smooth spectrum, $P^{2d}_{smooth}(k_\parallel, k_\perp)$, given by Eq.(2.10). The structure of BAOs, i.e., the oscillatory feature, is now apparent. The FITEX-2d method recovers the isotropic distribution of the BAO phases successfully, which makes it possible to use the distribution of the phases for measuring D_A and H simultaneously. (*Top*) Positive BAO peaks. (*Bottom*) Negative BAO peaks (troughs).

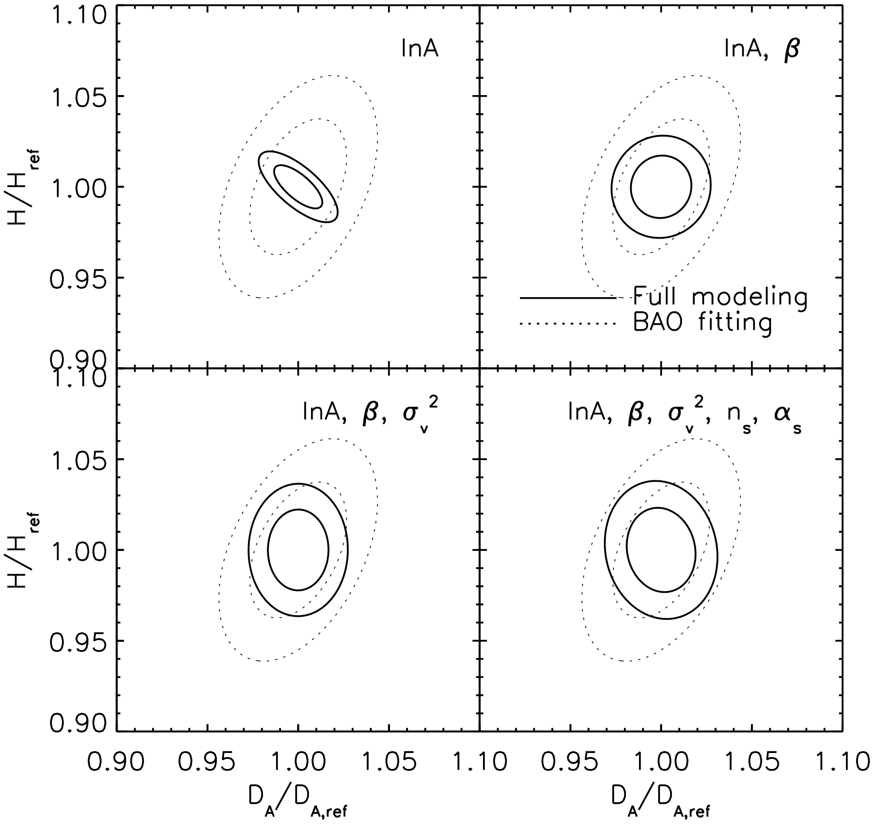

Figure 2.3: Accuracy of D_A and H extracted from BAOs with the FITEX-2d method applied to simulated Monte Carlo realizations that approximate the HETDEX survey (the larger, dotted contours; see § 2.3.1). The best-fitting values of D_A and H agree with the true values; thus, the FITEX-2d method yields unbiased estimates of D_A and H. The solid contours show D_A and H from the full modeling, including the overall shape of the power spectrum, with various parameters marginalized over. (Note that the BAO-only contours are unaffected by the marginalization.) For this we have used the Fisher matrix forecast (see § 2.3.2). The inner and outer ellipses show 68% and 95% C.L., respectively. (*Top Left*) the full modeling Fisher matrix is marginalized over the overall amplitude, $\ln A$, (*Top Right*) marginalized over $\ln A$ and the linear redshift distortion parameter, β, (*Bottom Left*) marginalized over $\ln A$, β, and the velocity dispersion in the FoG factor, $\tilde{\sigma}_v^2$, (*Bottom Right*) marginalized over $\ln A$, β, $\tilde{\sigma}_v^2$, and the shape of the initial power spectrum, n_s and α_s.

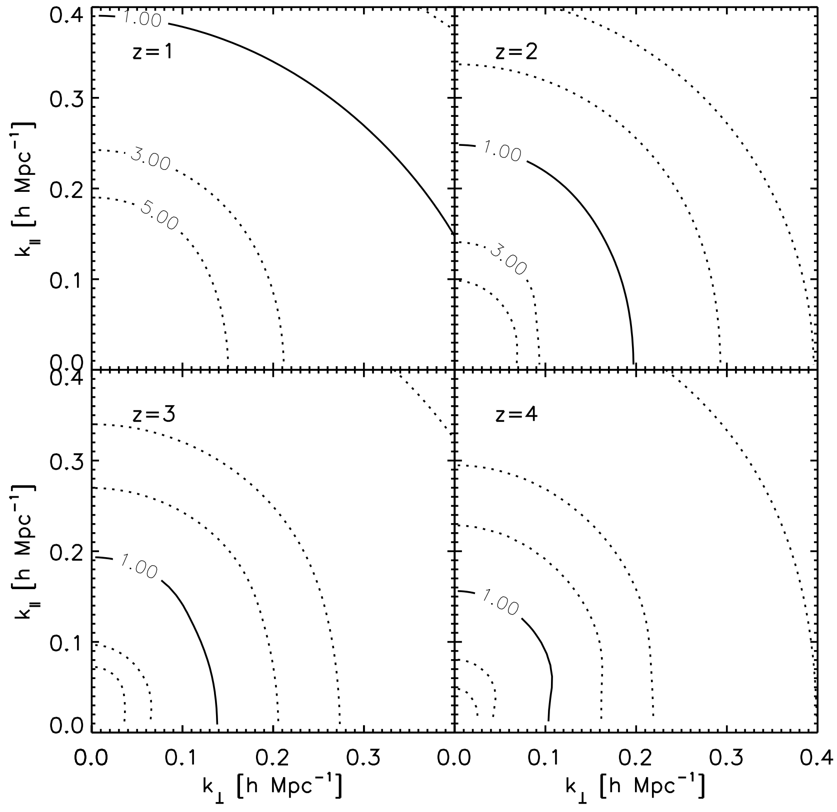

Figure 2.4: The galaxy power spectrum times the number density of galaxies, $n_g P_g(k, \mu)$, where the number of the galaxies is fixed for each redshift bin to $N_g = 0.755 \times 10^6$, and $P_g(k, \mu)$ is computed from Eq. (2.21) with $b_1 = 2.5$. The shot noise dominates the error budget when $n_g P_g(k, \mu) < 1$. Contour values are [0.1, 0.3, 0.5, 1.0, 3.0, 5.0]. (*Top Left*) $z = 1$, (*Top Right*) $z = 2$, (*Bottom Left*) $z = 3$, (*Bottom Right*) $z = 4$.

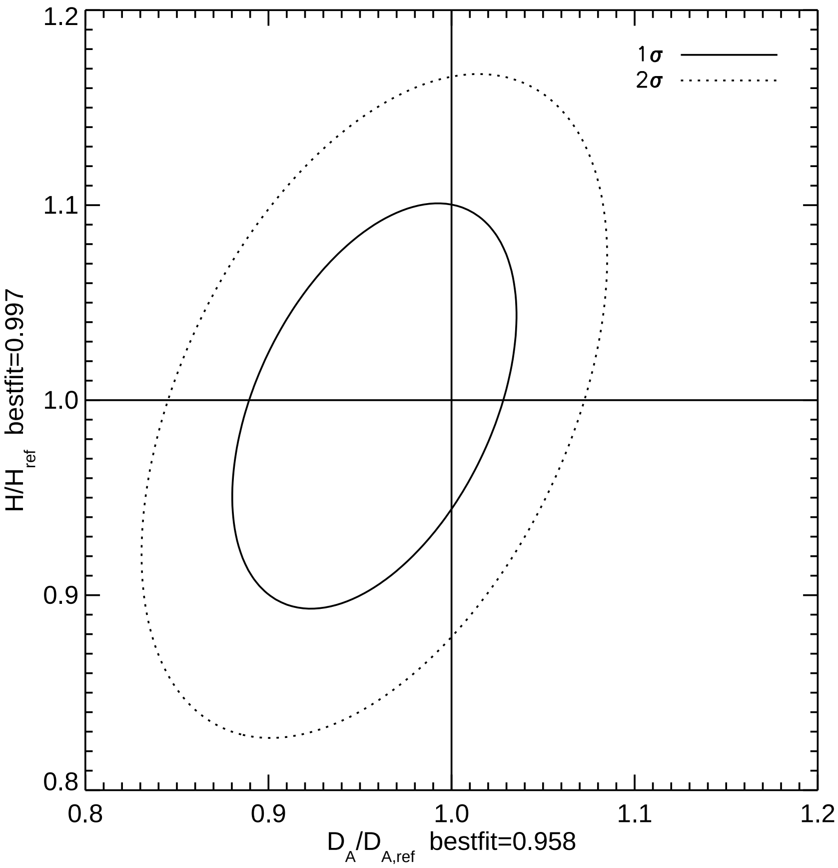

Figure 2.5: Accuracy of D_A and H extracted from BAOs with the FITEX-2d method applied to the Millennium Galaxy Simulation in redshift space at $z = 3$ (Springel et al., 2005; Bower et al., 2006; Benson et al., 2003; Cole et al., 2000). The best-fitting values of D_A and H agree with the true values to within statistical errors of the Millennium Simulation; thus, the FITEX-2d method also yields unbiased estimates of D_A and H for the Millennium Simulation. The solid and dotted lines show 68% and 95% C.L., respectively.

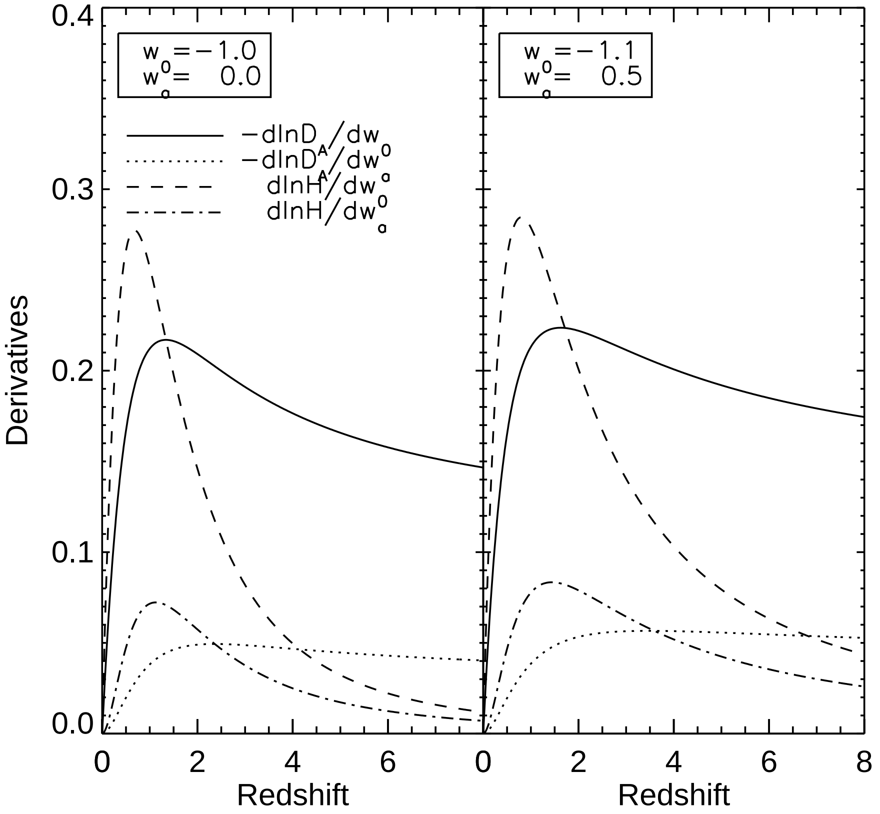

Figure 2.6: Partial derivatives of $\ln D_A$ and $\ln H$ with respect to the dark energy equation of state parameters, w_0 and w_a, as a function of z for two different cosmological models. (*Left*) $(w_0, w_a) = (-1.0, 0.0)$. (*Right*) $(w_0, w_a) = (-1.1, 0.5)$.

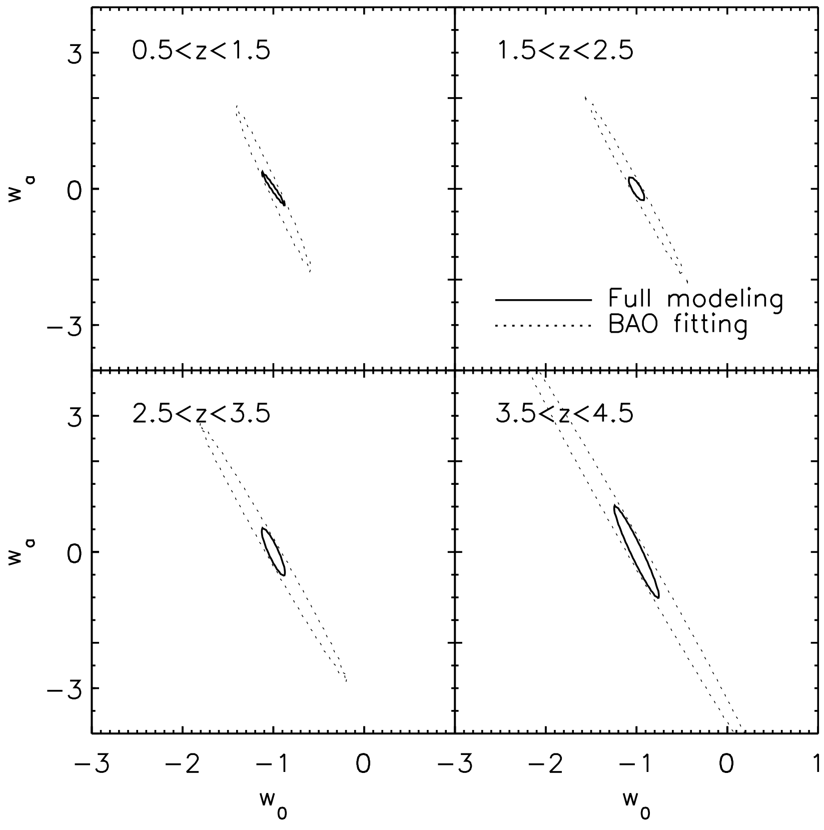

Figure 2.7: Projected 68% constraints on the dark energy parameters, w_0 and w_a: the BAO fitting with the FITEX-2d method (dotted) versus the full modeling (solid). For both cases, we use the power spectrum up to $k_{max} = 0.40\ h\ \mathrm{Mpc}^{-1}$, and we assume that the CMB experiment measures the angular diameter distance out to $z = 1090$ with 1% accuracy. The survey area and the number of galaxies are 420 deg^2 and $N_g = 0.755 \times 10^6$ for all cases. (*Top Left*) $0.5 \leq z \leq 1.5$, (*Top Right*) $1.5 \leq z \leq 2.5$, (*Bottom Left*) $2.5 \leq z \leq 3.5$, (*Bottom Right*) $3.5 \leq z \leq 4.5$.

Chapter 3

Third-order Perturbation Theory With Non-linear Pressure

In this chapter, we calculate the non-linear matter power spectrum using the 3rd-order perturbation theory without ignoring the pressure gradient term. We consider a semi-realistic system consisting of two matter components with and without pressure, and both are expanded into the 3rd order in perturbations in a self-consistent manner, for the first time. While the pressured component may be identified with baryons or neutrinos, in this paper we mainly explore the physics of the non-linear pressure effect using a toy model in which the Jeans length does not depend on time. [1]

3.1 Introduction

Pressure plays an important role for the structure formation in the universe. Pressure determines the Jeans scale, λ_J, below which the growth of structure slows down, and eventually stops and oscillates: while fluctuations in the cold dark matter (CDM) and the pressured component evolve in the same

---

[1] A significant part of this chapter was originally published in the Astrophysical Journal by Shoji, M. & Komatsu, E. Reproduced by permission of the American Astronomical Society.

way above the Jeans scale, their evolutions are significantly different below the Jeans scale.

The dominant source of gravity is CDM, which is cold and its velocity dispersion is negligible before the collapse of halos. However, the sub-dominant matter components - baryons and neutrinos - have significant velocity dispersions, which should be included in the calculation when precision is required. While the accurate calculations have been done for the linear perturbations, the effects of the pressure on the non-linear evolution of matter fluctuations on cosmological scales ($\sim 10 - 100$ Mpc) have not been studied very much in the literature.

We address this issue by calculating the non-linear matter power spectrum using the 3rd-order perturbation theory (3PT; see Bernardeau et al., 2002, for a review), with the pressure gradient term in the Euler equation explicitly included. This enables us to study the effects of the pressure on the non-linear evolution of matter fluctuations in a self-consistent manner.

The rest of this paper is organized as follows. In § 3.2, we find the linear, second-order, and third-order solutions of the coupled continuity, Euler, and Poisson equations for two matter components with and without the pressure gradient. In § 3.3, we calculate the non-linear matter power spectrum from the solutions obtained in § 3.2. In § 3.4, we compare our full 3PT calculation with the approximation used by Saito et al. (2008) for the effects of massive neutrinos on the matter power spectrum. Finally, in § 3.5, we discuss the implications of our results for a few practical astrophysical and cosmological applications. In Appendices we give the detailed derivations of the 3PT results used in the main body of the paper.

3.2 Third-order Perturbation Theory with Pressure

3.2.1 Basic Equations

The main goal of this paper is to find the perturbative solutions for the CDM density contrast, δ_c, for which the pressure gradient is ignored, and the density contrast of another matter component, δ_b, for which the pressure gradient is retained. This component may be identified with baryons (hence the subscript "b") or neutrinos, depending on the sound speed one uses in the Euler equation.[2]

The equations that we are going to solve include two continuity equations:

$$\dot{\delta}_c(\mathbf{x},\tau) + \nabla \cdot [(1+\delta_c(\mathbf{x},\tau))\mathbf{v}_c(\mathbf{x},\tau)] = 0, \tag{3.1}$$

$$\dot{\delta}_b(\mathbf{x},\tau) + \nabla \cdot [(1+\delta_b(\mathbf{x},\tau))\mathbf{v}_b(\mathbf{x},\tau)] = 0, \tag{3.2}$$

two Euler equations:

$$\dot{\mathbf{v}}_c(\mathbf{x},\tau) + [\mathbf{v}_c(\mathbf{x},\tau)\cdot\nabla]\mathbf{v}_c(\mathbf{x},\tau) = -\frac{\dot{a}}{a}\mathbf{v}_c(\mathbf{x},\tau) - \nabla\phi(\mathbf{x},\tau), \tag{3.3}$$

$$\begin{aligned}\dot{\mathbf{v}}_b(\mathbf{x},\tau) + [\mathbf{v}_b(\mathbf{x},\tau)\cdot\nabla]\mathbf{v}_b(\mathbf{x},\tau) &= -\frac{\dot{a}}{a}\mathbf{v}_b(\mathbf{x},\tau) - \nabla\phi(\mathbf{x},\tau) \\ &\quad -\frac{c_s^2(\mathbf{x},\tau)\nabla\delta_b(\mathbf{x},\tau)}{1+\delta_b(\mathbf{x},\tau)},\end{aligned} \tag{3.4}$$

---

[2] While we use "b" to denote the pressured matter component throughout this paper, we do not always mean baryons, but we we always refer to a general matter component with pressure.

and one Poisson equation:

$$\nabla^2\phi(\mathbf{x},\tau) = 4\pi G a^2[\bar{\rho}_c(\tau)\delta_c(\mathbf{x},\tau) + \bar{\rho}_b(\tau)\delta_b(\mathbf{x},\tau)], \qquad (3.5)$$

where $\delta_i \equiv (\rho_i - \bar{\rho}_i)/\bar{\rho}_i$ is the density contrast of a matter component $i = (c, b)$, $\bar{\rho}$ the background matter density, a the scale factor, $\mathbf{v}_i$ the peculiar velocity field of a matter component i, ϕ the gravitational potential, and c_s the sound speed of the matter component with pressure. Here, the dots denote the partial derivatives with respect to the conformal time, τ, i.e., $\dot{\delta} = \partial\delta/\partial\tau$, and ∇ denotes the partial derivatives with respect to the comoving coordinates.

We rewrite the Poisson equation as

$$\nabla^2\phi(\mathbf{x},\tau) = \frac{6}{\tau^2}\delta(\mathbf{x},\tau), \qquad (3.6)$$

where we have assumed an Einstein-de Sitter (EdS) universe (we shall generalize the results to other cosmological models later), for which the energy density of the universe is dominated entirely by the matter density, and $a \propto \tau^2$. The background Friedmann equation is given by

$$\frac{8\pi G}{3}[\bar{\rho}_c(\tau) + \bar{\rho}_b(\tau)]a^2 = \frac{4}{\tau^2}. \qquad (3.7)$$

We have also defined the total matter fluctuation, δ, which is given by

$$\delta(\mathbf{x},\tau) \equiv \frac{\bar{\rho}_c(\tau)\delta_c(\mathbf{x},\tau) + \bar{\rho}_b(\tau)\delta_b(\mathbf{x},\tau)}{\bar{\rho}_c(\tau) + \bar{\rho}_b(\tau)} = f_c\delta_c(\mathbf{x},\tau) + f_b\delta_b(\mathbf{x},\tau), \qquad (3.8)$$

where $f_c \equiv \bar{\rho}_c/(\bar{\rho}_c + \bar{\rho}_b) = \Omega_c/\Omega_m$, and $f_b \equiv \bar{\rho}_b/(\bar{\rho}_c + \bar{\rho}_b) = \Omega_b/\Omega_m$. For an EdS universe, $\Omega_m = 1$.

Taking the divergence of the Euler equations, we obtain the equations for the velocity divergence fields, $\theta_i \equiv \nabla \cdot \mathbf{v}_i$. Moving non-linear terms to the right hand side (RHS) of the equations and using the Poisson equation, we obtain

$$\begin{aligned}
\dot{\delta}_c(\mathbf{x},\tau) + \theta_c(\mathbf{x},\tau) &= -\nabla \cdot [\delta_c(\mathbf{x},\tau)\mathbf{v}_c(\mathbf{x},\tau)], && (3.9)\\
\dot{\delta}_b(\mathbf{x},\tau) + \theta_b(\mathbf{x},\tau) &= -\nabla \cdot [\delta_b(\mathbf{x},\tau)\mathbf{v}_b(\mathbf{x},\tau)], && (3.10)\\
\dot{\theta}_c(\mathbf{x},\tau) + \frac{2}{\tau}\theta_c(\mathbf{x},\tau) + \frac{6}{\tau^2}\delta(\mathbf{x},\tau) &= -\nabla \cdot \{[\mathbf{v}_c(\mathbf{x},\tau) \cdot \nabla]\mathbf{v}_c(\mathbf{x},\tau)\}\,, && (3.11)\\
\dot{\theta}_b(\mathbf{x},\tau) + \frac{2}{\tau}\theta_b(\mathbf{x},\tau) + \frac{6}{\tau^2}\delta(\mathbf{x},\tau) &= -\nabla \cdot \{[\mathbf{v}_b(\mathbf{x},\tau) \cdot \nabla]\mathbf{v}_b(\mathbf{x},\tau)\} \\
&- \nabla \cdot \left[\frac{c_s^2(\mathbf{x},\tau)\nabla\delta_b(\mathbf{x},\tau)}{1+\delta_b(\mathbf{x},\tau)}\right]. && (3.12)
\end{aligned}$$

Note that the second term in the RHS of eq. [3.12] still contains the linear order term. All the other terms in the RHS of the above equations are non-linear.

We shall simplify the pressure term, the second term in the RHS of eq. [3.12], as follows. First, we shall assume that the sound speed is homogeneous, i.e., $\nabla c_s^2 = 0$. See Naoz & Barkana (2005) for the analysis of linear perturbations with $\nabla c_s^2 \neq 0$. Second, we expand the pressure term to the 3rd order in perturbations:

$$\frac{\nabla \delta\rho_b}{\rho_b} = \frac{\nabla\delta_b}{1+\delta_b} \simeq \nabla\delta_b - \delta_b\nabla\delta_b + \delta_b^2\nabla\delta_b + \mathcal{O}(\delta_b^4). \qquad (3.13)$$

Going to Fourier space, we obtain

$$\begin{aligned}&\dot{\tilde{\delta}}_c(\mathbf{k},\tau)+\tilde{\theta}_c(\mathbf{k},\tau)\\&=-\frac{1}{(2\pi)^3}\int\!\!\int d\mathbf{q}_1 d\mathbf{q}_2\delta_D(\mathbf{q}_1+\mathbf{q}_2-\mathbf{k})\frac{\mathbf{k}\cdot\mathbf{q}_1}{q_1^2}\tilde{\theta}_c(\mathbf{q}_1,\tau)\tilde{\delta}_c(\mathbf{q}_2,\tau),\end{aligned} \tag{3.14}$$

$$\begin{aligned}&\dot{\tilde{\delta}}_b(\mathbf{k},\tau)+\tilde{\theta}_b(\mathbf{k},\tau)\\&=-\frac{1}{(2\pi)^3}\int\!\!\int d\mathbf{q}_1 d\mathbf{q}_2\delta_D(\mathbf{q}_1+\mathbf{q}_2-\mathbf{k})\frac{\mathbf{k}\cdot\mathbf{q}_1}{q_1^2}\tilde{\theta}_b(\mathbf{q}_1,\tau)\tilde{\delta}_b(\mathbf{q}_2,\tau),\end{aligned} \tag{3.15}$$

$$\begin{aligned}&\dot{\tilde{\theta}}_c(\mathbf{k},\tau)+\frac{2}{\tau}\tilde{\theta}_c(\mathbf{k},\tau)+\frac{6}{\tau^2}\tilde{\delta}(\mathbf{k},\tau)\\&=-\frac{1}{(2\pi)^3}\int\!\!\int d\mathbf{q}_1 d\mathbf{q}_2\delta_D(\mathbf{q}_1+\mathbf{q}_2-\mathbf{k})\frac{k^2(\mathbf{q}_1\cdot\mathbf{q}_2)}{2q_1^2q_2^2}\tilde{\theta}_c(\mathbf{q}_1,\tau)\tilde{\theta}_c(\mathbf{q}_2,\tau),\end{aligned} \tag{3.16}$$

$$\begin{aligned}&\dot{\tilde{\theta}}_b(\mathbf{k},\tau)+\frac{2}{\tau}\tilde{\theta}_b(\mathbf{k},\tau)+\frac{6}{\tau^2}\tilde{\delta}(\mathbf{k},\tau)\\&=-\frac{1}{(2\pi)^3}\int\!\!\int d\mathbf{q}_1 d\mathbf{q}_2\delta_D(\mathbf{q}_1+\mathbf{q}_2-\mathbf{k})\frac{k^2(\mathbf{q}_1\cdot\mathbf{q}_2)}{2q_1^2q_2^2}\tilde{\theta}_b(\mathbf{q}_1,\tau)\tilde{\theta}_b(\mathbf{q}_2,\tau)\\&\qquad\qquad-\mathcal{F}\left[\nabla\cdot\left(\frac{c_s^2(\tau)\nabla\delta_b(\mathbf{x},\tau)}{1+\delta_b(\mathbf{x},\tau)}\right)\right](\mathbf{k}),\end{aligned} \tag{3.17}$$

where

$$\begin{aligned}&\mathcal{F}\left[\nabla\cdot\left(\frac{c_s^2(\tau)\nabla\delta_b(\mathbf{x},\tau)}{1+\delta_b(\mathbf{x},\tau)}\right)\right](\mathbf{k})\\&\equiv -k^2c_s^2(\tau)\left[\tilde{\delta}_b(\mathbf{k})-\frac{1}{2(2\pi)^3}\int\!\!\int d\mathbf{q}_1 d\mathbf{q}_2\tilde{\delta}_b(\mathbf{q}_1,\tau)\tilde{\delta}_b(\mathbf{q}_2,\tau)\delta_D(\mathbf{q}_1+\mathbf{q}_2-\mathbf{k})\right.\\+&\left.\frac{1}{3(2\pi)^6}\int\!\!\int\!\!\int d\mathbf{q}_1 d\mathbf{q}_2 d\mathbf{q}_3\tilde{\delta}_b(\mathbf{q}_1,\tau)\tilde{\delta}_b(\mathbf{q}_2,\tau)\tilde{\delta}_b(\mathbf{q}_3,\tau)\delta_D(\mathbf{q}_1+\mathbf{q}_2+\mathbf{q}_3-\mathbf{k})\right].\end{aligned} \tag{3.18}$$

In the subsequent subsections we shall solve these coupled equations perturbatively. Hereafter we shall omit the tildes on the perturbation variables in Fourier space.

3.2.2 Linear Order Solution: Jeans Filtering Scale

In the linear order, one finds

$$\dot{\delta}_{1,c}(\mathbf{k},\tau) + \theta_{1,c}(\mathbf{k},\tau) = 0, \tag{3.19}$$

$$\dot{\delta}_{1,b}(\mathbf{k},\tau) + \theta_{1,b}(\mathbf{k},\tau) = 0, \tag{3.20}$$

$$\dot{\theta}_{1,c}(\mathbf{k},\tau) + \frac{2}{\tau}\theta_{1,c}(\mathbf{k},\tau) + \frac{6}{\tau^2}\delta_1(\mathbf{k},\tau) = 0, \tag{3.21}$$

$$\dot{\theta}_{1,b}(\mathbf{k},\tau) + \frac{2}{\tau}\theta_{1,b}(\mathbf{k},\tau) + \frac{6}{\tau^2}\delta_1(\mathbf{k},\tau) - k^2c_s^2(\tau)\delta_{1,b}(\mathbf{k},\tau) = 0, \tag{3.22}$$

where the subscripts "1" mean that these quantities denote the first-order perturbations, and $\delta_1 = f_c\delta_{1,c} + f_b\delta_{1,b}$. We rewrite eq. [3.22] as

$$\dot{\theta}_{1,b}(\mathbf{k},\tau) + \frac{2}{\tau}\theta_{1,b}(\mathbf{k},\tau) + \frac{6}{\tau^2}\left[\delta_1(\mathbf{k},\tau) - \frac{k^2c_s(\tau)^2\tau^2}{6}\delta_{1,b}(\mathbf{k},\tau)\right] = 0,$$

$$\dot{\theta}_{1,b}(\mathbf{k},\tau) + \frac{2}{\tau}\theta_{1,b}(\mathbf{k},\tau) + \frac{6}{\tau^2}\left[\delta_1(\mathbf{k},\tau) - \frac{k^2}{k_J^2}\delta_{1,b}(\mathbf{k},\tau)\right] = 0, \tag{3.23}$$

where we have used the usual definition of the Jeans wavenumber, k_J:

$$k_J(\tau) \equiv \frac{\sqrt{6}}{c_s(\tau)\tau}. \tag{3.24}$$

The Jeans wavenumber divides the solutions for $\delta_{1,b}$ into two classes: the growing solution for $k \ll k_J$, and the oscillatory solution for $k \gg k_J$, *when there is no CDM,* i.e., $f_b = 1$ and $\delta_1 = \delta_{1,b}$. When $\delta_1 \neq \delta_{1,b}$, the Jeans wavenumber does not provide a dividing scale for the solutions of $\delta_{1,b}$.

The Jeans wavenumber depends on the temperature of the matter component "b" as $k_J \propto T_b^{-1/2}\tau^{-1}$; thus, k_J depends on time in general, $k_J = k_J(\tau)$. However, in order to simplify the problem and obtain physical insights into the effects of pressure on the non-linear growth of structure, we shall assume that k_J is independent of time, which requires that the matter temperature evolve as if the matter were coupled to radiation, $T_b \propto 1/a \propto 1/\tau^2$. This is not a realistic assumption especially in a low redshift universe where baryons are decoupled from the radiation background and neutrinos are non-relativistic - in both cases the temperature evolves as $T_b \propto 1/a^2 \propto 1/\tau^4$ and thus k_J evolves as $k_J \propto \tau \propto a^{1/2}$, for the adiabatic evolution.

We shall solve the above coupled linear equations iteratively: as CDM is always the most dominant source of gravity, the zeroth-order iterative solution may be found by setting $\delta_1 \to \delta_{1,c}$ (i.e., $f_c \to 1$). We find the solution for the ratio of the density contrasts, which is often called the "Jeans filtering function," (Gnedin & Hui, 1998)

$$g_1(\mathbf{k},\tau) \equiv \frac{\delta_{1,b}(\mathbf{k},\tau)}{\delta_{1,c}(\mathbf{k},\tau)}, \tag{3.25}$$

which should be a decreasing function of k due to the effect of pressure. At the zeroth-order of iteration, the CDM density contrast grows as

$$\delta_{1,c}^{(0)}(\mathbf{k},\tau) \propto a \propto \tau^2, \tag{3.26}$$

and thus the equation for g_1 simplifies to

$$\ddot{g}_1^{(0)}(\mathbf{k},\tau) + \frac{6}{\tau}\dot{g}_1^{(0)}(\mathbf{k},\tau) + \frac{6}{\tau^2}\left(1+\frac{k^2}{k_J^2}\right) g_1^{(0)}(\mathbf{k},\tau) = \frac{6}{\tau^2}. \tag{3.27}$$

The solution for $g_1(\mathbf{k},\tau)$ must be normalized such that $g_1(k,\tau) \to 1$ as $k \to 0$. We find

$$g_1^{(0)}(k,\tau) = \frac{1}{1+\frac{k^2}{k_J^2}} + \mathcal{O}\left(\tau^{m(k)}\right), \tag{3.28}$$

where

$$m(k) \equiv -\frac{5}{2}\left[1 \pm \sqrt{1-\frac{24}{25}\left(1+\frac{k^2}{k_J^2}\right)}\right]. \tag{3.29}$$

The second term is a decaying mode, whose amplitude is set by the initial condition, e.g., at the epoch when the baryon temperature was raised (by, say, cosmic reionization) to the point where the pressure became important, or at the epoch when the neutrinos became non-relativistic.

Ignoring the decaying mode (although we shall come back to this later), we have the zeroth-order solution:

$$g_1^{(0)}(k) = \frac{1}{1+\frac{k^2}{k_J^2}}. \tag{3.30}$$

At the first-order iteration we have the pressure feedback on the growth of CDM. The evolution of $\delta_{1,c}^{(1)}$ depends on k, and is given by

$$\delta_{1,c}^{(1)}(k,\tau) \propto \tau^{n(k)}, \tag{3.31}$$

where

$$\begin{aligned} n(k) &\equiv \frac{1}{2}\left[-1 \pm 5\sqrt{1-\frac{24}{25}f_b(1-g_1^{(0)}(k))}\right] \\ &\simeq \left\{ \begin{array}{c} 2-\frac{6}{5}f_b[1-g_1^{(0)}(k)] \\ -3+\frac{6}{5}f_b[1-g_1^{(0)}(k)] \end{array} \right. . \end{aligned} \tag{3.32}$$

The second equality is valid for $f_b[1-g_1^{(0)}(k)] \ll 1$. The growing mode solution is given by

$$n_+(k) = 2 - \frac{6}{5} f_b[1 - g_1^{(0)}(k)]. \tag{3.33}$$

As $g^{(0)}(k) \to 1$ and 0 for $k \to 0$ and ∞, respectively, the large-scale and small-scale limits of the growing mode solution is (see, e.g., Sec. 8.3 of Weinberg, 2008, for a recent review)

$$\delta^{(1)}_{1,c+}(k,\tau) \;\propto\; \tau^2 \propto a, \qquad k \ll k_J, \tag{3.34}$$

$$\delta^{(1)}_{1,c+}(k,\tau) \;\propto\; \tau^{2-\frac{6}{5}f_b} \propto a^{1-\frac{3}{5}f_b}, \qquad k \gg k_J. \tag{3.35}$$

The growth of $\delta_{1,c}$ on the spatial scales below the Jeans scale is suppressed relative to that of the large-scale modes.

Taking the first order iteration solution for $\delta^{(1)}_{1,c+}$ into account, the first order iteration equation for $g_1^{(1)}$ is

$$\begin{aligned} &\ddot{g}_1^{(1)}(k,\tau) + \frac{1}{\tau}\left[1 + 5\sqrt{1 - \frac{24}{25} f_b(1 - g_1^{(0)}(k))}\right]\dot{g}_1^{(1)}(k,\tau) \\ &+\frac{6}{\tau^2}\left[1 + \frac{k^2}{k_J^2} - f_b(2 - g_1^{(0)}(k))\right] g_1^{(1)}(k,\tau) = \frac{6(1-f_b)}{\tau^2}, \end{aligned} \tag{3.36}$$

whose growing mode solution (with the normalization that $g_1^{(1)} \to 1$ for $k \to 0$) is

$$g_1^{(1)}(k) \;=\; \frac{1-f_b}{1 + \frac{k^2}{k_J^2} - f_b[2 - g_1^{(0)}(k)]} = \frac{1-f_b}{1 - f_b + \frac{k^2}{k_J^2}\left(1 - \frac{f_b}{1+k^2/k_J^2}\right)} \; . \tag{3.37}$$

This iteration converges quickly for $f_b < 0.5$, and further iterations are not necessary. The largest difference between $g_1^{(0)}(k)$ and $g_1^{(1)}(k)$ occurs as $k/k_J \to \infty$, and is 100% for $f_b = 0.5$. If the component "b" is identified with baryons, $f_b \simeq 1/6$, and the difference is reduced to $\sim 20\%$. The difference between $g_1^{(1)}(k)$ and $g_1^{(2)}(k)$ occurs at $k \sim k_J$, and is $\sim 4\%$ for $f_b = 0.5$, and 0.2% for $f_b \simeq 1/6$. The difference is much smaller for neutrinos.

To simplify the subsequent analysis, we shall adopt the zeroth-order iterative solution for the filtering function, $g_1^{(0)} = 1/(1 + k^2/k_J^2)$, and the first-order iterative solution for the CDM growth factor, eq. (3.33), as the solution at the first-order in perturbations. This solution is sufficiently accurate for our obtaining the physical insights.

Let us comment on the decaying mode that we have ignored in obtaining eq. [3.30]. This decaying mode is an oscillatory function at $k/k_J > 1/(2\sqrt{6}) \simeq 0.2$, representing the acoustic oscillation of the pressured component (Nusser, 2000). While this term is a decaying mode, it decays slowly, and is not quite negligible even at low redshift. We show the decaying mode at the zeroth-order iterative solution in Fig. 3.1,

$$\Delta g_1^{(0)}(k,\tau) \equiv g_1^{(0)}(k,\tau) - \frac{1}{1 + \frac{k^2}{k_J^2}}, \tag{3.38}$$

assuming that the pressure became important at $z_* = 10$. This figure shows that the decaying mode remains important even until $z \sim 0$; thus, technically speaking, ignoring the decaying mode results in an inaccurate form of the filtering function. Nevertheless, we shall ignore it and adopt $g_1(k) = 1/(1 +$

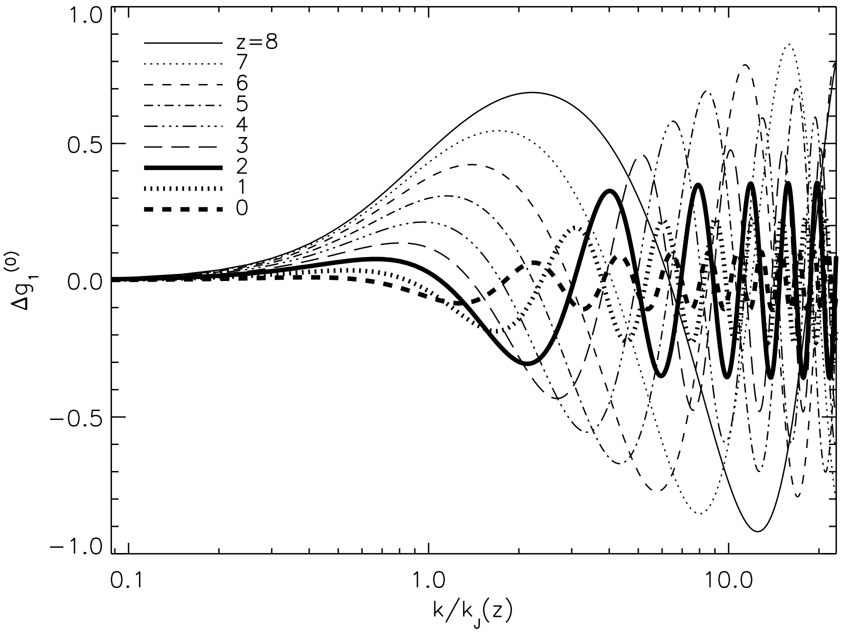

Figure 3.1: Decaying mode solution for the linear filtering function at the zeroth-order iteration ($f_c \to 1$), $\Delta g_1^{(0)}(k,\tau) \equiv g_1^{(0)}(k,\tau) - 1/(1+k^2/k_J^2)$, where $g_1^{(0)}(k,\tau)$ is the numerical solution of eq. (3.27), with the initial conditions given by $g_1^{(0)}(k,\tau_*) = 1$ and $\dot{g}_1^{(0)}(k,\tau_*) = 0$ where τ_* is the conformal time at $z_* = 10$. The top and bottom lines at $k/k_J \sim 1$ are at $z = 8$ and 0, respectively, and the other lines correspond to the intermediate redshifts.

k^2/k_J^2).

The exact form of $g_1(k,\tau)$ is not so important for our purposes. The main goal of this paper is to study how non-linearities affect this function. In other words, we are interested in how the higher-order filtering functions, $g_n(\mathbf{k},\tau)$, are related to the linear one, $g_1(k,\tau)$. One may use any forms of $g_1(k,\tau)$ for a better accuracy, depending on the problem (baryons or neutrinos).

3.2.3 Second and Third Order Solutions

For the higher order (n-th order) density perturbations and velocity-divergence fields, we define the Jeans filtering functions such that

$$g_n(\mathbf{k},\tau) \equiv \frac{\delta_{n,b}(\mathbf{k},\tau)}{\delta_{n,c}(\mathbf{k},\tau)}, \tag{3.39}$$

$$h_n(\mathbf{k},\tau) \equiv \frac{\theta_{n,b}(\mathbf{k},\tau)}{\theta_{n,c}(\mathbf{k},\tau)}. \tag{3.40}$$

Assuming that CDM dominates the gravitational potential, we find the zeroth-order iteration ansatz in an EdS universe:

$$\delta_b(\mathbf{k},\tau) = \sum_{n=1}^{\infty} a^n(\tau)\delta_{n,c}(\mathbf{k})g_n(\mathbf{k},\tau), \tag{3.41}$$

$$\theta_b(\mathbf{k},\tau) = \sum_{n=1}^{\infty} \dot{a}(\tau)a^{n-1}(\tau)\theta_{n,c}(\mathbf{k})h_n(\mathbf{k},\tau). \tag{3.42}$$

Detailed derivations of the non-linear filtering functions at the second order, $g_2(\mathbf{k},\tau)$, and the third order, $g_3(\mathbf{k},\tau)$, are given in Appendix § B.2. The second-order solution is

$$g_2(\mathbf{k},\tau) = \frac{\frac{10}{3} - \frac{7}{3}\left[1 - \frac{\delta'_{2,c}(\mathbf{k})}{\delta_{2,c}(\mathbf{k})}\right]}{\frac{10}{3} + \frac{k^2}{k_J^2}} + \mathcal{O}(\tau^{-9/2}), \tag{3.43}$$

where

$$\delta_{2,c}(\mathbf{k}) = \frac{1}{(2\pi)^3}\int d\mathbf{q}F_2^{(s)}(\mathbf{q},\mathbf{k}-\mathbf{q})\delta_{1,c}(\mathbf{q})\delta_{1,c}(\mathbf{k}-\mathbf{q}), \tag{3.44}$$

$$\begin{aligned}\delta'_{2,c}(\mathbf{k}) &= \frac{1}{(2\pi)^3}\int d\mathbf{q}\left[F_2^{(s)}(\mathbf{q},\mathbf{k}-\mathbf{q}) + \frac{3}{14}\frac{k^2}{k_J^2}\right] \\ &\times\ g_1(\mathbf{q})g_1(\mathbf{k}-\mathbf{q})\delta_{1,c}(\mathbf{q})\delta_{1,c}(\mathbf{k}-\mathbf{q}),\end{aligned} \tag{3.45}$$

and $F_2^{(s)}$ is a mathematical function given by eq. [B.28]. The third-order solution is

$$g_3(\mathbf{k},\tau) = \frac{7 - 6\left[1 - \frac{\delta'_{3,c}(\mathbf{k})}{\delta_{3,c}(\mathbf{k})}\right]}{7 + \frac{k^2}{k_J^2}} + \mathcal{O}(\tau^{-13/2}), \tag{3.46}$$

where

$$\begin{aligned}
\delta_{3,c}(\mathbf{k}) &= \frac{1}{(2\pi)^6}\int\int\int d\mathbf{q}_1 d\mathbf{q}_2 d\mathbf{q}_3 \delta_D(\mathbf{k}-\mathbf{q}_1-\mathbf{q}_2-\mathbf{q}_3) \\
&\quad \times F_3^{(s)}(\mathbf{q}_1,\mathbf{q}_2,\mathbf{q}_3)\delta_{1,c}(\mathbf{q}_1)\delta_{1,c}(\mathbf{q}_2)\delta_{1,c}(\mathbf{q}_3), \qquad (3.47)\\
\delta'_{3,c}(\mathbf{k}) &= \frac{1}{(2\pi)^6}\int\int\int d\mathbf{q}_1 d\mathbf{q}_2 d\mathbf{q}_3 \delta_D(\mathbf{k}-\mathbf{q}_1-\mathbf{q}_2-\mathbf{q}_3) \\
&\quad \times \mathcal{F}_3^{(s)}(\mathbf{q}_1,\mathbf{q}_2,\mathbf{q}_3)\delta_{1,c}(\mathbf{q}_1)\delta_{1,c}(\mathbf{q}_2)\delta_{1,c}(\mathbf{q}_3), \qquad (3.48)
\end{aligned}$$

and $F_3^{(s)}$ and $\mathcal{F}_3^{(s)}$ are mathematical functions given by eqs. [B.30] and [B.65], respectively. One may check that these functions are properly normalized, i.e., $g_n \to 1$ as $k \to 0$, using $\delta'_{2,c} \to \delta_{2,c}$ and $\delta'_{3,c} \to \delta_{3,c}$ as $k \to 0$.

Ignoring the decaying modes, let us rewrite g_2 and g_3 as

$$\begin{aligned}
g_2(\mathbf{k}) &= \frac{1 - \frac{7}{10}\left[1 - \frac{\delta'_{2,c}(\mathbf{k})}{\delta_{2,c}(\mathbf{k})}\right]}{1 + \frac{3}{10}\frac{k^2}{k_J^2}}, \qquad (3.49)\\
g_3(\mathbf{k}) &= \frac{1 - \frac{6}{7}\left[1 - \frac{\delta'_{3,c}(\mathbf{k})}{\delta_{3,c}(\mathbf{k})}\right]}{1 + \frac{1}{7}\frac{k^2}{k_J^2}}. \qquad (3.50)
\end{aligned}$$

These results may be interpreted as, roughly speaking, the non-linear filtering functions having smaller effective filtering scales (larger filtering wavenumbers): $k_J \to \tilde{k}_J = \sqrt{\frac{10}{3}}k_J$ for the second order, $k_J \to \tilde{k}_J = \sqrt{7}k_J$ for the third order, and $k_J \to \tilde{k}_J = \sqrt{\frac{2}{3}n(n+\frac{1}{2})}k_J$ for the n-th order perturbations. In other words, the higher-order solutions for $\delta_{n,b}$ are less suppressed relative to the CDM solutions. In the next section we shall quantify this effect in more detail.

3.3 Power Spectrum

In this section, we calculate the non-linear matter power spectrum using the results obtained in the previous section. The total matter fluctuation, δ, is given by $\delta = f_c\delta_c + f_b\delta_b$, and thus the total matter power spectrum, $P_{tot}(k)$, is given by the sum of three contributions:

$$P_{tot}(k,\tau) = f_c^2 P_c(k,\tau) + f_c f_b P_{bc}(k,\tau) + f_b^2 P_b(k,\tau), \tag{3.51}$$

where $P_c(k)$ and $P_b(k)$ are the power spectra of the CDM and another matter component with pressure, respectively, and $P_{bc}(k)$ is the cross-correlation power spectrum. Each term is the sum of the linear part, $P_{11}(k,\tau)$, and the non-linear parts, $P_{22}(k,\tau)$ and $P_{13}(k,\tau)$:

$$P_i(k,\tau) = P_{11,i}(k,\tau) + P_{22,i}(k,\tau) + 2P_{13,i}(k,\tau), \tag{3.52}$$

where $i = (c, b, bc)$.

The 3PT power spectrum of CDM has been found in the literature (see Bernardeau et al., 2002, for a review):

$$\begin{aligned} P_{22,c}(k,\tau) &= 2\int \frac{d\mathbf{q}}{(2\pi)^3} P_{11,c}(q,\tau) P_{11,c}(|\mathbf{k}-\mathbf{q}|,\tau) \\ &\quad \times \left[F_2^{(s)}(\mathbf{q},\mathbf{k}-\mathbf{q})\right]^2, \end{aligned} \tag{3.53}$$

where $F_2^{(s)}$ is a mathematical function given by eq. [B.28], and

$$\begin{aligned} P_{13,c}(k,\tau) &= \frac{2\pi}{252}k^2 P_{11,c}(k,\tau)\int_0^\infty \frac{dq}{(2\pi)^3}P_{11,c}(q,\tau) \\ &\times \left[50\frac{q^2}{k^2} - 21\frac{q^4}{k^4} - 79 + 6\frac{k^2}{q^2} \right. \\ &\left. + \frac{3}{2}\frac{(q^2-k^2)^3(2k^2+7q^2)}{k^5q^3}\ln\frac{k+q}{|k-q|}\right]. \end{aligned} \tag{3.54}$$

See Appendix § B.1 for the detailed derivations.

Here, we have implicitly generalized the results from an EdS universe to general cosmological models, by writing

$$\begin{aligned} &\frac{a^2(\tau)}{a^2(\tau_i)}P_{11}(k,\tau_i) \rightarrow \\ &P_{11}(k,\tau) = \frac{D^2(\tau)}{D^2(\tau_i)}\left(\frac{\delta^{(1)}_{1,c+}(k,\tau)/\delta^{(0)}_{1,c+}(k,\tau)}{\delta^{(1)}_{1,c+}(k,\tau_*)/\delta^{(0)}_{1,c+}(k,\tau_*)}\right)^2 P_{11}(k,\tau_i), \end{aligned} \tag{3.55}$$

where τ_i is some arbitrary epoch, τ_* is the epoch where the pressure effect becomes non-negligible (i.e., reionization epoch for baryons and the relativistic to non-relativistic transition epoch for massive neutrinos), and $D(\tau)$ is the linear growth factor appropriate to a given cosmological model. This simple generalization has been shown to provide an excellent approximation to the full calculation: see Bernardeau et al. (2002) for models with non-zero curvature and/or a cosmological constant, and Takahashi (2008) for dynamical dark energy models with a constant equation of state of dark energy.

The linear spectra of the other contributions, $P_{11,bc}$ and $P_{11,b}$, are given by

$$
\begin{aligned}
P_{11,bc}(k,\tau) &= g_1(k) P_{11,c}(k,\tau), &(3.56)\\
P_{11,b}(k,\tau) &= g_1^2(k) P_{11,c}(k,\tau). &(3.57)
\end{aligned}
$$

The non-linear terms, the main results of this paper, are given by

$$
\begin{aligned}
P_{22,bc}(k,\tau) &= \frac{1}{\frac{10}{3}+\frac{k^2}{k_J^2}}\left[P_{22,c}(k,\tau)\right.\\
&+ \frac{14}{3}\int\frac{d\mathbf{q}}{(2\pi)^3}P_{11,c}(q,\tau)P_{11,c}(\left|\mathbf{k}-\mathbf{q}\right|,\tau)\\
&\left.\times F_2^{(s)}(\mathbf{q},\mathbf{k}-\mathbf{q})\mathcal{F}_2^{(s)}(\mathbf{q},\mathbf{k}-\mathbf{q})\right], \qquad (3.58)
\end{aligned}
$$

$$
\begin{aligned}
P_{22,b}(k,\tau) &= \frac{1}{\left(\frac{10}{3}+\frac{k^2}{k_J^2}\right)^2}\left[P_{22,c}(k,\tau)+\frac{28}{3}\int\frac{d\mathbf{q}}{(2\pi)^3}P_{11,c}(q,\tau)P_{11,c}(\left|\mathbf{k}-\mathbf{q}\right|,\tau)\right.\\
&\times F_2^{(s)}(\mathbf{q},\mathbf{k}-\mathbf{q})\mathcal{F}_2^{(s)}(\mathbf{q},\mathbf{k}-\mathbf{q})\\
&+ \left.\frac{98}{9}\int\frac{d\mathbf{q}}{(2\pi)^3}P_{11,c}(q,\tau)P_{11,c}(\left|\mathbf{k}-\mathbf{q}\right|,\tau)\left(\mathcal{F}_2^{(s)}(\mathbf{q},\mathbf{k}-\mathbf{q})\right)^2\right], \qquad (3.59)
\end{aligned}
$$

$$
\begin{aligned}
P_{13,bc}(k,\tau) &= \frac{1}{2}\left[\left(g_1(k)+\frac{1}{7+\frac{k^2}{k_J^2}}\right)P_{13,c}(k,\tau)\right.\\
&+ \left.\frac{18}{7+\frac{k^2}{k_J^2}}P_{11,c}(k,\tau)\int\frac{d\mathbf{q}}{(2\pi)^3}\mathcal{F}_3^{(s)}(\mathbf{q},-\mathbf{q},\mathbf{k})P_{11,c}(q,\tau)\right], \qquad (3.60)
\end{aligned}
$$

$$
\begin{aligned}
P_{13,b}(k,\tau) &= \frac{g_1(k)}{7+\frac{k^2}{k_J^2}}\left[P_{13,c}(k,\tau)+18P_{11,c}(k,\tau)\right.\\
&\left.\times\int\frac{d\mathbf{q}}{(2\pi)^3}\mathcal{F}_3^{(s)}(\mathbf{q},-\mathbf{q},\mathbf{k})P_{11,c}(q,\tau)\right]. \qquad (3.61)
\end{aligned}
$$

See Appendix § B.3 for the detailed derivations.

How would $P_{tot}(k)$ compare with the CDM part, $P_c(k)$?

- In the linear limit, we should recover $P_{tot}(k)/P_c(k) \to [f_c + f_b g_1(k)]^2$, which approaches unity as $k \to 0$.
- In the very small scale limit ($k \to \infty$), the pressured component is completely smooth ($\delta_b(k) \to 0$) because $g_1(k) \to 0$; thus, $P_{tot}(k)/P_c(k)$ approaches a constant value, f_c^2.
- In the intermediate regime, especially at the transition scale between the super-Jeans scale ($k < k_J$) and the sub-Jeans scale ($k > k_J$), the shape of $P_{tot}(k)/P_c(k)$ is significantly distorted away from the linear prediction. Non-linear clustering of the pressured component adds power at $k \sim k_J$, which shifts the effective filtering scale to smaller spatial scales as we go to lower redshifts.

In Fig. 3.2 we show the ratio, $P_{tot}(k,z)/P_c(k,z)$ (solid lines), for different redshifts ($z = 0.1$, 1, 3, 5, 10, and 30), and different k_J ($k_J = 1$ and 3 h Mpc^{-1} for the left and right panels, respectively). In the linear regime (see the bottom lines, $z = 30$) the ratio agrees with the linear prediction shown by the dashed lines. As we go to lower redshifts, we find that the filtering wavenumbers continue to shift to larger values, i.e., the filtering scales continue to shift to smaller spatial scales as we go to lower redshifts. This effect cannot be predicted from the linear theory, where all the modes evolve in the same way.

3.4 Comparison with Approximate Treatment of Saito et al. (2008)

The non-linear power spectrum with a significant contribution from a pressured component has not been studied very much in the literature, with one exception. Saito et al. (2008) (hereafter, STT) have studied effects of massive neutrinos on the non-linear matter power spectrum using 3PT (also see Wong, 2008; Lesgourgues et al., 2009). However, their treatment is not satisfactory: they have entirely ignored non-linearities in neutrinos, but approximated the neutrino perturbations as linear perturbations. More precisely, they calculated the non-linear matter power spectrum as

$$P_{tot}^{\mathrm{STT}}(k,z) = f_c^2 P_c(k,z) + 2 f_c f_\nu P_{11,\nu c}(k,z) + f_\nu^2 P_{11,\nu}(k,z). \tag{3.62}$$

In our language this leads to

$$P_{tot}^{\mathrm{STT}}(k,z) = f_c^2 P_c(k) + [2 f_c f_\nu g_1(k) + f_\nu^2 g_1^2(k)] P_{11,c}(k,z). \tag{3.63}$$

Here, we have replaced the subscripts "b" with "ν" to avoid confusion in notation.

How accurate is the STT approximation? To study this, we compare eq. [3.63] to the full calculation given in the previous section. Figure 3.3 shows the fractional difference between our full calculation and STT's approximation, $[P_{tot}(k) - P_{tot}^{\mathrm{STT}}(k)]/P_{tot}(k)$, for $\Omega_\nu/\Omega_m = 1/10$, $1/20$, and $1/100$, which correspond to the sum of neutrino masses of $\sum_i m_{\nu,i} \simeq 1.3$, 0.64, and 0.13 eV, respectively, where $i = (e, \mu, \tau)$. We find that STT's approximation clearly underestimates the power at $k \approx k_{FS}$, where k_{FS} is the neutrino free-streaming scale, or it is the Jeans wavenumber computed with the velocity dispersion of the neutrinos. More precisely,

$$k_{FS,i}(\tau) \equiv \frac{\sqrt{6}}{\sigma_{\nu,i}(\tau)\tau}, \tag{3.64}$$

in an EdS universe, where $\sigma^2_{\nu,i}(\tau)$ is the velocity dispersion of neutrino species i (see, e.g., Appendix A.3 of Takada et al., 2006).

One may argue that STT's approximation should be better for a smaller neutrino mass: the errors in the total matter power spectrum are 3.5%, 0.6%, and 0.003% $\sum_i m_{\nu,i} = 1.3$, 0.64, and 0.13 eV, respectively, at $z = 0.1$; however, our results indicate that their approximation is conceptually not correct: neutrinos should not be treated as linear perturbations, as the neutrino velocity dispersion has no effect in suppressing the neutrino perturbations at and above the free-streaming scale. In other words, the errors may happen to be small in the *total* matter power spectrum for small neutrino masses because neutrinos contribute only a tiny fraction of the total matter density anyway, but the errors in the neutrino power spectrum are large. Figure 3.4 shows the fractional difference between the non-linear neutrino power spectrum, $P_\nu(k)$, and the linear power spectrum, $P_\nu^{lin}(k)$, i.e., $\Delta P/P = [P_\nu(k) - P_\nu^{lin}(k)]/P_\nu(k)$. It is clear that neutrinos are significantly non-linear, even well below the free-streaming scale, $k \gg k_{FS}$. Nevertheless, the STT approximation may still provide a convenient phenomenological tool for calculating the non-linear total matter power spectrum in the presence of massive neutrinos.

3.5 Discussions and Conclusions

In this paper, we have obtained the second- and third-order solutions for the density perturbations in a system consisting of two matter components with and without the pressure gradient. This is the first self-consistent analytical calculation, with non-linearities in the pressured component fully retained up to the 3rd order in perturbations.

As our study is focused on understanding the physics of the non-linear pressure effect on the matter power spectrum, we have studied a toy model in which the Jeans wavenumber, k_J, is independent of time. This is equivalent to the temperature of the pressured component following that of radiation, i.e., $T \propto 1/a$.

Nevertheless, we have found several results that have qualitative implications for the practical applications. We have found that non-linearities in the pressured component shift the filtering scale from the well-known linear filtering scale (Gnedin & Hui, 1998) to a smaller spatial scale (larger wavenumber) by a factor depending on the redshift and the Jeans scale. In other words, the actual filtering scale for a given sound speed (or temperature) is *smaller* than the linear scale. Therefore, if one used the linear filtering scale to interpret the fall-off of, e.g., the flux power spectrum of the Lyman-α forests (Zaldarriaga et al., 2001), one would underestimate the temperature of the pressured component.

How important is this effect? For example, when the Jeans wavenumber is $k_J = 10\ h\ \mathrm{Mpc}^{-1}$, our calculation predicts that the effective filtering wavenumber is $\simeq 10$, 12, 13, 13, and 14 $h\ \mathrm{Mpc}^{-1}$ at $z = 30$, 10, 5, 3, and 1, respectively. While we do not expect 3PT to be valid at such high wavenumbers, our results clearly indicate that the expected changes in the filtering scale cannot be ignored. Table 3.1 summarizes the ratios of the effective (actual) and the linear filtering wavenumbers. Note that the linear filtering wavenumber is the same as the Jeans wavenumber in our model; thus, we show $k_{F,eff}/k_J$ in Table 3.1. We extracted the effective filtering wavenumber, $k_{F,eff}$, by fitting $[f_c + f_b/(1 + k^2/k^2_{F,eff})]^2$ to $P_{tot}(k, z)/P_c(k, z)$. We find that a factor of 1.4 change in the filtering scale is quite common over a wide range of redshifts and k_J.

A factor of 1.4 change in the filtering scale changes the inferred temperature by a factor of two; thus, one implication of our result is that the temperature of the Inter-galactic Medium (IGM) obtained from the Lyman-α forests at $z = 3$ by Zaldarriaga et al. (2001) might have been underestimated by a factor of two.

A factor of 1.4 change in the filtering scale gives a factor of ~ 3 change in the filtering mass. Our calculation shows that the actual filtering mass is similar to the linear one only in high redshifts, while the former is significantly smaller than the latter in low redshift. This result is qualitatively similar to those found in Okamoto et al. (2008) and Hoeft et al. (2006); however, a quantitative comparison is not possible, as our results apply only to the system with a constant Jeans wavenumber.

k_J (h Mpc^{-1})	z=0.1	1.0	3.0	5.0	10	30
0.1	1.08	1.04	1.01	1.00	1.00	1.00
0.5	1.37	1.21	1.07	1.03	1.01	1.00
1.0	1.43	1.32	1.14	1.08	1.03	1.00
3.0	1.41	1.38	1.28	1.20	1.08	1.01
5.0	1.40	1.39	1.32	1.24	1.12	1.02
10	1.41	1.40	1.35	1.29	1.16	1.03

Table 3.1: This table shows the ratios of the effective ($k_{F,eff}$) and the linear (k_J) filtering scales for different redshifts and k_J. The ratios are closer to unity at higher redshifts because non-linearities are weaker.

What is next? As for baryons, we need to extend our formalism for incorporating a realistic thermal history of the universe with a proper time dependence of k_J. As for neutrinos, we need to incorporate not only the pressure gradient but also the anisotropic stress in the Euler equation. To do this we need to solve the Boltzmann equation. Nevertheless, our results presented in this paper show that neutrinos are significantly non-linear, even well below the free-streaming scale.

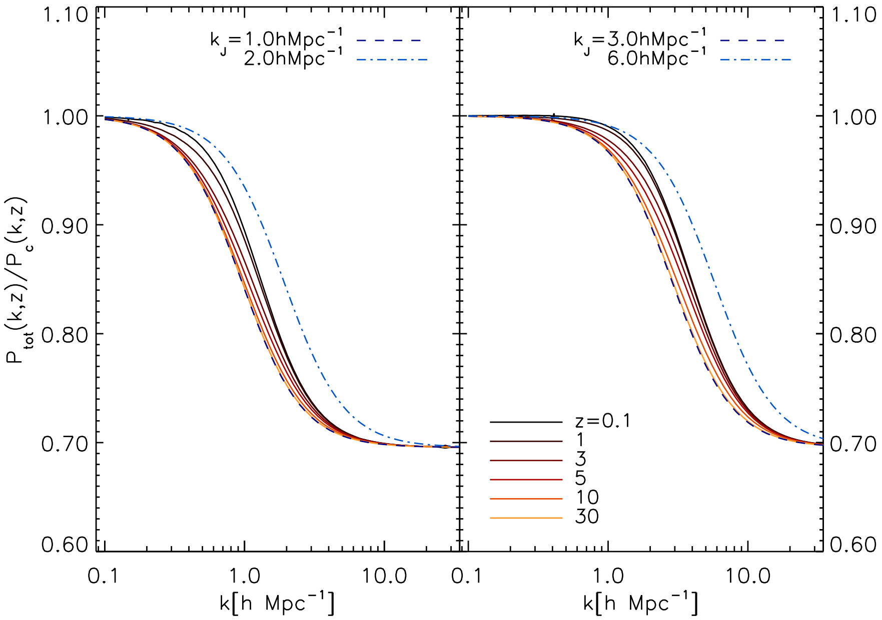

Figure 3.2: Ratio of the total matter power spectrum, $P_{tot}(k, z)$, to the CDM part, $P_c(k, z)$, at $z = 0.1$ (top), 1, 3, 5, 10, and 30 (bottom). (Left) The input Jeans wavenumber of $k_J = 1$ h Mpc^{-1}. (Right) $k_J = 3$ h Mpc^{-1}. The dashed lines show the ratios calculated from the linear theory, whereas the dot-dashed lines show the linear calculations with $k_J = 2$ and 6 h Mpc^{-1} for the left and right panels respectively, to show that the actual filtering wavenumbers, predicted by the 3PT calculations, can be ∼40% as large as the linear filtering wavenumber at low redshift.

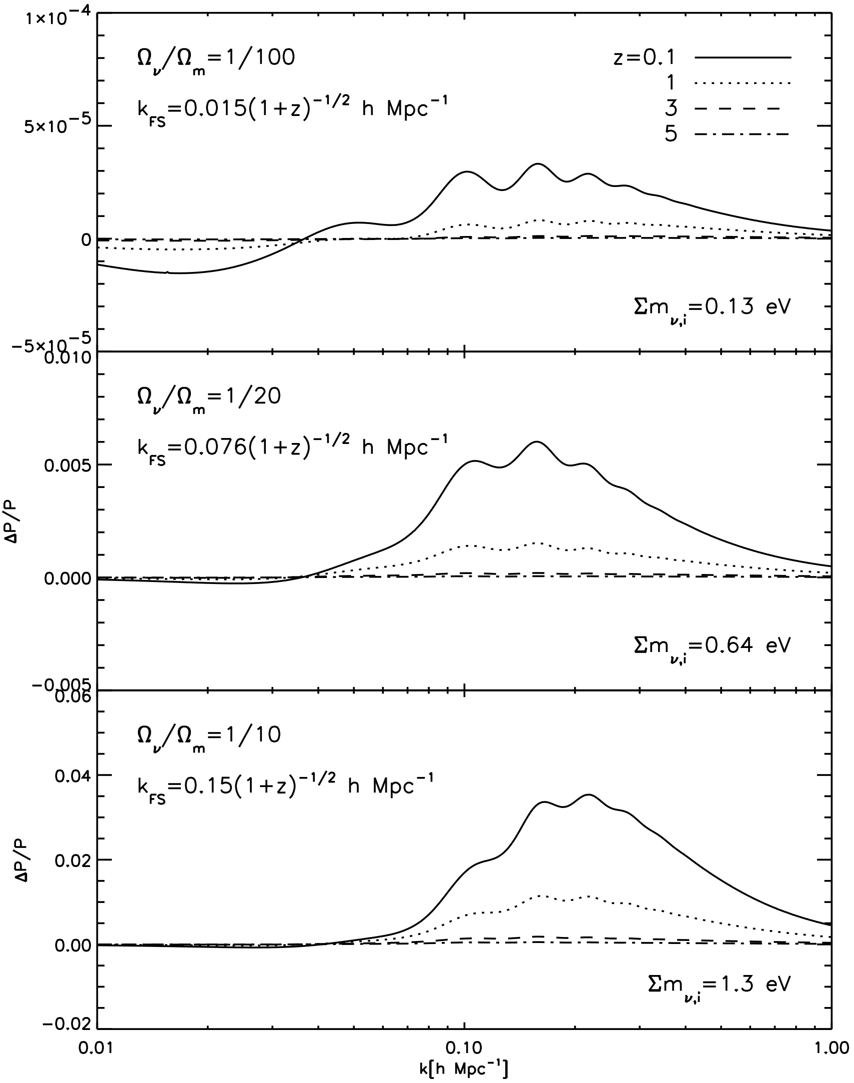

Figure 3.3: Fractional difference between our full calculation and the approximation used by Saito et al. (2008) (STT), $\left[P_{tot}(k) - P_{tot}^{\rm STT}(k)\right] / P_{tot}(k)$, for $\Omega_\nu/\Omega_m = 1/100$ (top), 1/20 (middle), and 1/10 (bottom), which corresponds to $\sum m_\nu \simeq 0.13$, 0.64, and 1.3 eV, respectively.

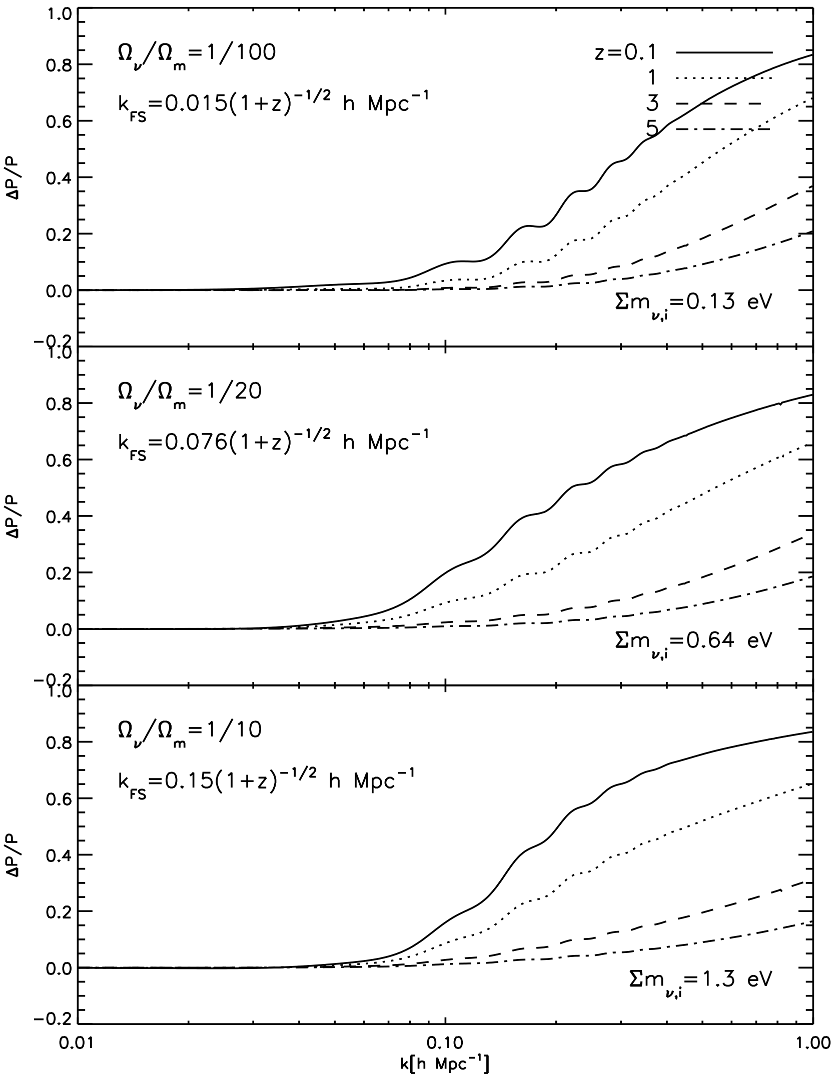

Figure 3.4: Fractional difference between the non-linear neutrino power spectrum, $P_\nu(k)$, and the linear power spectrum, $P_\nu^{lin}(k)$, $[P_\nu(k) - P_\nu^{\rm lin}(k)]/P_\nu(k)$, for $\Omega_\nu/\Omega_m = 1/100$ (top), 1/20 (middle), and 1/10 (bottom), which corresponds to $\sum m_\nu \simeq 0.13$, 0.64, and 1.3 eV, respectively.

Chapter 4

Massive Neutrinos in Cosmology: Analytic Solutions and Fluid Approximation

In the previous chapter, we show how to include the pressure gradient term into the 3rd-order perturbation theory in a self-consistent manner. Although the use of fluid approximation for the CDM particle is common due to its negligible pressure, we do not know the extent to which the fluid approximation is valid for massive neutrinos. In this chapter, we study the evolution of linear density fluctuations of free-streaming massive neutrinos at redshift of $z < 1000$, with an explicit justification on the use of a fluid approximation. We solve the collisionless Boltzmann equation in an Einstein de-Sitter (EdS) universe, truncating the Boltzmann hierarchy at $l_{\max} = 1$ and 2, and compare the resulting density contrast of neutrinos, $\delta_\nu^{\rm fluid}$, with that of the exact solutions of the Boltzmann equation that we derive in this chapter. [1]

---

[1] A significant part of this chapter was originally published in Physical Review D by Shoji, M. & Komatsu, E. Reproduced by permission of the American Physical Society.

4.1 Introduction

What is the mass of neutrinos? We know that at least two of three standard model neutrino species have finite masses. The constraints on the squared mass differences of the three species of neutrinos obtained from solar (Davis, 1994; Itoh et al., 1996; Cleveland et al., 1998; Abdurashitov et al., 1999; Hampel et al., 1999; Altmann et al., 2000; Abdurashitov et al., 2002; Ahmad et al., 2002a,b; Fukuda et al., 2002; Ahmed et al., 2004; Gno Collaboration et al., 2005; Hosaka et al., 2006a) and atmospheric oscillation experiments (Fukuda et al., 1998; Surdo, 2002; Sanchez et al., 2003; Ashie et al., 2005; Hosaka et al., 2006b) (reviews can be found in Maltoni et al. (2004); Lesgourgues & Pastor (2006); Gonzalez-Garcia & Maltoni (2008); Schwetz et al. (2008)) are (3 σ errors)

$$\Delta m_{21}^2 = \left(7.65^{+0.69}_{-0.60}\right) \times 10^{-5}\ \mathrm{eV}^2, \tag{4.1}$$

$$\left|\Delta m_{31}^2\right| = \left(2.40^{+0.35}_{-0.33}\right) \times 10^{-3}\ \mathrm{eV}^2. \tag{4.2}$$

Therefore, the lower limit on the sum of neutrino masses is 0.058 eV. Observations of the CMB and large-scale structure of the universe can provide limits on the *absolute* mass of neutrinos. The current upper bounds on the sum of neutrino masses are $\simeq 0.3 - 0.6$ eV (Mantz et al., 2009; Thomas et al., 2009; Vikhlinin et al., 2009; Hannestad et al., 2010; Reid et al., 2010; Sekiguchi et al., 2010). In this paper, we use 0.58 eV (95% CL) from WMAP7yr as a conservative upper bound on the sum of neutrino masses (Komatsu et al., 2010b).

The large-scale structure of the universe is a sensitive probe of neutrino masses (Bond et al., 1980; Doroshkevich et al., 1980b,a; Doroshkevich & Khlopov, 1981; Doroshkevich et al., 1981; Hu, 1998; Hu & Eisenstein, 1998; Valdarnini et al., 1998; Eisenstein & Hu, 1999; Lewis & Challinor, 2002; Lesgourgues & Pastor, 2006). Massive neutrinos suppress the small-scale matter power spectrum by their large velocity dispersion, The fractional amount of the suppression in the small-scale limit is roughly given by

$$\left|\frac{\Delta P(k)}{P(k)}\right| \simeq 8\frac{\Omega_\nu}{\Omega_m}, \tag{4.3}$$

with

$$\Omega_\nu h^2 = \frac{\sum m_{\nu,\mathrm{i}}}{94.1\ \mathrm{eV}}, \tag{4.4}$$

where the summation is taken over the i-th species of neutrinos (Hu & Eisenstein, 1998; Hu et al., 1998; Takada et al., 2006).

Relativistic neutrinos are not a fluid. Massive neutrinos, being collisionless, are not a fluid, either. However, when the velocity dispersion of massive neutrinos becomes low enough, they may be approximately treated as a fluid, just as we normally treat Cold Dark Matter (CDM) particles as a fluid on large-scales. While this is a reasonable expectation, as far as we know, the extent to which the fluid approximation is valid for massive neutrinos has not been discussed in the literature.

Then, why is a fluid approximation useful while we have Boltzmann codes such as CMBfast (Seljak & Zaldarriaga, 1996) and CAMB (Lewis et al., 2000), which solve the Boltzmann equations numerically to the accuracy of order $\sim 0.1\%$? First, we will have more physical insight to the growth of the neutrino density fluctuations by directly solving continuity and Euler equations rather than numerically solving a set of infinite order of Boltzmann hierarchy. Second, and most importantly, as the density fluctuations become non-linear, i.e., $\delta \sim 1$, we need to use higher-order perturbation theories to accurately model the small-scale density fluctuations. Since the higher-order perturbation theories have been constructed for CDM with a fluid approximation, we cannot simply modify theories to include massive neutrinos if a fluid approximation is not valid for those particles. On the other hand, if a fluid approximation is valid for some range of redshifts, length scales and neutrino masses, we can greatly simplify the model of non-linear density fluctuations in the presence of massive neutrino, as shown in Shoji & Komatsu (2009).

In this paper, we shall study the validity of a fluid approximation of massive neutrinos. To achieve this goal, we first solve the Boltzmann equations describing the evolution of the perturbed phase-space distribution function of massive neutrinos *exactly* and compare the exact results to the results with the fluid approximation, i.e., solutions with the higher multipole moments ($l \geq 3$) ignored. Then, we shall examine the ranges of applicability of fluid approximation in both spatial and time scales, as a function of neutrino masses.

The rest of this paper is organized as follows. In § 4.2, we briefly review the effects of massive neutrino free-streaming on the structure formation of the universe. In § 4.3, we provide the basic fluid equations and the linearized Boltzmann equation required for our theoretical flame work. In § 4.4, we briefly discuss the analytic solutions of the Boltzmann equation for collision-less particles. In § 4.5, we compare the exact solutions of the Boltzmann equations with the fluid approximation, and discuss the limitation of the fluid approximation for several masses of massive neutrino. Finally, in § 4.6, we discuss the implications of our results and conclude. In Appendix C.1, we discuss how to define the free-streaming scale starting from the fluid equations. In Appendix C.2, we give the detailed derivation of the exact solution of the Boltzmann equation both for massless and massive neutrinos. Even though our main interest is in massive neutrinos, our results shown here are also applicable to collision-less particles in general, whose time evolution of the perturbed phase space distribution follows the linearized collision-less Boltzmann equation with the zero-th order phase space distribution function being frozen at sufficiently early time (i.e., we set the initial conditions of the neutrino transfer function after the decoupling of neutrino, ~ 1 MeV).

4.2 The Free-Streaming of the Massive Neutrino

We are interested in the mass range of $0.05 < m_{\nu,\mathrm{i}} < 0.58$ eV for the most massive species of neutrinos, which became non-relativistic well after the matter radiation equality. The mass density of the massive neutrinos relative to the total matter density is given by

$$f_\nu \equiv \frac{\Omega_\nu h^2}{\Omega_m h^2} = \frac{1}{\Omega_m h^2} \frac{\sum_\mathrm{i} m_{\nu,\mathrm{i}}}{94.1\mathrm{eV}}, \tag{4.5}$$

where the summation is taken over the different species of neutrinos. Neutrinos become non-relativistic when the mean energy per particle of neutrinos in the relativistic limit,

$$\begin{aligned}\langle E\rangle &\equiv \frac{\int d^3p\, p\, (\exp[p/T_\nu(z)]+1)^{-1}}{\int d^3p\, (\exp[p/T_\nu(z)]+1)^{-1}} \\ &= \frac{7\pi^4}{180\zeta(3)}T_\nu \simeq 3.15T_\nu, \end{aligned} \tag{4.6}$$

falls below $m_{\nu,\mathrm{i}}$. By solving $3.15T_{\nu,0}(1+z_{\mathrm{nr}}) = m_{\nu,\mathrm{i}}$, one finds the redshift of relativistic to non-relativistic transition epoch, z_{nr}, as

$$1+z_{\mathrm{nr,i}} \simeq 1890\left(\frac{m_{\nu,\mathrm{i}}}{1\mathrm{eV}}\right), \tag{4.7}$$

for the i-th neutrino species.

The density fluctuation of neutrinos cannot grow within the horizon size until neutrinos become non-relativistic. Once neutrinos become non-relativistic, the neutrino density fluctuation begins to grow on scale greater than the so called "free-streaming scale," which is set by the velocity dispersion of neutrinos:

$$\begin{aligned}\sigma^2_{\nu,\mathrm{i}}(z) &\equiv \frac{\int d^3p\, p^2/m^2_{\nu,\mathrm{i}}(\exp[p/T_\nu(z)]+1)^{-1}}{\int d^3p\, (\exp[p/T_\nu(z)]+1)^{-1}} \\ &= \frac{15\zeta(5)}{\zeta(3)}\left(\frac{4}{11}\right)^{\frac{2}{3}}\frac{T^2_{\gamma,0}(1+z)^2}{m^2_{\nu,\mathrm{i}}}, \end{aligned} \tag{4.8}$$

where p is the proper momentum of the massive neutrino (see Appendix of Takada et al. (2006)).

The wavenumber corresponding to the free-streaming scale, $k_{\rm FS}$, is defined by the single-fluid continuity and Euler equations:

$$\dot{\delta}(\mathbf{k},\tau) + \theta(\mathbf{k},\tau) = 0 \tag{4.9}$$

$$\dot{\theta}(\mathbf{k},\tau) + \mathcal{H}(\tau)\theta(\mathbf{k},\tau) + \left[\frac{3}{2}\mathcal{H}^2(\tau) - k^2 c_{\rm s}^2(\tau)\right]\delta(\mathbf{k},\tau) = 0, \tag{4.10}$$

where [2]

$$\begin{aligned} k_{\rm FS,i}(z) &\equiv \sqrt{\frac{3}{2}}\frac{\mathcal{H}(z)}{c_{\rm s}(z)} \simeq \sqrt{\frac{3}{2}}\frac{\mathcal{H}(z)}{\sigma_{\nu,{\rm i}}(z)} \\ &\simeq \frac{0.677}{(1+z)^2}\left(\frac{m_{\nu,{\rm i}}}{1\ {\rm eV}}\right)\left[\Omega_m(1+z)^3 + \Omega_\Lambda\right]^{\frac{1}{2}}\ h\ {\rm Mpc}^{-1}. \end{aligned} \tag{4.11}$$

Here, derivatives are with respect to a conformal time, $d\tau = dt/a$, $\mathcal{H}(\tau) \equiv \frac{\dot{a}(\tau)}{a(\tau)}$, and $\theta(\mathbf{k},\tau)$ is a velocity divergence of the fluid. Note that Eq.(4.8) assumes that neutrinos are non-relativistic.

In Figure 4.1, we show $k_{\rm FS,i}$ from Eq.(4.11) (dotted line), comoving horizon scale, $aH(a)$, (thick solid line) and $k_{\rm FS,i}$ calculated numerically from Eq.(4.8), where $m_{\nu,{\rm i}}$ is replaced by $\sqrt{p^2 + m_{\nu,{\rm i}}^2}$ (thin solid line). In this figure, we use $m_{\nu,{\rm i}} = 0.13$ eV.

We find that the free-streaming scale is close to the horizon size until the relativistic to non-relativistic transition of a neutrino, and once the neutrino

---

[2] Here, we say $c_{\rm s} \simeq \sigma_{\nu,{\rm i}}$; however, strictly speaking, the velocity dispersion defined in Eq.(4.8) should not be used to define the free-streaming scale, $k_{\rm FS}$, as the Euler equation contains sound speed, $c_{\rm s}^2 \equiv \frac{\delta P}{\delta\rho}$, not the velocity dispersion. In the non-relativistic limit, we have $c_s = \frac{\sqrt{5}}{3}\sigma_{\nu,{\rm i}} \simeq 0.745\sigma_{\nu,{\rm i}}$. We derive this relation in Appendix C.1.

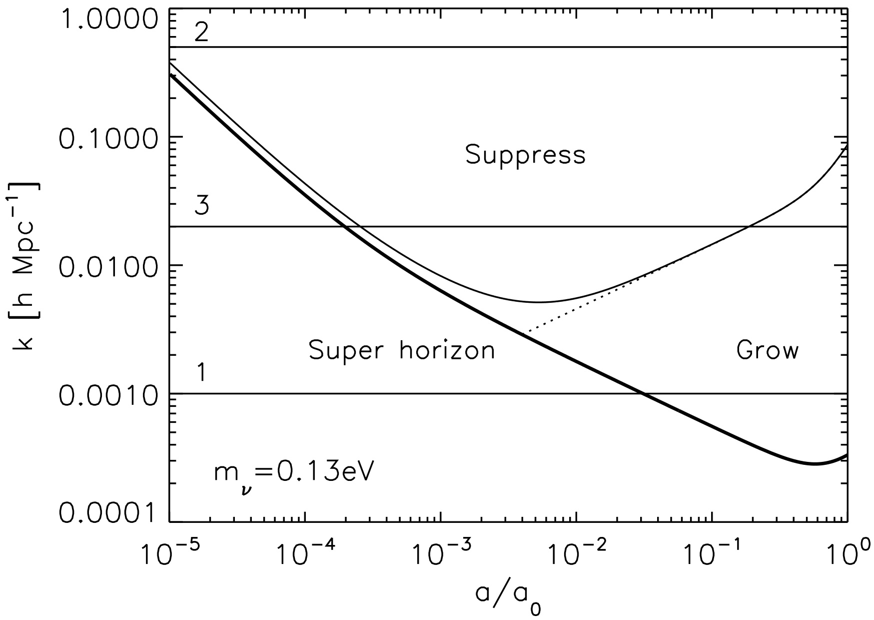

Figure 4.1: Free-streaming scale of a massive neutrino, $k_{\mathrm{FS,i}}$, (black line), comoving horizon scale, $aH(a)$, (thick black line) and an approximation to the free-streaming scale in the non-relativistic limit given by Eq.(4.11), (dotted line) as functions of the scale factor, a. We use $m_{\nu,\mathrm{i}} = 0.13$ eV. The horizontal lines show (1) large, (2) small, and (3) intermediate scale modes as described in § 4.2.

becomes non-relativistic, the free-streaming scale decreases as $k_{\mathrm{FS}}(a) \propto a^{1/2}$. Let us examine the evolution of the neutrino density fluctuations at three length scales:

1. At the large-scale, where $k \ll k_{\mathrm{FS}}(a)$ for all $a \leq a_0$ (a_0 is the present-day scale factor), the neutrino density fluctuation starts to grow soon after the mode enters the horizon, and its time evolution is identical to that of CDM, $\delta_\nu(k, a) = \delta_{\mathrm{c}}(k, a)$.

2. At the small-scale, where $k \gg k_{\rm FS}(a)$ for all $a \leq a_0$, the neutrino density fluctuation oscillates around its initial value due to the free-streaming effect, $\delta_\nu(k,a) \sim \delta_\nu(k,a_{\rm i}) \simeq 0$.

3. At the intermediate scale, the mode first experiences the free-streaming phase, and thus does not grow. Once $k < k_{\rm FS}(a)$ is satisfied, the mode starts to grow, rapidly catching up with the gravitational potential set up by CDM.

4.3 The Boltzmann Hierarchy and Fluid Approximation

In this section, we provide all the relevant equations and definitions needed for our theoretical flame work, following Ma & Bertschinger (1995) in the conformal-Newtonian gauge.

For fermions and bosons, we have the phase space distribution (in natural units) given by

$$f_0(q,\tau) \;=\; \frac{g_s}{(2\pi)^3}\frac{1}{e^{\epsilon(q,\tau)/aT(a)} \pm 1}, \tag{4.12}$$

where the sign of "+" is for fermions and "−" is for bosons, q and $\epsilon(q,\tau) \equiv \sqrt{q^2 + a^2(\tau)m^2}$ are the co-moving momentum (i.e., $q = a(\tau)p$) and the co-moving energy of a particle, respectively. Here, τ is a conformal time, which is related to the proper time by $d\tau = dt/a(t)$, and g_s is a number of degrees of freedom. The linear order perturbation to the distribution function,

$\Psi(\mathbf{k}, \hat{\mathbf{n}}, q, \tau)$, is defined as

$$f(\mathbf{k}, \hat{\mathbf{n}}, q, \tau) = f_0(q, \tau)[1 + \Psi(\mathbf{k}, \hat{\mathbf{n}}, q, \tau)], \tag{4.13}$$

where $q \equiv |\mathbf{q}|$ and $\hat{\mathbf{n}} \equiv \mathbf{q}/q$.

Since neutrinos decoupled while they were highly relativistic, the unperturbed distribution function after the neutrino decoupling continues to be given by its relativistic form:

$$f_0(q) = \frac{g_s}{(2\pi)^3} \frac{1}{e^{q/aT(a)} \pm 1}, \tag{4.14}$$

even after neutrinos become non-relativistic. The temperature of such collision-less particles decreases as $T(a) = T_0(a_0/a)$, even when they are non-relativistic.

The evolution of the linearized phase-space distribution for collision-less particles such as CDM and neutrinos is governed by the linearized collision-less Boltzmann equation,

$$\begin{aligned} &\frac{\partial \Psi(\mathbf{k}, \hat{\mathbf{n}}, q, \tau)}{\partial \tau} + i \frac{q}{\epsilon(q, \tau)} (\mathbf{k} \cdot \hat{\mathbf{n}}) \Psi(\mathbf{k}, \hat{\mathbf{n}}, q, \tau) \\ &+ \frac{d \ln f_0(q)}{d \ln q} \left[\dot{\phi}(k, \tau) - i \frac{\epsilon(q, \tau)}{q} (\mathbf{k} \cdot \hat{\mathbf{n}}) \psi(k, \tau) \right] = 0, \end{aligned} \tag{4.15}$$

where ψ and ϕ are a Newtonian gravitational potential and a curvature perturbation, respectively. [3]

---

[3] In the original work of Ma & Bertschinger (1995), ψ and ϕ are defined as scalar perturbations in the metric in the conformal Newtonian gauge: $ds^2 = a^2(\tau)[-(1 + 2\psi)d\tau^2 + (1 - 2\phi)dx^i dx_i]$. They are related to the gauge invariant variables Φ_A and Φ_H of Bardeen (1980) and Ψ and Φ of Kodama & Sasaki (1984) by $\psi = \Phi_A = \Psi$ and $\phi = -\Phi_H = -\Phi$.

To simplify the equation, we define $\tilde{\Psi}(\mathbf{k}, \hat{\mathbf{n}}, q, \tau) \equiv \Psi(\mathbf{k}, \hat{\mathbf{n}}, q, \tau) \left(\frac{d\ln f_0(q)}{d\ln q}\right)^{-1}$, and replace the time derivative from τ to $x \equiv k\tau$, and re-write Eq.(4.15) as

$$\begin{aligned}\frac{\partial\tilde{\Psi}(\mathbf{k},\hat{\mathbf{n}},q,x)}{\partial x} + i\frac{q}{\epsilon(q,x)}\mu\tilde{\Psi}(\mathbf{k},\hat{\mathbf{n}},q,x) + \frac{\partial\phi(k,x)}{\partial x}& \\ -i\frac{\epsilon(q,x)}{q}\mu\psi(k,x) = 0,& \qquad (4.16)\end{aligned}$$

where μ is a cosine between the wavenumber and momentum, i.e., $\mathbf{k}\cdot\hat{\mathbf{n}} \equiv k\mu$. Finally, we expand the Boltzmann equation (Eq.(4.16)) by Legendre polynomials, using

$$\tilde{\Psi}(\mathbf{k},\hat{\mathbf{n}},q,x) = \sum_{l=0}^{\infty}(-i)^l(2l+1)\tilde{\Psi}_l(k,q,x)P_l(\mu), \qquad (4.17)$$

and obtain a set of infinite series of differential equations (also known as Boltzmann hierarchy) as follows:

$$\begin{aligned}\tilde{\Psi}_0'(k,q,x) &= -\frac{q}{\epsilon(q,x)}\tilde{\Psi}_1(k,q,x) - \phi'(k,x), & (4.18)\\ \tilde{\Psi}_1'(k,q,x) &= \frac{q}{3\epsilon(q,x)}[\tilde{\Psi}_0(k,q,x) - 2\tilde{\Psi}_2(k,q,x)] & \\ &- \frac{\epsilon(q,x)}{3q}\psi(k,x), & (4.19)\\ \tilde{\Psi}_l'(k,q,x) &= \frac{q}{(2l+1)\epsilon(q,x)}[l\tilde{\Psi}_{l-1}(k,q,x) & \\ &- (l+1)\tilde{\Psi}_{l+1}(k,q,x)] \quad (\text{for } l \geq 2), & (4.20)\end{aligned}$$

where the primes denote derivatives with respect to $x \equiv k\tau$. Here, $\tilde{\Psi}_0(k,q,x)$ is sourced by $\tilde{\Psi}_1(k,q,x)$. All the successive multipoles with $l \geq 1$, $\tilde{\Psi}_{l\geq 1}(k,q,x)$, are sourced by $\tilde{\Psi}_{l-1}(k,q,x)$ and $\tilde{\Psi}_{l+1}(k,q,x)$, so that the evolution of l-th multipole propagates the whole system of equations back and forth. In order to close the system of equations, we need to truncate the Boltzmann hierarchy at some finite multipole, $l_{\max}$. Now, the question is, "*in which condition the fluid approximation (i.e.,* $l_{\max}=1$ *or* 2*) is valid?*"

To make a contact with the familiar form of fluid equations, we relate multipoles of the perturbed distribution function, $\Psi_l(k,q,\tau)$, to the quantities such as the density contrast, $\delta(k,\tau)\equiv\frac{\delta\rho(k,\tau)}{\bar{\rho}(\tau)}$, velocity dispersion, $\theta(k,\tau)$, and anisotropic stress, $\sigma(k,\tau)$, by integrating $\Psi_l(k,q,\tau)$ over the momentum space with appropriate powers of q:

$$\begin{aligned}
\bar{\rho}(\tau) &= \frac{4\pi}{a^4(\tau)}\int q^2dq\ \epsilon(q,\tau)f_0(q), &(4.21)\\
\bar{P}(\tau) &= \frac{4\pi}{3a^4(\tau)}\int q^2dq\frac{q^2}{\epsilon(q,\tau)}f_0(q), &(4.22)\\
\delta\rho(k,\tau) &= \frac{4\pi}{a^4(\tau)}\int q^2dq\ \epsilon(q,\tau)f_0(q)\Psi_0(k,q,\tau), &(4.23)\\
\delta P(k,\tau) &= \frac{4\pi}{3a^4(\tau)}\int q^2dq\frac{q^2}{\epsilon(q,\tau)}f_0(q)\Psi_0(k,q,\tau), &(4.24)\\
(\bar{\rho}+\bar{P})\theta(k,\tau) &= \frac{4\pi k}{a^4(\tau)}\int q^2dq\ qf_0(q)\Psi_1(k,q,\tau), &(4.25)\\
(\bar{\rho}+\bar{P})\sigma(k,\tau) &= \frac{8\pi}{3a^4(\tau)}\int q^2dq\frac{q^2}{\epsilon(q,\tau)}f_0(q)\Psi_2(k,q,\tau). &(4.26)
\end{aligned}$$

We obtain the fluid equations by truncating the Boltzmann hierarchy at $l_{\max}=$

2:

$$\begin{aligned}
\dot{\delta}(k,\tau) &= -[1+w(\tau)][\theta(k,\tau)-3\dot{\phi}(k,\tau)] \\
&- 3\frac{\dot{a}(\tau)}{a(\tau)}\left[\frac{\delta P(k,\tau)}{\delta\rho(k,\tau)}-w(\tau)\right]\delta(k,\tau), \qquad (4.27)\\
\dot{\theta}(k,\tau) &= -\frac{\dot{a}(\tau)}{a(\tau)}[1-3w(\tau)]\theta(k,\tau)-\frac{\dot{w}(\tau)}{1+w(\tau)}\theta(k,\tau) \\
&+ \frac{\delta P(k,\tau)/\delta\rho(k,\tau)}{1+w(\tau)}k^2\delta(k,\tau)-k^2\sigma(k,\tau)+k^2\psi, \\
&\qquad (4.28)\\
\dot{\sigma}(k,\tau) &= -\frac{\dot{a}(\tau)}{a(\tau)}[2-3w(\tau)]\sigma(k,\tau)-\frac{\dot{w}(\tau)}{1+w(\tau)}\sigma(k,\tau) \\
&+ \frac{4}{15}\Theta(k,\tau)+\frac{\dot{a}(\tau)}{a(\tau)}\Sigma(k,\tau), \qquad (4.29)
\end{aligned}$$

where $w(\tau)\equiv\bar{P}(\tau)/\bar{\rho}(\tau)$ is an equation of state, and we have defined the following variables:

$$(\bar{\rho}+\bar{P})\Theta(k,\tau)=\frac{4\pi k}{a^4(\tau)}\int q^2dq\, q\left(\frac{q}{\epsilon(q,\tau)}\right)^2 f_0(q)\Psi_1(k,q,\tau), \qquad (4.30)$$

$$(\bar{\rho}+\bar{P})\Sigma(k,\tau)=\frac{8\pi}{3a^4(\tau)}\int q^2dq\frac{q^2}{\epsilon(q,\tau)}\left(\frac{q}{\epsilon(q,\tau)}\right)^2 f_0(q)\Psi_2(k,q,\tau). \qquad (4.31)$$

In the relativistic and non-relativistic limits, where majority of neutrinos in the phase space distribution have momenta of $q\sim\epsilon(q,\tau)$ and $q\ll\epsilon(q,\tau)$, we have $(w,\dot{w},\frac{\delta P}{\delta\rho},\Theta,\Sigma)=(\frac{1}{3},0,\frac{1}{3},\theta,\sigma)$ and $(0,0,0,0,0)$, respectively.

Since CDM is non-relativistic throughout the redshift of our interest, we can greatly simplify the calculation of the density contrast of CDM by fluid approximation (i.e., $l_{\max}=1$). We have

$$\begin{aligned}
\dot{\delta}(k,\tau) &= -\theta(k,\tau)+3\dot{\phi}(k,\tau), \qquad (4.32)\\
\dot{\theta}(k,\tau) &= -\frac{\dot{a}(\tau)}{a(\tau)}\theta(k,\tau)+k^2\psi(k,\tau). \qquad (4.33)
\end{aligned}$$

As for massive neutrinos, the fluid approximation may or may not be valid, depending on the mass, scale or redshift of interest. We check the validity of the fluid approximation for massive neutrinos by comparing to the exact solutions in section § 4.5.

When $l_{\max} = 2$, Eq.(4.18) and (4.20) give a useful relation between $\tilde{\Psi}_0(k, q, x)$ and $\tilde{\Psi}_2(k, q, x)$:

$$\frac{\partial}{\partial x}\left[\tilde{\Psi}_2(k, q, x) + \frac{2}{5}\tilde{\Psi}_0(k, q, x) + \frac{2}{5}\phi(k, x)\right] = 0, \tag{4.34}$$

which gives

$$\begin{aligned} &\tilde{\Psi}_2(k, q, x) + \frac{2}{5}\tilde{\Psi}_0(k, q, x) + \frac{2}{5}\phi(k, x) \\ &= \tilde{\Psi}_2(k, q, x_i) + \frac{2}{5}\tilde{\Psi}_0(k, q, x_i) + \frac{2}{5}\phi(k, x_i), \end{aligned} \tag{4.35}$$

where $x_i \ll 1$ is an initial time. With this relation and Eqs.(4.24) and (4.26), we can rewrite the anisotropic stress, $\sigma(k, \tau)$, in the Euler equation (Eq.(4.28)) in terms of pressure, $\delta P(k, \tau)$, as

$$k^2\sigma(k, \tau) + \frac{4}{5}\frac{\delta P(k, \tau)/\delta\rho(k, \tau)}{1 + w(\tau)}k^2\delta(k, \tau) = const, \tag{4.36}$$

where we have set $\phi = const$. At late times, $\tau \gg \tau_i$, where $\delta(k, \tau) \gg \delta(k, \tau_i)$ and $\sigma(k, \tau) \gg \sigma(k, \tau_i)$, the right hand side of Eq.(4.36) is negligible compared to the second term on the left hand side. Therefore, we have

$$k^2\sigma(k, \tau) \simeq -\frac{4}{5}\frac{\delta P(k, \tau)/\delta\rho(k, \tau)}{1 + w(\tau)}k^2\delta(k, \tau), \tag{4.37}$$

This result shows that σ increases the pressure by a factor of $\frac{9}{5}$. The free-streaming scale, $k_{\rm FS}$, is then reduced by a factor of $\frac{3}{\sqrt{5}} \sim 1.34$.

4.4 Analytic Solutions for the Boltzmann Equation

In this section, we briefly describe analytic solutions of the Boltzmann equation (Eq.(4.16)), to which the fluid approximation is compared. We give a detailed derivation of the solutions in Appendix C.2.

Instead of expanding the Boltzmann equation by Legendre polynomials as in Ma & Bertschinger (1995), we first find a formal solution of Eq.(4.16):

$$\begin{aligned}\tilde{\Psi}(k,q,\mu,x) &= \tilde{\Psi}(k,q,\mu,x_i)e^{-i\mu[z(x)-z(x_i)]} \\ &+ \int_{x_i}^{x} dx' e^{-i\mu[z(x)-z(x')]} S(k,q,\mu,x'), \end{aligned} \tag{4.38}$$

where

$$S(k,q,\mu,x) \equiv i\frac{\epsilon(q,x)}{q}\mu\psi(k,x) - \frac{\partial\phi(k,x)}{\partial x}, \tag{4.39}$$

and we have defined

$$z(x) \equiv \int_C^x \frac{q}{\epsilon(q,x')}dx'. \tag{4.40}$$

The lower integration boundary, $C \in \Re$, is an arbitrary constant. We then expand the above formal solution with Legendre polynomials. We will need the following relation of the Wigner 3-j symbols,

$$\int_{-1}^{1}\frac{d\mu}{2}P_l(\mu)P_{l'}(\mu)P_{l''}(\mu) = \begin{pmatrix} l & l' & l'' \\ 0 & 0 & 0 \end{pmatrix}^2. \tag{4.41}$$

The solution for $\tilde{\Psi}_l(k,q,x)$ for a given l is given by

$$\begin{aligned}\tilde{\Psi}_l(k,q,x) = &\sum_{l'}\sum_{l''}(-i)^{l'+l''-l}(2l'+1)(2l''+1)\\ &\times\tilde{\Psi}_{l'}(k,q,x_i)j_{l''}(z-z_i)\begin{pmatrix} l & l' & l'' \\ 0 & 0 & 0 \end{pmatrix}^2\\ - \ \psi(k)&\int_{x_i}^{x}dx'\frac{\epsilon(q,x')}{q}\left[\frac{l}{2l+1}j_{l-1}(z-z') - \frac{l+1}{2l+1}j_{l+1}(z-z')\right],\end{aligned} \tag{4.42}$$

where we have assumed $\dot{\psi}(k,x) = \dot{\phi}(k,x) = 0$ (which is satisfied in an Einstein de-Sitter, EdS, universe). We derive solutions for the most general case (i.e., $\dot{\psi}(k,x) \neq 0$ and $\dot{\phi}(k,x) \neq 0$) in Appendix C.2.

As we see in Eq.(4.42), the infinite series of the Boltzmann hierarchy, Eqs.(4.18)∼(4.20), is now expressed in terms of the spherical Bessel functions, $j_l(x)$, its integrals weighted by $\epsilon(q,x)/q$, and the infinite sum of the initial values of $\tilde{\Psi}_l(k,q,x)$.

While Eq.(4.42) appears to have infinite sums over l, the sum actually truncates because, at initial time (which is taken to be before the horizon re-entry), $\tilde{\Psi}_l(k,q,x)$ for $l \geq 3$ can be ignored (Ma & Bertschinger, 1995). Together with the triangular inequalities of the Wigner 3-j symbols,

$$|l-l'| \leq l'' \leq l+l', \tag{4.43}$$

only finite terms remain in the solution of $\tilde{\Psi}_l(k,q,x)$.

The explicit solutions of $\tilde{\Psi}_0(k,q,x)$ and $\tilde{\Psi}_1(k,q,x)$ are

$$\begin{aligned}
&\tilde{\Psi}_0(k,q,x) = \tilde{\Psi}_0(k,q,x_i)j_0(z-z_i) - 3\tilde{\Psi}_1(k,q,x_i)j_1(z-z_i) \\
&+5\tilde{\Psi}_2(k,q,x_i)j_2(z-z_i) + \psi(k)\int_{x_i}^{x} dx' \frac{\epsilon(q,x')}{q} j_1(z-z'), \qquad (4.44)
\end{aligned}$$

$$\begin{aligned}
&\tilde{\Psi}_1(k,q,x) = \tilde{\Psi}_0(k,q,x_i)j_1(z-z_i) \\
&+\tilde{\Psi}_1(k,q,x_i)j_0(z-z_i) - 2\tilde{\Psi}_2(k,q,x_i)j_1(z-z_i) \\
&-2\tilde{\Psi}_1(k,q,x_i)j_2(z-z_i) + 3\tilde{\Psi}_2(k,q,x_i)j_3(z-z_i) \\
&-\psi(k)\int_{x_i}^{x} dx' \frac{\epsilon(q,x')}{q}\left[\frac{1}{3}j_0(z-z') - \frac{2}{3}j_2(z-z')\right].
\end{aligned} \qquad (4.45)$$

Let us examine the behavior of $\tilde{\Psi}_l(k,q,x)$. At sufficiently late time, $z(x) \gg z(x_i)$, all the terms containing initial values of $\tilde{\Psi}_l(k,q,x)$ become negligible, as $j_l(z) \to 0$ for $z \gg l$. The last term, which does not depend on initial values, is the dominant term. For relativistic neutrinos, $\epsilon(q,x) = q$, the last term is proportional to $\int_{x_i}^{x} dx' j_l(x-x')$, which approaches constant for $x \gg l$. For non-relativistic neutrinos, $\epsilon(q,x) = a(\tau)m \propto x^2$, $j_l(z)$ does not oscillate for $x \gg 1$ (because $z(x) = \int \frac{q}{a(x)m}dx \propto \frac{1}{x}$). Thus, the integrand, $\frac{\epsilon(q,x)}{q} j_l(z)$, grows.

4.5 The Validity of the Fluid Approximation

Before we start, let us remember why fluid approximation may be valid for massive particles. Eq.(4.19) shows that the $l = 2$ mode becomes unimportant when the gravitational force (the last term) becomes dominant. The ratio of the last term to the first two terms is of order $(\epsilon/q)^2$, which is unity for relativistic particles, but it is much greater than unity for non-relativistic particles. Thus, $l \geq 2$ modes become irrelevant for the evolution of $l = 0$ and 1 modes, allowing us to truncate the Boltzmann hierarchy at $l_{\max} = 1$.

For example, when the distribution function of neutrinos is dominated by the non-relativistic states (i.e., $q \ll a(x)m$), we have the following solutions for $\tilde{\Psi}_0(k,q,x)$ and $\tilde{\Psi}_1(k,q,x)$ with constant ϕ and ψ,

$$\tilde{\Psi}_0(k,q,x) = \frac{\psi}{18}\left[x\left(4\frac{k}{C}+x\right)-16\left(\frac{k}{C}\right)^2\ln\left(4\frac{k}{C}+x\right)\right], \tag{4.46}$$

$$\tilde{\Psi}_1(k,q,x) = -\frac{x^2}{36}\left(\frac{C}{k}\right)^2\frac{m}{q}\left(6\frac{k}{C}+x\right)\psi, \tag{4.47}$$

where C is a constant, and the fastest growing modes grow as $\tilde{\Psi}_0(k,q,x) \propto a(x)$ and $\tilde{\Psi}_1(k,q,x) \propto a(x)\sqrt{1+a(x)}$.

The observable quantities such as $\delta(k,x)$ and $\theta(k,x)$ are given by the integrals of $\tilde{\Psi}_0(k,q,x)$ and $\tilde{\Psi}_1(k,q,x)$. They pick up contributions from the relativistic particles ($\epsilon(q,x) \sim q$) as well, but the phase-space number density of those relativistic particles is exponentially suppressed. To see this, we rewrite f_0 of relativistic particles as

$$f_0(q) = \frac{g_s}{(2\pi)^3}\frac{1}{e^{\frac{q}{m}\frac{m}{aT(a)}} \pm 1}, \tag{4.48}$$

where $\frac{q}{m} > 1$ for relativistic particles in the phase space distribution.

For CDM with $m \sim 1$ GeV, the mass to temperature ratio, $m/aT(a)$, is very large for the time that is relevant to the structure formation; thus, only extremely non-relativistic particles, $q/m \ll 1$, contribute to the density contrast, $\delta(k, \tau)$. As neutrinos are much lighter than CDM, relativistic particles may or may not contribute to the density contrast significantly. For example, to calculate the massless neutrino density contrast accurately, we need to calculate the $\tilde{\Psi}_0(k, q, x)$ for relativistic particles including all the higher multipoles in principle. If the neutrinos are sufficiently massive, then the last term in Eq.(4.19) becomes dominant over the first two terms for most of the particles in the phase-space distribution, $f_0(q)$, making the fluid approximation (i.e., $l_{\rm max} = 1$ or 2) valid.

Note that a fluid approximation does not imply that all the higher moments of the Boltzmann equations are small. It just means that the evolution equations of $\delta(k, x)$ and $\theta(k, x)$ are decoupled from the higher moments of the Boltzmann equations.

4.5.1 $\tilde{\Psi}_l(k, q, x)$ with various $l_{\rm max}$

To check the validity of fluid approximation, we need to compare the exact solutions of $\tilde{\Psi}_0(k, q, x)$ and $\tilde{\Psi}_1(k, q, x)$ to the approximate solutions of $\tilde{\Psi}_0(k, q, x)$ and $\tilde{\Psi}_1(k, q, x)$ with finite $l_{\rm max} = 1$, 2 and 3. To simplify the problem, we make the following (reasonable) approximations:

1. The universe is flat and matter dominated (EdS), for which $\dot{\phi} = \dot{\psi} = 0$.
2. We ignore the evolution of ϕ and ψ caused by massive neutrinos, which is a good approximation for proving the validity of the fluid approximation.

That is, ψ is determined by CDM only.

3. The initial perturbations are adiabatic and the wave lengths of the initial perturbations are greater than the horizon size, i.e., $x_i \ll 1$. Specifically, we have (Eq.(97) of Ma & Bertschinger (1995)):

$$\begin{aligned}
\tilde{\Psi}_0(k,q,x_i) &= -\frac{1}{4}\delta_\nu(k,x_i) = \frac{1}{2}\psi, & (4.49)\\
\tilde{\Psi}_1(k,q,x_i) &= -\frac{1}{3}\frac{\epsilon(q,x_i)}{q}\frac{\theta_\nu(k,x_i)}{k} = -\frac{1}{6}\frac{\epsilon(q,x_i)}{q}x_i\psi, & (4.50)\\
\tilde{\Psi}_2(k,q,x_i) &= -\frac{1}{2}\sigma_\nu(k,x_i) = -\frac{1}{30}x_i^2\psi, & (4.51)\\
\tilde{\Psi}_{l\geq 3}(k,q,x_i) &= 0, & (4.52)
\end{aligned}$$

where the most of neutrinos in the phase-space distribution are initially highly relativistic, $\epsilon(q,x_i) \sim q$.

We rewrite the Boltzmann equations (Eqs.(4.18) $\sim$ (4.20)) in terms of dimensionless parameters k/C and m/q defined below: the ratio of the comoving energy to the comoving momentum of a particle is given as

$$\frac{\epsilon(q,x)}{q} = \sqrt{1 + a^2(x)\left(\frac{m}{q}\right)^2}, \tag{4.53}$$

and the scale factor is given as

$$a(x) = \frac{C}{k}x + \left(\frac{C}{k}\frac{x}{2}\right)^2, \tag{4.54}$$

where

$$\begin{aligned}
C = \sqrt{\frac{8\pi G\bar{\rho}_m(a_{\rm eq})}{3}} &= H_0\sqrt{\Omega_m}\left(\frac{a_{eq}}{a_0}\right)^{-\frac{1}{2}}\\
&= 0.0183\sqrt{\Omega_m}\ h\ \mathrm{Mpc}^{-1}, & (4.55)
\end{aligned}$$

with $a_{\rm eq} \equiv 1$, $\bar{\rho}_{eq} = \bar{\rho}(a_{\rm eq})$, and we assume the matter radiation equality to happen at $1 + z_{\rm eq} = a_0/a_{\rm eq} = 3000$. For $\Omega_r = 8.47 \times 10^{-5}$, $\Omega_m = 0.25$ and $C = 0.0092h$ Mpc^{-1}.

With this convention for the scale factor, given comoving momentum is equal to the physical momentum (i.e., $q = p$) at the matter radiation equality, $a = a_{eq}$, and therefore, Eq.(4.48) becomes, [4]

$$\begin{aligned} f_0(q) &= \frac{g_s}{(2\pi)^3} \frac{1}{e^{\frac{q}{m}\frac{m}{T_{eq}}} \pm 1} \\ &= \frac{g_s}{(2\pi)^3} \frac{1}{e^{\frac{q}{m}\frac{m}{T_0}\frac{a_{eq}}{a_0}} \pm 1}. \end{aligned} \tag{4.56}$$

4.5.1.1 $\tilde{\Psi}_0(k, q, x)$

Figure 4.2 shows the evolution of $\tilde{\Psi}_0(k, q, x)$ for two different scales ($k/C = 10$ and 100) and two different momenta ($m/q = 10$ and 100). We calculate $\tilde{\Psi}_0^{\rm fluid}(k, q, x)$ by truncating the Boltzmann equations at $l_{\rm max} = 1$, 2 and 3 (fluid approximation), while we calculate $\tilde{\Psi}_0^{\rm exact}(k, q, x)$ from the exact solution of the Boltzmann equations given in Eq.(4.44). The fractional error in the fluid approximation is defined as $\Delta\tilde{\Psi}_0/\tilde{\Psi}_0 \equiv \tilde{\Psi}_0^{\rm fluid}/\tilde{\Psi}_0^{\rm exact} - 1$. For each

---

[4] The original paper did not take this factor of a_{eq}/a_0 into account, and therefore, neutrino mass was overestimated by $a_0/a_{eq} = 3000$. This correction does not affect any qualitative/quantitative argument for $\tilde{\Psi}_l$, but changes the interpretations of the resulting δ_ν and θ_ν.

combination of m/q and k/C, we show both $\tilde{\Psi}_0^{\rm exact}(k,q,x)$ (top), and $|\Delta\tilde{\Psi}_0/\tilde{\Psi}_0|$ (bottom) with $l_{\rm max}=1$ (solid lines), 2 (dotted lines) and 3 (dashed lines).

At large-scale ($k/C=10$ or $k\simeq 0.1\,h\,{\rm Mpc}^{-1}$), neutrinos with $m/q=10$ become non-relativistic at around the horizon re-entry, and neutrinos with $m/q=100$ become non-relativistic well *before* the horizon re-entry ($x_{nr}=k\tau_{nr}=0.98$ and 0.10 for $m/q=10$ and 100, respectively), and fractional errors of the fluid approximation peak at $x=x_H\sim 1$. At small-scale ($k/C=100$ or $k\simeq 1.0\,h\,{\rm Mpc}^{-1}$), neutrinos with $m/q=100$ become non-relativistic at around the horizon re-entry, while neutrinos with $m/q=10$ become non-relativistic well *after* the horizon re-entry ($x_{nr}=k\tau_{nr}=8.3$ and 0.98 for $m/q=10$ and 100, respectively). For neutrinos becoming non-relativistic after the horizon re-entry, fractional errors of the fluid approximation peak at $x=x_{nr}$.

We see that the asymptotic growth rate is $\tilde{\Psi}_0^{\rm exact}(k,q,x)\propto x^2\propto a$ (see Eq.(4.46)). For neutrinos with $m/q=10$ and $k/C=100$, the growth of $\tilde{\Psi}_0^{\rm exact}(k,q,x)$ is suppressed between the horizon re-entry and the epoch of relativistic to non-relativistic transition ($x_{nr}=8.3$); however, once neutrinos become non-relativistic, $\tilde{\Psi}_0^{\rm exact}(k,q,x)$ grows rapidly, catching up with the gravitational potential set up by CDM. [5] For both large and small-scales, fluid approximation becomes more accurate as we increase the $l_{\rm max}$, but for neutri-

---

[5] Even though we do not include CDM explicitly, by setting $\dot{\phi}=\dot{\psi}=0$, we are including CDM as a dominant source of the gravitational potential in the Boltzmann equations (i.e., the last term of Eq.(4.19)). If we calculate $\psi(k,x)$ including the suppression of the gravitational potential due to massive neutrino free-streaming, the neutrino catch-up will be slightly slower.

nos with $m/q = 100$ and $k/C = 10$, $l_{\max} = 1$ is sufficient to approximate the exact solution to better than 1% accuracy for almost entire evolution history ($x_H < x < x_0$). For small-scale, $k/C = 100$, with nearly relativistic neutrinos ($m/q = 10$), fluid approximation with low multipole cutoff (i.e., $l_{\max} = 1$, 2 and 3) breaks down for almost entire evolution history, while at late time ($x > 1000$), we start to see an accuracy of better than 1% for $l_{\max} = 2$ and 3.

4.5.1.2 $\tilde{\Psi}_1(k, q, x)$

Figure 4.3 shows the evolution of $\tilde{\Psi}_1(k, q, x)$ for two different scales ($k/C = 10$ and 100) and two different momenta ($m/q = 10$ and 100). We calculate $\tilde{\Psi}_1^{\text{fluid}}(k, q, x)$ and the fractional error in the fluid approximation in the same ways as before, while we calculate $\tilde{\Psi}_1^{\text{exact}}(k, q, x)$ from the exact solution of the Boltzmann equations given in Eq.(4.45). Results are almost the same as the case for $\tilde{\Psi}_0(k, q, x)$, except for the asymptotic growth rate is $\tilde{\Psi}_1^{\text{exact}}(k, q, x) \propto x^3 \propto a^{3/2}$ (see Eq.(4.47)). Since $\delta(k, x) \propto \tilde{\Psi}_0(k, q, x) \propto x^2$ and $\theta(k, x) \propto \tilde{\Psi}_1(k, q, x) \propto x^3$, the late-time evolution of $\delta(k, x)$ and $\theta(k, x)$ from the Boltzmann equations is consistent with the continuity equation (i.e., $\dot{\delta}(k, \tau) = -\theta(k, \tau)$).

4.5.1.3 $\tilde{\Psi}_2(k, q, x)$

Figure 4.4 shows the ratio of $\tilde{\Psi}_2(k, q, x)$ to $\tilde{\Psi}_0(k, q, x)$ for exact solutions (solid lines), $l_{\max} = 2$ (dotted lines) and $l_{\max} = 3$ (dashed lines) for two different scales ($k/C = 10$ and 100) and two different momenta ($m/q = 10$ and

100). As we discussed in § 4.3, we have a useful relation between $\tilde{\Psi}_0(k, q, x)$ and $\tilde{\Psi}_2(k, q, x)$ if we truncate the Boltzmann equations at $l_{\max} = 2$ (see Eq.(4.34)). Here, we check how late-time evolution can simplify the relation between $\tilde{\Psi}_0(k, q, x)$ and $\tilde{\Psi}_2(k, q, x)$. At sufficiently late time, we have an asymptotic value of $\tilde{\Psi}_2(k, q, x) = -\frac{2}{5}\tilde{\Psi}_0(k, q, x)$, which allows us to replace the anisotropic stress term in the fluid equations by the sound speed (Eq.(4.37)). As we see in the figure, the asymptotic value of $\tilde{\Psi}_2(k, q, x)/\tilde{\Psi}_0(k, q, x) = -2/5$ is reached at relatively early times.

4.5.1.4 Summary

We found that the applicability of the fluid approximation on the perturbed distribution function, $\tilde{\Psi}_l(k, q, x)$, depends crucially on our choice of wavenumber, k, momentum, q and mass, m, of particles. Generally speaking, wavenumber, k, sets the time of the horizon crossing, $a_H = a(x \sim 1)$, and the momentum and mass of the particles give the epoch of the relativistic to non-relativistic transition, $a_{\rm nr} \simeq q/m$. As long as a given particle becomes non-relativistic before the horizon crossing, $a_{\rm nr} < a_H$, the fluid approximation and the exact solution of $\tilde{\Psi}_l(k, q, x)$ agree to better than 1% accuracy. Re-writing $a_{\rm nr} < a_H$ in terms of m/q and k/C, we have,

$$\frac{q}{m} < \frac{C}{k} + \frac{1}{4}\left(\frac{C}{k}\right)^2 . \tag{4.57}$$

This condition can be easily satisfied for a large-scale mode, where $C/k \gg 1$ ($k \ll 0.01\ h$ Mpc^{-1}), and the condition can be satisfied in a small-scale mode, $C/k \ll 1$ ($k \gg 0.01\ h$ Mpc^{-1}), if $\frac{m}{q} > \frac{k}{C}$.

So far, we discussed the validity of the fluid approximation for $\tilde{\Psi}_l(k,q,x)$ with a given momentum and a given wavenumber. However, quantities such as $\delta(k,x)$ and $\theta(k,x)$ are given as integrals of $\tilde{\Psi}_l(k,q,x)$ over momentum space ($0 < q < \infty$) weighted by $f_0(q)$ and appropriate powers of q. The unperturbed distribution function, $f_0(q)$, exponentially suppresses the population of nearly relativistic neutrinos with an exponent of $\frac{q}{m_\nu}\frac{m_\nu}{T_{\nu,0}}\frac{a_{eq}}{a_0}$ (see Eq.(4.48)). For a given lower limit of neutrino mass, $m_\nu > 0.05$ eV, and the current temperature of neutrinos, $T_{\nu,0} \sim 1.9$ K, we have $\frac{m_\nu}{T_{\nu,0}} > 340$. Therefore, the population of relativistic neutrinos with $\frac{m}{q} \ll 0.1$ is negligible, and does not affect calculations of $\delta(k,x)$ or $\theta(k,x)$.

4.5.2 Limitation of Fluid Approximation on $\delta_\nu(k,x)$

Here, we study the limitation of the fluid approximation on the neutrino density contrast, $\delta_\nu(k,x)$, and the velocity divergence, $\theta_\nu(k,x)$, with two different masses of neutrinos, $m_\nu = 0.05$ and 0.5 eV. As we have seen in the previous section, for given k and a_0/a_{eq}, the ratio of the neutrino mass to the current temperature of neutrinos determines the validity of the fluid approximation.

With the current temperature of neutrinos, $T_{\nu,0} \sim 1.9$ K, we have $m_\nu/T_{\nu,\mathrm{eq}} = 305$ and 3050 for $m_\nu = 0.05$ and 0.5 eV, respectively. To find $\delta_\nu(k,x)$ and $\theta_\nu(k,x)$, we integrate $\tilde{\Psi}_l(k,q,x)$ using Eqs.(4.21)$\sim$(4.26) for several l_{max}.

4.5.2.1 $\delta_\nu(k,x)$ and $\theta_\nu(k,x)$ with small m_ν

Figure 4.5 shows the evolution of the fractional errors of the fluid approximation, $\Delta\delta_\nu(k,x)/\delta_\nu(k,x) \equiv \delta_\nu^{\rm fluid}(k,x)/\delta_\nu^{\rm exact}(k,x) - 1$ and $\Delta\theta_\nu(k,x)$ $/\theta_\nu(k,x) \equiv \theta_\nu^{\rm fluid}(k,x)/\theta_\nu^{\rm exact}(k,x) - 1$, as functions of a/a_0 for three different scales $k/C = 1$, 10 and 100 with $m_\nu = 0.05$ eV ($C = 0.01\ h$ Mpc^{-1}). As expected, the fluid approximation does not yield accurate results for such a small mass. As was the case for $\tilde{\Psi}_l^{\rm fluid}(k,q,x)$, the fractional error increases shortly after the horizon entrance, and then decreases as neutrinos become non-relativistic. For neutrinos with $m_\nu = 0.05$ eV, Eq.(4.7) gives $a_{\rm nr}/a_0 = 0.01$, or $x_{nr} = 9.4\frac{k}{C}$, and as a result the fluid approximation breaks down during entire evolution history of $\delta_\nu(k,x)$ and $\theta_\nu(k,x)$ between the horizon crossing and the present epoch ($a_H < a < a_0$). Nevertheless, for the largest scale ($k/C = 1$), the error is below 10% level at low redshit, as the neutrinos become sufficiently non-relativistic. We also show the fractional errors of fluid approximation for $\delta_\nu(k,x)$ and $\theta_\nu(k,x)$ calculated using the late time asymptotic value of Eq.(4.34): $\tilde{\Psi}_2(k,q,x) = -\frac{2}{5}\tilde{\Psi}_0(k,q,x)$ (dashed lines). As we have seen in Figure 4.4, this simple ansatz works well and follows the fractional error with $l_{\rm max} = 2$ at late time, $a \ll a_{\rm nr}$.

4.5.2.2 $\delta_\nu(k,x)$ and $\theta_\nu(k,x)$ with large m_ν

Figure 4.6 shows the evolution of the fractional errors of a fluid approximation as functions of a/a_0 for three different scales $k/C = 1$, 10 and 100 with $m_\nu = 0.5$ eV. For neutrinos with $m_\nu = 0.5$ eV, Eq.(4.7) gives $a_{\rm nr}/a_0 = 0.001$, or $x_{nr} = 2.1\frac{k}{C}$, and all the scale with $k/C \gtrsim 0.5$ enter the horizon when neutrinos are relativistic. As a result, the fluid approximation with $l_{\rm max} = 1$ is only accurate to $\sim$ 1% at large scale ($k/C = 1$) and $\sim$ 20% at small scale ($k/C = 100$) at low redshift.

We see that $l_{\rm max} = 2$ and the ansatz approximates the small-scale density contrast and velocity divergence better than the case with $l_{\rm max} = 1$, and the fluid approximation becomes accurate to $\lesssim 1\%$ at large scale ($k/C = 1$).

4.5.3 Range of Validity of Fluid Approximation

We have seen that the fractional errors of fluid approximation for $\delta_\nu(k, x)$ and $\theta_\nu(k, x)$ decrease for heavier particles, but the errors are still significant on small-scales. Now, the question is what is the maximum wavenumber, k_{max}, below which we can use the fluid approximation with 10 or 20% accuracy for a given mass of neutrinos at a given time. Figure 4.7 shows the fractional error, $\Delta\delta_\nu(k, x)/\delta_\nu(k, x) \equiv \delta_\nu^{\rm fluid}(k, x)/\delta_\nu^{\rm exact}(k, x) - 1$, for four different masses of neutrinos at three different redshifts, $z = 0, 5$ and 10. We find that the fluid approximation is only accurate to few$\sim$ 25% over a wide range of k at low redshift.

Table 4.1 shows k_{max} with $l_{\rm max} = 1$ and 2 for various neutrino masses, $m_\nu = 0.05,\ 0.10,\ 0.50$ and 1.0 eV, at five redshifts, $z = 0,\ 1,\ 3,\ 5$ and 10. The smaller the redshift is and the larger m_ν is, the larger k_{max} becomes. We see that k_{max} is $3 \sim 4$ times larger with $l_{\rm max} = 2$ than with $l_{\rm max} = 1$.

We are particularly interested in the k-range of linear to mildly non-

$l_{\max} = 1$	$m_\nu = 0.05$ eV	0.1 eV	0.5 eV	1.0 eV
z=0	0.009 (0.032)	0.018 (0.064)	0.090 (0.31)	0.18 (0.62)
z=1	0.007 (0.021)	0.012 (0.042)	0.060 (0.19)	0.12 (0.38)
z=3	0.005 (0.015)	0.009 (0.028)	0.039 (0.13)	0.079 (0.25)
z=5	0.003 (0.012)	0.008 (0.023)	0.032 (0.097)	0.060 (0.19)
z=10	0.002 (0.009)	0.004 (0.017)	0.023 (0.068)	0.042 (0.14)

$l_{\max} = 2$	$m_\nu = 0.05$ eV	0.1 eV	0.5 eV	1.0 eV
z=0	0.037 (0.097)	0.073 (0.19)	0.36 (0.94)	0.72 (1.88)
z=1	0.024 (0.064)	0.045 (0.13)	0.22 (0.58)	0.44 (1.16)
z=3	0.016 (0.042)	0.032 (0.079)	0.15 (0.36)	0.27 (0.72)
z=5	0.013 (0.034)	0.024 (0.064)	0.11 (0.29)	0.22 (0.54)
z=10	0.009 (0.024)	0.018 (0.045)	0.079 (0.19)	0.15 (0.38)

Table 4.1: The maximum wavenumber, $k_{max}[h \text{ Mpc}^{-1}]$, for which the fluid approximation is accurate at 10 (20)% or better.

linear regime on the matter density power spectrum at the redshifts relevant to the future and on-going galaxy redshift surveys ($z \lesssim 3$), and for that purpose, $0.1 \lesssim k_{max} \lesssim 0.4$ h Mpc^{-1} will be necessary with sufficient accuracy: on smaller scales, the non-linearity is too large for power spectrum to be used for cosmology.

4.6 Discussions and Conclusions

We have calculated the evolution of the perturbed distribution functions of massive neutrinos, $\tilde{\Psi}_l(k, q, x)$, using the fluid approximation, i.e., truncation of the Boltzmann equations at $l_{\max} = 1$, 2 and 3. We compared the approximate solutions to the exact solutions that we have derived in this paper. When the distribution function is dominated by the relativistic neutrinos, fluid approximation poorly represents the exact oscillation phase of $\tilde{\Psi}_l(k, q, x)$ calculated from the exact solution. When the distribution function is dominated by non-relativistic neutrinos, $\tilde{\Psi}_0(k,q,x)$ and $\tilde{\Psi}_1(k,q,x)$ are sourced mainly by the gravitational potential, $\psi(k,x)$, and decoupled from the higher multipoles, $\tilde{\Psi}_{l\geq 2}(k,q,x)$. This allows the fluid approximation to be an excellent approximation to the growth of $\tilde{\Psi}_0(k,q,x)$ and $\tilde{\Psi}_1(k,q,x)$ for small q. Then, we integrated the perturbed distribution functions to calculate the quantities such as $\delta_\nu(k,x)$ and $\theta_\nu(k,x)$. Comparing the density contrasts of massive neutrinos calculated from the fluid approximation to the exact solutions, we found that the fluid approximation is only accurate to few$\sim$ 25% for $k \lesssim 0.4\ h\ \mathrm{Mpc}^{-1}$ and $0.05 \leq m_\nu \leq 0.5$eV To increase the accuracy of the fluid approximation further, it is necessary to either directly solve for the Boltzmann hierarchy with $l_{max} \geq 3$ as in Eqs.(4.18)$\sim$(4.20), or solve fluid equations, Eqs.(4.27) and (4.28), with an ansatz for an anisotropic stress, $k^2\sigma(k,\tau)$, as we did for $l_{max} = 2$ in Eq.(4.37).

We solved the Boltzmann equation for massive neutrinos in an EdS universe for which $\dot{\phi}(k,x) = \dot{\psi}(k,x) = 0$. In a more realistic multi-component fluid case, we have $\dot{\phi}(k,x) \neq 0$ and $\dot{\psi}(k,x) \neq 0$ due to the effect of massive neutrinos even during the matter dominated epoch. Including this effect is straightforward. For the observationally allowed range of neutrino masses, we expect the correction to be small, as the dominant source of gravitational potential is still CDM ($f_\nu \lesssim 0.05$). Therefore, our conclusions regarding the limitation of the fluid approximation is not affected by our using an EdS universe. During the dark energy dominated epoch, the EdS approximation breaks down, and ϕ and ψ evolve. Nevertheless, the correction will be limited to the dark energy dominated epoch, $a > a_{DE}$, and the scale around $k \gtrsim k_{\rm FS}(a_{DE}) \gg k_{\rm FS}(a_{\rm nr})$. We found that, as long as the term proportional to the gravitational potential, $\psi(k,x)$, dominates the right hand side of Eq.(4.19), the fluid approximation is valid. Therefore, unless the effect of the dark energy suppresses $\psi(k,x)$ much faster than the growth of $\epsilon^2(q,x) \propto a^2$, k_{max} at $a > a_{DE}$ will not change significantly.

Since we have studied the evolution of the distribution function solving the collision-less Boltzmann equation, one can apply these results to other collision-less particles in general.

Now, why is fluid approximation useful? Future and on-going dark energy missions aim at the accurate measurement of the galaxy/matter power spectrum with an accuracy better than 1%. One might think that the cosmological linear perturbation theory has already been well established, and the numerical codes such as CMBfast and CAMB can calculate the linear matter power spectrum with an accuracy better than 1%.

However, the linear perturbation theory breaks down at small-scale and low redshift, where the density contrast becomes non-linear ($k \gtrsim 0.1\ h\ \mathrm{Mpc}^{-1}$ at $z \sim 1$) (Jeong & Komatsu, 2006; Carlson et al., 2009). Therefore, in order to exploit the cosmological information contained in a given survey, one needs to understand the non-linearities on the galaxy/matter power spectrum (Yamamoto et al., 2005; Rassat et al., 2008; Shoji et al., 2009).

Among the non-linearities, the matter clustering has been well understood in the mildly non-linear regime (see Bernardeau et al. (2002), for a review), but the theories have been limited to CDM dominated universe. The pressure gradient term in the Euler equation was completely ignored.

In our previous work, we developed the 3rd-order perturbation theory with the pressure gradient terms explicitly included (Shoji & Komatsu, 2009) (also see Saito et al. (2008); Wong (2008); Lesgourgues et al. (2009); McDonald (2009)). With this extension to the higher order perturbation theory as well as within the limitation on the accuracy of δ_ν calculated from the fluid approximation, we can now calculate the next-to-linear order matter power spectrum with massive neutrino free-streaming effect, properly included.

Since the structure formation is mostly affected by the most massive species of neutrinos, and the current constraints on the total mass of neutrinos indicate that at least one of the neutrino species has a mass of order a tenth of eV, the use of fluid approximation is limited with an accuracy of few to 25% over $k \lesssim 0.4\ h\ \mathrm{Mpc}^{-1}$ for $z < 10$. As a result, for a small fraction of massive neutrino, $f_\nu \lesssim 0.04$ for $\sum_i m_{\nu,\mathrm{i}} \lesssim 0.5$ eV, the fractional error on the matter density contrast, $\delta_m = (1 - f_\nu)\delta_\mathrm{c} + f_\nu \delta_\nu$, calculated with the fluid approximation is accurate to sub-percent level.

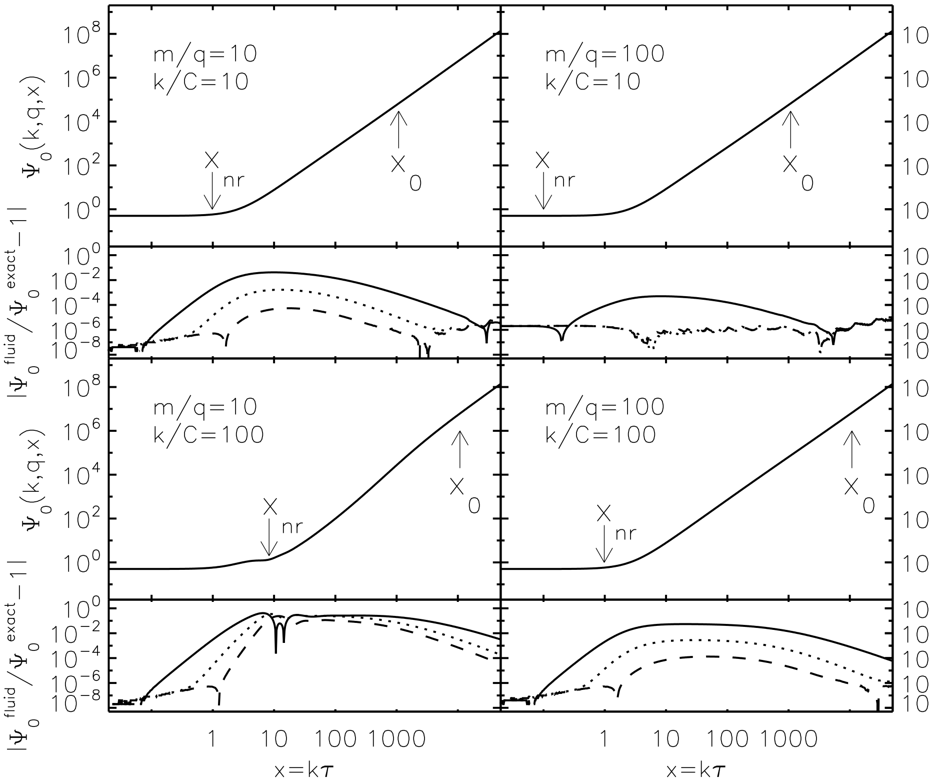

Figure 4.2: We show $\tilde{\Psi}_0(k,q,x)$ as functions of $x \equiv k\tau$ with two different scales ($k/C = 10$ and 100, where $C = 0.0092\ h\ \text{Mpc}^{-1}$) and two different momenta ($m/q = 10$ and 100). $\tilde{\Psi}_0(k,q,x)$ is calculated from the exact solution, and the fractional difference is given as $\Delta\tilde{\Psi}_0/\tilde{\Psi}_0 \equiv \tilde{\Psi}_0^{\text{fluid}}/\tilde{\Psi}_0^{\text{exact}} - 1$, where the solid line is for $l_{\max} = 1$, the dotted line is for $l_{\max} = 2$ and the dashed line is for $l_{\max} = 3$.

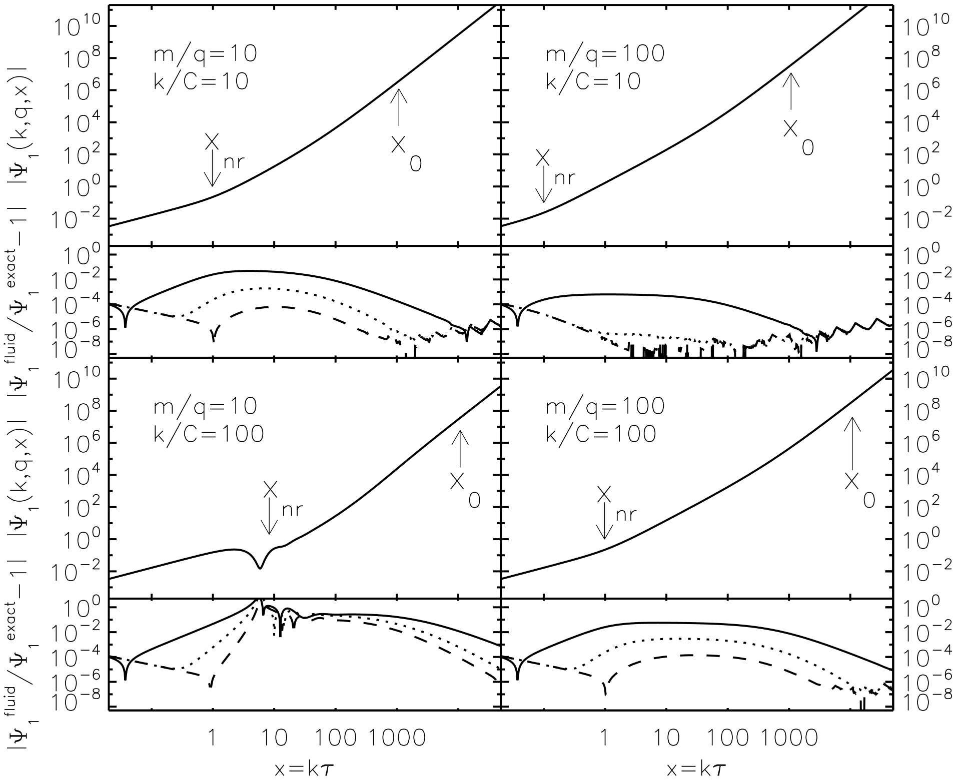

Figure 4.3: Same as Figure 4.2 for $\tilde{\Psi}_1(k, q, x)$.

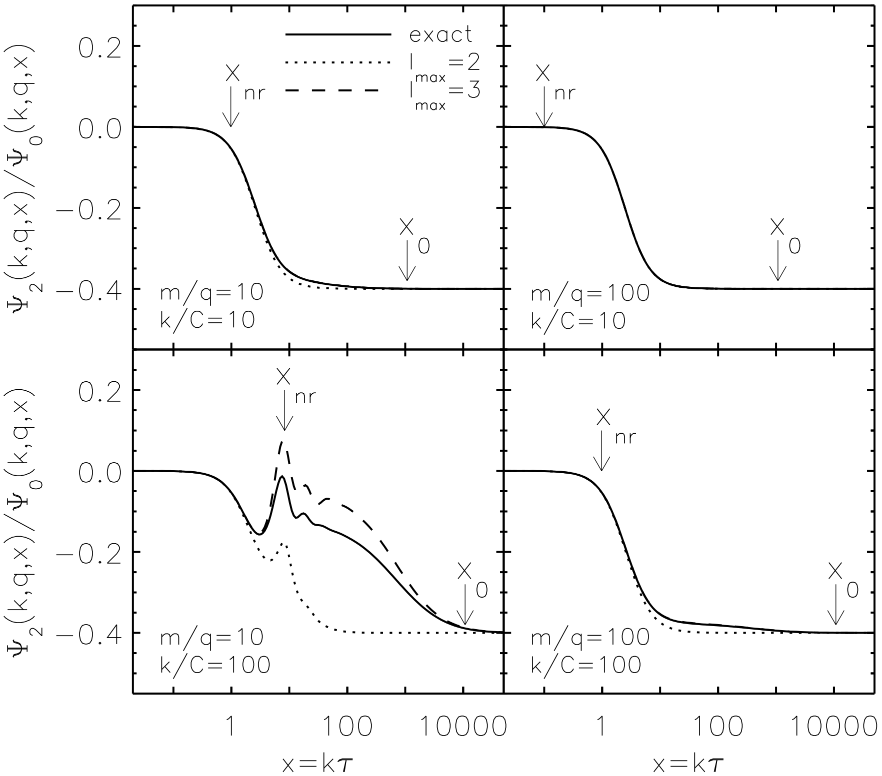

Figure 4.4: We show $\tilde{\Psi}_2(k,q,x)/\tilde{\Psi}_0(k,q,x)$ as functions of $x \equiv k\tau$ with two different scales ($k/C = 10$ and 100) and two different momenta ($m/q = 10$ and 100). Both $\tilde{\Psi}_0(k,q,x)$ and $\tilde{\Psi}_2(k,q,x)$ are calculated from the exact solution (solid line), or fluid approximation with $l_{\max} = 2$ (dotted line) and 3 (dashed line).

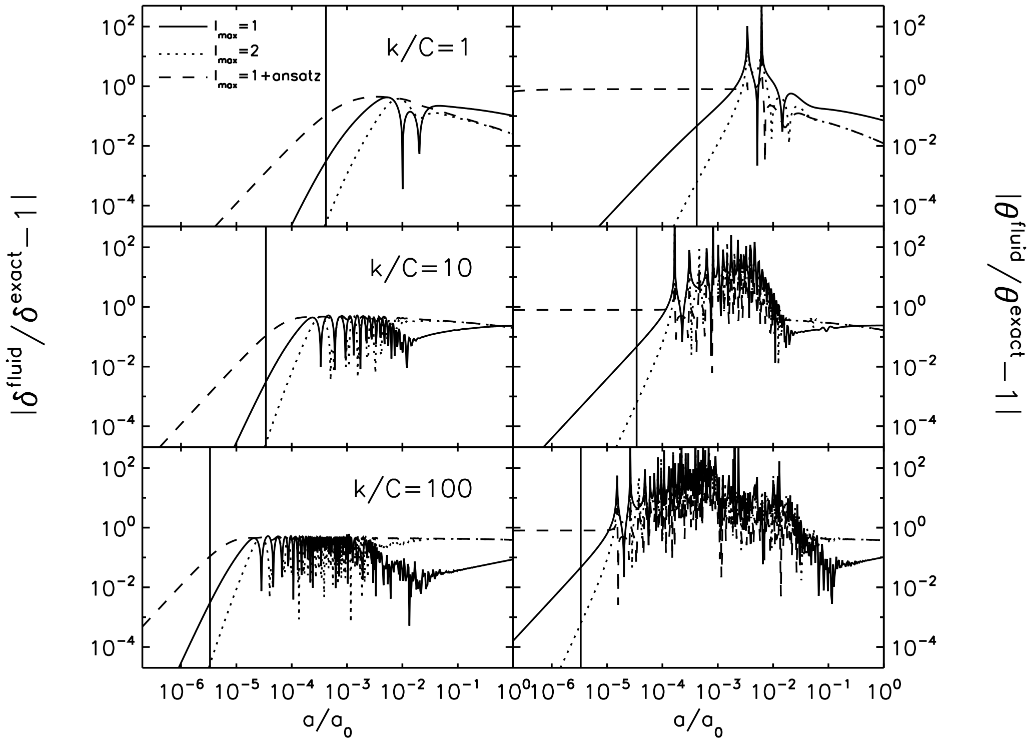

Figure 4.5: (*left*): Time evolution of the fractional errors of $\Delta\delta_\nu(k,x)/\delta_\nu(k,x) \equiv \delta_\nu^{\rm fluid}(k,x)/\delta_\nu^{\rm exact}(k,x) - 1$. The solid lines show $l_{\rm max} = 1$, while the dotted lines show $l_{\rm max} = 2$. The dashed lines show $l_{\rm max} = 1$, but with the ansatz for $l = 2$, $\tilde{\Psi}_2(k,q,x) = -\frac{2}{5}\tilde{\Psi}_0(k,q,x)$. (*right*): Time evolution of the fractional errors of $\Delta\theta_\nu(k,x)/\theta_\nu(k,x) \equiv \theta_\nu^{\rm fluid}(k,x)/\theta_\nu^{\rm exact}(k,x) - 1$. Here, we use $m_\nu = 0.05$ eV, and show the results at three different scales, $k/C = 1, 10$ and 100, corresponding to $k \simeq 0.01, 0.1$ and 1.0 h Mpc^{-1}, respectively. The vertical lines show the time of the horizon crossing for each mode. The present-day scale factor is $a_0 = 3000$.

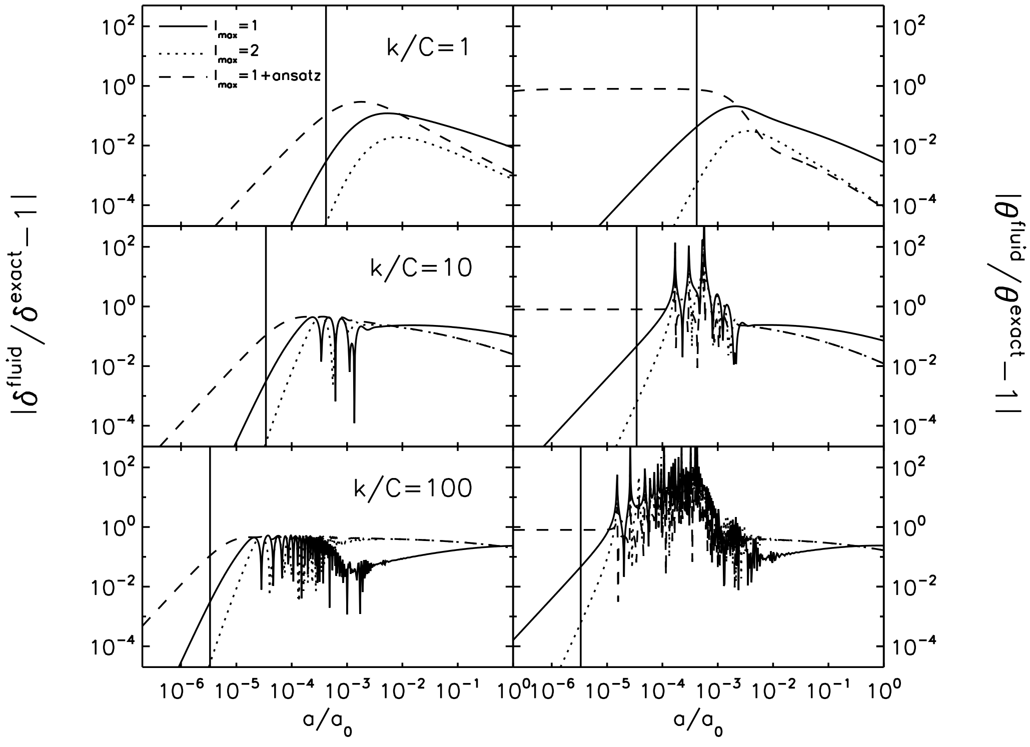

Figure 4.6: Same as Figure 4.5 for $m_\nu = 0.5$ eV.

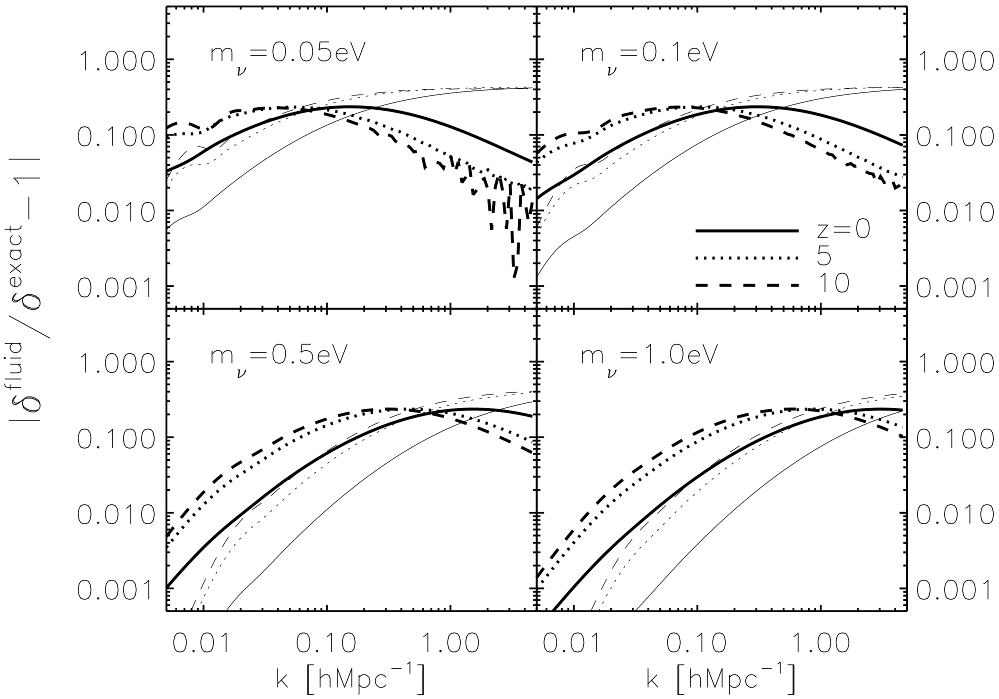

Figure 4.7: We show the fractional errors, $\Delta\delta_\nu(k,x)/\delta_\nu(k,x) \equiv \delta_\nu^{\rm fluid}(k,x)$ $/\delta_\nu^{\rm exact}(k,x)-1$, for four different masses of neutrino at three different redshifts, $z = 0,\ 5$ and 10 as functions of wavenumber, where the thick and thin lines are for $l_{\rm max} = 1$ and 2, respectively.

Chapter 5

Void in the Redshift Space

5.1 Introduction

The abundance of on-going and future galaxy surveys is pointing to the deeper understanding of the nature of accelerated expansion of the universe, as discovered via observations of luminosity distances to Type Ia supernovae (Riess et al., 1998; Perlmutter et al., 1999). The main observables of galaxy surveys are characteristic length scales encoded in the matter power spectrum, $P(k)$, such as the comoving Hubble horizon, $H(z)$, and the angular diameter distance, $D_A(z)$ (Shoji et al., 2009).

Not only can we measure geometric distances, $D_A(z)$ and $H(z)$, from a galaxy survey, but we also measure the growth rate of the matter density fluctuation, $f(z) \equiv \frac{d \ln D_+(z)}{d \ln a(z)}$, via redshift space distortions (Guzzo et al., 2008).

The matter density fluctuation grows via gravitational instability competing against the expansion of the universe. One can obtain the growth rate by solving the following differential equation (Wang & Steinhardt, 1998; Linder

& Jenkins, 2003; Komatsu et al., 2009),

$$\frac{d^2g}{d\ln a^2}+\left[\frac{5}{2}+\frac{1}{2}\left(\Omega_k(a)-3w(a)\Omega_{DE}(a)\right)\right]\frac{dg}{d\ln a}$$
$$+\left[2\Omega_k(a)+\frac{3}{2}\left(1-w(a)\right)\Omega_{DE}(a)\right]g(a)=0, \qquad (5.1)$$

where

$$g(a) \equiv \frac{D_+(a)}{a}, \qquad (5.2)$$
$$\Omega_k(a) \equiv \frac{\Omega_k H_0^2}{a^2H^2(a)}, \qquad (5.3)$$
$$\Omega_{DE}(a) \equiv \frac{\Omega_{DE}H_0^2}{a^{3[1+w_{\rm eff}(a)]}H^2(a)}, \qquad (5.4)$$
$$w_{\rm eff}(a) \equiv \frac{1}{\ln a}\int_0^{\ln a} d\ln a' w(a'). \qquad (5.5)$$

As we see in the Eq.(5.1), growth rate has an explicit dependence on the dark energy equation of state. Therefore, by measuring the growth rate, one can obtain the information about the dark energy, thereby, the nature of accelerated expansion of the universe.

Predictions for the growth rate from different theories of gravity and the nature of dark energy can be well parameterized in the simple form of $f(z)=\Omega_m(z)^\gamma$. For example, $\gamma=4/7$ for a ΛCDM model (Peebles, 1980; Hamilton, 2001), where the cosmological constant plays the role of observed accelerated expansion of the universe, and $\gamma=0.68$ for the DGP model of modifications of gravity (Lightman & Schechter, 1990). Thus, it is crucial to measure $f(z)$ from a given galaxy power spectrum to observationally unveil the nature of this mysterious component of the universe. Although a galaxy power spectrum gives a way to measure $f(z)$ at different redshifts, due to the vast parameter space allowed, an accurate measurement of $f(z)$ from a galaxy power spectrum alone is difficult (Simpson & Peacock, 2010). Especially, when we use the redshift space galaxy power spectrum to the linear order, it is inevitable to have the growth rate, $f(z)$, be degenerate with a linear galaxy bias, b_L, such that $P_g^s(k, \mu) = P_m(k, \mu)(1 + \beta\mu^2)^2$, where $\beta(z) \equiv f(z)/b_L$ (Kaiser, 1987). Thus, it is important to have an alternative method to measure the growth rate in addition to a redshift space galaxy power spectrum. Here, we propose the shape of voids in the redshift space as a sensitive probe of linear growth rate, $f(z)$.

The shape of the voids in redshift space has been studied in literature (Ryden, 1995; Ryden & Melott, 1996; Maeda et al., 2011). According to their study, the void volume increases in the redshift space as its boundary is stretched along the line of sight by redshift space distortion. This elongation of the void volume in the redshift space is diametrically opposite to what would happen to the distribution of galaxies in overdense regions, due to a reversed sign of the equation of motion sourced by local density field (Icke, 1984) (i.e., $\delta > 0$ for over dense regions and $\delta < 0$ for voids). Schmidt et al. (2001) studied the effect of redshift space distortion on the void probability function (VPF). The VPF is a measure of probability, $P_0(V)$, that a randomly placed sphere of volume V contains no galaxy within (White, 1979). For a given void in the real space, redshift space distortion stretches the void along the line of sight, increasing the volume of voids; thus, VPF, $P_0(V)$, increases toward a larger

V.

Here, we study the *ellipticity* of voids in the redshift space as a probe of the linear growth rate, $f(z)$. Specifically, we shall use the ellipticity probability distribution function of Park & Lee (2007) (hereafter, PL07) and Lee & Park (2009). PL07 proposed a void ellipticity distribution function as a sensitive probe of cosmology, noting that the shapes of voids are modulated by the competition between the tidal distortion and the cosmic expansion. Their model is based on the assumption that the underlying tidal field can be well described by the Zel'dovich approximation. They tested the model against the results from the Millennium simulations (Springel et al., 2005), finding a good agreement.

In practice, defining a void from a distribution of galaxies is non-trivial, as the definition of a void differs from one void finding algorithm to another (Colberg et al. (2008) and references there in). Regardless of the ambiguity in the exact definition and the boundary shape of a void, the method of PL07 gives a robust measurement of ellipticities of voids (i.e., defined as space around local density minima): it uses the distribution of galaxies inside a void as a tracer of the underlying shape of the tidal field. Void statistics have been studied both in simulations and galaxy redshift surveys (Hoyle & Vogeley, 2002; Patiri et al., 2006; Foster & Nelson, 2009; Pan et al., 2011). With the abundant data of the galaxy redshift survey available from on-going and future galaxy surveys, properties of voids can be better understood. Furthermore, voids found from these surveys will provide a unique way to probe the history of the structure formation, and henceforth, the nature of dark energy.

Throughout this paper we use the maximum likelihood cosmological parameters of Komatsu et al. (2009) (WMAP+BAO+SN of Table 1).

The goal of this paper is to provide an analytic insight into the observed ellipticities of voids, and establish basis for their application to cosmology. In § 5.2, we briefly review notations and definitions used in PL07 for a real space void ellipticity probability distribution function. In § 5.3, we study the effect of linear galaxy bias on the void ellipticity PDF. In § 5.4, we study the effect of redshift space distortion on the shape and ellipticity of observed voids. In § 5.5, we study the effect of the Poisson noise on the void ellipticity PDF, which arises as a consequence of tracing a void shape by a limited number of field galaxies inside the void. We also show that this Poisson noise can be the biggest limitation on the use of PL07 method for voids with a small number of field galaxies inside. In § 5.6, we compare the analytic prescriptions derived in the previous sections against the void ellipticity PDF extracted from the galaxy catalog of the Millennium simulation. Finally, our conclusions are in § 5.7.

5.2 Void in the real space

In this section, we briefly review the method of PL07. First, voids are extracted from a given galaxy distribution using a given void finding algorithm. We then find the ellipticities of voids, and construct a void ellipticity distribution function.

For each detected void, we define void galaxies, which reside inside a void, and calculate the inertia tensor of equal weight using $N_{\rm vg}$ void galaxies,

$$I^r_{ij} \equiv \sum_{\alpha=1}^{N_{\rm vg}} x^r_{i,\alpha} x^r_{j,\alpha}, \tag{5.6}$$

where x_i is the distance from the center of a void (i.e., the mean, $\bar{x}_i$, has been removed). Suppose that lengths of the semiaxis of the best-fit ellipsoid to a void are p_1, p_2 and p_3, ordered as $p_1 \geq p_2 \geq p_3 \geq 0$. Then, one finds that they are proportional to the square root of the eigenvalues of the inertia tensor, I_1, I_2 and I_3, ordered as $I_1 \geq I_2 \geq I_3 \geq 0$. This motivates our defining the ellipticity of a void such that,

$$\begin{aligned} \epsilon &\equiv 1 - \frac{p_3}{p_1} = 1 - \sqrt{\frac{I_3}{I_1}} \\ \eta &\equiv 1 - \frac{p_2}{p_1} = 1 - \sqrt{\frac{I_2}{I_1}}. \end{aligned} \tag{5.7}$$

For a fixed volume of an ellipsoid, $V = \frac{4\pi}{3} p_1 p_2 p_3$, we can exhaust all the possible shapes of the ellipsoid in terms of ϵ and η. Figure 5.1 shows five special configurations of ellipsoids on the ϵ-η plane. Note that according to our definition (i.e., $p_1 \geq p_2 \geq p_3 \geq 0$), we have $0 \leq \eta \leq \epsilon \leq 1$.

(a) For $\epsilon = \eta = 0$ (i.e., $p_1 = p_2 = p_3$), we have a spherical void.

(b) For $\epsilon = \eta = 1$ (i.e., $p_1 \gg p_2 = p_3 = 0$), we have a filamentary void.

(c) For $\epsilon = 1$ and $\eta = 0$ (i.e., $p_1 = p_2 \gg p_3 = 0$), we have a pancake void.

(d) For $\epsilon = \eta$ (i.e., $p_1 > p_2 = p_3$), we have a prolate spheroid.

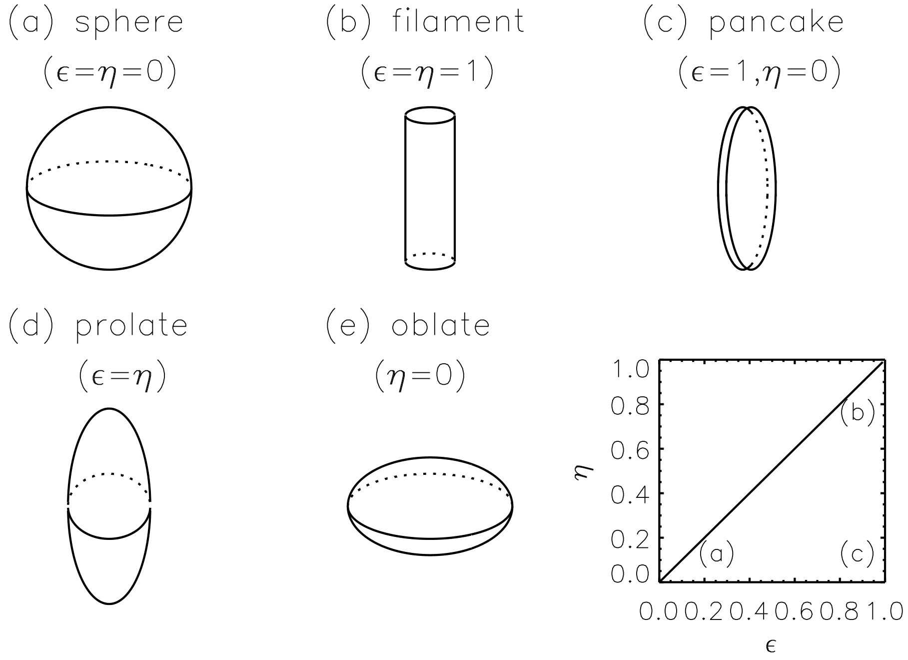

Figure 5.1: We show five special configurations of ellipsoids: (a) sphere, (b) filament, (c) pancake, (d) prolate spheroid and (e) oblate spheroid. In a plane of $\epsilon - \eta$, the lower triangle shows the possible configurations of ellipsoid, where each corner corresponds to a special configuration such as a sphere (lower left), a filament (upper right) and a pancake (lower right). Genuine triaxial ellipsoids are located in the middle of the triangle.

(e) For $\eta = 0$ (i.e., $p_1 = p_2 > p_3$), we have an oblate spheroid.

We define the triaxiality parameter following Franx et al. (1991),

$$T \equiv \frac{p_1^2 - p_2^2}{p_1^2 - p_3^2} = \frac{\eta(2-\eta)}{\epsilon(2-\epsilon)}, \tag{5.8}$$

and further divide the triaxial ellipsoid into two categories: prolate ellipsoids ($T > 0.5$) and oblate ellipsoids ($T < 0.5$).

5.2.1 Real-Space Ellipticity PDF

Here, we calculate the ellipticity probability distribution function of PL07 based on the unconditional joint probability density distribution of eigenvalues of a tidal tensor, $\{\lambda_1, \lambda_2, \lambda_3\}$ (Doroshkevich, 1970).

An unconditional PDF is given by

$$\begin{aligned} p(\lambda_1, \lambda_2, \lambda_3; \sigma_{R_L}) &= \frac{3375}{8\sqrt{5}\pi\sigma_{R_L}^6} \exp\left(-\frac{3K_1^2}{2\sigma_{R_L}^2} + \frac{15K_2}{2\sigma_{R_L}^2}\right) \\ &\times (\lambda_1 - \lambda_2)(\lambda_2 - \lambda_3)(\lambda_1 - \lambda_3), \end{aligned} \tag{5.9}$$

where $K_1 \equiv \lambda_1 + \lambda_2 + \lambda_3$, $K_2 \equiv \lambda_1\lambda_2 + \lambda_2\lambda_3 + \lambda_1\lambda_3$, and σ_{R_L} is the rms density fluctuation smoothed at the Lagrangean void size, R_L, with a top-hat window function, $W(kR_L)$,

$$\sigma_{R_L}^2 \equiv \int_{-\infty}^{\infty} \Delta^2(k) W^2(kR_L) d\ln k. \tag{5.10}$$

Here, we calculate $\Delta^2(k) \equiv \frac{k^3 P(k)}{2\pi^2}$ with a linear Boltzmann code, CAMB (Lewis et al., 2000), with the best-fit cosmological parameters of WMAP+BAO+SN (Komatsu et al., 2009).

We derive a Lagrangean void size, R_L, from conservation of the number density within the volume elements of Eulerian and Lagrangean space,

$$n(\mathbf{x}, z) d^3x = \bar{n} d^3q, \tag{5.11}$$

where $n(\mathbf{x}, z) = \bar{n}(1 + \delta(\mathbf{x}, z))$ is a real-space comoving number density of matter, $\bar{n}$ is a mean comoving number density, and $\mathbf{x}$ and $\mathbf{q}$ are Eulerian and Lagrangean coordinates, respectively. Therefore, we have

$$R_L(\mathbf{q}, z) = R_E(\mathbf{x}, z)(1 + \delta(\mathbf{x}, z))^{1/3}, \tag{5.12}$$

where R_E is an Eulerian size of void. PL07 derived the conditional PDF of $\{\lambda_1, \lambda_2\}$ for a given density contrast, $\delta = \sum_{i=1}^{3} \lambda_i$ as follows,

$$
\begin{aligned}
& p(\lambda_1, \lambda_2 | \delta, \sigma_{R_L}) = \frac{3375}{\sqrt{5\pi}\sigma_{R_L}^5} \\
& \times \exp\left[-\frac{5\delta^2}{2\sigma_{R_L}^2}\left(1 - \frac{3(\lambda_1 + \lambda_2)}{\delta} + \frac{3(\lambda_1^2 + \lambda_1\lambda_2 + \lambda_2^2)}{\delta^2}\right)\right] \\
& \times (2\lambda_1 + \lambda_2 - \delta)(\lambda_1 - \lambda_2)(\lambda_1 + 2\lambda_2 - \delta). \qquad (5.13)
\end{aligned}
$$

Here, as studied by Lavaux & Wandelt (2010), signs of eigenvalues, λ_i tell us whether the void is spatially expanding or contracting along the corresponding semiaxes. In our notation, a given void spatially expands when $\lambda_i < 0$, and contracts when $\lambda_i > 0$. Here, we only consider three dimensionally expanding genuine voids, $0 > \lambda_1 \geq \lambda_2 \geq \lambda_3$ and $\delta = \sum_{i=1}^{3} \lambda_i < 0$.

Now, under the premise of the strong correlation between the void shape, I_{ij}, and the underlying tidal tensor, $T_{ij} \equiv \frac{\partial^2 \Phi(\mathbf{q})}{\partial q_i \partial q_j}$, we have the following relations between the semimajor axis length, p_i, and the eigenvalues of the tidal tensor, λ_i:

$$\mu \equiv \frac{p_2}{p_1} = \left(\frac{1 - \lambda_2}{1 - \lambda_3}\right)^{1/2}, \qquad (5.14)$$

$$\nu \equiv \frac{p_3}{p_1} = \left(\frac{1 - \lambda_1}{1 - \lambda_3}\right)^{1/2}, \qquad (5.15)$$

where we assume $\lambda_1 \geq \lambda_2 \geq \lambda_3$. Using these, one can define the PDF of ϵ and η as

$$
\begin{aligned}
p(\epsilon, \eta | \delta, \sigma_{R_L}) &= p(\lambda_1(\mu, \nu), \lambda_2(\mu, \nu) | \delta, \sigma_{R_L}) \\
&\times \frac{4(\delta - 3)^2 \mu\nu}{(\mu^2 + \nu^2 + 1)^3}, \qquad (5.16)
\end{aligned}
$$

where $\mu = 1 - \eta$ and $\nu = 1 - \epsilon$, and

$$\lambda_1(\mu, \nu) = \frac{1 + (\delta - 2)\nu^2 + \mu^2}{\mu^2 + \nu^2 + 1} \tag{5.17}$$

$$\lambda_2(\mu, \nu) = \frac{1 + (\delta - 2)\mu^2 + \nu^2}{\mu^2 + \nu^2 + 1}. \tag{5.18}$$

From Eq.(5.9), we see that the probability of having two of the three eigenvalues, λ_i, being equal is suppressed due to the last three factors (i.e., $(\lambda_1 - \lambda_2)(\lambda_2 - \lambda_3)(\lambda_1 - \lambda_3)$). Therefore, we have small probabilities of having ellipsoids with special configurations such as $\epsilon = \eta$ (prolate spheroids), $\eta = 0$ (oblate spheroids) and $\epsilon = 0$ (sphere): these special configurations correspond to $\lambda_1 = \lambda_2$, $\lambda_2 = \lambda_3$ and $\lambda_1 = \lambda_3$, respectively. In figure 5.2, we plot the ellipticity PDF of Eq.(5.16) for $R_L = 5$ (*left*) and 10 h^{-1}Mpc (*right*), where $\delta_v = -0.9$. PDF is normalized so that the peak value is unity (stars). Note that for a fixed density contrast, δ, the exponential factor in Eq.(5.9) is maximized when $\lambda_1 = \lambda_2 = \lambda_3$ allowing nearly spherical voids to have a finite probability.

We also plot the line separating the prolate and oblate ellipsoids (i.e., $T = 0.5$) (solid line). We see that locations of the ellipticity PDF peaks lie roughly on the line of $T = 0.5$, and PDF shifts toward smaller ellipticity both in ϵ and η for larger voids (i.e., smaller σ_{R_L} for a fixed set of cosmological parameters).

Also note that the ellipticity PDF in the real space has almost no preference for prolate or oblate ellipsoids ($T \simeq 0.5$). For $R_L = 5h\mathrm{Mpc}^{-1}$,

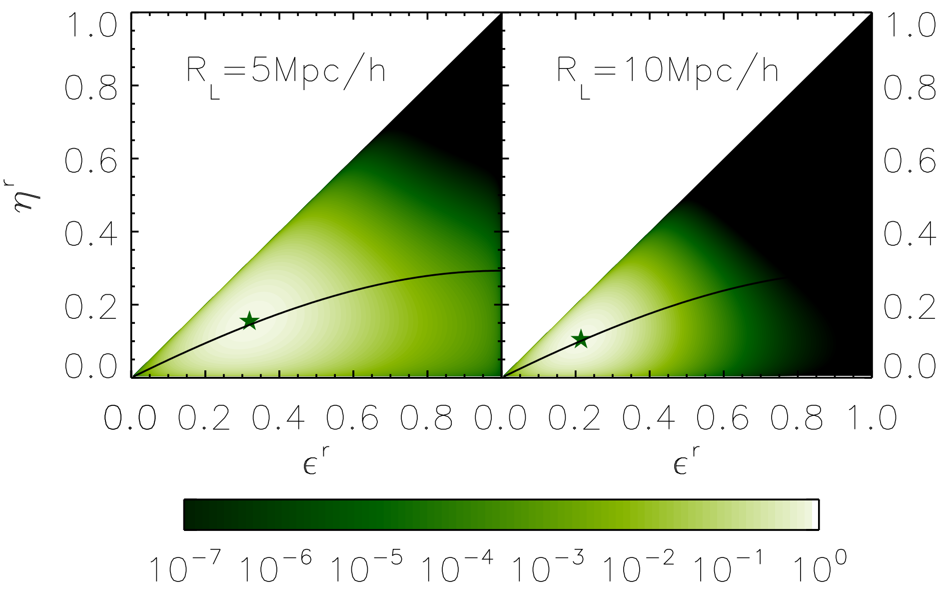

Figure 5.2: We show the ellipticity PDF for $R_L = 5$ and $10h^{-1}$Mpc at $z = 0$. PDF is normalized so that the peak values are 1. Solid lines show $T = 0.5$ and stars show the peaks of each PDF.

$\delta = -0.9$ and $z = 0$, we have mean ellipticities, $\bar{\epsilon}$ and $\bar{\eta}$ as follows,

$$\bar{\epsilon} = \int_0^1 d\epsilon \int_0^{\epsilon/2} d\eta \; \epsilon \; p(\epsilon, \eta|\delta, \sigma_{R_L}) = 0.37, \tag{5.19}$$

$$\bar{\eta} = \int_0^1 d\epsilon \int_0^{\epsilon/2} d\eta \; \eta \; p(\epsilon, \eta|\delta, \sigma_{R_L}) = 0.16, \tag{5.20}$$

$$\bar{T} = \int_0^1 d\epsilon \int_0^{\epsilon/2} d\eta \; T(\epsilon, \eta) \; p(\epsilon, \eta|\delta, \sigma_{R_L}) = 0.50, \tag{5.21}$$

and for $R_L = 1h\mathrm{Mpc}^{-1}$, $\delta = -0.9$ and $z = 0$, we have $\bar{\epsilon} = 0.62$, $\bar{\eta} = 0.27$ and $\bar{T} = 0.55$.

However, previous observations and numerical studies indicate a preference for prolate ellipsoids. From voids detected in a ΛCDM N-body simulation, Platen et al. (2008) claimed the axis ratio of best-fit ellipsoids to be 1 : 0.7 : 0.5

(i.e., $\epsilon = 0.5$, $\eta = 0.3$ and $T = 0.68$), and FN09 also found a preference for the prolate ellipsoids from the voids detected in the SDSS DR5 with $\epsilon = 0.33$, $\eta = 0.21$ and $\bar{T} = 0.66$. In figure 5.3, we show the distribution of ellipticities of 232 voids from the SDSS DR5 based on the catalog of Foster & Nelson (2009). We also show the corresponding ellipticity PDF just as a reference. The volume limited sample has a total of 52281 galaxies in a volume of $0.021h^{-3}\text{Gpc}^3$ ($\bar{n}_g \simeq 2.45 \times 10^{-3} h\text{Mpc}^{-3}$). In the ϵ-η plane, we clearly see the dominance of prolate voids, while analytic PDF has a slight to no preference of prolateness in the shape of voids. We think that the difference arises from the way we calculate ellipticities of voids. Earlier works extracted void shapes by calculating the shape tensor from volume elements inside detected voids. In this way, an extracted ellipticity is sensitive to the boundary shape of the void as defined from a given void finder. Since a boundary is defined from galaxies in an overdense region, $\delta \gtrsim 0$, the tidal field around the boundary is subject to a stronger distortion from the external gravitational force. An unconditional ellipticity PDF of Doroshkevich (1970), on the other hand, describes a tidal field at and around the density minima. Therefore, when we compare the analytic ellipticity PDF of PL07 against that of a simulation or galaxy survey, it is important to know whether the extracted ellipticity truly represents the shape of the tidal field around density minima.

5.3 Linear Galaxy Bias in the Real-Space Void ellipticity PDF

In the previous section, we have related the ellipticity PDF of voids to the tidal field generated by the matter density distributions. However, in reality, we obtain a void ellipticity PDF from a given galaxy distribution. In order to deduce the underlying matter density field, δ_m, from galaxy distributions, we use the well known linear galaxy bias, b_L, such that $\delta_v = b_L \delta_m$. Here, δ_v represents the density contrast of a void calculated from the number density of galaxies within the void, $n_{\rm vg}$, and that of the cosmic mean, $\bar{n}_g$, (i.e, average number density of galaxies in a survey volume),

$$\delta_v \equiv \frac{n_{\rm vg} - \bar{n}_g}{\bar{n}_g}. \tag{5.22}$$

Since the unconditional PDF of Doroshkevich (1970) gives eigenvalues of tidal tensor, T_{ij}, generated by the matter density field, we use $\delta_m = \delta_v / b_L$ in Eqs.(5.13) $\sim$ (5.18), where b_L is a linear galaxy bias to be calibrated from an observed ellipticity PDF. The filtering scale, R^m_L, should also be calculated following the definition of the linear bias,

$$R^m_L \quad = \quad R^m_E (1 + \delta_v / b_L)^{1/3}. \tag{5.23}$$

Here, an Eulerian size of void traced by the matter density field, R^m_E, is not a direct observable in a galaxy survey (i.e., the void size measured by the galaxy distribution, R^v_E, is a direct observable). Patiri et al. (2006) showed that the radial density profiles of voids defined from dark matter and halo distribution of N-body simulations have similar shapes, and at large radii, haloes trace the dark matter. Based on this result, we set $R_E^m \simeq R_E^v$ here, and have

$$R_L^m = R_E^v(1+\delta_v/b_L)^{1/3}. \tag{5.24}$$

Figure 5.4 shows the effect of linear galaxy bias on the real space ellipticity PDF both in 1-D (*bottom right*) and in 2-D (*top left to bottom left*). We normalize the 2-D PDFs to their peak values, and set the parameters to $R_L = 5h^{-1}$Mpc, $\delta_v = -0.9$ and $z = 0$. In the 1-D plot, we have PDF for four different linear galaxy biases, $b_L = 1.0$ (solid), 1.1(dotted), 2.0 (dashed) and 5.0 (dot-dashed), and in the 2-D plots, we have $b_L = 1.0$ (top left), 1.1 (top right) and 2.0 (bottom left).

In the 2-D plots, the solid lines show $T = 0.5$, and the stars show the peaks of each PDF. Regardless of the values of bias, peaks of PDF lie on the solid lines ($T = 0.5$), and the ratio of prolate to oblate spheroids is ~ 0.5 as in the case of unbiased (i.e., $b_L = 1$) ellipticity PDF.

We clearly see an effect of bias on the void PDF as we increase the galaxy bias b_L from its unbiased value, $b_L = 1$, to biased value, $b_L > 1$. As we increase the bias from $b_L = 1$, the ellipticity PDF peaks at smaller ellipticities more sharply. For $b_L > 2.0$, the shape of PDF converges quickly, and becomes insensitive to the further change in b_L. As a larger bias reduces the matter density contrast, δ_m, for a fixed value of δ_v, a smaller matter density contrast yields a less pronounced tidal field around the density minima, yielding smaller ellipticity.

In Eqs.(5.13) $\sim$ (5.18), we see the effect of bias through σ_{R_L}. Since the Lagrangean size of void, R_L^m, (as defined in Eq.(5.24)) sets the smoothing scale of the density field for calculating σ_{R_L}, the larger the R_L^m is, the smaller the σ_{R_L} becomes. Again, a smaller rms fluctuation of the matter density field leads to a weaker tidal field, and hence, the smaller ellipticity of the void. We see that, although the linear bias, b_L, and σ_8, which is directly proportional to the σ_{R_L}, are nearly degenerate in the parameter space of the biased ellipticity PDF, their correlation is directly opposite in the case of the galaxy power spectrum, $P_g(k) \propto b_L^2\sigma_8^2$. This feature of the biased void ellipticity PDF allows us to better constrain both the linear bias, b_L, and the rms density fluctuations, σ_8, when combined with the galaxy power spectrum.

5.4 Void in the redshift space

In order to compare the analytic and observed ellipticity PDFs, we need to understand the effect of the redshift space distortion on the ellipticity of a given void. Unlike galaxies and galaxy clusters, which reside in density maxima, voids reside in density minima, where the diverging velocity field pushes the boundary and the field galaxies inside the voids outward, expanding their volume in all directions (Icke, 1984).

A real-space inertia tensor is defined in Eq.(5.6), and that of the redshift-space is similarly defined as

$$I_{ij}^s \equiv \sum_{\alpha=1}^{N_{\rm vg}} x_{\alpha,i}^s x_{\alpha,j}^s, \tag{5.25}$$

where N_{vg} is the number of void galaxies, and $\mathbf{x}^s_\alpha$ is the redshift-space position of an α-th void galaxy. An inertia tensor is symmetric by definition (i.e., $I_{ij} = I_{ji}$), and traces a shape of a void from an underlying void galaxy distribution. Park & Lee (2007) identified voids from the Millennium simulation using the void finding algorithm of Hoyle & Vogeley (2002), and extracted the ellipticity PDF of voids using the inertia tensor using void galaxies as tracers. They found that the distribution of ellipticities of voids from the Millennium simulation follows that of linear theory (Zel'dovich Approximation) prediction in real space.

Here, we study the effect of the redshift space distortion on the ellipticity PDF. First, we calculate the redshift space inertia tensor as follows.

A mapping between the real-space and the redshift space is given by

$$x^s_1 = x^r_1 \tag{5.26}$$

$$x^s_2 = x^r_2 \tag{5.27}$$

$$x^s_3 = x^r_3 - f\mathbf{u}\cdot\hat{\mathbf{x}}^r_3, \tag{5.28}$$

where $f \equiv \frac{d\ln\delta(a)}{d\ln a}$ is the growth rate, and the unit vector, $\hat{\mathbf{x}}^r_3$, is along the line of sight. Here, $\mathbf{u} \equiv \frac{-\mathbf{v}}{\mathcal{H}f}$, where $\mathbf{v}$ is the peculiar velocity of a void galaxy, and $\mathcal{H}(a) = aH(a)$ is a comoving Hubble rate.

We define $\kappa(\mathbf{x}^r)$ to quantify the strength of the redshift space distortion as

$$\kappa(\mathbf{x}^r) \equiv -\frac{f\widehat{\mathbf{x}^r_3}\cdot\mathbf{u}(\mathbf{x}^r)}{x^r_3}. \tag{5.29}$$

With $\kappa(\mathbf{x}^r)$, we re-write Eq.(5.28) as

$$x_3^s = x_3^r(1+\kappa(\mathbf{x}^r)), \tag{5.30}$$

and we relate the redshift-space inertia tensor to the real-space inertia tensor as follows,

$$I_{11}^s = I_{11}^r \tag{5.31}$$

$$I_{12}^s = I_{12}^r \tag{5.32}$$

$$I_{22}^s = I_{22}^r \tag{5.33}$$

$$I_{13}^s = I_{13}^r + \sum_{\alpha=1}^{N_{\rm vg}} x_{\alpha,1}^r x_{\alpha,3}^r \kappa_\alpha \tag{5.34}$$

$$I_{23}^s = I_{23}^r + \sum_{\alpha=1}^{N_{\rm vg}} x_{\alpha,2}^r x_{\alpha,3}^r \kappa_\alpha \tag{5.35}$$

$$I_{33}^s = I_{33}^r + 2\sum_{\alpha=1}^{N_{\rm vg}} x_{\alpha,3}^r x_{\alpha,3}^r \kappa_\alpha + \sum_{\alpha=1}^{N_{\rm vg}} x_{\alpha,3}^r x_{\alpha,3}^r \kappa_\alpha^2, \tag{5.36}$$

where

$$\kappa_\alpha = -\frac{f\mu_\alpha u_\alpha}{x_{\alpha,3}^r}, \tag{5.37}$$

and μ is the angle between the peculiar velocity, $\mathbf{u}$, and the line of sight (i.e., $\mu \equiv \hat{\mathbf{u}} \cdot \hat{x}_3^r$).

Once we have the redshift space inertia tensor either numerically, from Eq.(5.25), or analytically in terms of κ, from Eqs.(5.31) $\sim$ (5.36), we can calculate the ellipticity of a given void, ϵ and η, from eigenvalues of the redshift space inertia tensor, $(I_1^s \geq I_2^s \geq I_3^s)$ as in Eq.(5.7).

Since κ is a function of the peculiar velocity field, we can use linear theory to calculate κ for an arbitrary density field, $\delta(\mathbf{x}^r)$, as,

$$\begin{aligned}
\kappa(\mathbf{x}^r) &\equiv -\frac{f\widehat{\mathbf{x}_3^r}\cdot\mathbf{u}(\mathbf{x}^r)}{x_3^r} = -\frac{f\widehat{\mathbf{x}_3^r}\cdot\nabla\Phi(\mathbf{x}^r)}{4\pi G a^2\bar{\rho}x_3^r} \\
&= -\frac{f}{4\pi G a^2\bar{\rho}x_3^r}\int\frac{d^3k}{(2\pi)^3}i\mathbf{k}\cdot\hat{\mathbf{x}}_3^r\tilde{\Phi}(\mathbf{k})e^{i\mathbf{k}\cdot\mathbf{x}^r} \\
&= \frac{f}{x_3^r}\int\frac{d^3k}{(2\pi)^3}i\mathbf{k}\cdot\hat{\mathbf{x}}_3^r\frac{\tilde{\delta}(\mathbf{k})}{k^2}e^{i\mathbf{k}\cdot\mathbf{x}^r} \\
&= \frac{f}{x_3^r}\int_0^\infty\frac{dk}{(2\pi)^3}ik\int_0^{2\pi}d\phi_k\int_{-1}^{1}d\mu_k\mu_k\tilde{\delta}(\mathbf{k})e^{i\mathbf{k}\cdot\mathbf{x}^r},
\end{aligned} \tag{5.38}$$

where $\mu_k \equiv \cos\theta_k$. Here, we used the linear relation between a peculiar velocity and a gravitational field derived from Zel'dovich Approximation (Hui & Bertschinger, 1996),

$$\mathbf{v} = -\frac{\mathcal{H}f}{4\pi G a^2\bar{\rho}}\nabla\Phi, \tag{5.39}$$

and a Poisson equation,

$$\nabla^2\Phi = 4\pi G a^2\bar{\rho}\delta. \tag{5.40}$$

We explicitly write a cosine angle between $\mathbf{k}$ and $\mathbf{x}$, in a spherical coordinate as

$$\cos\gamma \equiv \cos\theta_k\cos\theta_x + \cos(\phi_k - \phi_x)\sin\theta_k\sin\theta_x, \tag{5.41}$$

where $\mathbf{k}\cdot\mathbf{x} = kx\cos\gamma$. Here, in order to calculate the effect of peculiar velocity on the void shape, we need to know the density profile of a void, $\delta(\mathbf{x})$ in the real space. Sheth & van de Weygaert (2004) studied an evolution of a radial density profile of an isolated void, and found that the density profile evolves into an increasingly similar shape to a top-hat function. With N-body simulations both in sCDM and ΛCDM, Colberg et al. (2005) found that the radial density profile of a void is universal, having $\rho(r < r_{\rm eff})/\rho(r_{\rm eff}) \propto \exp[(r/r_{\rm eff})^{\alpha}]$, where $r_{\rm eff}$ is the effective radius of the void and $\alpha \sim 2$. These analytic radial density profiles are also seen in the voids identified from the galaxy distribution of the Sloan Digital Sky Survey as a sharp rise of density contrast near the boundary of the void (Patiri et al., 2006; Pan et al., 2011). In this section, we approximate the radial density profile of the void, $\delta(r)$, to be a top-hat function for simplicity,

$$\delta(\mathbf{x}^r) = \begin{cases} \bar{\delta} & \text{within the void} \\ 0 & \text{outside the void} \end{cases}, \tag{5.42}$$

where $\bar{\delta}$ is the average density contrast within the void. We will discuss further about more general density profiles at the end of this section.

Below, we will show analytic solutions for the redshift space ellipticity for some of the limiting cases.

5.4.1 Spherical Void

First, we consider a sphere with zero real space ellipticity, $\epsilon^r = 0$ and $\eta^r = 0$, with three eigenvalues of the inertia tensor of $I_1^r = I_2^r = I_3^r$. For a spherical top hat density field, we have

$$\tilde{\delta}(\mathbf{k}) = 4\pi R^3 \bar{\delta} \frac{j_1(kR)}{kR}. \tag{5.43}$$

Therefore, Eq.(5.38) becomes

$$\begin{aligned}\kappa(\mathbf{x}^r) &= \frac{4\pi R^3 f\bar{\delta}}{x_3^r}\int_0^\infty \frac{dk}{(2\pi)^3} ik\frac{j_1(kR)}{kR} \\ &\times \int_0^{2\pi} d\phi_k \int_{-1}^{1} d\mu_k \mu_k e^{i\mathbf{k}\cdot\mathbf{x}^r}. \end{aligned} \tag{5.44}$$

We first integrate the angular portion of the integration, $\int d\Omega_k \mu_k e^{i\mathbf{k}\cdot\mathbf{x}^r}$, by expanding the exponent into Legendre polynomials,

$$e^{i\mathbf{k}\cdot\mathbf{x}^r} = \sum_l^\infty (-i)^l (2l+1) j_l(-kx) P_l(\cos\gamma), \tag{5.45}$$

and using the Spherical harmonics addition theorem (a.k.a., Legendre addition theorem). We find

$$\int d\Omega_k \mu_k e^{i\mathbf{k}\cdot\mathbf{x}^r} = 4\pi i j_1(kx)\cos\theta_x. \tag{5.46}$$

Finally, we obtain κ for a spherical void as

$$\begin{aligned}\kappa(\mathbf{x}^r) &= \frac{4\pi R^3 f\bar{\delta}}{x_3^r}\int_0^\infty \frac{dk}{(2\pi)^3} ik\frac{j_1(kR)}{kR}[4\pi i j_1(kx)\cos\theta_x] \\ &= -\frac{2R^2 f\bar{\delta}\cos\theta_x}{\pi x_3^r}\int_0^\infty dk j_1(kR) j_1(kx) \\ &= -\frac{2R^2 f\bar{\delta}\cos\theta_x}{\pi x_3^r}\left(\frac{\pi x}{6R^2}\right) = -\frac{f\bar{\delta}}{3}. \end{aligned} \tag{5.47}$$

As we see from Eq.(5.47), κ is independent of positions in the void, and therefore the three eigenvalues of the redshift space inertia tensor for a redshift space void, $I_1^s \geq I_2^s \geq I_3^s$, are

$$I_1^s = I_1^r(1+\kappa)^2 \tag{5.48}$$

$$I_2^s = I_2^r \tag{5.49}$$

$$I_3^s = I_3^r, \tag{5.50}$$

and the ellipticity, ϵ and η are

$$\epsilon^s = \eta^s = 1 - \frac{1}{1+\kappa} = 1 - \frac{1}{1 - f\bar{\delta}/3}, \tag{5.51}$$

following Eq.(5.7). Now, the linear growth rate, $f \equiv \frac{d \ln D(a)}{d \ln a}$, for the ΛCDM model is approximately given as (Peebles, 1980; Hamilton, 2001),

$$f(z) = \Omega(z)^{4/7}, \tag{5.52}$$

where

$$\Omega(z) = \frac{\Omega_m (1+z)^3}{\Omega_m (1+z)^3 + \Omega_\Lambda}. \tag{5.53}$$

For $\Omega_m = 0.25$ and $\Omega_\Lambda = 0.75$, $f \simeq 0.5$ at $z = 0$, and thus, for a spherical void with an average density contrast of $\bar{\delta} = -0.9$, we have $\epsilon^s = \eta^s \simeq 0.13$. Since there is no special orientation for a spherical void, any void with sufficiently small real space ellipticity, $\epsilon^r \sim \eta^r \sim 0$, becomes a prolate ellipsoid (i.e., $\epsilon^s \sim \eta^s \neq 0$) in the redshift space with its ellipticity given by Eq.(5.51).

5.4.2 Spheroidal Void

When two of the three lengths of the semiaxis are equal, we have a spheroidal void. We set the direction of the longest and shortest semiaxis to be along the line of sight for prolate and oblate spheroids respectively. As in the spherical void, we assume a spheroidal top hat density contrast and solve Eq.(5.38) to have κ to the first order in ϵ^r,

$$\kappa(\mathbf{x}^r) \simeq -\frac{f\bar{\delta}}{3}(1 \mp 2\epsilon^r,) \tag{5.54}$$

where "$-$" and "$+$" signs are for prolate and oblate spheroids respectively. Here, we set the longest axis along the line of sight for prolate spheroids, and set the shortest axis along the line of sight for oblate spheroids. We compared the analytic prediction against numerical calculations, and found that

$$\kappa(\mathbf{x}^r) \simeq -\frac{f\bar{\delta}}{3}(1 \mp \epsilon^r,) \tag{5.55}$$

fits the result better. For each case, we have redshift space ellipticity as a function of real space ellipticity and κ as follows,

$$\epsilon^s = 1 - \frac{1-\epsilon^r}{1+\kappa}, \tag{5.56}$$

$$\epsilon^s = 1 - (1-\epsilon^r)(1+\kappa). \tag{5.57}$$

In contrast to the spherical void, whose redshift space ellipticity is always larger than that of real space, ellipticity of a spheroid either increases or decreases in the redshift space.

In figure 5.5, we show the result of numerical calculations for the spatial distribution of the value of $\kappa(\mathbf{x}^r)$ in the x-z plane for prolate spheroids with its longest axis along the line of sight (*top*), and oblate ellipsoids with its shortest axis along the line of sight (*bottom*) for different real space ellipticities, ϵ^r. In the figure, the center of the spheroids corresponds to the origin of the coordinate, and the x-z plane cuts the middle of the spheroid. We also plot the real space (solid lines) and redshift space (dotted lines) shapes of voids. Here, we use $f = 0.5$ and $\delta = -0.9$.

We see that the deformation of the void shape, $\kappa \propto u_3$, is the largest when the shortest semiaxis is along the line of sight due to the largest line-of-sight peculiar velocity. This result is in agreement with the earlier work of Icke (1984). When the longest semiaxis is along the line of sight (i.e., *top* figures), ellipticity only *increases* in the redshift space, while ellipticity only *decreases* when the shortest semiaxis is along the line of sight (i.e., *bottom* figures). For the spherical void, $\epsilon^r = 0$, we have $\epsilon^s = 0.13$ as expected from Eq.(5.51). For prolate and oblate spheroids with $\epsilon^r = 0.2$, 0.4 and 0.6, we have $\kappa = 0.12$, 0.09 and 0.06, and $\kappa = 0.18$, 0.21 and 0.26 from the numerical calculations respectively. This is in a good agreement with the fitting function of Eq.(5.55): for prolate and oblate spheroids with $\epsilon^r = 0.2$, 0.4 and 0.6, Eq.(5.55) yields $\kappa = 0.12$, 0.09 and 0.06, and $\kappa = 0.18$, 0.21 and 0.24, respectively.

Using Eqs.(5.57) and (5.57), for prolate and oblate spheroids with $\epsilon^r = 0.2$, 0.4 and 0.6, we have redshift space ellipticities of $\epsilon^s = 0.29$, 0.45 and 0.62, and $\epsilon^s = 0.06$, 0.27 and 0.50 respectively. In general, the fractional change in the ellipticity, $(\epsilon^s - \epsilon^r)/\epsilon^r$, becomes smaller for a larger ϵ^r.

Although we have constant κ here (i.e., independent of the position in the void), this is not true for arbitrarily oriented voids. In the case of tilted voids, $\kappa(\mathbf{x}^r)$ is a function of the real space coordinate, $\mathbf{x}^r$, and has both positive and negative values by definition, $\kappa(\mathbf{x}^r) \propto u_3/x_3$.

5.4.3 Redshift-Space Ellipticity Distribution Function

For a given ellipticity in real space, the corresponding redshift-space ellipticity can either increase or decrease, depending on the real space shape and orientation of the void with respect to the line of sight, except for a spherical void, whose ellipticity can only increase. Here, we calculate changes in ellipticities for a given set of real space ellipticities, ϵ^r and η^r,

$$\Delta\epsilon(\epsilon^r, \eta^r) \equiv \epsilon^s(\epsilon^r, \eta^r) - \epsilon^r \tag{5.58}$$

$$\Delta\eta(\epsilon^r, \eta^r) \equiv \eta^s(\epsilon^r, \eta^r) - \eta^r, \tag{5.59}$$

averaged over possible orientations. We numerically solve Eq.(5.38) for $\kappa(\mathbf{x}^r)$, with a top-hat density contrast, $\delta(\mathbf{x}^r)$, and calculate the redshift-space ellipticity, ϵ^s and η^s, from the redshift-space inertial tensor, I^s_{ij}. In figure 5.6, we show $\Delta\epsilon(\epsilon^r, \eta^r)$ (*left*) and $\Delta\eta(\epsilon^r, \eta^r)$ (*right*) for $\bar{\delta} = -0.9$ and $f = 0.5$. As expected, a spherical void in the real space becomes a prolate spheroid (i.e., $\epsilon = \eta \neq 0$) in the redshift space with its ellipticity given by Eq.(5.51). Also, we see a clear preference for positive $\Delta\epsilon$ for any triaxial void, especially at a small ϵ^r. As for $\Delta\eta$, spheroidal voids tend to be triaxial voids in the redshift space. From both $\Delta\epsilon$ and $\Delta\eta$, we find that an oblate void ($T < 0.5$) in real space tends to be a more prolate shape ($T > 0.5$) in the redshift space, and we have more prolate voids in redshift space ellipticity PDF.

In figure 5.7, we compare the ellipticity PDF of real space and redshift space for $R_L = 4h^{-1}$Mpc (*top*) and $R_L = 9h^{-1}$Mpc (*bottom*). Here, we use $b_L = 1$ and $\bar{\delta} = -0.9$, while varying the linear growth rate, f, from 0.5 to 1.5. We show the redshift space ellipticity PDF together with that of real space as a reference. Since the expansion rate of the void is set by the matter density distribution inside the void, in linear theory, it is proportional to the linear growth rate. As the effect of the redshift space distortion on the ellipticity

PDF is more prominent for a larger $f(z)$ and smaller ϵ^r, the redshift space ellipticity PDF becomes more skewed in shape with the mean ellipticity being higher than that of real space, $\bar{\epsilon}^s > \bar{\epsilon}^r$. Also note that the left tails of each redshift space ellipticity PDF approximately show the redshift space ellipticity, ϵ^s, of a spherical void, $\epsilon^r = 0$, and thus, we have

$$\epsilon^{\text{left}} \sim \epsilon^s(\epsilon^r = 0) = 1 - \frac{1}{1 - \frac{f\bar{\delta}}{3}}. \tag{5.60}$$

Therefore, in principle, with only the location of the left tail of PDF determined, we can put a constraint on $f\bar{\delta}$. This is a great benefit of using morphological information of structure, which is directly distorted in the redshift space. Although what we can actually measure is $f\bar{\delta} = \beta\bar{\delta}_v$, where $\beta \equiv f/b_L$, the entire shape of ellipticity PDF can lift the degeneracy between f and b_L. We can easily see this in the figure 5.4, where the increase in b_L decreases the mean ellipticity, $\bar{\epsilon^r}$, shifting the right tails of PDF toward lower ϵ^r, while the left tails are almost unaffected. Unlike a galaxy power spectrum, $P(k)$, which gives a constraint on the linear growth rate that is degenerate with the linear bias, $\beta \equiv f/b_L$, a void ellipticity PDF has a potential to constrain the linear growth rate separately from the other cosmological parameters. In other words, for a given galaxy survey, we have the situation in which we "*buy one, get one free*".

5.4.4 Void With General Radial Density Profile

So far, we have derived the redshift space ellipticity PDF for the top-hat density contrast, $\delta(\mathbf{x})$; however, the realistic radial profile of void density contrast does not necessarily follow the top-hat shape. The main parameter controlling the shape of the redshift space ellipticity PDF is $\kappa(\mathbf{x}^r)$ as in Eq.(5.38), and its value is given by $\kappa(\mathbf{x}^r) = A(\mathbf{x}^r) f \bar{\delta}$, where $A(\mathbf{x}^r)$ is solely determined by the density profile of a void (e.g., a void with a spherical top hat density profile has $A(\mathbf{x}^r) = -1/3$).

As an example, we parametrize the radial density profile of the void following the accumulated density profile of voids from the N-body simulation of Colberg et al. (2005), $\rho(< r)/\rho(r_{\rm eff}) \propto \exp[(r/r_{\rm eff})^\alpha]$, where the dentity profile at a given radius, $\rho(r)$, is given as follows

$$\rho(r) \propto \exp\left[\left(\frac{r}{r_{\rm eff}}\right)^\alpha\right]\left[1 + \frac{\alpha}{3}\left(\frac{r}{r_{\rm eff}}\right)^\alpha\right]. \tag{5.61}$$

Here, instead of using the original form of Colberg et al. (2005), we use an exponential density profile,

$$\delta(r) = \delta_0 \left(\frac{e^{[(r/r_{\rm eff})^\alpha - 1]} - 1}{e^{-1} - 1}\right), \tag{5.62}$$

where we forced $\rho(r_{\rm eff}) = \bar{\rho}$, at the effective radius, $r_{\rm eff}$, (i.e., $\delta(r_{\rm eff}) = 0$), and $\delta_0 \equiv \delta(r = 0)$. Figure 5.8 shows the profiles of the density contrast, $\delta(r)$, for top-hat (solid) and exponential profiles of Eq.(5.62) with $\alpha = 1$ (dotted), 2 (dashed) and 4 (dot-dashed). Note that for a top-hat density contrast, we have $\bar{\delta} = \delta_0$, while for the exponential profiles, we have

$$\bar{\delta} = \frac{\int_0^{r_{\rm eff}} r^2 \delta(r) dr}{\int_0^{r_{\rm eff}} r^2 dr}, \tag{5.63}$$

where $\delta(r)$ is given as Eq.(5.62). In figure 5.9, we show the redshift space ellipticity PDF for $f = 0.5$ (green), 1.0 (red) and 1.5 (orange) together with the real space ellipticity PDF (blue). Here, we use $R_L = 9h^{-1}$Mpc and the radial density profile of the density contrast is set to be either a top-hat (solid), $\delta(r < R_{\rm void}) = \bar{\delta}$, or an exponential (dotted) given by Eq.(5.62) with $r_{\rm eff} = R_{\rm void}$ and $\alpha = 2$. We use $\delta_0 = -0.40$ and -0.82 for the top-hat density profile and the exponential profile, respectively, in order to keep the same mean density contrasts, $\bar{\delta} = -0.4$, for different density profiles. Here, we clearly see degeneracy between the shape of the potential and the linear growth rate, f. Therefore, a better understanding of the density profile of a void is required when constraining the linear growth rate from the redshift space ellipticity PDF.

5.5 Effect of Void Finding and Poisson Noise on the Void Ellipticity PDF

In the previous sections, we have shown how to incorporate the galaxy bias and redshift space distortion into the calculation of the ellipticity PDF. In this section, we investigate the biases and errors that arise when using the inertia tensor, I_{ij}, as an estimate of the void ellipticity. Since a void is a sparse region in a galaxy distribution, the number of galaxies inside a void, $N_{\rm vg}$, is limited. Therefore the error in the ellipticity calculated from the inertia tensor of the void galaxy distribution is dominated by the Poisson statistics.

Let us define two stochastic variables, x and y, as follows,

$$x \equiv \mu_x + \Delta x, \tag{5.64}$$

$$y \equiv \mu_y + \Delta y, \tag{5.65}$$

where μ_x and μ_y are the means of x and y, respectively, and $\langle \Delta x \rangle = \langle \Delta y \rangle = 0$. We have variances and covariance defined as,

$$\begin{aligned}
\sigma_x^2 &\equiv \left\langle (x-\mu_x)^2 \right\rangle = \left\langle (\Delta x)^2 \right\rangle, &(5.66)\\
\sigma_y^2 &\equiv \left\langle (y-\mu_y)^2 \right\rangle = \left\langle (\Delta y)^2 \right\rangle, &(5.67)\\
\sigma_{xy} &\equiv \left\langle (x-\mu_x)(y-\mu_y) \right\rangle = \left\langle \Delta x \Delta y \right\rangle. &(5.68)
\end{aligned}$$

A mean of a rational is given by the following form,

$$\mu_{x/y} = \left\langle \frac{\mu_x + \Delta x}{\mu_y + \Delta y} \right\rangle. \tag{5.69}$$

Expanding Δy up to the second order, we have

$$\begin{aligned}
\mu_{x/y} &\simeq \frac{\mu_x}{\mu_y} \left\langle \left[1 + \frac{\Delta x}{\mu_x}\right] \left[1 - \frac{\Delta y}{\mu_y} + \left(\frac{\Delta y}{\mu_y}\right)^2\right] \right\rangle \\
&\simeq \frac{\mu_x}{\mu_y} \left(1 + \frac{\sigma_y^2}{\mu_y^2} - \frac{\sigma_{xy}}{\mu_x \mu_y}\right). &(5.70)
\end{aligned}$$

Similarly, variance of the rational is

$$\begin{aligned}
\sigma_{x/y}^2 &= \left\langle \left(\frac{\mu_x + \Delta x}{\mu_y + \Delta y}\right)^2 \right\rangle - \mu_{x/y}^2 \\
&\simeq \frac{\mu_x^2}{\mu_y^2} \left(\frac{\sigma_x^2}{\mu_x^2} + \frac{\sigma_y^2}{\mu_y^2} - \frac{2\sigma_{xy}}{\mu_x \mu_y}\right). &(5.71)
\end{aligned}$$

Now, ellipticity, ϵ, is defined as $\epsilon = 1 - \frac{p_3}{p_1} = 1 - \sqrt{\frac{I_3}{I_1}}$, where $p_1 \geq p_2 \geq p_3$ are the three principal axes of the ellipsoid, and $I_1 \geq I_2 \geq I_3$ are the eigenvalues of the inertia tensor I_{ij}. From $p_i^2 \propto I_i$, we have

$$\frac{\Delta p_i}{\mu_{p_i}} = \frac{1}{2} \frac{\Delta I_i}{\mu_{I_i}}, \tag{5.72}$$

and therefore, we have

$$\begin{aligned}
\mu_\epsilon &= 1-\mu_{p3/p_1} \simeq 1-\frac{\mu_{p_3}}{\mu_{p_1}}\left(1+\frac{\sigma_{p_1}^2}{\mu_{p_1}^2}-\frac{\sigma_{p_1p_3}}{\mu_{p_1}\mu_{p_3}}\right) \\
&= 1-\sqrt{\frac{\mu_{I_3}}{\mu_{I_1}}}\left(1+\frac{1}{4}\frac{\sigma_{I_1}^2}{\mu_{I_1}^2}-\frac{1}{4}\frac{\sigma_{I_1I_3}}{\mu_{I_1}\mu_{I_3}}\right), \qquad (5.73)
\end{aligned}$$

and

$$\begin{aligned}
\sigma_\epsilon^2 = \sigma_{p_3/p_1}^2 &\simeq \frac{\mu_{p_3}^2}{\mu_{p_1}^2}\left(\frac{\sigma_{p_1}^2}{\mu_{p_1}^2}+\frac{\sigma_{p_3}^2}{\mu_{p_3}^2}-\frac{2\sigma_{p_1p_3}}{\mu_{p_1}\mu_{p_3}}\right) \\
&= \frac{1}{4}\frac{\mu_{I_3}^2}{\mu_{I_1}^2}\left(\frac{\sigma_{I_1}^2}{\mu_{I_1}^2}+\frac{\sigma_{I_3}^2}{\mu_{I_3}^2}-\frac{2\sigma_{I_1I_3}}{\mu_{I_1}\mu_{I_3}}\right). \qquad (5.74)
\end{aligned}$$

From Eq.(5.6), we have

$$I_{ij} \equiv \frac{1}{N_{\rm vg}}\sum_{\alpha=1}^{N_{\rm vg}} x_{i,\alpha}x_{j,\alpha}, \qquad (5.75)$$

and in the continuous density field, we have

$$\begin{aligned}
I_{ij} &\equiv \int_{V_{void}} d^3x\ n(\mathbf{x})x_ix_j \\
&= \int_{V_{void}} d^3x\ \left[\bar{n}+\delta n(\mathbf{x})\right]x_ix_j = \mu_{I_{ij}}+\Delta I_{ij}, \qquad (5.76)
\end{aligned}$$

where

$$\mu_{I_{ij}} = \int_{V_{void}} d^3x\ \bar{n}x_ix_j, \qquad (5.77)$$

$$\Delta I_{ij} = \int_{V_{void}} d^3x\ \delta n(\mathbf{x})x_ix_j. \qquad (5.78)$$

Also, the variance of the inertia tensor is given as

$$\sigma_{I_{ij}}^2 = \left\langle (\Delta I_{ij})^2\right\rangle = \left\langle I_{ij}^2\right\rangle - \mu_{I_{ij}}^2. \qquad (5.79)$$

5.5.1 Void With a Well-defined Boundary: $\langle p_i \rangle \to P_i$

Let us calculate the bias in the mean and the variance of the ellipticity calculated from a rectangular void with a diagonalized inertia tensor of $I_1 \equiv I_{11}$, $I_2 \equiv I_{22}$ and $I_3 \equiv I_{33}$. The number of void galaxies is $N_{\rm vg}$. Here, we assume an idealized setup, where the boundary shape of a void is well defined (i.e., $\langle p_i \rangle \to P_i$) to see whether the estimator of an output ellipticity based on the inertia tensor yields unbiased result. For more realistic estimate on the bias in mean and the variance of output ellipticities, see § 5.5.2.

For a rectangular void with volume, $V_{void} = 8P_1P_2P_3$ (i.e., $x_i \in [-P_i, P_i]$ $\forall\ i$), where P_i is a well-defined length of the principal axis of the rectangular void, we have

$$\mu_{I_i} = \int_{V_{void}} d^3x\ \bar{n}x_i^2 = \frac{1}{3}\bar{n}V_{void}P_i^2 = \frac{1}{3}N_{\rm vg}P_i^2, \tag{5.80}$$

and

$$\begin{aligned}
\sigma_{I_i}^2 &= \int_{V_{void}}\int_{V'_{void}} d^3xd^3x'\ \langle n(\mathbf{x})n(\mathbf{x}')\rangle\, x_i^2x_i'^2 - \mu_{I_i}^2 \\
&= \int_{V_{void}}\int_{V'_{void}} d^3xd^3x'\ \bar{n}\delta_D(\mathbf{x}-\mathbf{x}')x_i^2x_i'^2 - \mu_{I_i}^2 \\
&= \bar{n}\int_{V_{void}} d^3x\ x_i^4 - \mu_{I_i}^2 = \frac{1}{5}\bar{n}V_{void}P_i^4 - \mu_{I_i}^2 \\
&= \frac{1}{5}N_{\rm vg}P_i^4 - \frac{1}{9}N_{\rm vg}^2P_i^4,
\end{aligned} \tag{5.81}$$

where we have assumed that the distribution of void galaxies follows the Poisson statistics with $\langle n(\mathbf{x})\rangle = \bar{n}$ and $\langle n(\mathbf{x})n(\mathbf{x}')\rangle = \bar{n}\delta_D(\mathbf{x}-\mathbf{x}')$. Similarly, we have

$$\begin{aligned}
\sigma_{I_iI_j} &= \bar{n}\int_{V_{void}} d^3x\ x_i^2x_j^2 - \mu_{I_i}\mu_{I_j} \\
&= \frac{1}{9}N_{\rm vg}P_i^2P_j^2 - \frac{1}{9}N_{\rm vg}^2P_i^2P_j^2, \qquad (5.82)
\end{aligned}$$

Therefore, Eqs(5.73) and (5.74) are re-written as follows,

$$\begin{aligned}
\mu_\epsilon &= 1 - \frac{P_3}{P_1} - \frac{P_3}{P_1}\frac{1}{5N_{\rm vg}}, \qquad (5.83) \\
\sigma_\epsilon^2 &= \frac{P_3^2}{P_1^2}\frac{2}{5N_{\rm vg}}. \qquad (5.84)
\end{aligned}$$

We see that for a given rectangular void with $N_{void} = 20$, we can accurately extract its ellipticity from void galaxies to $\sim 1\%$, but its standard deviation remains significant (i.e., $\sigma_\epsilon \sim 0.14$ for a void with zero ellipticity). As is expected, the variance of ellipticity, σ_ϵ^2, scales as inversely proportional to the number of void galaxies, $N_{\rm vg}$. Note that the above result is derived in the limit of $\langle p_i \rangle \rightarrow P_i$.

5.5.2 Void With an Undefined Boundary: $\langle p_i \rangle \neq P_i$

With a small number of field galaxies randomly distributed inside the well-defined boundary, P_i, we generally have $\langle p_i \rangle \neq P_i$. For example, let us imagine a spherical boundary, where $P_1 = P_2 = P_3$ and $\epsilon_{in} = 1 - \frac{P_3}{P_1} = 0$, with $N_{\rm vg} = 4$ field galaxies. This spherical boundary represents the shape of the underlying tidal field, and we sample this by 4 galaxies. No matter how we distribute those four galaxies, unless the four galaxies align at each of four apexes of an equilateral tetrahedron, calibrated ellipticity cannot be zero, $\epsilon_{out} \neq \epsilon_{in}$. As a result, we have a significant deviation of $\langle \epsilon_{out} \rangle$ from its boundary ellipticity, $\epsilon_{in} \equiv 1 - \frac{P_3}{P_1}$, and a correspondingly large standard deviation.

As we increase $N_{\rm vg}$, those randomly scattered particles fill in the bounded space more densely, and $\langle \epsilon_{out} \rangle$ gradually approaches the boundary ellipticity, ϵ_{in}. This uncertainty in ϵ_{out} due to small $N_{\rm vg}$ introduces an additional bias and scatter to the ones given by Eqs. (5.83) and (5.84).

For the case of elliptical voids, the analytic prediction of the mean and variance is non-trivial; thus, we have performed numerical experiments. First, we create an ellipsoidal boundary with a fixed size and ellipticity (i.e., P_1, P_2 and P_3), and then fill this bounded volume by $N_{\rm vg}$ random particles. For each realization, we calculate the inertia tensor and its eigenvalues (p_1, p_2 and p_3), where the output ellipticity is defined as

$$\epsilon_{out} \equiv 1 - \frac{p_3}{p_1}, \tag{5.85}$$

$$\eta_{out} \equiv 1 - \frac{p_2}{p_1}, \tag{5.86}$$

while the input ellipticity is defined as

$$\epsilon_{in} \equiv 1 - \frac{P_3}{P_1}, \tag{5.87}$$

$$\eta_{in} \equiv 1 - \frac{P_2}{P_1}. \tag{5.88}$$

Finally, we have a bias in the mean and variance of the output ellipticity, ϵ^{out}

as follows

$$\langle\epsilon_{out}\rangle - \epsilon_{in} = \frac{P_3}{P_1} - \left\langle\frac{p_3}{p_1}\right\rangle, \tag{5.89}$$

$$\sigma^2_{\epsilon_{out}} = \left\langle\epsilon^2_{out}\right\rangle - \left\langle\epsilon_{out}\right\rangle^2. \tag{5.90}$$

Figure 5.10 shows the result of 500 realizations for a given set of $\epsilon^{\rm in}$ and $N_{\rm vg}$. The top figures show the bias in the mean of the ellipticities ϵ (*left*) and η (*right*), and the bottom figures show the standard deviations of ϵ (*left*) and η (*right*). We see that both bias in the mean and variance of $\epsilon_{\rm out}$ are large enough to change the shape of ellipticity PDF significantly for $N_{\rm vg} \lesssim 100$. In order to correct the ellipticity PDF, we define a response function, $R(\epsilon_{\rm out}|\epsilon_{\rm in}, N_{\rm vg})$, such that

$$\begin{aligned} & p(\epsilon_{\rm out}|\sigma_{R_L}, \delta, N_{\rm vg}) \\ & = \int d\epsilon_{\rm in} R(\epsilon_{\rm out}|\epsilon_{\rm in}, N_{\rm vg}) p(\epsilon_{\rm in}|\sigma_{R_L}, \delta). \end{aligned} \tag{5.91}$$

In figure 5.11, we show the normalized histograms for the number of voids with output ellipticity, $\epsilon_{\rm out}$, from the numerical simulation with a given $N_{\rm vg}$ and $\epsilon_{\rm in}$. We also show Gaussian distributions (red lines) with the mean $\langle\epsilon_{\rm out}\rangle$ and variance $\sigma^2_{\epsilon_{\rm out}}$,

$$R(\epsilon_{\rm out}|\epsilon_{\rm in}, N_{\rm vg}) = \frac{1}{\sqrt{2\pi\sigma^2_{\epsilon_{\rm out}}}} \exp\left[-\frac{(\epsilon_{\rm out} - \langle\epsilon_{\rm out}\rangle)^2}{2\sigma^2_{\epsilon_{\rm out}}}\right], \tag{5.92}$$

where both mean and variance are functions of the input ellipticity and the number of void galaxies (i.e., $\langle\epsilon_{\rm out}\rangle = \langle\epsilon_{\rm out}(\epsilon_{\rm in}, N_{\rm vg})\rangle$ and $\sigma_{\epsilon_{\rm out}} = \sigma_{\epsilon_{\rm out}}(\epsilon_{\rm in}, N_{\rm vg})$).

In figure 5.12, we show the ellipticity PDF without the correction for the response function (black lines) as well as the corrected ellipticity PDF (red lines) for four different redshifts, $z = 0$ (solid), 1 (dotted), 2 (dashed) and 3 (dot-dashed) with different values of $N_{\rm vg}$. Here, we use $R_L = 4\text{Mpc}^{-1}$ and $\delta_m = -0.9$ to calculate the original PDFs at four different redshifts. We see that the shapes of PDF with higher redshifts are more susceptible to the small $N_{\rm vg}$ effect. For a typical void studied in PL07 using the Millennium Run catalog at $z = 0$, $\bar{N}_{\rm vg}$ is roughly between 20 to 60, R_L ranges from 4 to $6.4h^{-1}$Mpc, and $\delta_v \sim -0.9$. We clearly see that voids with small initial ellipticity $\epsilon_{\rm in}$ are most vulnerable to the Poisson noise, and with $N_{\rm vg} \sim 10$, the original shape of ellipticity PDF is almost washed out to leave only the distribution of the Poisson noise. On the other hand, the ellipticity PDF at low redshift ($z = 0$) maintains its original shape with the number of void galaxies as small as $N_{\rm vg} \lesssim 45$. In short, a shape with small ellipticity is hard to trace with a small number of tracers. For example, if we have a sphere of radius $R = 10h^{-1}$Mpc in the simulation box with a resolution of $1h^{-1}$Mpc, the possible number of configurations of randomly scattered tracing particles with $N_{\rm vg} = 4$ will be ${}_{4187}C_4 \sim 1.3 \times 10^{13}$, while the possible number of configurations of an equilateral tetrahedron (i.e., $\epsilon = 0$) is vanishingly small. Also, the scatter of the output ellipticity σ_ϵ will not center around $\epsilon_{\rm in}$ for a small ellipticity as $0 \leq \epsilon \leq 1$, and as a result, $\langle \epsilon_{\rm out} \rangle$ converges to $\epsilon_{\rm in}$ only slowly as we increase $N_{\rm vg}$. On the other hand, the ellipticity of a highly elongated shape can be well traced even with a limited number of tracers.

	p_0	p_1	p_2	p_3
α_1	1.282	2.384	-7.280	3.587
α_2	0.2636	-0.3103	0.9557	-0.9404
β_1	0.4500	1.708	-0.8460	-0.02668
β_2	0.3650	-0.6260	1.680	-0.9296

Table 5.1: We show the best-fit coefficients, p_0, p_1, p_2 and p_3 for α_1, α_2, β_1, and β_2 of Eq.(5.93) and (5.94), where α_1, α_2, β_1, and β_2 are given as polynomials to the third order, $p_0 + p_1\epsilon_{\rm in} + p_2\epsilon_{\rm in}^2 + p_3\epsilon_{\rm in}^3$.

For $N_{\rm vg} \lesssim 100$, we use a fitting function derived from figure 5.10,

$$\langle\epsilon_{out}\rangle - \epsilon_{in} = \alpha_1(\epsilon_{in})N_{\rm vg}^{-\beta_1(\epsilon_{in})} \tag{5.93}$$

$$\sigma_{\epsilon_{\rm out}} = \alpha_2(\epsilon_{in})N_{\rm vg}^{-\beta_2(\epsilon_{in})}, \tag{5.94}$$

where α_1, α_2, β_1, and β_2 are given as polynomials to the third order, $p_0 + p_1\epsilon_{\rm in} + p_2\epsilon_{\rm in}^2 + p_3\epsilon_{\rm in}^3$, and we show the best-fit coefficients, p_0, p_1, p_2 and p_3 in table 5.1.

5.6 Voids from N-body Simulation

To test the analytic predictions made in the previous sections, we use a catalog of galaxies from the Millennium simulation (Croton et al., 2006; De Lucia & Blaizot, 2007). In a comoving box of $L_{\rm box} = 500\ h^{-1}$Mpc, there are 26690265, 26359329, and 23885840 galaxies in the simulation at $z = 0$, 1, and 2, respectively. For each redshift, we select a subset of galaxies whose halo masses are above $M_h = 2.6 \times 10^{12}$, 2.6×10^{12}, and $8.6 \times 10^{11} h^{-1} M_\odot$. We find 182081, 121454, and 261471 such halos for $z = 0$, 1, and 2, respectively.

Here, we use the void finding algorithm of FN09 to identify voids from the subsets of galaxies. Their algorithm first divides a given set of galaxies into wall galaxies, which define boundaries of holes, and void galaxies, which are allowed to be within holes by calculating the distances to the third nearest galaxies, D_3. When a galaxy has the third nearest distance, D_3, smaller than the user-defined threshold distance, $R_3 > D_3$, the galaxy is labeled as a wall galaxy, and when $R_3 < D_3$, the galaxy is labeled as a void galaxy. Here, $R_3 \equiv \langle D_3 \rangle + \lambda\sigma_{D_3}$, where $\langle D_3 \rangle$ and σ_{D_3} are the mean third distance and its standard deviation, respectively, and λ is a user-defined parameter. We use the value of $\lambda = 2$ recommended by FN09. Then, a hole is defined as a sphere with maximal radius in a galaxy distribution containing no wall galaxy, and by definition, a hole can contain void galaxies. Finally, a void is identified by the subsequent merger of neighboring holes with user-defined criteria (i.e., a percentage of volume overwrap with the neighboring holes and a minimum size of hole, ξ), where, we use $\xi = 1.5R_3$. As a result, voids identified by the algorithm of FN09 have aspherical shape with a finite number of void galaxies within. For each identified void, FN09 found a volume, a size and an ellipticity of the best-fit ellipsoid by calculating the inertia tensor from randomly scattered particles within the boundary of the void.

Using a void-finder of FN09, we identify 569, 327, and 804 voids for $z = 0$, 1, and 2, respectively. Here, as we noted earlier, since we are interested in a shape of a tidal field near the density minima, we have modified the void finding algorithm of FN09 so that an ellipticity of a void can be evaluated from the distributions of galaxies inside a void (i.e., we directly calculate an inertia tensor from void galaxies, not from randomly scattered particles as in FN09).

With this modification, the extracted ellipticity PDF has a closer contact with the analytic ellipticity PDF derived from the tidal field of the local minima of the density field.

We measure the linear galaxy biases by comparing the galaxy power spectra of input galaxy distributions against linear matter power spectra from CAMB at each redshift. In figure 5.13, we show the linear matter power spectra, $P_m(k)$, from CAMB with the cosmological parameters same as the Millennium simulation (i.e., $\Omega_m = 0.25$, $\Omega_\Lambda = 0.75$, $n_s = 1$ and $\sigma_8 = 0.9$) (solid), linear galaxy spectra, $P_g(k) = b_L^2 P_m(k)$, (dotted) and power spectra of the subset of galaxies from the Millennium simulation (crosses with error bars) at $z = 0$ (top), 1 (middle) and 2 (bottom). With fittings up to $k_{max} = 0.03h$ Mpc^{-1} (i.e., using the first two data points of $P_g(k)$), we find $b_L = 1.0$, 1.6, and 2.0 for $z = 0$, 1, and 2, respectively. Here, non-linearity of the power spectrum is rather small at this scale, $k < 0.03h$ Mpc^{-1}.

In figure 5.14, we show the ellipticity PDF extracted from the Millennium simulation at $z = 0$ (top), 1 (middle) and 2 (bottom) together with the analytic ellipticity PDF corrected for the linear galaxy biases and response functions (red lines). As references, we also show the analytic ellipticity PDF (black lines) with (dotted black lines) and without the linear galaxy bias (solid black lines). We also show the 1-σ range of the histograms calculated with bootstrapping method (grey).

Here, for each redshift, we demand voids have at least 10 void galaxies. Table 5.2 shows redshifts, z, the numbers of voids used to draw histograms, $N_{\rm v}$, the minimum numbers of void galaxies per void, $N_{\rm vg,min}$, the median numbers of void galaxies per void, $N_{\rm vg,med}$, the linear galaxy biases, b_L, the mean density contrasts of void, $\bar{\delta}_{\rm v}$, the mean Eulerian radii of voids, $\bar{R}_E \equiv (\overline{p_1 p_2 p_3})^{1/3}$, the mean ellipticities of extracted voids, $\bar{\epsilon}^{\rm obs}$, and those of the analytic PDF, $\bar{\epsilon}^{\rm theory}$, and the errors in the mean, $\Delta\epsilon^{\rm obs}$.

We find from the figure 5.14 that the analytic ellipticity PDFs convolved with the response function (red lines) show a good agreement with the extracted ellipticity PDFs from the simulations, with the chi square values of $\chi^2 = 23.0$, 16.9 and 20.1 with the degrees of freedom of 15, 16 and 13 for redshifts of $z = 0$, 1.078 and 2.070, respectively. We test the null hypothesis that the extracted ellipticity PDF is drawn from the analytic ellipticity PDF convolved with the response function, calculating the probability-to-exceed (PTE) the measured χ^2,

$$\alpha = \int_{\chi^2}^{\infty} P_n(x)dx, \tag{5.95}$$

where $P_n(x)$ is a PDF of χ^2-distribution with a n-degree of freedom,

$$P_n(x) = \frac{x^{n/2-1}e^{-x^2/2}}{2^{n/2}\Gamma(n/2)}. \tag{5.96}$$

We find that our analytic model is consistent with the void ellipticity PDF extracted from the Millennium simulation with PTE = 0.12, 0.39 and 0.094 for redshifts of $z = 0$, 1.078 and 2.070, respectively.

z	$N_{\rm v}$	$N_{\rm vg,min}$	$N_{\rm vg,med}$	b_L	δ_v	$\bar{R}_E$	$\bar{\epsilon}^{\rm obs}$	$\bar{\epsilon}^{\rm theory}$	$\Delta\epsilon^{\rm obs}$
0	157	15	19	1.0	-0.66	21.8	0.343	0.360	0.008
1.078	110	10	15	1.6	-0.59	21.9	0.377	0.356	0.012
2.070	163	20	24	2.0	-0.60	19.9	0.302	0.291	0.008

Table 5.2: We show the statistics of voids used to make the histogram in the figure 5.14. From left to right, we have redshifts, z, numbers of voids used to draw histograms, $N_{\rm v}$, minimum numbers of void galaxies per void, $N_{\rm vg,min}$, median numbers of void galaxies per void, $N_{\rm vg,med}$, linear galaxy biases, b_L, mean density contrasts of void, $\bar{\delta}_{\rm v}$, mean Eulerian radii of voids, $\bar{R}_E \equiv (\overline{p_1 p_2 p_3})^{1/3}$ (h^{-1}Mpc), mean ellipticities of extracted voids, $\bar{\epsilon}^{\rm obs}$, and those of analytic PDF, $\bar{\epsilon}^{\rm theory}$, and errors in the mean, $\Delta\epsilon^{\rm obs}$.

Although we have good fits for all redshifts, the extracted ellipticity PDFs are entirely dominated by the Poisson noise due to the small number of void galaxies, $N_{\rm vg} \ll 100$. To see this, we have performed a null test with a top-hat PDF with the mean and the width equal to the analytic ellipticity PDF. After convolving the top-hat PDF with the response functions, we find an equally good fit with a similar χ^2. We repeat the null tests for different values of the mean and the width of the analytic ellipticity PDF. We find that the extracted ellipticity PDF is well fitted with an arbitrary shape of PDF, whose mean ellipticity is the same as the one predicted from the analytic ellipticity PDF, convolved with the response function.

5.6.1 Comments on the Void-Finder Dependence

In this work, we have assumed that voids are the local minima of density field with three dimensionally expanding volume. In the Lagrangian picture, this is equivalent to having all the eigenvalues of the tidal tensor,

$T_{ij} \equiv \partial_i \partial_j \Psi(\mathbf{q})$, being negative (i.e., $\lambda_3 \geq \lambda_2 \geq \lambda_1 < 0$, and $\sum_{i=1}^{3} \lambda_i = \delta_m$).

However, as Lavaux & Wandelt (2010) pointed out, in a saddle-like density distribution, voids can contract along one of the axis, while it expands along the rest of the axes. Lavaux & Wandelt (2010) studied these spurious voids in the Lagrangian picture together with their own void-finding algorithm (DIVA). They found that among those spurious voids, pancake voids (i.e., two dimensionally expanding, one dimensionally contracting voids) are as abundant as three dimensionally expanding genuine voids, and the shape of the ellipticity distribution function of PL07 needs to be modified. Nevertheless, we focused our work on the three dimensionally expanding voids, as the result of PL07 suggests that the void finding algorithm of Hoyle & Vogeley (2002) mostly finds three dimensionally expanding genuine voids. There seems to be an algorithm dependent selection of the type of voids.

FN09 reported a slight preference for prolate ellipsoids in the ellipticity PDF drawn from voids detected in the SDSS DR5, while the analytic ellipticity PDF of PL07 shows a clear preference for oblate ellipsoids. FN09 used the best-fit ellipsoid of Jang-Condell & Hernquist (2001) to estimate the ellipticity of a void with a Monte-Carlo simulation. For each realization, they calculated an inertia tensor for each void from test particles randomly spread inside the void. In this way, their measurements of ellipticity tend to be more sensitive to the shape of the void boundary (i.e., $I_{ij} \propto p_i p_j$). On the other hand, PL07 uses field galaxies *inside* the void to calculate the inertia tensor. An ellipticity calculated from void galaxies is more sensitive to the shape of the tidal field around a density minimum, and therefore, has a closer contact with the analytic ellipticity PDF of PL07. Indeed, the mean effective volume of voids, $V_{\rm eff} = \frac{4\pi}{3}p_1 p_2 p_3$, extracted from the Millennium simulation with the method of PL07 is $\sim$ 4 times smaller than that of FN09 (i.e., most void galaxies are within $\sim 60\%$ of radius from the void center).

5.7 Discussion and Conclusion

We have derived the ellipticity PDF of voids in the redshift space. We have found that the redshift space distortion on the shape of voids statistically increases the ellipticities of voids, and leaves a prominent feature on the ellipticity PDF as a substantial reduction in the probability of having voids with small ellipticity, $\epsilon < -\frac{f\bar{\delta}}{3}$. This characteristic cutoff in the ellipticity PDF can be used as a probe of the growth rate, $f(a) \equiv \frac{d\ln D_+(a)}{d\ln a}$, once the radial density profile of voids is better understood. Acquaviva & Gawiser (2010) proposed a model independent test of GR by checking the scale dependence/independence of the growth rate, $f(k, z)$ from a galaxy power spectrum at small scale, $P_g(k_S, z)$, and large scale $P_g(k_L, z)$. In principle, we can use the redshift space ellipticity PDF of a void to measure the growth rate at different scales by binning the observed voids into small and large sizes.

However, as we have shown in § 5.5, the biggest limiting factor for the use of ellipticity PDF as a probe of cosmology lies in the Poisson noise from a small number of $N_{\rm vg}$ inside a given void. We have found that from a sample of galaxies with a minimum halo mass of $2.6 \times 10^{12} h^{-1} M_\odot$ for $z = 0$ and 1, and $8.6 \times 10^{11} h^{-1} M_{\odot}$ for 2, we have $N_{\rm vg} \sim 20$ void galaxies per each identified void. This small number of void galaxies per each void creates a significant contamination of the resulting ellipticity PDF so that the shape of the original PDF is almost washed-out.

As we have seen, the biggest limiting factor for the use of ellipticity PDF as a probe of cosmology lies in the Poisson noise from a small number of $N_{\rm vg}$ inside a given void. We have found that from a sample of galaxies with a minimum halo mass of $2.6 \times 10^{12} h^{-1} M_{\odot}$ for $z = 0$ and 1, and $8.6 \times 10^{11} h^{-1} M_{\odot}$ for 2, we have $N_{\rm vg} \sim 20$ void galaxies per each identified void. This small number of void galaxies per each void creates a significant contamination of the resulting ellipticity PDF so that the shape of the original PDF is almost washed-out.

Nevertheless, there is a way to overcome the Poisson noise. Recently, Lavaux & Wandelt (2011) proposed the stacking analysis of the void ellipticity in the redshift space as a way to put a constraint on the cosmological parameters via the Alcock Paczynski (AP) test (Alcock & Paczynski, 1979). The AP test uses the deviation from the isotropy and homogeneity of the observed structure, which is known to be spherical (e.g., galaxy distributions at large scale), to determine $D_A H$. For example, when one calibrates comoving distances perpendicular, $r_{\perp}$, and parallel to the line of sight, $r_{\parallel}$, from the angular,

θ, and redshift, z, distribution of galaxies with

$$\theta = \frac{r_\perp(z)}{(1+z)D_A(z)}, \tag{5.97}$$

$$\delta z = \frac{r_\parallel(z)H(z)}{c}, \tag{5.98}$$

one need to assume a reference cosmological model to calculate $D_A^{\rm ref}(z)$ and $H^{\rm ref}(z)$. If the observed structure has $r_\perp = r_\parallel$, and we have observed values of the angular, θ, and the redshift, z, distributions of galaxies, a combination of D_A and H can be constrained as follows,

$$D_A(z)H(z) = \frac{c\delta z}{(1+z)\theta} \tag{5.99}$$

(see, e.g., Shoji et al. (2009) for the use of AP test on the two-dimentional power spectrum, $P(k,\mu)$).

In real space, the stacked void should have zero ellipticity, while the deviation from zero ellipticity in real space indicates the deviation of the assumed cosmology from the true cosmology. In redshift space, since the void is elongated toward the line of sight, the stacked void has non-zero ellipticity, which can be a tell-tale of the logarithmic growth rate, $f(a) = \frac{d\ln D_+(a)}{d\ln a}$. Although some useful information of void ellipticity will be lost by stacking, in this way, we can see the effect of redshift space distortion as a source of anisotropy in the stacked void ellipticity. We think that the stacking analysis of the voids in redshift space is potentially a powerful tool to probe the cosmology.

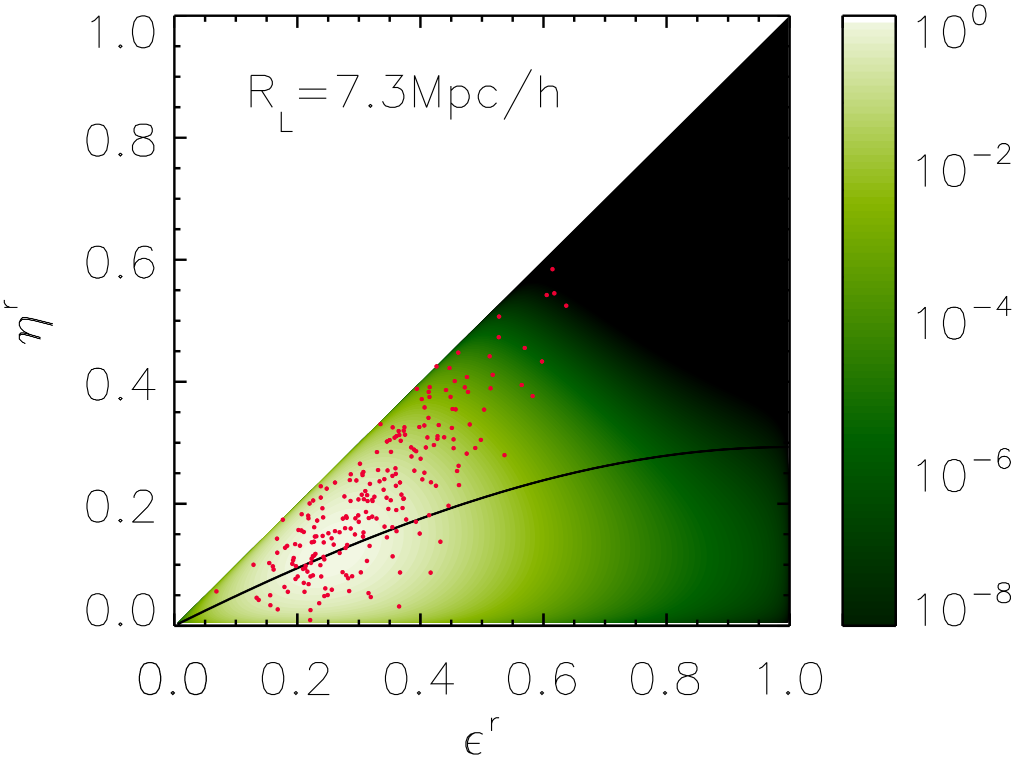

Figure 5.3: We show the 232 identified voids from the SDSS DR5 based on the catalog of Foster & Nelson (2009), and the corresponding ellipticity PDF. From the catalog, we find $\bar{\epsilon} = 0.33$, $\bar{\eta} = 0.21$, $\bar{T} = 0.68$, $\bar{\delta}_v = -0.97$, $\bar{z} = 0.11$ and $R_L = 7.3h^{-1}$Mpc. PDF is normalized so that the peak values are 1, and the solid line shows $T = 0.5$. Note that the PDF is drawn only as a reference, and we do not correct for bias and redshift space distortion.

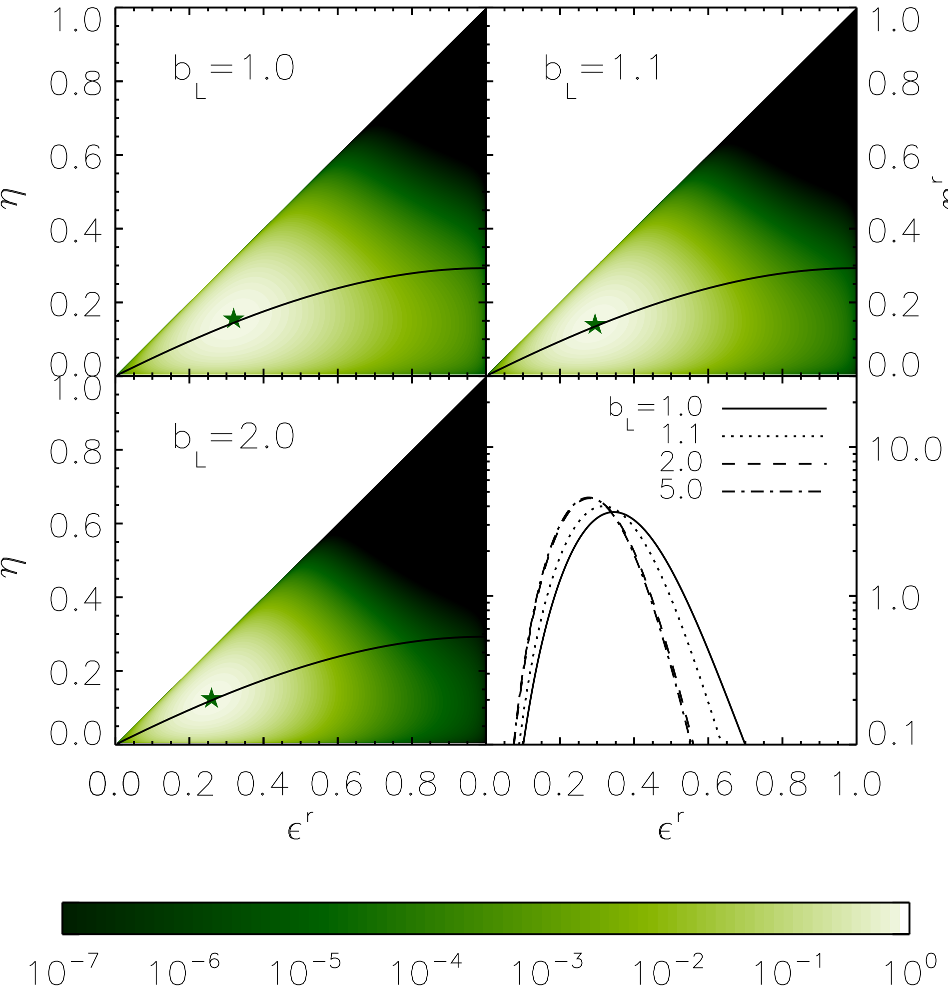

Figure 5.4: In this figure, we show the effect of linear galaxy bias on the real space void ellipticity PDF both in 1-D (*bottom right*) and 2-D (*top left to bottom left*). The 2-D PDFs are normalized so that the peak values are 1. In the 1-D plot, we have PDF for four different biases, $b_L = 1.0$ (solid), 1.1(dotted), 2.0 (dashed) and 5.0 (dot-dashed). In the 2-D plots, the solid lines show $T = 0.5$, and the stars show the peaks of each PDF. Here, we have used $R_L = 5h^{-1}$Mpc, $\delta_v = -0.9$ and $z = 0$.

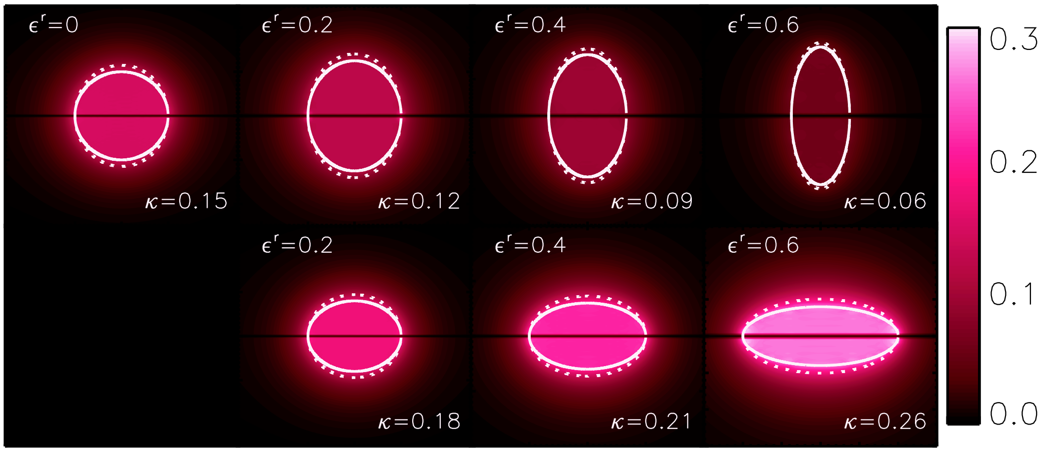

Figure 5.5: We show the spatial distribution of the value of $\kappa(\mathbf{x}^r)$ in x-z plane for prolate spheroids with its longest axis along the line of sight (*top*), and oblate ellipsoids with its shortest axis along the line of sight (*bottom*) for different real space ellipticities, ϵ^r. We also plot real space (solid lines) and redshift space (dotted lines) shapes of voids. Here, we use $f = 0.5$ and $\delta = -0.9$.

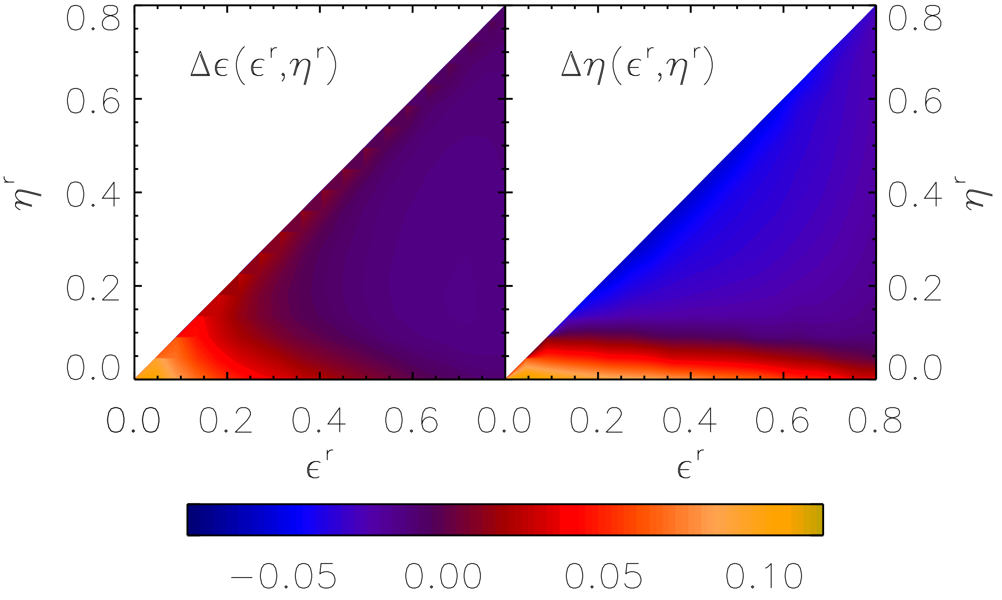

Figure 5.6: We show the effect of redshift space distortion on real space void ellipticities, ϵ^r and η^r. For a given set of ellipticities in real space, we plot the change in ellipticities, $\Delta\epsilon(\epsilon^r,\eta^r) \equiv \epsilon^s(\epsilon^r,\eta^r) - \epsilon^r$ (*left*) and $\Delta\eta(\epsilon^r,\eta^r) \equiv \eta^s(\epsilon^r,\eta^r) - \eta^r$ (*right*). Here, we have assumed a top-hat density profile with $\bar{\delta} = -0.9$ and $f = 0.5$.

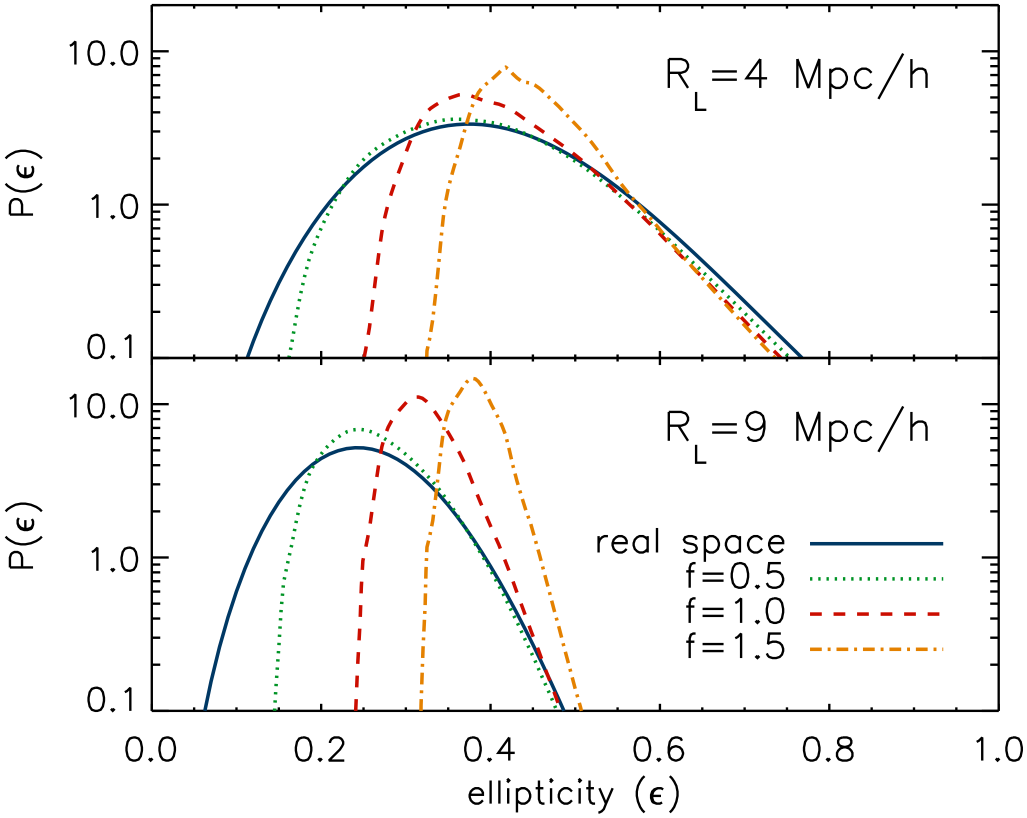

Figure 5.7: We compare the ellipticity PDF of real space and redshift space for $R_L = 4h^{-1}$Mpc (*top*) and $R_L = 9h^{-1}$Mpc (*bottom*). Here, we use $b_L = 1$ and $\bar{\delta} = -0.9$, while varying the linear growth rate: $f = 0.5$ (dotted), 1.0 (dashed) and 1.5 (dot-dashed). We also show the real space ellipticity PDF (solid) as a reference.

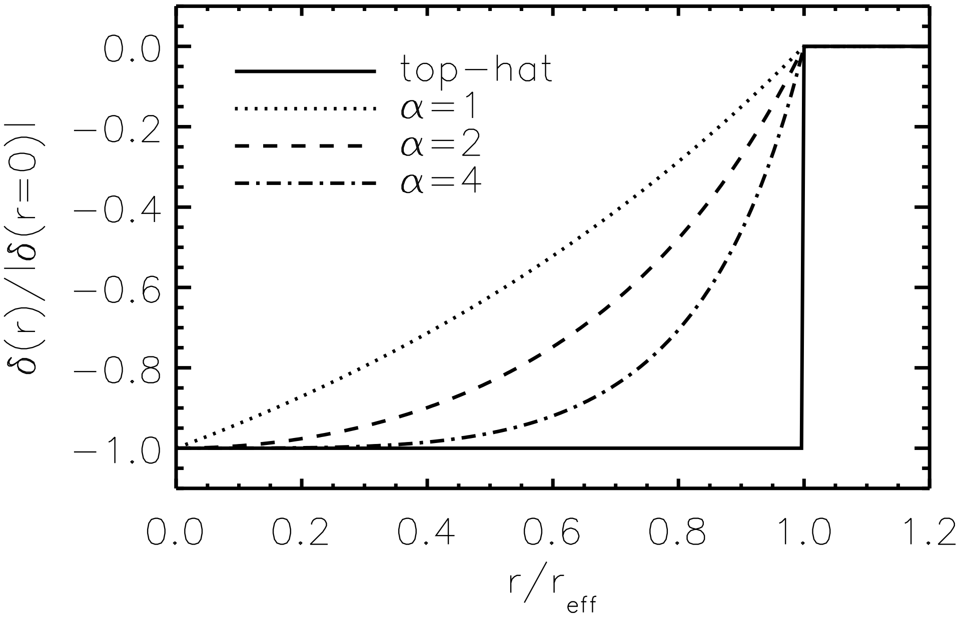

Figure 5.8: We show profiles of the density contrast, $\delta(r)$, for top-hat (solid) and exponential profiles of Eq.(5.62) with $\alpha = 1$ (dotted), 2 (dashed) and 4 (dot-dashed). Here, we assumed that the density at the effective radius, $r_{\rm eff}$, becomes that of the cosmic mean, $\rho(r_{\rm eff}) = \bar{\rho}$, or, $\delta(r_{\rm eff}) = 0$.

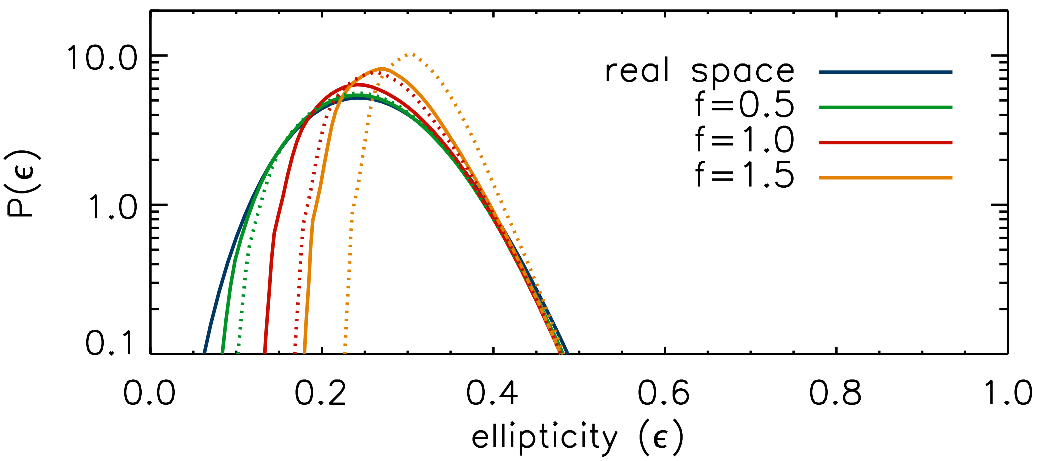

Figure 5.9: We show the redshift space ellipticity PDF for $f = 0.5$ (green), 1.0 (red) and 1.5 (orange) together with real space ellipticity PDF (blue). Here, we use $R_L = 9h^{-1}$Mpc. The radial density profile of density contrast is set to be either a top-hat (solid), $\delta(r < R_{\rm void}) = \bar{\delta}$, or an exponential (dotted) as in Eq.(5.62), with $r_{\rm eff} = R_{\rm void}$ and $\alpha = 2$. We use $\delta_0 = -0.40$ and -0.82 for the top-hat and the exponential density profile, respectively, in order to keep the same mean density contrasts, $\bar{\delta} = -0.4$, for different density profiles. Here, we see degeneracy between the shape of the potential and the linear growth rate, f.

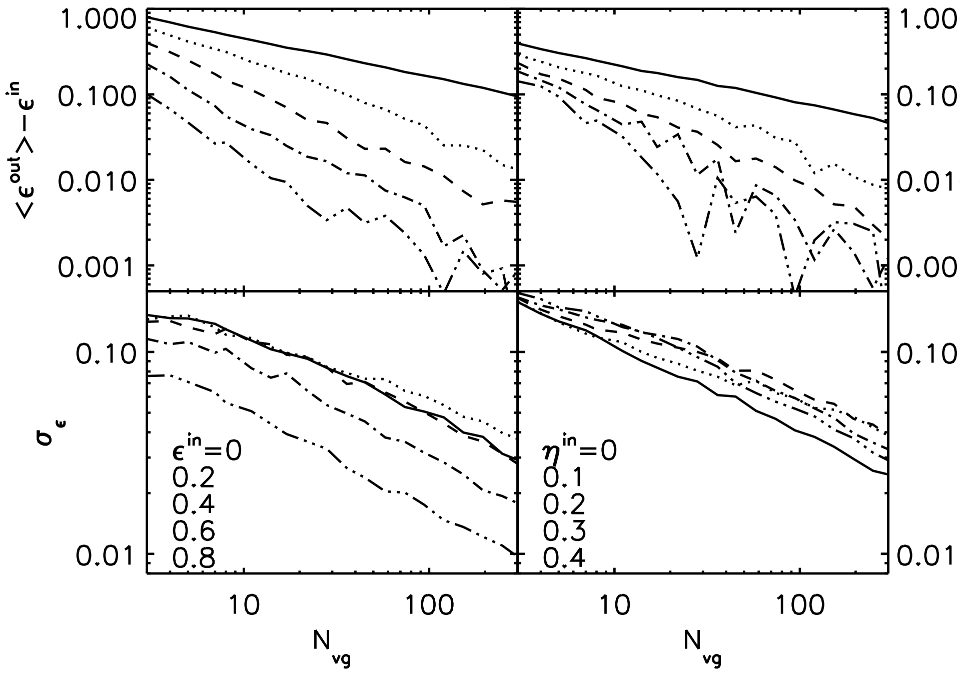

Figure 5.10: Bias and variance in the measured ellipticities. We place $N_{\rm vg}$ particles within a boundary of a given set of size and input ellipticities, $\epsilon^{\rm in}$ and $\eta^{\rm in}$, and calculate the mean ellipticities, $\langle\epsilon^{\rm out}\rangle$ and $\langle\eta^{\rm out}\rangle$, and their standard deviations σ_ϵ and σ_η, from 500 realizations for each $N_{\rm vg}$ and input ellipticity. Top figures show the biases in finding the input ellipticities (i.e., true underlying ellipticities of a tidal field), $\langle\epsilon^{\rm out}\rangle-\epsilon^{\rm in}$ and $\langle\eta^{\rm out}\rangle-\eta^{\rm in}$, and bottom figures show the standard deviations, σ_ϵ and σ_η.

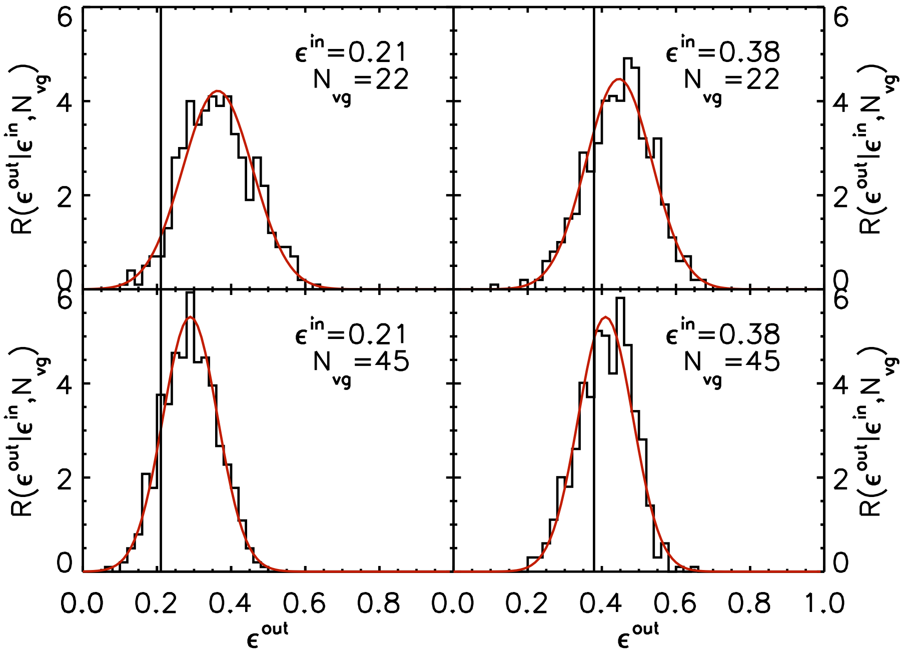

Figure 5.11: We show the normalized histograms of output ellipticities, $\epsilon_{\rm out}$ for a fixed input ellipticity, $\epsilon_{\rm in}$, and a number of void galaxies, $N_{\rm vg}$. We find that the Gaussian profile of Eq.(5.92) with mean, $\langle\epsilon_{\rm out}\rangle$, and variance, $\sigma_{\epsilon_{\rm out}}$, fits the measured histograms (red lines) well. Also, we show the locations of the input ellipticity, $\epsilon_{\rm in}$, with vertical lines.

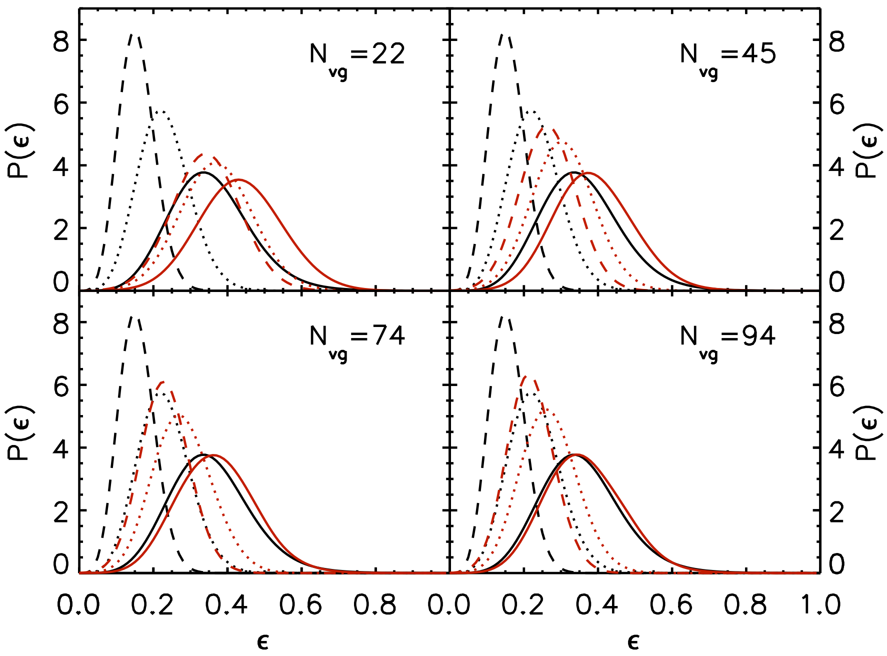

Figure 5.12: We show the real space ellipticity PDFs without Poisson noise (black lines) at $z = 0$ (solid), 1 (dotted) and 2 (dashed). We then convolve each noise-free PDF with the response function given by Eq.(5.92), and show the resulting PDFs for four different $N_{\rm vg}$ (red lines).

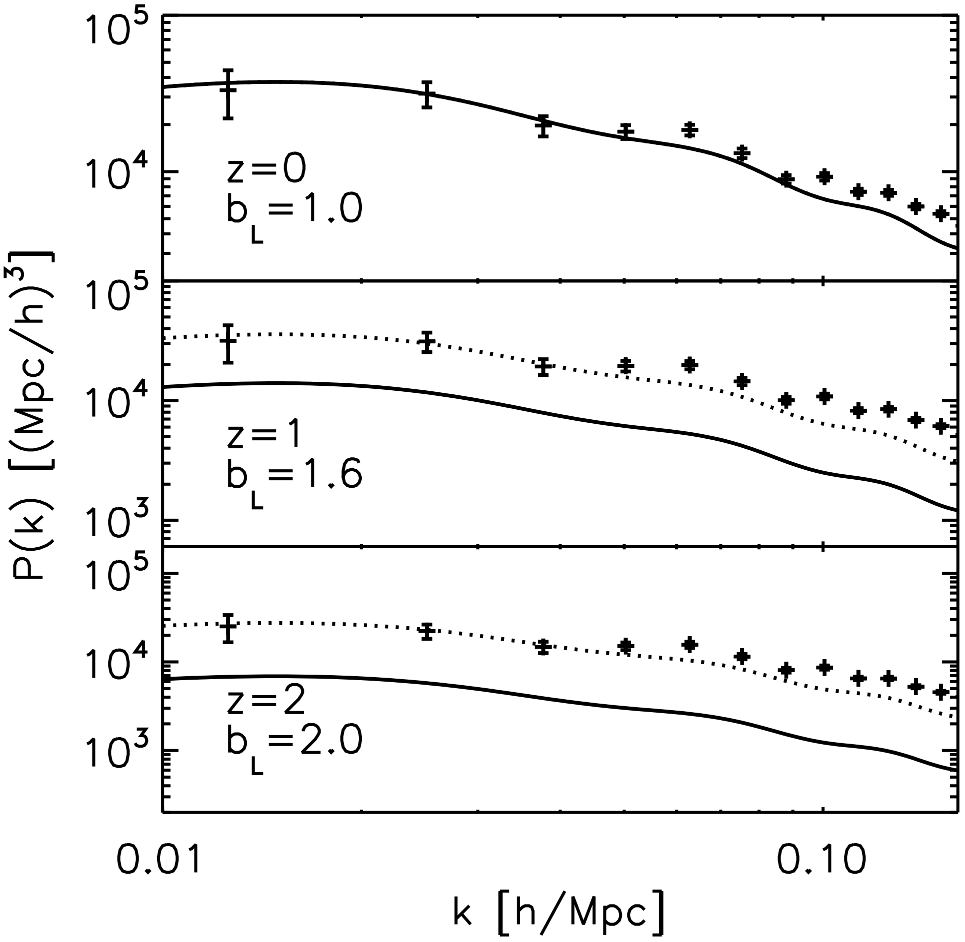

Figure 5.13: We show the linear matter power spectra, $P_m(k)$, from CAMB with the cosmological parameters same as the Millennium simulation (i.e., $\Omega_m = 0.25$, $\Omega_\Lambda = 0.75$, $n_s = 1$ and $\sigma_8 = 0.9$) (solid), linear galaxy spectra, $P_g(k) = b_L^2 P_m(k)$, (dotted) and power spectra of the subset of galaxies from the Millennium simulation (crosses with error bars) at $z = 0$ (top), 1 (middle) and 2 (bottom).

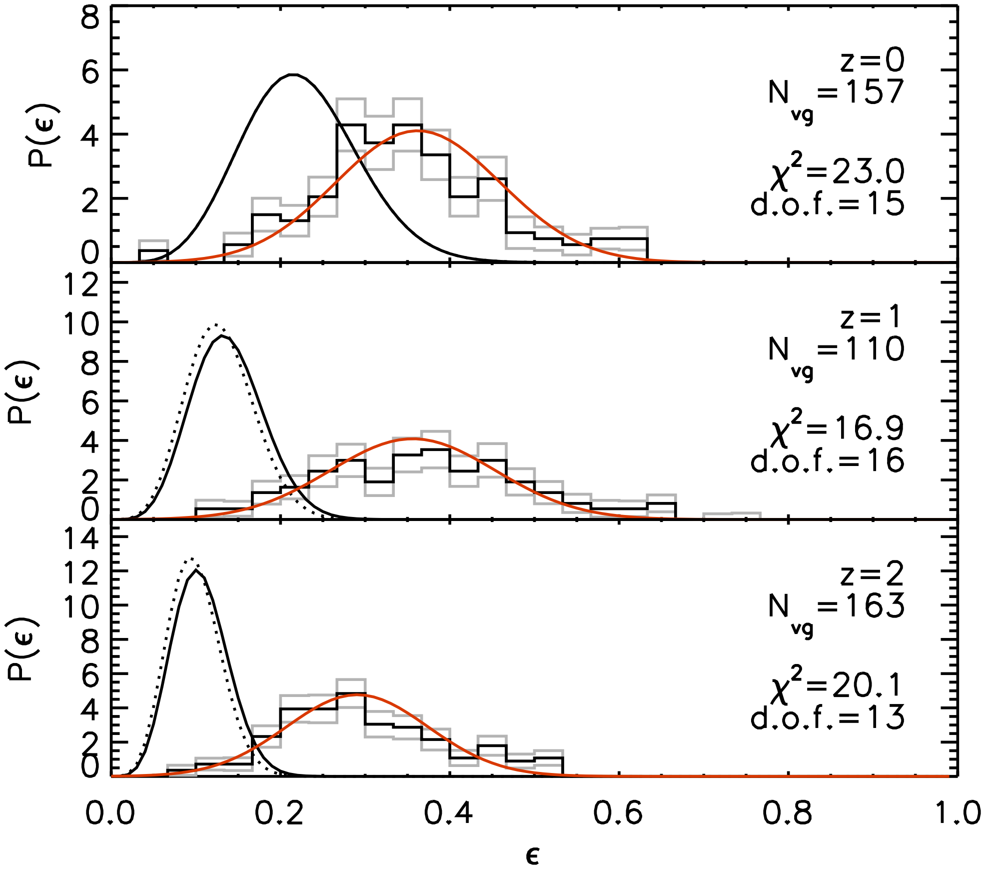

Figure 5.14: We show the ellipticity PDF extracted from the Millennium simulation at $z = 0$ (top), 1 (middle) and 2 (bottom) together with the analytic ellipticity PDF corrected for galaxy biases and convolved with the response functions (red lines). As references, we also show the analytic ellipticity PDF (black lines) with (dotted black lines) and without galaxy bias (solid black lines). We also show the $1 - \sigma$ range of the histogram, σ_ϵ, estimated via the bootstrap method (gray histograms). For each redshift, the chi-square values are $\chi^2 = 21.5$, 17.0 and 20.0, and the degree of freedoms are 15, 16 and 13 for $z = 0$, 1 and 2, respectively.

Appendices

Appendix A

Fisher Matrix Code

In this Appendix we describe what we have implemented in our Fisher matrix code, which is publicly available as a part of "Cosmology Routine Library (CRL)," developed by one of the authors (EK). This code includes the non-linear matter power spectrum in both real and redshift space, as well as marginalization over the amplitude, the linear redshift space distortion, the velocity dispersion of Fingers-of-God, the primordial tilt and running index. In the future release we plan to include non-linear galaxy bias and primordial non-Gaussianity.

A.1 Basics

A simple, approximate formula of the Fisher matrix for galaxy survey is given by (e.g., Seo & Eisenstein, 2003)

$$F_{ij} = \int_{k_{min}}^{k_{max}} \frac{4\pi k^2 dk}{(2\pi)^3} \int_0^1 d\mu \frac{\partial \ln P_g(k,\mu)}{\partial \theta_i} \frac{\partial \ln P_g(k,\mu)}{\partial \theta_j} w(k,\mu), \tag{A.1}$$

where $P_g(k,\mu)$ is the galaxy survey power spectrum calculated theoretically as a function of parameters, θ_i are the parameters to be extracted from the data, and $w(k,\mu)$ is a function given by

$$w(k,\mu) \equiv \frac{1}{2}\left[\frac{n_g P_g(k,\mu)}{1+n_g P_g(k,\mu)}\right] V_{survey} \tag{A.2}$$

Here, n_g and V_{survey} are the number density of galaxies and the volume of survey, respectively.

In linear theory, $P_g(k,\mu)$ is given by

$$P_g(k,\mu) = b_1^2 R(\mu^2) P^{linear}(k), \tag{A.3}$$

where b_1 is the scale independent linear bias factor, $P^{linear}(k)$ is the linear matter power spectrum, and $R(\mu^2)$ describes the linear redshift space distortion effect (Kaiser effect):

$$R(\mu^2) \equiv (1+\beta\mu^2)^2 \tag{A.4}$$

$$\beta = (d\ln D/d\ln a)/b_1, \tag{A.5}$$

where D is the growth factor of the linear density fluctuations, and a is the scale factor.

A.2 Derivatives

To calculate the logarithmic derivatives of $P(k)$ in Eq. (A.1), let us write down the non-linear galaxy power spectrum (with linear bias) as (Eq. (2.21)):

$$P_g(k,\mu) = b_1^2\left[P_{\delta\delta}(k) + 2\beta\mu^2 P_{\delta\theta}(k) + \beta^2\mu^4 P_{\theta\theta}(k)\right] \times \frac{1}{1+f^2k^2\mu^2\tilde{\sigma}_v^2}.$$

We compute the derivatives with respect to the following seven parameters: the angular diameter distance, D_A, the Hubble expansion rate, H, the overall amplitude of the galaxy power spectrum, A, the linear redshift space distortion factor, $\beta \equiv f/b_1$, the velocity dispersion with an empirically calibrated fudge factor, $\tilde{\sigma}_v^2$, the tilt of the primordial power spectrum, n_s, and the running index, α_s ($P_{ini} \propto k^{n_s+1/2\alpha_s \ln[k/k_{pivot}]}$). We choose the convention such that

$$(\theta_1, \theta_2, \theta_3, \theta_4, \theta_5, \theta_6, \theta_7) = (\ln D_A, \ln H, \ln A, \beta, \tilde{\sigma}_v^2, n_s, \alpha_s). \tag{A.6}$$

The derivatives with respect to $\ln A$, β, $\tilde{\sigma}_v^2$, n_s, and α_s are easy to evaluate. They are given by

$$\begin{aligned}
\frac{\partial \ln P_g(k,\mu)}{\partial \ln A} &= 1, && \text{(A.7)}\\
\frac{\partial \ln P_g(k,\mu)}{\partial \beta} &= \frac{2\mu^2 P_{\delta\theta}(k) + 2\beta\mu^4 P_{\theta\theta}(k)}{P_{\delta\delta}(k) + 2\beta\mu^2 P_{\delta\theta}(k) + \beta^2\mu^4 P_{\theta\theta}(k)} && \text{(A.8)}\\
,\frac{\partial \ln P_g(k,\mu)}{\partial \tilde{\sigma}_v^2} &= -\frac{f^2k^2\mu^2}{1+f^2k^2\mu^2\tilde{\sigma}_v^2}, && \text{(A.9)}\\
\frac{\partial \ln P_g(k,\mu)}{\partial n_s} &= \frac{\partial \ln P_{ini}(k)}{\partial n_s} = \ln k, && \text{(A.10)}\\
\frac{\partial \ln P_g(k,\mu)}{\partial \alpha_s} &= \frac{\partial \ln P_{ini}(k)}{\partial \alpha_s} = \frac{1}{2}\left[\ln\left(\frac{k}{k_{pivot}}\right)\right]^2. && \text{(A.11)}
\end{aligned}$$

We compute the derivatives with respect to $\ln D_A$ and $\ln H$ in a two step process. First, we write

$$\begin{aligned}
\frac{\partial \ln P_g(k,\mu)}{\partial \ln D_A} &= \frac{\partial \ln P_g(k,\mu)}{\partial \ln k}\frac{\partial \ln k}{\partial \ln D_A} + \frac{\partial \ln P_g(k,\mu)}{\partial \mu^2}\frac{\partial \mu^2}{\partial \ln D_A}, && \text{(A.12)}\\
\frac{\partial \ln P_g(k,\mu)}{\partial \ln H} &= \frac{\partial \ln P_g(k,\mu)}{\partial \ln k}\frac{\partial \ln k}{\partial \ln H} + \frac{\partial \ln P_g(k,\mu)}{\partial \mu^2}\frac{\partial \mu^2}{\partial \ln H}, && \text{(A.13)}
\end{aligned}$$

where

$$
\begin{aligned}
\frac{\partial \ln k}{\partial \ln D_A} &= 1-\mu^2, && \text{(A.14)}\\
\frac{\partial \ln k}{\partial \ln H} &= -\mu^2, && \text{(A.15)}\\
\frac{\partial \mu^2}{\partial \ln D_A} &= -2\mu^2(1-\mu^2), && \text{(A.16)}\\
\frac{\partial \mu^2}{\partial \ln H} &= -2\mu^2(1-\mu^2), && \text{(A.17)}\\
\frac{\partial \ln P_g(k,\mu)}{\partial \mu^2} &= \frac{2\beta P_{\delta\theta}(k)+2\beta^2\mu^2 P_{\theta\theta}(k)}{P_{\delta\delta}(k)+2\beta\mu^2 P_{\delta\theta}(k)+\beta^2\mu^4 P_{\theta\theta}(k)}\\
&- \frac{f^2k^2\tilde{\sigma}_v^2}{1+f^2k^2\mu^2\tilde{\sigma}_v^2}. && \text{(A.18)}
\end{aligned}
$$

Finally, we need to know the "effective spectral index", $n_{eff}(k,\mu)$, given by

$$
n_{eff}(k,\mu) \equiv \frac{\partial \ln P_g(k,\mu)}{\partial \ln k}, \tag{A.19}
$$

or explicitly

$$
\begin{aligned}
n_{eff}(k,\mu) &= \frac{P_{\delta\delta}(k)n_{\delta\delta}(k)+2\beta\mu^2 P_{\delta\theta}(k)n_{\delta\theta}(k)+\beta^2\mu^4 P_{\theta\theta}(k)n_{\theta\theta}(k)}{P_{\delta\delta}(k)+2\beta\mu^2 P_{\delta\theta}(k)+\beta^2\mu^4 P_{\theta\theta}(k)}\\
&-\frac{2f^2k^2\mu^2\tilde{\sigma}_v^2}{1+f^2k^2\mu^2\tilde{\sigma}_v^2}, && \text{(A.20)}
\end{aligned}
$$

where

$$
\begin{aligned}
n_{\delta\delta}(k) &\equiv \frac{\partial \ln P_{\delta\delta}(k)}{\partial \ln k}, && \text{(A.21)}\\
n_{\delta\theta}(k) &\equiv \frac{\partial \ln P_{\delta\theta}(k)}{\partial \ln k}, && \text{(A.22)}\\
n_{\theta\theta}(k) &\equiv \frac{\partial \ln P_{\theta\theta}(k)}{\partial \ln k}. && \text{(A.23)}
\end{aligned}
$$

A.3 Correlation Coefficients

In this subsection we explore the behaviour of the cross-correlation coefficient between D_A and H in various cases. In particular we focus on the effect of the marginalization over the overall amplitude with (§ A.3.2) and without (§ A.3.1) the additional marginalization over the redshift space distortion.

A.3.1 No redshift space distortion, $\beta = 0$

Let us evaluate the Fisher matrices in the limit that the redshift space distortion is absent, i.e., $\beta = 0$. In this limit, the weighting function in Eq. (A.1) and the effective spectral index in Eq. (A.19) become independent of μ, i.e., $w(k,\mu) \to w(k)$ and $n_{eff}(k,\mu) \to n_{eff}(k)$. We obtain

$$F_{11} = \int_{k_{min}}^{k_{max}} \frac{k^2 dk}{2\pi^2}[n_{eff}(k)]^2 w(k) \int_0^1 d\mu (1-\mu^2)^2 \quad (A.24)$$

$$F_{12} = \int_{k_{min}}^{k_{max}} \frac{k^2 dk}{2\pi^2}[n_{eff}(k)]^2 w(k) \int_0^1 d\mu (1-\mu^2)(-\mu^2) \quad (A.25)$$

$$F_{13} = \int_{k_{min}}^{k_{max}} \frac{k^2 dk}{2\pi^2} n_{eff}(k) w(k) \int_0^1 d\mu (1-\mu^2) \quad (A.26)$$

$$F_{22} = \int_{k_{min}}^{k_{max}} \frac{k^2 dk}{2\pi^2}[n_{eff}(k)]^2 w(k) \int_0^1 d\mu (-\mu^2)^2 \quad (A.27)$$

$$F_{23} = \int_{k_{min}}^{k_{max}} \frac{k^2 dk}{2\pi^2} n_{eff}(k) w(k) \int_0^1 d\mu (-\mu^2) \quad (A.28)$$

$$F_{33} = \int_{k_{min}}^{k_{max}} \frac{k^2 dk}{2\pi^2} w(k) \int_0^1 d\mu \quad (A.29)$$

Now, in order to understand the effect of the structure of n_{eff}, let us assume that the galaxy power spectrum is a pure power-law, i.e., $n_{eff}(k) = n$ and n

is the independent of k. In this limit, we obtain

$$F_{ij} = \bar{w} \begin{pmatrix} \frac{8n^2}{15} & -\frac{2n^2}{15} & \frac{2n}{3} \\ -\frac{2n^2}{15} & \frac{n^2}{5} & -\frac{n}{3} \\ \frac{2n}{3} & -\frac{n}{3} & 1 \end{pmatrix} \tag{A.30}$$

where $\bar{w} \equiv \int \frac{k^2 dk}{2\pi^2} w(k)$.

The marginalized errors of parameters and the correlation coefficients are computed from the inverse of the Fisher matrix. However, one can show that the matrix given in Eq. (A.30) is singular. In other words, D_A and H are completely degenerate with the amplitude for a power-law power spectrum. This result shows that only the departure of the power spectrum from a pure power-law, i.e., the existence of characteristic scales, can break the degeneracy between D_A and H, and A. These scales are often called the “standard rulers.”

To understand the structure of the Fisher matrix in Eq. (A.30) better, let us add small perturbations, $\epsilon > 0$, to the diagonal elements, and invert the matrix. The result is

$$(F^{-1})_{ij} = \frac{1}{\bar{w}} \begin{pmatrix} \frac{1}{(2+n^2)\epsilon} & -\frac{1}{(2+n^2)\epsilon} & -\frac{n}{(2+n^2)\epsilon} \\ -\frac{1}{(2+n^2)\epsilon} & \frac{1}{(2+n^2)\epsilon} & \frac{n}{(2+n^2)\epsilon} \\ -\frac{n}{(2+n^2)\epsilon} & \frac{n}{(2+n^2)\epsilon} & \frac{n^2}{(2+n^2)\epsilon} \end{pmatrix} + \mathcal{O}(\epsilon^0) \tag{A.31}$$

We find that the correlation coefficient between D_A and H is

$$r_{12} \equiv \frac{(F^{-1})_{12}}{\sqrt{(F^{-1})_{11}(F^{-1})_{22}}} \to -1 \tag{A.32}$$

as $\epsilon \to 0$. Therefore, $\ln D_A$ and $\ln H$ are totally anti-correlated, which implies that, although we cannot determine $\ln D_A$ and $\ln H$ simultaneously, we can determine $\ln D_A + \ln H = \ln(D_A H)$, even for a power-law power spectrum. [1] This is known as the Alcock-Paczyński (AP) test (Alcock & Paczynski, 1979).

There is a special case in which the covariance between A and D_A or H may be ignored. One may imagine the situation where $n_{eff}(k)$ depends upon k such that A is uncorrelated with D_A or H. For example, if $n_{eff}(k)$ oscillates about zero, then $\int_{k_{min}}^{k_{max}} \frac{k^2 dk}{2\pi^2} n_{eff}(k) w(k)$ would be small compared with $\int_{k_{min}}^{k_{max}} \frac{k^2 dk}{2\pi^2} [n_{eff}(k)]^2 w(k)$ or $\int_{k_{min}}^{k_{max}} \frac{k^2 dk}{2\pi^2} w(k)$. Therefore, F_{13} and F_{23} may be ignored, making A de-correlated with D_A and H. In this case, the Fisher matrix is a 2-by-2 matrix given by

$$F_{ij} = \bar{w} n^2 \begin{pmatrix} \frac{8}{15} & -\frac{2}{15} \\ -\frac{2}{15} & \frac{1}{5} \end{pmatrix} \tag{A.33}$$

The inverse of this matrix is then

$$(F^{-1})_{ij} = \frac{1}{\bar{w} n^2} \begin{pmatrix} \frac{9}{4} & \frac{3}{2} \\ \frac{3}{2} & 6 \end{pmatrix} \tag{A.34}$$

The correlation coefficient between D_A and H is thus given by

$$r_{12} = \frac{3/2}{\sqrt{9/4 \times 6}} = \frac{1}{\sqrt{6}} \simeq 0.408. \tag{A.35}$$

This result has been derived by Seo & Eisenstein (2007), and justifies the use of BAOs as a way to measure D_A and H with a correlation coefficient of 0.408.

From these studies we are led to the following conclusion:

---

[1] The other cross-correlation coefficients are $r_{13} \to \mp 1$ and $r_{23} \to \pm 1$ for $n > 0$ and $n < 0$ respectively.

- When the information is dominated by BAOs, the correlation coefficient between D_A and H is $r_{12} \simeq 0.408$. The amplitude of the BAOs contributes little to the errors on D_A and H, as the amplitude information is de-correlated with D_A and H.
- When the information is dominated by the AP test, $r_{12} \simeq -1$.
- In reality, as we have shown in this paper, BAOs contribute less than the overall shape of the power spectrum. Also, the shape of the power spectrum is not exactly a power-law. As a result, the correlation coefficient from the full analysis is usually negative (or small positive), but always greater than -1 (see Table 2.1).

A.3.2 With redshift space distortion, $\beta > 0$

Next, let us consider the case where the redshift space distortion cannot be ignored. In this case, we see from Eq. (A.2) and Eq. (A.20) that the weighting function, $w(k, \mu)$, and the effective spectral index, $n_{eff}(k, \mu)$, are no longer independent of μ. The analytical treatment is also possible for this case, although the results are too complicated to be useful. We therefore report on the numerical results.

Here, we choose the survey parameters given in § 2.3.2 with the non-linear power spectrum of Eq. (2.21). The results from the numerical calculations of the Fisher matrix are given in Table 2.1. We find that the marginalization over the amplitude information, and that over the amplitude and the shape of the primordial power spectrum (i.e., n_s and α_s) give the cross-correlation close to -1; thus, one relies on the AP test. The marginalization over the amplitude and the linear redshift space distortion (i.e., β) drive the cross-correlation towards zero, as the AP test no longer works when the linear redshift space distortion is marginalized over. However, in both cases the errors in the combined 1-d distance scale, R, are about the same. In other words, while one changes the orientation of the ellipse, the area is approximately preserved.

In summary, when the amplitude information is marginalized over, the information is mostly coming from the dependence of $P(k, \mu)$ on μ^2, which yields a constraint on $D_A H$ via the AP test, while when both the amplitude and the linear redshift space distortion are marginalized, the most information is coming from the standard rulers, which can constrain D_A and H separately, driving the cross-correlation towards zero.

Finally, in Fig. A.1 we show how different choices of marginalization over parameters influence the error contours of w_0 and w_a: $(\Delta w_0, \Delta w_a) = (0.08, 0.27), (0.08, 0.30), (0.24, 0.85)$, and $(0.24, 0.86)$, for the cases of no marginalization, marginalization over $\ln A$, marginalization over $\ln A$, β and $\tilde{\sigma}_v^2$, and marginalization over $\ln A$, β, $\tilde{\sigma}_v^2$, n_s and α_s respectively.

A.4 User's Guide

When using the Fisher matrix code, one may choose the form of the model galaxy power spectrum from:

- Linear power spectrum with the linear redshift space distortion (Kaiser effect),
- Non-linear power spectrum from the 3rd-order perturbation theory with the linear redshift space distortion,
- Non-linear power spectrum from the 3rd-order perturbation theory with the non-linear redshift space distortion given by Eq. (71) of Scoccimarro (2004), or
- Non-linear power spectrum from the 3rd-order perturbation theory with the non-linear redshift space distortion given by Eq. (2.21).

Next, specify the number of parameters one wishes to marginalize over, and then choose the parameters from: $\ln A$, β, $\tilde{\sigma}_v^2$, n_s, and α_s.

A given galaxy survey can be sliced up into multiple redshift bins. After entering the survey area in units of deg^2, one is asked to enter the following parameters at each redshift bin: the redshift range ($z_{min} < z < z_{max}$), the number of galaxies in units of millions in the bin, b_1, k_{max} in units of h Mpc^{-1}, and the redshift error in units of km/s.

The linear power spectrum at $z = 30$ has been precomputed using the CAMB code (Lewis et al., 2000) for the maximum likelihood parameters given in Table 1 of Komatsu et al. (2010a) ("WMAP+BAO+SN"). The ingredients of the non-linear power spectra, $P_{\delta\delta}$, $P_{\delta\theta}$, and $P_{\theta\theta}$, have been precomputed from the linear spectrum at $z = 30$. These spectra are then evolved to a specified redshift by the appropriate growth factor obtained by solving the differential equation given in Eq. (76) of Komatsu et al. (2010a).

Finally, the code yields the errors on $\ln D_A$, $\ln H$, $r_{D_A,H}$, and $\ln R$ (see Eq. (2.29) for the definition of the error in the combined distance scale, R).

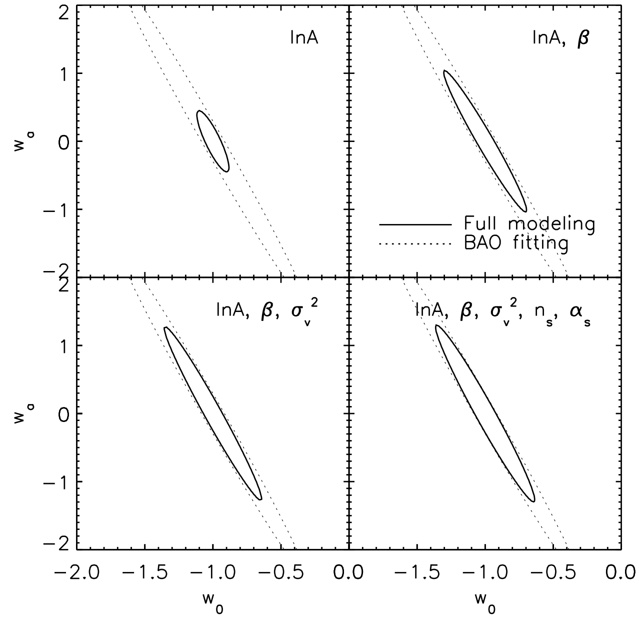

Figure A.1: Projected 68% constraints on the dark energy parameters, w_0 and w_a. The full modeling (solid) marginalized over different combinations of parameters as well as the BAO-only analysis (dotted) are shown. For all cases, we use the power spectrum up to $k_{max} = 0.40\ h$ Mpc^{-1}, and we assume that the CMB experiment measures the angular diameter distance out to $z = 1090$ with 1% accuracy. The survey area and the number of galaxies are 420 deg^2 and $N_g = 0.755 \times 10^6$, and the redshift range is $1.9 \le z \le 3.5$ for all cases. (*Top Left*) marginalized over $\ln A$, (*Top Right*) marginalized over $\ln A$, β, (*Bottom Left*) marginalized over $\ln A$, β and $\tilde{\sigma}_v^2$, (*Bottom Right*) marginalized over $\ln A$, β, $\tilde{\sigma}_v^2$, n_s and α_s.

Appendix B

Third Order Perturbation Theory

B.1 3PT for CDM

The continuity, Euler, and Poisson equations of CDM are given by

- Continuity equation:

$$\dot{\delta}(\mathbf{x},\tau) + \nabla\cdot[(1+\delta(\mathbf{x},\tau))\mathbf{v}(\mathbf{x},\tau)] = 0, \tag{B.1}$$

- Euler equations:

$$\dot{\mathbf{v}}(\mathbf{x},\tau) + [\mathbf{v}(\mathbf{x},\tau)\cdot\nabla]\mathbf{v}(\mathbf{x},\tau) = -\frac{\dot{a}}{a}\mathbf{v}(\mathbf{x},\tau) - \nabla\phi(\mathbf{x},\tau), \tag{B.2}$$

- Poisson equation (for an EdS universe):

$$\nabla^2\phi(\mathbf{x},\tau) = \frac{6}{\tau^2}\delta(\mathbf{x},\tau). \tag{B.3}$$

First, we take the divergence of Eq.[B.2] and substitute Eq.[B.3]. Moving all the non-linear terms to the RHS of the equations, we find

$$\dot{\delta}(\mathbf{x},\tau) + \nabla\cdot\mathbf{v}(\mathbf{x},\tau) = -\nabla\cdot[\delta(\mathbf{x},\tau)\mathbf{v}(\mathbf{x},\tau)], \tag{B.4}$$

$$\begin{aligned}&\frac{\partial}{\partial\tau}[\nabla\cdot\mathbf{v}(\mathbf{x},\tau)] + \frac{\dot{a}}{a}[\nabla\cdot\mathbf{v}(\mathbf{x},\tau)] + \frac{6}{\tau^2}\delta(\mathbf{x},\tau)\\ &= -\nabla\cdot\{[\mathbf{v}(\mathbf{x},\tau)\cdot\nabla]\mathbf{v}(\mathbf{x},\tau)\}.\end{aligned} \tag{B.5}$$

Let us take the Fourier transform of Eqs. [B.4] and [B.5]:

$$\begin{aligned}&\dot{\tilde{\delta}}(\mathbf{k},\tau)+\tilde{\theta}(\mathbf{k},\tau)\\&=-\frac{1}{(2\pi)^3}\int\!\!\int d\mathbf{q}_1 d\mathbf{q}_2\delta_D(\mathbf{q}_1+\mathbf{q}_2-\mathbf{k})\frac{\mathbf{k}\cdot\mathbf{q}_1}{q_1^2}\tilde{\theta}(\mathbf{q}_1,\tau)\tilde{\delta}(\mathbf{q}_2,\tau),\end{aligned}\tag{B.6}$$

$$\begin{aligned}&\dot{\tilde{\theta}}(\mathbf{k},\tau)+\frac{\dot{a}}{a}\tilde{\theta}(\mathbf{k},\tau)+\frac{6}{\tau^2}\tilde{\delta}(\mathbf{k},\tau)\\&=-\frac{1}{(2\pi)^3}\int\!\!\int d\mathbf{q}_1 d\mathbf{q}_2\delta_D(\mathbf{q}_1+\mathbf{q}_2-\mathbf{k})\frac{k^2(\mathbf{q}_1\cdot\mathbf{q}_2)}{2q_1^2q_2^2}\tilde{\theta}(\mathbf{q}_1,\tau)\tilde{\theta}(\mathbf{q}_2,\tau),\end{aligned}\tag{B.7}$$

where we have defined $\theta \equiv \nabla\cdot\mathbf{v}$, and its Fourier transform is given by

$$\tilde{\mathbf{v}}(\mathbf{k},\tau)=-i\frac{\mathbf{k}}{k^2}\tilde{\theta}(\mathbf{k},\tau).\tag{B.8}$$

One can decompose the solutions of the non-linear continuity and Euler equations, $\tilde{\delta}$ and $\tilde{\theta}$, into the sum of infinite series of n-th order perturbations of density and velocity divergence fields:

$$\tilde{\delta}(\mathbf{k},\tau) = \sum_{n=1}^{\infty}a^n(\tau)\delta_n(\mathbf{k}),\tag{B.9}$$

$$\tilde{\theta}(\mathbf{k},\tau) = \sum_{n=1}^{\infty}\dot{a}(\tau)a^{n-1}(\tau)\theta_n(\mathbf{k}),\tag{B.10}$$

respectively. Note that, strictly speaking, this particular decomposition, a decomposition into a series with powers of $a(\tau)$, is valid only for an EdS universe. However, generalization to arbitrary cosmological models can be done in the end by replacing $a(\tau)$ with the appropriate growth factor, $D(\tau)$ (Bernardeau et al., 2002; Takahashi, 2008).

Now, let us solve Eqs. [B.6] and [B.7] at each order of perturbations. The n-th ($n > 1$) term of the Eq. [B.6] is given by

$$\begin{aligned}
&\dot{a}(\tau)a^{n-1}(\tau)[n\delta_n(\mathbf{k}) + \theta_n(\mathbf{k})] \\
&= -\frac{1}{(2\pi)^3}\int\!\!\int d\mathbf{q}_1 d\mathbf{q}_2 \delta_D(\mathbf{q}_1 + \mathbf{q}_2 - \mathbf{k})\frac{\mathbf{k}\cdot\mathbf{q}_1}{q_1^2} \\
&\sum_{m=1}^{n-1} \dot{a}(\tau)a^{n-1}(\tau)\theta_m(\mathbf{q}_1)\delta_{n-m}(\mathbf{q}_2).
\end{aligned} \tag{B.11}$$

Dividing both sides by $\dot{a}(\tau)a^{n-1}(\tau)$, one obtains

$$n\delta_n(\mathbf{k}) + \theta_n(\mathbf{k}) = A_n(\mathbf{k}), \tag{B.12}$$

where

$$A_n(\mathbf{k}) = -\frac{1}{(2\pi)^3}\int\!\!\int d\mathbf{q}_1 d\mathbf{q}_2 \delta_D(\mathbf{q}_1 + \mathbf{q}_2 - \mathbf{k})\frac{\mathbf{k}\cdot\mathbf{q}_1}{q_1^2}\sum_{m=1}^{n-1}\theta_m(\mathbf{q}_1)\delta_{n-m}(\mathbf{q}_2). \tag{B.13}$$

Similarly, from the Euler equation, Eq. [B.7], one obtains

$$3\delta_n(\mathbf{k}) + (1 + 2n)\theta_n(\mathbf{k}) = B_n(\mathbf{k}), \tag{B.14}$$

where

$$\begin{aligned}
B_n(\mathbf{k}) &= -\frac{1}{(2\pi)^3}\int\!\!\int d\mathbf{q}_1 d\mathbf{q}_2 \delta_D(\mathbf{q}_1 + \mathbf{q}_2 - \mathbf{k})\frac{k^2(\mathbf{q}_1\cdot\mathbf{q}_2)}{q_1^2 q_2^2} \\
\times &\sum_{m=1}^{n-1}\theta_m(\mathbf{q}_1)\theta_{n-m}(\mathbf{q}_2).
\end{aligned} \tag{B.15}$$

The forms of Eqs. [B.12] and [B.14] indicate that the n-th order solutions are written in terms of the sum of 1-st to $(n-1)$-th order solutions, with $\delta_1(\mathbf{k}) = -\theta_1(\mathbf{k})$. By solving Eqs. [B.12] and [B.14] for δ_n and θ_n, one obtains

$$\delta_n(\mathbf{k}) = \frac{(1+2n)A_n(\mathbf{k}) - B_n(\mathbf{k})}{(2n+3)(n-1)}, \tag{B.16}$$

$$\theta_n(\mathbf{k}) = \frac{-3A_n(\mathbf{k}) + nB_n(\mathbf{k})}{(2n+3)(n-1)}, \tag{B.17}$$

which can be rewritten as

$$\begin{aligned} \delta_n(\mathbf{k}) &= \frac{1}{(2\pi)^{3n-3}} \int d\mathbf{q}_1 ... d\mathbf{q}_n \delta_D(\mathbf{q}_1 + ... + \mathbf{q}_n - \mathbf{k}) \\ \times & \quad F_n(\mathbf{q}_1, ..., \mathbf{q}_n)\delta_1(\mathbf{q}_1)...\delta_1(\mathbf{q}_n), \end{aligned} \tag{B.18}$$

$$\begin{aligned} \theta_n(\mathbf{k}) &= -\frac{1}{(2\pi)^{3n-3}} \int d\mathbf{q}_1 ... d\mathbf{q}_n \delta_D(\mathbf{q}_1 + ... + \mathbf{q}_n - \mathbf{k}) \\ \times & \quad G_n(\mathbf{q}_1, ..., \mathbf{q}_n)\delta_1(\mathbf{q}_1)...\delta_1(\mathbf{q}_n). \end{aligned} \tag{B.19}$$

Here, the newly defined kernels, F_n and G_n, can be found from the following recursion relations:

$$\begin{aligned} F_n(\mathbf{q}_1, ..., \mathbf{q}_n) &= \sum_{m=1}^{n-1} \frac{G_m(\mathbf{q}_1, ..., \mathbf{q}_m)}{(2n+3)(n-1)} \left[(1+2n)\frac{\mathbf{k}\cdot\mathbf{q}_1}{q_1^2} F_{n-m}(\mathbf{q}_{m+1}, ..., \mathbf{q}_n) \right. \\ &+ \left. \frac{k^2(\mathbf{q}_1\cdot\mathbf{q}_2)}{q_1^2 q_2^2} G_{n-m}(\mathbf{q}_{m+1}, ..., \mathbf{q}_n) \right], \end{aligned} \tag{B.20}$$

and

$$\begin{aligned} G_n(\mathbf{q}_1, ..., \mathbf{q}_n) &= \sum_{m=1}^{n-1} \frac{G_m(\mathbf{q}_1, ..., \mathbf{q}_m)}{(2n+3)(n-1)} \left[3\frac{\mathbf{k}\cdot\mathbf{q}_1}{q_1^2} F_{n-m}(\mathbf{q}_{m+1}, ..., \mathbf{q}_n) \right. \\ &+ \left. n\frac{k^2(\mathbf{q}_1\cdot\mathbf{q}_2)}{q_1^2 q_2^2} G_{n-m}(\mathbf{q}_{m+1}, ..., \mathbf{q}_n) \right], \end{aligned} \tag{B.21}$$

with the boundary conditions of $F_1 = 1 = G_1$. The 2nd-order solutions are

$$\begin{aligned} F_2(\mathbf{q}_1, \mathbf{q}_2) &= \frac{5}{7}\frac{\mathbf{k}\cdot\mathbf{q}_1}{q_1^2} + \frac{k^2(\mathbf{q}_1\cdot\mathbf{q}_2)}{7q_1^2q_2^2}, & \text{(B.22)}\\ G_2(\mathbf{q}_1, \mathbf{q}_2) &= \frac{3}{7}\frac{\mathbf{k}\cdot\mathbf{q}_1}{q_1^2} + \frac{2k^2(\mathbf{q}_1\cdot\mathbf{q}_2)}{7q_1^2q_2^2}, & \text{(B.23)}\end{aligned}$$

where $\mathbf{k} = \mathbf{q}_1 + \mathbf{q}_2$. The 3rd-order solutions are

$$\begin{aligned} F_3(\mathbf{q}_1, \mathbf{q}_2, \mathbf{q}_3) &= \frac{1}{18}\left[\frac{7\mathbf{k}\cdot\mathbf{q}_1}{q_1^2}F_2(\mathbf{q}_2, \mathbf{q}_3) + \frac{k^2(\mathbf{q}_1\cdot\mathbf{q}_{23})}{q_1^2q_{23}^2}G_2(\mathbf{q}_2, \mathbf{q}_3)\right] \\ &+ \frac{G_2(\mathbf{q}_1, \mathbf{q}_2)}{18}\left[\frac{7\mathbf{k}\cdot\mathbf{q}_{12}}{q_{12}^2} + \frac{k^2(\mathbf{q}_{12}\cdot\mathbf{q}_3)}{q_{12}^2q_3^2}\right], & \text{(B.24)}\end{aligned}$$

where $\mathbf{q}_{ij} \equiv \mathbf{q}_i + \mathbf{q}_j$ and $\mathbf{k} = \sum \mathbf{q}_i$.

It is often convenient to have the symmetrized forms of the above kernels. They are

$$\begin{aligned} F_2^{(s)}(\mathbf{q}_1, \mathbf{q}_2) &= \frac{1}{2}\left[F_2(\mathbf{q}_1, \mathbf{q}_2) + F_2(\mathbf{q}_2, \mathbf{q}_1)\right], & \text{(B.25)}\\ G_2^{(s)}(\mathbf{q}_1, \mathbf{q}_2) &= \frac{1}{2}\left[G_2(\mathbf{q}_1, \mathbf{q}_2) + G_2(\mathbf{q}_2, \mathbf{q}_1)\right], & \text{(B.26)}\\ F_3^{(s)}(\mathbf{q}_1, \mathbf{q}_2, \mathbf{q}_3) &= \frac{1}{6}\left[F_3(\mathbf{q}_1, \mathbf{q}_2, \mathbf{q}_3) + F_3(\mathbf{q}_1, \mathbf{q}_3, \mathbf{q}_2) + F_3(\mathbf{q}_2, \mathbf{q}_1, \mathbf{q}_3)\right. \\ &\left. + F_3(\mathbf{q}_2, \mathbf{q}_3, \mathbf{q}_1) + F_3(\mathbf{q}_3, \mathbf{q}_1, \mathbf{q}_2) + F_3(\mathbf{q}_3, \mathbf{q}_2, \mathbf{q}_1)\right]. \\ & & \text{(B.27)}\end{aligned}$$

The explicit forms are

$$F_2^{(s)}(\mathbf{q}_1,\mathbf{q}_2) = \frac{5}{7} + \frac{2}{7}\frac{(\mathbf{q}_1\cdot\mathbf{q}_2)^2}{q_1^2 q_2^2} + \frac{1}{2}\frac{(\mathbf{q}_1\cdot\mathbf{q}_2)(q_1^2+q_2^2)}{q_1^2 q_2^2}, \tag{B.28}$$

$$G_2^{(s)}(\mathbf{q}_1,\mathbf{q}_2) = \frac{3}{7} + \frac{4}{7}\frac{(\mathbf{q}_1\cdot\mathbf{q}_2)^2}{q_1^2 q_2^2} + \frac{1}{2}\frac{(\mathbf{q}_1\cdot\mathbf{q}_2)(q_1^2+q_2^2)}{q_1^2 q_2^2}, \tag{B.29}$$

$$\begin{aligned} F_3^{(s)}(\mathbf{q}_1,\mathbf{q}_2,\mathbf{q}_3) &= \frac{7}{54}\mathbf{k}\cdot\left[F_2^{(s)}(\mathbf{q}_2,\mathbf{q}_3)\frac{\mathbf{q}_1}{q_1^2} + F_2^{(s)}(\mathbf{q}_1,\mathbf{q}_3)\frac{\mathbf{q}_2}{q_2^2} + F_2^{(s)}(\mathbf{q}_1,\mathbf{q}_2)\frac{\mathbf{q}_3}{q_3^2}\right] \\ &+\frac{1}{27}k^2\left[G_2^{(s)}(\mathbf{q}_2,\mathbf{q}_3)\frac{\mathbf{q}_1\cdot\mathbf{q}_{23}}{q_1^2 q_{23}^2} + G_2^{(s)}(\mathbf{q}_1,\mathbf{q}_3)\frac{\mathbf{q}_2\cdot\mathbf{q}_{13}}{q_2^2 q_{13}^2} + G_2^{(s)}(\mathbf{q}_1,\mathbf{q}_2)\frac{\mathbf{q}_3\cdot\mathbf{q}_{12}}{q_3^2 q_{12}^2}\right] \\ &+\frac{7}{54}\mathbf{k}\cdot\left[G_2^{(s)}(\mathbf{q}_2,\mathbf{q}_3)\frac{\mathbf{q}_{23}}{q_{23}^2} + G_2^{(s)}(\mathbf{q}_1,\mathbf{q}_3)\frac{\mathbf{q}_{13}}{q_{13}^2} + G_2^{(s)}(\mathbf{q}_1,\mathbf{q}_2)\frac{\mathbf{q}_{12}}{q_{12}^2}\right]. \end{aligned} \tag{B.30}$$

In order to calculate the next-to-linear-order density power spectrum, one needs to use the solutions of the density fluctuations up to the 3rd order:

$$\begin{aligned} &(2\pi)^3 P(k,\tau)\delta_D(\mathbf{k}+\mathbf{k}') \\ &= \langle\tilde{\delta}(\mathbf{k},\tau)\tilde{\delta}(\mathbf{k}',\tau)\rangle = \left\langle\left(\sum_{m=1}^{\infty} a^m(\tau)\tilde{\delta}_m(\mathbf{k})\right)\left(\sum_{l=1}^{\infty} a^l(\tau)\tilde{\delta}_l(\mathbf{k}')\right)\right\rangle \\ &\simeq a^2(\tau)\langle\delta_1(\mathbf{k})\delta_1(\mathbf{k}')\rangle + a^4(\tau)\langle\delta_1(\mathbf{k})\delta_3(\mathbf{k}') + \delta_2(\mathbf{k})\delta_2(\mathbf{k}') + \delta_3(\mathbf{k})\delta_1(\mathbf{k}')\rangle, \end{aligned} \tag{B.31}$$

which yields

$$P(k,\tau) = a^2(\tau)P_{11}(k) + a^4(\tau)\left[P_{22}(k) + 2P_{13}(k)\right] + \mathcal{O}(\delta^6). \tag{B.32}$$

Here, we have defined the quantity, $P_{ij}(k)$, given by

$$(2\pi)^3 P_{ij}(k)\delta_D(\mathbf{k}+\mathbf{k}') = \langle\delta_i(\mathbf{k})\delta_j(\mathbf{k}')\rangle. \tag{B.33}$$

The non-linear corrections, $P_{22}(k)$ and $P_{13}(k)$, are

$$P_{22}(k) = 2\int\frac{d\mathbf{q}}{(2\pi)^3}P_{11}(q)P_{11}(|\mathbf{k}-\mathbf{q}|)\left[F_2^{(s)}(\mathbf{q},\mathbf{k}-\mathbf{q})\right]^2, \tag{B.34}$$

where

$$F_2^{(s)}(\mathbf{q}, \mathbf{k}-\mathbf{q}) = \frac{5}{7} + \frac{1}{14}\left[\frac{-10q^4 + 20kq^3\mu - 10k^2q^2\mu^2 - 7k^2q^2 + 7k^3q\mu}{q^2(k^2+q^2-2kq\mu)}\right], \tag{B.35}$$

and $\mu \equiv \hat{\mathbf{k}} \cdot \hat{\mathbf{q}}$, and

$$P_{13}(k) = 3P_{11}(k)\int \frac{d\mathbf{q}}{(2\pi)^3} F_3^{(s)}(\mathbf{q}, -\mathbf{q}, \mathbf{k}) P_{11}(q). \tag{B.36}$$

Using

$$\begin{aligned} \int_{-1}^{1} d\mu F_3^{(s)}(\mathbf{q}, -\mathbf{q}, \mathbf{k}) &= \frac{1}{756}\left[50 - 21\frac{q^2}{k^2} - 79\frac{k^2}{q^2} + 6\frac{k^4}{q^4}\right. \\ &+ \left.\frac{3}{2}\frac{(q^2-k^2)^3(2k^2+7q^2)}{k^3q^5}\ln\frac{k+q}{|k-q|}\right], \end{aligned} \tag{B.37}$$

one obtains (Makino et al., 1992)

$$\begin{aligned} P_{13}(k) &= \frac{2\pi}{252}k^2P_{11}(k)\int_0^\infty \frac{dq}{(2\pi)^3}P_{11}(q)\left[50\frac{q^2}{k^2} - 21\frac{q^4}{k^4} - 79 + 6\frac{k^2}{q^2}\right. \\ &+ \left.\frac{3}{2}\frac{(q^2-k^2)^3(2k^2+7q^2)}{k^5q^3}\ln\frac{k+q}{|k-q|}\right]. \end{aligned} \tag{B.38}$$

B.2 3PT with Pressure

In this Appendix we shall derive the higher-order filtering functions. We shall solve Eqs. [3.14]–[3.17] perturbatively, up to the 3rd-order in perturbations. The density contrasts and velocity divergence fields of CDM and the matter with pressure are all expanded into the infinite sum of n-th order perturbations as

$$\tilde{\delta}_c(\mathbf{k},\tau) = \sum_{n=1}^{\infty} a^n(\tau)\delta_{n,c}(\mathbf{k}), \tag{B.39}$$

$$\tilde{\theta}_c(\mathbf{k},\tau) = \sum_{n=1}^{\infty} \dot{a}(\tau)a^{n-1}(\tau)\theta_{n,c}(\mathbf{k}), \tag{B.40}$$

$$\begin{aligned} \tilde{\delta}_b(\mathbf{k},\tau) &= \sum_{n=1}^{\infty} a^n(\tau)\delta_{n,c}(\mathbf{k})g_n(\mathbf{k},\tau), & \text{(B.41)} \\ \tilde{\theta}_b(\mathbf{k},\tau) &= \sum_{n=1}^{\infty} \dot{a}(\tau)a^{n-1}(\tau)\theta_{n,c}(\mathbf{k})h_n(\mathbf{k},\tau), & \text{(B.42)} \end{aligned}$$

where $g_n(\mathbf{k},\tau)$ and $h_n(\mathbf{k},\tau)$ are the filtering functions for the density and velocity divergence fields, respectively, at the n-th order.

With the above series expansion, Eqs. [3.15] and [3.17] yield

$$
\begin{aligned}
&\sum_{n=1}^{\infty}\Big[\big(n\dot{a}(\tau)a^{n-1}(\tau)g_n(\mathbf{k},\tau)+a^n(\tau)\dot{g}_n(\mathbf{k},\tau)\big)\,\delta_{n,c}(\mathbf{k})\\
&+\dot{a}(\tau)a^{n-1}(\tau)h_n(\mathbf{k},\tau)\theta_{n,c}(\mathbf{k})\Big]\\
&=-\frac{1}{(2\pi)^3}\int\!\!\int d\mathbf{q}_1 d\mathbf{q}_2\delta_D(\mathbf{q}_1+\mathbf{q}_2-\mathbf{k})\frac{\mathbf{k}\cdot\mathbf{q}_1}{q_1^2}\\
&\times\sum_{m=1}^{\infty}\sum_{l=1}^{\infty}\dot{a}a^{m+l-1}h_m(\mathbf{q}_1,\tau)g_l(\mathbf{q}_2,\tau)\theta_{m,c}(\mathbf{q}_1)\delta_{l,c}(\mathbf{q}_2),
\end{aligned}
\tag{B.43}
$$

$$
\begin{aligned}
&\sum_{n=1}^{\infty}\Big[\big(\ddot{a}(\tau)a^{n-1}(\tau)+\dot{a}^2(\tau)a^{n-2}(\tau)(n-1)\big)\,h_n(\mathbf{k},\tau)\theta_{n,c}(\mathbf{k})\\
&+\dot{a}(\tau)a^{n-1}(\tau)\dot{h}_n(\mathbf{k},\tau)\theta_{n,c}(\mathbf{k})+\frac{2}{\tau}\dot{a}(\tau)a^{n-1}(\tau)h_n(\mathbf{k})(\mathbf{k},\tau)\theta_{n,c}(\mathbf{k})\\
&+\frac{6}{\tau^2}a^n(\tau)\left(f_c+f_b g_n(\mathbf{k},\tau)\right)\delta_{n,c}(\mathbf{k})\Big]\\
&=-\frac{1}{(2\pi)^3}\int\!\!\int d\mathbf{q}_1 d\mathbf{q}_2\delta_D(\mathbf{q}_1+\mathbf{q}_2-\mathbf{k})\frac{k^2(\mathbf{q}_1\cdot\mathbf{q}_2)}{2q_1^2q_2^2}\\
&\times\sum_{m=1}^{\infty}\sum_{l=1}^{\infty}\dot{a}^2(\tau)a^{m+l-2}(\tau)h_m(\mathbf{q}_1,\tau)h_l(\mathbf{q}_2,\tau)\theta_{m,c}(\mathbf{q}_1)\theta_{l,c}(\mathbf{q}_2)\\
&+k^2c_s^2(\tau)\sum_{n=1}^{\infty}a^n(\tau)g_n(\mathbf{k},\tau)\delta_{n,c}(\mathbf{k})\\
&-\frac{1}{2(2\pi)^3}k^2c_s^2(\tau)\int\!\!\int d\mathbf{q}_1 d\mathbf{q}_2\delta_D(\mathbf{q}_1+\mathbf{q}_2-\mathbf{k})\\
&\times\sum_{m=1}^{\infty}\sum_{l=1}^{\infty}a^{m+l}(\tau)g_m(\mathbf{q}_1,\tau)g_l(\mathbf{q}_2,\tau)\delta_{m,c}(\mathbf{q}_1)\delta_{l,c}(\mathbf{q}_2)\\
&+\frac{1}{3(2\pi)^6}k^2c_s^2(\tau)\int\!\!\int\!\!\int d\mathbf{q}_1 d\mathbf{q}_2 d\mathbf{q}_3\delta_D(\mathbf{q}_1+\mathbf{q}_2+\mathbf{q}_3-\mathbf{k})\\
&\times\sum_{m=1}^{\infty}\sum_{l=1}^{\infty}\sum_{p=1}^{\infty}a^{m+l+p}(\tau)g_m(\mathbf{q}_1,\tau)g_l(\mathbf{q}_2,\tau)g_p(\mathbf{q}_3,\tau)\delta_{m,c}(\mathbf{q}_1)\delta_{l,c}(\mathbf{q}_2)\delta_{p,c}(\mathbf{q}_3).
\end{aligned}
\tag{B.44}
$$

From now on, we shall write the sound speed, c_s, in terms of the usual Jeans wavenumber, k_J, as $c_s = \sqrt{6}/(k_J\tau)$. We shall ignore the inhomogeneity in c_s (i.e., spatial dependence of c_s) throughout this paper. For the linear analysis for $\nabla c_s \neq 0$, see Naoz & Barkana (2005).

B.2.1 Second Order Solutions

We have derived the linear filtering function, $g_1(k)$, in Eq. [3.30]. For $n = 2$, the continuity and Euler equations are given by

$$
\begin{aligned}
&\delta_{2,c}(\mathbf{k})\dot{g}_2(\mathbf{k},\tau) + \frac{4}{\tau}\delta_{2,c}(\mathbf{k})g_2(\mathbf{k},\tau) + \frac{2}{\tau}\theta_{2,c}(\mathbf{k})h_2(\mathbf{k},\tau) \\
&= \frac{2}{\tau}\frac{1}{(2\pi)^3}\int\int d\mathbf{q}_1 d\mathbf{q}_2 \delta_D(\mathbf{q}_1 + \mathbf{q}_2 - \mathbf{k})\frac{\mathbf{k}\cdot\mathbf{q}_1}{q_1^2} \\
&\times\delta_{1,c}(\mathbf{q}_1)\delta_{1,c}(\mathbf{q}_2)g_1(\mathbf{q}_1)g_1(\mathbf{q}_2) \\
&\equiv \frac{2}{\tau}A_2(\mathbf{k}), \qquad \text{(B.45)}
\end{aligned}
$$

$$
\begin{aligned}
&\frac{10}{\tau^2}\theta_{2,c}(\mathbf{k})h_2(\mathbf{k},\tau) + \frac{2}{\tau}\theta_{2,c}(\mathbf{k})\dot{h}_2(\mathbf{k},\tau) + \frac{6}{\tau^2}\delta_{2,c}(\mathbf{k}) - \frac{6}{\tau^2}\frac{k^2}{k_J^2}\delta_{2,c}(\mathbf{k})g_2(\mathbf{k},\tau) \\
&= \frac{4}{\tau^2}\frac{1}{(2\pi)^3}\int\int d\mathbf{q}_1 d\mathbf{q}_2 \delta_D(\mathbf{q}_1 + \mathbf{q}_2 - \mathbf{k})\left[-\frac{3}{4}\frac{k^2}{k_J^2} - \frac{k^2(\mathbf{q}_1\cdot\mathbf{q}_2)}{2q_1^2q_2^2}\right] \\
&\times\delta_{1,c}(\mathbf{q}_1)\delta_{1,c}(\mathbf{q}_2)g_1(\mathbf{q}_1)g_1(\mathbf{q}_2) \\
&\equiv \frac{4}{\tau^2}B_2(\mathbf{k}). \qquad \text{(B.46)}
\end{aligned}
$$

Here, $\theta_{1,c}(\mathbf{k}) = -\delta_{1,c}(\mathbf{k})$. Combining Eqs. [B.45] and [B.46], we get the second order inhomogeneous partial differential equation:

$$\begin{aligned} &\ddot{g}_2(\mathbf{k},\tau)+\frac{10}{\tau^2}\dot{g}_2(\mathbf{k},\tau)+\frac{1}{\tau^2}\left[20+6\frac{k^2}{k_J^2}\right]g_2(\mathbf{k},\tau)\\ &+\frac{1}{\tau^2}\left[-6-\frac{10A_2(\mathbf{k})}{\delta_{2,c}(\mathbf{k})}+\frac{4B_2(\mathbf{k})}{\delta_{2,c}(\mathbf{k})}\right]=0, \end{aligned} \tag{B.47}$$

where $\delta_{2,c}(\mathbf{k})$ is given by

$$\delta_{2,c}(\mathbf{k})=\frac{1}{(2\pi)^3}\int d\mathbf{q}F_2^{(s)}(\mathbf{q},\mathbf{k}-\mathbf{q})\delta_{1,c}(\mathbf{q})\delta_{1,c}(\mathbf{k}-\mathbf{q}). \tag{B.48}$$

Solving the above differential equation, we have:

$$g_2(\mathbf{k},\tau)=\frac{6+\frac{10A_2(\mathbf{k})}{\delta_{2,c}(\mathbf{k})}-\frac{4B_2(\mathbf{k})}{\delta_{2,c}(\mathbf{k})}}{20+6\frac{k^2}{k_J^2}}+\mathcal{O}(\tau^{-9/2}), \tag{B.49}$$

where the oscillation component,

$$\mathcal{O}(\tau^{-9/2})\propto\tau^{-\frac{9}{2}\left(1\pm\sqrt{1-\frac{4}{81}(20+6\frac{k^2}{k_J^2})}\right)}, \tag{B.50}$$

decays for any choice of $0\leq k/k_J$. The 2nd-order filtering function for the velocity divergence field, $h_2(\mathbf{h},\tau)$, is given by

$$h_2(\mathbf{k})=\frac{1}{\theta_{2,c}(\mathbf{k})}\left[A_2(\mathbf{k})-2\delta_{2,c}(\mathbf{k})g_2(\mathbf{k})\right], \tag{B.51}$$

where we have ignored the decaying term.

Using the explicit forms of $A_2(\mathbf{k})$ and $B_2(\mathbf{k})$ given by Eqs. [B.45] and [B.46], respectively, we obtain

$$g_2(\mathbf{k},\tau)=\frac{\frac{10}{3}-\frac{7}{3}\left[1-\frac{\delta'_{2,c}(\mathbf{k})}{\delta_{2,c}(\mathbf{k})}\right]}{\frac{10}{3}+\frac{k^2}{k_J^2}}+\mathcal{O}(\tau^{-9/2}), \tag{B.52}$$

where $\delta'_{2,c}$ is

$$\delta'_{2,c}(\mathbf{k}) = \frac{1}{(2\pi)^3}\int d\mathbf{q}\mathcal{F}_2^{(s)}(\mathbf{q},\mathbf{k}-\mathbf{q})\delta_{1,c}(\mathbf{q})\delta_{1,c}(\mathbf{k}-\mathbf{q}), \tag{B.53}$$

where

$$\mathcal{F}_2^{(s)}(\mathbf{q}_1,\mathbf{q}_2) \equiv \left[F_2^{(s)}(\mathbf{q}_1,\mathbf{q}_2) + \frac{3}{14}\frac{k^2}{k_J^2}\right] g_1(\mathbf{q}_1)g_1(\mathbf{q}_2). \tag{B.54}$$

In the limit where $k_J \to \infty$, $\mathcal{F}_2^{(s)}(\mathbf{q}_1,\mathbf{q}_2) = F_2^{(s)}(\mathbf{q}_1,\mathbf{q}_2)$, and thus $g_2 \to 1$. For the velocity divergence filtering function, we find

$$\begin{aligned}
h_2(\mathbf{k}) &= \frac{1}{\theta_{2,c}(\mathbf{k})}\left[\frac{1}{(2\pi)^3}\iint d\mathbf{q}_1 d\mathbf{q}_2 \delta_D(\mathbf{q}_1+\mathbf{q}_2-\mathbf{k})\delta_{1,c}(\mathbf{q}_1)\delta_{1,c}(\mathbf{q}_2)\right.\\
&\times \left.(2F_2^{(s)}(\mathbf{q}_1,\mathbf{q}_2) - G_2^{(s)}(\mathbf{q}_1,\mathbf{q}_2))g_1(\mathbf{q}_1)g_1(\mathbf{q}_2) - 2\delta_{2,c}(\mathbf{k})g_2(\mathbf{k})\right]\\
&= \frac{1}{\theta_{2,c}(\mathbf{k})}\left[\frac{1}{(2\pi)^3}\iint d\mathbf{q}_1 d\mathbf{q}_2 \delta_D(\mathbf{q}_1+\mathbf{q}_2-\mathbf{k})\delta_{1,c}(\mathbf{q}_1)\delta_{1,c}(\mathbf{q}_2)\right.\\
&\quad \times \left.\left(1+\frac{(\mathbf{q}_1\cdot\mathbf{q}_2)(q_1^2+q_2^2)}{2q_1^2q_2^2}\right)g_1(\mathbf{q}_1)g_1(\mathbf{q}_2)\right] - 2\frac{\delta_{2,c}(\mathbf{k})}{\theta_{2,c}(\mathbf{k})}g_2(\mathbf{k}),
\end{aligned} \tag{B.55}$$

where we have used $2F_2(\mathbf{q}_1,\mathbf{q}_2) - G_2(\mathbf{q}_1,\mathbf{q}_2) = \frac{\mathbf{k}\cdot\mathbf{q}_1}{q_1^2}$. This expression also converges to $h_2 = 1$ as we take the limit of $\mathbf{k}_J \to \infty$.

B.2.2 Third Order Solutions

For $n = 3$, the continuity and Euler equations are given by

$$\begin{aligned}
&3\dot{a}(\tau)a^2(\tau)g_3(\mathbf{k},\tau)\delta_{3,c}(\mathbf{k}) + a^3(\tau)\dot{g}_3(\mathbf{k},\tau)\delta_{3,c}(\mathbf{k}) \\
&+\dot{a}(\tau)a^2(\tau)h_3(\mathbf{k},\tau)\theta_{3,c}(\mathbf{k}) \\
&= \dot{a}(\tau)a^2(\tau)\frac{1}{(2\pi)^6} \\
&\times \int\!\!\int\!\!\int d\mathbf{q}_1 d\mathbf{q}_2 d\mathbf{q}_3 \delta_D(\mathbf{q}_1+\mathbf{q}_2+\mathbf{q}_3-\mathbf{k})\delta_{1,c}(\mathbf{q}_1)\delta_{1,c}(\mathbf{q}_2)\delta_{1,c}(\mathbf{q}_3) \\
&\times \left[\frac{\mathbf{k}\cdot\mathbf{q}_1}{q_1^2}g_1(\mathbf{q}_1)g_2(\mathbf{q}_{23})F_2^{(s)}(\mathbf{q}_2,\mathbf{q}_3) + \frac{\mathbf{k}\cdot\mathbf{q}_{12}}{q_{12}^2}h_2(\mathbf{q}_{12})g_1(\mathbf{q}_3)G_2^{(s)}(\mathbf{q}_1,\mathbf{q}_2)\right] \\
&\equiv \dot{a}(\tau)a^2(\tau)A_3(\mathbf{k}),
\end{aligned} \tag{B.56}$$

$$\begin{aligned}
&\left[\ddot{a}(\tau)a^2(\tau) + 2\dot{a}^2(\tau)a(\tau)\right] h_3(\mathbf{k},\tau)\theta_{3,c}(\mathbf{k}) + \dot{a}(\tau)a^2(\tau)\dot{h}_3(\mathbf{k},\tau)\theta_{3,c}(\mathbf{k}) \\
&+\frac{2}{\tau}\dot{a}(\tau)a^2(\tau)h_3(\mathbf{k},\tau)\theta_{3,c}(\mathbf{k}) + \frac{6}{\tau^2}a^3(\tau)\delta_{3,c}(\mathbf{k}) - \frac{6}{\tau^2}\frac{k^2}{k_J^2}a^3(\tau)\delta_{3,c}(\mathbf{k}) \\
&= \dot{a}^2(\tau)a(\tau)\frac{1}{(2\pi)^6} \\
&\times \int\!\!\int\!\!\int d\mathbf{q}_1 d\mathbf{q}_2 d\mathbf{q}_3 \delta_D(\mathbf{q}_1+\mathbf{q}_2+\mathbf{q}_3-\mathbf{k})\delta_{1,c}(\mathbf{q}_1)\delta_{1,c}(\mathbf{q}_2)\delta_{1,c}(\mathbf{q}_3) \\
&\times \left[-\frac{k^2(\mathbf{q}_1\cdot\mathbf{q}_{23})}{2q_1^2q_{23}^2}g_1(\mathbf{q}_1)h_2(\mathbf{q}_{23})G_2^{(s)}(\mathbf{q}_2,\mathbf{q}_3)\right. \\
&-\frac{k^2(\mathbf{q}_{12}\cdot\mathbf{q}_3)}{2q_{12}^2q_3^2}h_2(\mathbf{q}_{12})g_1(\mathbf{q}_3)G_2^{(s)}(\mathbf{q}_1,\mathbf{q}_2) \\
&-\frac{3}{4}\frac{k^2}{k_J^2}g_1(\mathbf{q}_1)g_2(\mathbf{q}_{23})F_2^{(s)}(\mathbf{q}_2,\mathbf{q}_3) - \frac{3}{4}\frac{k^2}{k_J^2}g_2(\mathbf{q}_{12})g_1(\mathbf{q}_3)F_2^{(s)}(\mathbf{q}_1,\mathbf{q}_2) \\
&\left.+\frac{1}{2}\frac{k^2}{k_J^2}g_1(\mathbf{q}_1)g_1(\mathbf{q}_2)g_1(\mathbf{q}_3)\right] \equiv \dot{a}^2(\tau)a(\tau)B_3(\mathbf{k}).
\end{aligned} \tag{B.57}$$

In an EdS universe, $a(\tau) = \frac{\tau^2}{9}$, we have

$$\delta_{3,c}(\mathbf{k})\dot{g}_3(\mathbf{k},\tau) + \frac{6}{\tau}\delta_{3,c}(\mathbf{k})g_3(\mathbf{k},\tau) + \frac{2}{\tau}\theta_{3,c}(\mathbf{k})h_3(\mathbf{k},\tau) = \frac{2}{\tau}A_3(\mathbf{k}), \quad \text{(B.58)}$$

$$\frac{14}{\tau^2}h_3(\mathbf{k},\tau)\theta_{3,c}(\mathbf{k}) + \frac{2}{\tau}\dot{h}_3(\mathbf{k},\tau)\theta_{3,c}(\mathbf{k}) + \frac{6}{\tau^2}\delta_{3,c}(\mathbf{k}) - \frac{6}{\tau^2}\frac{k^2}{k_J^2}\delta_{3,c}(\mathbf{k})g_3(\mathbf{k},\tau)$$
$$= \frac{4}{\tau^2}B_3(\mathbf{k}). \quad \text{(B.59)}$$

Combining Eqs. [B.58] and [B.59], we have the second-order differential equation:

$$\begin{aligned}\ddot{g}_3(\mathbf{k},\tau) + \frac{14}{\tau}\dot{g}_3(\mathbf{k},\tau) &+ \frac{1}{\tau^2}\left(42 + 6\frac{k^2}{k_J^2}\right)g_3(\mathbf{k},\tau) \\ &+ \frac{1}{\tau^2}\left(-6 - \frac{14A_3(\mathbf{k})}{\delta_{3,c}(\mathbf{k})} + \frac{4B_3(\mathbf{k})}{\delta_{3,c}(\mathbf{k})}\right) = 0. \quad \text{(B.60)}\end{aligned}$$

Solving this, we obtain

$$g_3(\mathbf{k},\tau) = \frac{1 + \frac{7A_3(\mathbf{k})}{3\delta_{3,c}(\mathbf{k})} - \frac{2B_3(\mathbf{k})}{3\delta_{3,c}(\mathbf{k})}}{7 + \frac{k^2}{k_J^2}} + \mathcal{O}(\tau^{-13/2}), \quad \text{(B.61)}$$

where the oscillation component,

$$\mathcal{O}(\tau^{-13/2}) \propto \tau^{-13/2\left(1 \pm \sqrt{1 - \frac{24}{169}(7 + \frac{k^2}{k_J^2})}\right)}, \quad \text{(B.62)}$$

decays for any $0 \leq \frac{k}{k_J}$. The velocity divergence filtering function at the 3rd-order is

$$h_3(\mathbf{k}) = \frac{1}{\theta_{3,c}(\mathbf{k})}\left[A_3(\mathbf{k}) - 3\delta_{3,c}(\mathbf{k})g_3(\mathbf{k})\right], \quad \text{(B.63)}$$

where we have ignored the decaying term.

Let us rewrite $7A_3(\mathbf{k}) - 2B_3(\mathbf{k})$ in Eq. [B.61] as

$$
\begin{aligned}
&7A_3(\mathbf{k}) - 2B_3(\mathbf{k})\\
&= \frac{1}{(2\pi)^6}\int\!\!\int\!\!\int d\mathbf{q}_1 d\mathbf{q}_2 d\mathbf{q}_3 \delta_D(\mathbf{q}_1+\mathbf{q}_2+\mathbf{q}_3-\mathbf{k})\delta_{1,c}(\mathbf{q}_1)\delta_{1,c}(\mathbf{q}_2)\delta_{1,c}(\mathbf{q}_3)\\
&\times\left[\frac{7\mathbf{k}\cdot\mathbf{q}_1}{q_1^2}g_1(\mathbf{q}_1)g_2(\mathbf{q}_{23})F_2^{(s)}(\mathbf{q}_2,\mathbf{q}_3) + \frac{7\mathbf{k}\cdot\mathbf{q}_{12}}{q_{12}^2}h_2(\mathbf{q}_{12})g_1(\mathbf{q}_3)G_2^{(s)}(\mathbf{q}_1,\mathbf{q}_2)\right.\\
&+\frac{k^2(\mathbf{q}_1\cdot\mathbf{q}_{23})}{q_1^2 q_{23}^2}g_1(\mathbf{q}_1)h_2(\mathbf{q}_{23})G_2^{(s)}(\mathbf{q}_2,\mathbf{q}_3)\\
&+\frac{k^2(\mathbf{q}_{12}\cdot\mathbf{q}_3)}{q_{12}^2 q_3^2}h_2(\mathbf{q}_{12})g_1(\mathbf{q}_3)G_2^{(s)}(\mathbf{q}_1,\mathbf{q}_2)\\
&+\frac{3}{2}\frac{k^2}{k_J^2}g_1(\mathbf{q}_1)g_2(\mathbf{q}_{23})F_2^{(s)}(\mathbf{q}_2,\mathbf{q}_3) + \frac{3}{2}\frac{k^2}{k_J^2}g_2(\mathbf{q}_{12})g_1(\mathbf{q}_3)F_2^{(s)}(\mathbf{q}_1,\mathbf{q}_2)\\
&\left.-\frac{k^2}{k_J^2}g_1(\mathbf{q}_1)g_1(\mathbf{q}_2)g_1(\mathbf{q}_3)\right]\\
&\equiv \frac{18}{(2\pi)^6}\int\!\!\int\!\!\int d\mathbf{q}_1 d\mathbf{q}_2 d\mathbf{q}_3 \delta_D(\mathbf{q}_1+\mathbf{q}_2+\mathbf{q}_3-\mathbf{k})\\
&\times\mathcal{F}_3(\mathbf{q}_1,\mathbf{q}_2,\mathbf{q}_3)\delta_{1,c}(\mathbf{q}_1)\delta_{1,c}(\mathbf{q}_2)\delta_{1,c}(\mathbf{q}_3)\\
&\equiv 18\delta'_{3,c}(\mathbf{k}). \qquad\qquad \text{(B.64)}
\end{aligned}
$$

The new kernel, $\mathcal{F}_3(\mathbf{q}_1, \mathbf{q}_2, \mathbf{q}_3)$, can be symmetrized as

$$
\begin{aligned}
&\mathcal{F}_3^{(s)}(\mathbf{q}_1, \mathbf{q}_2, \mathbf{q}_3) \\
&= \frac{1}{6}\left[\mathcal{F}_3(\mathbf{q}_1, \mathbf{q}_2, \mathbf{q}_3) + \mathcal{F}_3(\mathbf{q}_1, \mathbf{q}_3, \mathbf{q}_2) + \mathcal{F}_3(\mathbf{q}_2, \mathbf{q}_1, \mathbf{q}_3)\right. \\
&\left.+\mathcal{F}_3(\mathbf{q}_2, \mathbf{q}_3, \mathbf{q}_1) + \mathcal{F}_3(\mathbf{q}_3, \mathbf{q}_1, \mathbf{q}_2) + \mathcal{F}_3(\mathbf{q}_3, \mathbf{q}_2, \mathbf{q}_1)\right] \\
&= \frac{7}{54}\mathbf{k}\cdot\left[F_2^{(s)}(\mathbf{q}_2, \mathbf{q}_3)\frac{\mathbf{q}_1}{q_1^2}g_1(\mathbf{q}_1)g_2(\mathbf{q}_{23}) + F_2^{(s)}(\mathbf{q}_1, \mathbf{q}_3)\frac{\mathbf{q}_2}{q_2^2}g_1(\mathbf{q}_2)g_2(\mathbf{q}_{13})\right. \\
&\left.+ F_2^{(s)}(\mathbf{q}_1, \mathbf{q}_2)\frac{\mathbf{q}_3}{q_3^2}g_1(\mathbf{q}_3)g_2(\mathbf{q}_{12})\right] \\
&+\frac{1}{27}k^2\left[G_2^{(s)}(\mathbf{q}_2, \mathbf{q}_3)\frac{\mathbf{q}_1\cdot\mathbf{q}_{23}}{q_1^2 q_{23}^2}g_1(\mathbf{q}_1)h_2(\mathbf{q}_{23})\right. \\
&+G_2^{(s)}(\mathbf{q}_1, \mathbf{q}_3)\frac{\mathbf{q}_2\cdot\mathbf{q}_{13}}{q_2^2 q_{13}^2}g_1(\mathbf{q}_2)h_2(\mathbf{q}_{13}) \\
&\left.+G_2^{(s)}(\mathbf{q}_1, \mathbf{q}_2)\frac{\mathbf{q}_3\cdot\mathbf{q}_{12}}{q_3^2 q_{12}^2}g_1(\mathbf{q}_3)h_2(\mathbf{q}_{12})\right] \\
&+\frac{7}{54}\mathbf{k}\cdot\left[G_2^{(s)}(\mathbf{q}_2, \mathbf{q}_3)\frac{\mathbf{q}_{23}}{q_{23}^2}g_1(\mathbf{q}_1)h_2(\mathbf{q}_{23}) + G_2^{(s)}(\mathbf{q}_1, \mathbf{q}_3)\frac{\mathbf{q}_{13}}{q_{13}^2}g_1(\mathbf{q}_2)h_2(\mathbf{q}_{13})\right. \\
&\left.+ G_2^{(s)}(\mathbf{q}_1, \mathbf{q}_2)\frac{\mathbf{q}_{12}}{q_{12}^2}g_1(\mathbf{q}_3)h_2(\mathbf{q}_{12})\right] \\
&+\frac{1}{18}\frac{k^2}{k_J^2}\left[g_1(\mathbf{q}_1)g_2(\mathbf{q}_{23})F_2^{(s)}(\mathbf{q}_2, \mathbf{q}_3) + g_1(\mathbf{q}_2)g_2(\mathbf{q}_{13})F_2^{(s)}(\mathbf{q}_1, \mathbf{q}_3)\right. \\
&\left.+g_1(\mathbf{q}_3)g_2(\mathbf{q}_{12})F_2^{(s)}(\mathbf{q}_1, \mathbf{q}_2) - g_1(\mathbf{q}_1)g_1(\mathbf{q}_2)g_1(\mathbf{q}_3)\right].
\end{aligned}
\tag{B.65}
$$

In the limit of $k_J \to \infty$, $\mathcal{F}_3 \to F_3$, and $g_3(k) = 1$. Using $\delta'_{3,c}(\mathbf{k})$ introduced above, we write g_3 as

$$
g_3(\mathbf{k}) = \frac{7 - 6\left[1 - \frac{\delta'_{3,c}(\mathbf{k})}{\delta_{3,c}(\mathbf{k})}\right]}{7 + \frac{k^2}{k_J^2}}. \tag{B.66}
$$

B.3 3PT Total Power Spectrum

We calculate the power spectrum of the total matter fluctuations, $\delta = f_c\delta_c + f_b\delta_b = f_c\delta_c + (1-f_c)\delta_b$, which is given, up to the third-order in perturbations, by

$$\begin{aligned}
&\delta(\mathbf{k},\tau) = f_c\delta_c(\mathbf{k},\tau) + f_b\delta_b(\mathbf{k},\tau)\\
&= f_c\left[\delta_{1,c}(\mathbf{k},\tau) + \delta_{2,c}(\mathbf{k},\tau) + \delta_{3,c}(\mathbf{k},\tau)\right]\\
&+(1-f_c)\left[\delta_{1,b}(\mathbf{k},\tau) + \delta_{2,b}(\mathbf{k},\tau) + \delta_{3,b}(\mathbf{k},\tau)\right]\\
&= f_c\left[\delta_{1,c}(\mathbf{k},\tau) + \delta_{2,c}(\mathbf{k},\tau) + \delta_{3,c}(\mathbf{k},\tau)\right]\\
&+(1-f_c)\left[g_1(k)\delta_{1,c}(\mathbf{k},\tau) + g_2(\mathbf{k})\delta_{2,c}(\mathbf{k},\tau) + g_3(\mathbf{k})\delta_{3,c}(\mathbf{k},\tau)\right].
\end{aligned} \tag{B.67}$$

The power spectrum is

$$\begin{aligned}
&(2\pi)^3 P_{tot}(k)\delta_D(\mathbf{k}+\mathbf{k}') = \langle\delta(\mathbf{k})\delta(\mathbf{k}')\rangle\\
&= \langle\{f_c\delta_c(\mathbf{k}) + (1-f_c)\delta_b(\mathbf{k})\}\{f_c\delta_c(\mathbf{k}') + (1-f_c)\delta_b(\mathbf{k}')\}\rangle\\
&= f_c^2\langle\delta_c(\mathbf{k})\delta_c(\mathbf{k}')\rangle + 2f_c(1-f_c)\langle\delta_b(\mathbf{k})\delta_c(\mathbf{k}')\rangle + (1-f_c)^2\langle\delta_b(\mathbf{k})\delta_b(\mathbf{k}')\rangle\\
&\equiv (2\pi)^3\left[f_c^2P_c(k) + 2f_c(1-f_c)P_{b,c}(k) + (1-f_c)^2P_b(k)\right]\delta_D(\mathbf{k}+\mathbf{k}'),
\end{aligned} \tag{B.68}$$

where P_c, $P_{b,c}$ and P_b are

$$(2\pi)^3 P_c(k)\delta_D(\mathbf{k}+\mathbf{k}') = \langle\delta_c(\mathbf{k})\delta_c(\mathbf{k}')\rangle$$

$$= \langle\{\delta_{1,c}(\mathbf{k})+\delta_{2,c}(\mathbf{k})+\delta_{3,c}(\mathbf{k})\}\{\delta_{1,c}(\mathbf{k}')+\delta_{2,c}(\mathbf{k}')+\delta_{3,c}(\mathbf{k}')\}\rangle$$

$$= \langle\delta_{1,c}(\mathbf{k})\delta_{1,c}(\mathbf{k}')\rangle + 2\langle\delta_{1,c}(\mathbf{k})\delta_{3,c}(\mathbf{k}')\rangle + \langle\delta_{2,c}(\mathbf{k})\delta_{2,c}(\mathbf{k}')\rangle$$

$$\equiv (2\pi)^3\left[P_{11,c}(k) + 2P_{13,c}(k) + P_{22,c}(k)\right]\delta_D(\mathbf{k}+\mathbf{k}'), \tag{B.69}$$

$$(2\pi)^3 P_{bc}(k)\delta_D(\mathbf{k}+\mathbf{k}') = \langle\delta_b(\mathbf{k})\delta_c(\mathbf{k}')\rangle$$

$$= \langle\{g_1(k)\delta_{1,c}(\mathbf{k})+g_2(\mathbf{k})\delta_{2,c}(\mathbf{k})+g_3(\mathbf{k})\delta_{3,c}(\mathbf{k})\}$$

$$\times\{\delta_{1,c}(\mathbf{k}')+\delta_{2,c}(\mathbf{k}')+\delta_{3,c}(\mathbf{k}')\}\rangle$$

$$= g_1(k)\langle\delta_{1,c}(\mathbf{k})\delta_{1,c}(\mathbf{k}')\rangle + g_1(k)\langle\delta_{1,c}(\mathbf{k})\delta_{3,c}(\mathbf{k}')\rangle$$

$$+\langle g_3(\mathbf{k})\delta_{3,c}(\mathbf{k})\delta_{1,c}(\mathbf{k}')\rangle + \langle g_2(\mathbf{k})\delta_{2,c}(\mathbf{k})\delta_{2,c}(\mathbf{k}')\rangle$$

$$\equiv (2\pi)^3\left[P_{11,bc}(k) + 2P_{13,bc}(k) + P_{22,bc}(k)\right]\delta_D(\mathbf{k}+\mathbf{k}'), \tag{B.70}$$

$$(2\pi)^3 P_b(k)\delta_D(\mathbf{k}+\mathbf{k}') = \langle\delta_b(\mathbf{k})\delta_b(\mathbf{k}')\rangle$$

$$= \langle\{g_1(k)\delta_{1,c}(\mathbf{k})+g_2(\mathbf{k})\delta_{2,c}(\mathbf{k})+g_3(\mathbf{k})\delta_{3,c}(\mathbf{k})\}$$

$$\times\{g_1(k')\delta_{1,c}(\mathbf{k}')+g_2(\mathbf{k}')\delta_{2,c}(\mathbf{k}')+g_3(\mathbf{k}')\delta_{3,c}(\mathbf{k}')\}\rangle$$

$$= g_1^2(k)\langle\delta_{1,c}(\mathbf{k})\delta_{1,c}(\mathbf{k}')\rangle + 2g_1(k)\langle\delta_{1,c}(\mathbf{k})g_3(\mathbf{k}')\delta_{3,c}(\mathbf{k}')\rangle$$

$$+\langle g_2(\mathbf{k})\delta_{2,c}(\mathbf{k})g_2(\mathbf{k}')\delta_{2,c}(\mathbf{k}')\rangle$$

$$\equiv (2\pi)^3\left[P_{11,b}(k) + 2P_{13,b}(k) + P_{22,b}(k)\right]\delta_D(\mathbf{k}+\mathbf{k}'), \tag{B.71}$$

respectively.

Now, $P_{11,c}(k)$, $P_{13,c}(k)$ and $P_{22,c}(k)$ can be numerically calculated with the corresponding kernels, $F_2^{(s)}$ and $F_3^{(s)}$;

$$(2\pi)^3 P_{11,bc}(k)\delta_D(\mathbf{k}+\mathbf{k}') = \langle \delta_{1,b}(\mathbf{k})\delta_{1,c}(\mathbf{k}')\rangle$$

$$= g_1(k)\langle \delta_{1,c}(\mathbf{k})\delta_{1,c}(\mathbf{k}')\rangle, \tag{B.72}$$

$$(2\pi)^3 P_{13,bc}(k)\delta_D(\mathbf{k}+\mathbf{k}') = \frac{1}{2}\left[\langle \delta_{1,b}(\mathbf{k})\delta_{3,c}(\mathbf{k}')\rangle + \langle \delta_{1,c}(\mathbf{k})\delta_{3,b}(\mathbf{k}')\rangle\right]$$

$$= \frac{1}{2}\left[g_1(k)\langle \delta_{1,c}(\mathbf{k})\delta_{3,c}(\mathbf{k}')\rangle + \langle \delta_{1,c}(\mathbf{k})g_3(\mathbf{k}')\delta_{3,c}(\mathbf{k}')\rangle\right]$$

$$= \frac{1}{2}\left[\left(g_1(k) + \frac{1}{7+\frac{k^2}{k_J^2}}\right)\langle \delta_{1,c}(\mathbf{k})\delta_{3,c}(\mathbf{k}')\rangle + \frac{6}{7+\frac{k^2}{k_J^2}}\langle \delta_{1,c}(\mathbf{k})\delta'_{3,c}(\mathbf{k}')\rangle\right], \tag{B.73}$$

$$(2\pi)^3 P_{22,bc}(k)\delta_D(\mathbf{k}+\mathbf{k}') = \langle \delta_{2,b}(\mathbf{k})\delta_{2,c}(\mathbf{k}')\rangle$$

$$= \langle g_2(\mathbf{k})\delta_{2,c}(\mathbf{k})\delta_{2,c}(\mathbf{k}')\rangle$$

$$= \frac{1}{\frac{10}{3}+\frac{k^2}{k_J^2}}\left[\langle \delta_{2,c}(\mathbf{k})\delta_{2,c}(\mathbf{k}')\rangle + \frac{7}{3}\langle \delta'_{2,c}(\mathbf{k})\delta_{2,c}(\mathbf{k}')\rangle\right], \tag{B.74}$$

$$(2\pi)^3 P_{11,b}(k)\delta_D(\mathbf{k}+\mathbf{k}') = \langle \delta_{1,b}(\mathbf{k})\delta_{1,b}(\mathbf{k}')\rangle$$

$$= g_1^2(k)\langle \delta_{1,c}(\mathbf{k})\delta_{1,c}(\mathbf{k}')\rangle, \tag{B.75}$$

$$(2\pi)^3 P_{13,b}(k)\delta_D(\mathbf{k}+\mathbf{k}') = \langle \delta_{1,b}(\mathbf{k})\delta_{3,b}(\mathbf{k}')\rangle$$

$$= g_1(k)\langle \delta_{1,c}(\mathbf{k})g_3(\mathbf{k}')\delta_{3,c}(\mathbf{k}')\rangle$$

$$= \frac{g_1(k)}{7+\frac{k^2}{k_J^2}}\left[\langle \delta_{1,c}(\mathbf{k})\delta_{3,c}(\mathbf{k}')\rangle + 6\langle \delta_{1,c}(\mathbf{k})\delta'_{3,c}(\mathbf{k}')\rangle\right], \tag{B.76}$$

$$(2\pi)^3 P_{22,b}(k)\delta_D(\mathbf{k}+\mathbf{k}') = \langle \delta_{2,b}(\mathbf{k})\delta_{2,b}(\mathbf{k}')\rangle$$

$$= \langle g_2(\mathbf{k})\delta_{2,c}(\mathbf{k})g_2(\mathbf{k}')\delta_{2,c}(\mathbf{k}')\rangle$$

$$= \frac{1}{\left(\frac{10}{3}+\frac{k^2}{k_J^2}\right)^2}\left[\langle \delta_{2,c}(\mathbf{k})\delta_{2,c}(\mathbf{k}')\rangle + \frac{14}{3}\langle \delta_{2,c}(\mathbf{k})\delta'_{2,c}(\mathbf{k}')\rangle + \frac{49}{9}\langle \delta'_{2,c}(\mathbf{k})\delta'_{2,c}(\mathbf{k}')\rangle\right]. \tag{B.77}$$

The ensemble averages of the products involving $\delta'_{n,c}(\mathbf{k})$ are given by

$$\langle\delta_{1,c}(\mathbf{k})\delta'_{3,c}(\mathbf{k}')\rangle = 3\delta_D(\mathbf{k}+\mathbf{k}')P_{11,c}(k)\int d\mathbf{q}\mathcal{F}_3^{(s)}(\mathbf{q},-\mathbf{q},\mathbf{k})P_{11,c}(q)$$

$$= 6\pi\delta_D(\mathbf{k}+\mathbf{k}')P_{11,c}(k)\int_0^\infty dq\ q^2P_{11,c}(q)\int_{-1}^1 d\mu\mathcal{F}_3^{(s)}(\mathbf{q},-\mathbf{q},\mathbf{k}), \tag{B.78}$$

$$\langle\delta_{2,c}(\mathbf{k})\delta'_{2,c}(\mathbf{k}')\rangle = 2\delta_D(\mathbf{k}+\mathbf{k}')\int d\mathbf{q}P_{11,c}(q)P_{11,c}(|\mathbf{k}-\mathbf{q}|)$$

$$\times F_2^{(s)}(\mathbf{q},\mathbf{k}-\mathbf{q})\mathcal{F}_2^{(s)}(\mathbf{q},\mathbf{k}-\mathbf{q}), \tag{B.79}$$

$$\langle\delta'_{2,c}(\mathbf{k})\delta'_{2,c}(\mathbf{k}')\rangle = 2\delta_D(\mathbf{k}+\mathbf{k}')\int d\mathbf{q}P_{11,c}(q)P_{11,c}(|\mathbf{k}-\mathbf{q}|)\left[\mathcal{F}_2^{(s)}(\mathbf{q},\mathbf{k}-\mathbf{q})\right]^2. \tag{B.80}$$

Here, the term, $\int \frac{d\mathbf{q}}{(2\pi)^3}\mathcal{F}_3(\mathbf{q},-\mathbf{q},\mathbf{k})P_{11,c}(q)$, i n Eq. [B.78] is given by

$$
\begin{aligned}
&\int \frac{d\mathbf{q}}{(2\pi)^3}\mathcal{F}_3^{(s)}(\mathbf{q},-\mathbf{q},\mathbf{k})P_{11,c}(q) \\
&= \int \frac{d\mathbf{q}}{(2\pi)^3}\left\{\frac{7}{54}\mathbf{k}\cdot\left[F_2^{(s)}(-\mathbf{q},\mathbf{k})\frac{\mathbf{q}}{q^2}g_1(\mathbf{q})g_2(\mathbf{k}-\mathbf{q})\right.\right. \\
&\left. - F_2^{(s)}(\mathbf{q},\mathbf{k})\frac{\mathbf{q}}{q^2}g_1(\mathbf{q})g_2(\mathbf{k}+\mathbf{q})\right] \\
&+\frac{2}{27}k^2\left[F_2^{(s)}(-\mathbf{q},\mathbf{k})\frac{\mathbf{q}\cdot(\mathbf{k}-\mathbf{q})}{q^2(\mathbf{k}-\mathbf{q})^2}g_1(\mathbf{q})g_2(\mathbf{k}-\mathbf{q})\right. \\
&\left. - F_2^{(s)}(\mathbf{q},\mathbf{k})\frac{\mathbf{q}\cdot(\mathbf{k}+\mathbf{q})}{q^2(\mathbf{k}+\mathbf{q})^2}g_1(\mathbf{q})g_2(\mathbf{k}+\mathbf{q})\right] \\
&+\frac{14}{54}\mathbf{k}\cdot\left[F_2^{(s)}(-\mathbf{q},\mathbf{k})\frac{\mathbf{k}-\mathbf{q}}{(\mathbf{k}-\mathbf{q})^2}g_1(\mathbf{q})g_2(\mathbf{k}-\mathbf{q})\right. \\
&\left. +F_2^{(s)}(\mathbf{q},\mathbf{k})\frac{\mathbf{k}+\mathbf{q}}{(\mathbf{k}+\mathbf{q})^2}g_1(\mathbf{q})g_2(\mathbf{k}+\mathbf{q})\right] \\
&-\frac{1}{27}k^2\left[\left(1+\frac{(-\mathbf{q}\cdot\mathbf{k})(q^2+k^2)}{2q^2k^2}\right)\frac{\mathbf{q}\cdot(\mathbf{k}-\mathbf{q})}{q^2(\mathbf{k}-\mathbf{q})^2}g_1^2(\mathbf{q})g_1(\mathbf{k})\right. \\
&\left. -\left(1+\frac{(\mathbf{q}\cdot\mathbf{k})(q^2+k^2)}{2q^2k^2}\right)\frac{\mathbf{q}\cdot(\mathbf{k}+\mathbf{q})}{q^2(\mathbf{k}+\mathbf{q})^2}g_1^2(\mathbf{q})g_1(\mathbf{k})\right] \\
&-\frac{7}{54}\mathbf{k}\cdot\left[\left(1+\frac{(-\mathbf{q}\cdot\mathbf{k})(q^2+k^2)}{2q^2k^2}\right)\frac{\mathbf{k}-\mathbf{q}}{(\mathbf{k}-\mathbf{q})^2}g_1^2(\mathbf{q})g_1(\mathbf{k})\right. \\
&\left. +\left(1+\frac{(\mathbf{q}\cdot\mathbf{k})(q^2+k^2)}{2q^2k^2}\right)\frac{\mathbf{k}+\mathbf{q}}{(\mathbf{k}+\mathbf{q})^2}g_1^2(\mathbf{q})g_1(\mathbf{k})\right] \\
&+\frac{1}{18}\frac{k^2}{k_J^2}\left[g_1(\mathbf{q})g_2(\mathbf{k}-\mathbf{q})F_2^{(s)}(-\mathbf{q},\mathbf{k})\right. \\
&\left.\left. +\ g_1(\mathbf{q})g_2(\mathbf{k}+\mathbf{q})F_2^{(s)}(\mathbf{q},\mathbf{k})-g_1^2(\mathbf{q})g_1(\mathbf{k})\right]\right\}P_{11,c}(q), \qquad \text{(B.81)}
\end{aligned}
$$

where we have used Eq. [B.55] and $F_2^{(s)}(\mathbf{q},-\mathbf{q}) = G_2^{(s)}(\mathbf{q},-\mathbf{q}) = 0$. We then calculate the angular average of $\mathcal{F}_3^{(s)}$, i.e., $\int d\mu\mathcal{F}_3^{(s)}$, for the linear filtering function of $g_1(k) = 1/(1 + k^2/k_J^2)$:

$$
\begin{aligned}
&\int_{-1}^{1} d\mu \mathcal{F}_3^{(s)} = \frac{1}{612360 r^8 s (1+r^2)(r^2+s^2)^2} \llbracket 30 r^2 s^3 [-14000 s^6 \\
&+ 810 r^{10}(1+s^2) + 900 r^2 s^4(-7+5s^2) + 60 r^4 s^2 (105 - 125 s^2 + 78 s^4) \\
&+ 9 r^8 (321 - 248 s^2 + 159 s^4) + 27 r^6 (126 - 87 s^2 + 70 s^4 + 9 s^6)] \\
&- 243 r^8 (-7 + 5s^2 + 2s^4)[5(r^4+s^2)(-1+s^2)^2 + r^2(5 - 5s^2 - 19 s^4 + 5 s^6)] \\
&\times \ln \frac{1+s}{|1-s|} \\
&+ [10 s^2 + 3 r^2 (1+s^2)][-35 s^2 + 3r^2(-7+s^2)][-2000 s^6 + 135 r^8 (-1+s^2)^2 \\
&+ 240 r^4 s^2 (3 - 4s^2 + 3s^4) + 300 r^2 (s^4 + s^6) + 27 r^6 (5 + 5s^2 - 9s^4 + 5s^6)] \\
&\times \frac{1}{2} \ln \left[\frac{10 s^2 + 3 r^2 (1+s)^2}{10 s^2 + 3 r^2 (1-s)^2} \right] \rrbracket ,
\end{aligned}
\tag{B.82}
$$

where $r \equiv k/k_J$ and $s \equiv k/q$. We find that the calculation of $\mathcal{F}_3$ is numerically unstable as $k/k_J \to 0$ ($r \to 0$). The exact limit of $\mathcal{F}_3$ is $\lim_{k/k_J \to 0} \mathcal{F}_3 \to F_3$, and thus one may replace $\mathcal{F}_3$ with F_3 for a sufficiently small value of k/k_J.

Finally, we generalize the above results from an EdS universe to general cosmological models, by writing

$$
\frac{a^2(\tau)}{a^2(\tau_i)} P_{11}(k, \tau_i) \to P_{11}(k, \tau) = \frac{D^2(\tau)}{D^2(\tau_i)} \left(\frac{\delta_{1,c+}^{(1)}(k,\tau)/\delta_{1,c+}^{(0)}(k,\tau)}{\delta_{1,c+}^{(1)}(k,\tau_*)/\delta_{1,c+}^{(0)}(k,\tau_*)} \right)^2 P_{11}(k, \tau_i),
\tag{B.83}
$$

where τ_i is some arbitrary epoch, τ_* is the epoch where the pressure effect becomes non-negligible (i.e., reionization epoch for baryons and non-relativistic transition for massive neutrinos), and $D(\tau)$ is the linear growth factor appropriate to a given cosmological model. We obtain Eq. [3.58] from combining Eqs. [B.74], [B.79], and $P_{22,c}$ given by Eq. [B.34]. Similarly, we obtain

Eq. [3.59] from combining Eqs. [B.77], [B.80], and $P_{22,c}$, Eq. [3.60] from combining Eqs. [B.73], [B.78], and $P_{13,c}$ given by Eq. [B.36], and Eq. [3.61] from combining Eqs. [B.76], [B.78], and $P_{13,c}$.

Figure B.3 shows the dimensionless 3PT and linear power spectra, $\Delta^2(k) = k^3 P(k)/(2\pi^2)$, for a matter component with pressure at different redshifts ($z = 0.1$, 1.0, 3.0, 5.0, 10 and 30) with $k_J = 1.0$ and 3.0 h Mpc^{-1}. The 3PT and linear power spectra are similar at the highest redshift, whereas the 3PT has significantly more power than the linear spectrum at larger wavenumbers as we go to lower redshifts. As a result, the filtering scale for a given linear filtering scale migrates toward larger wavenumbers in lower redshifts.

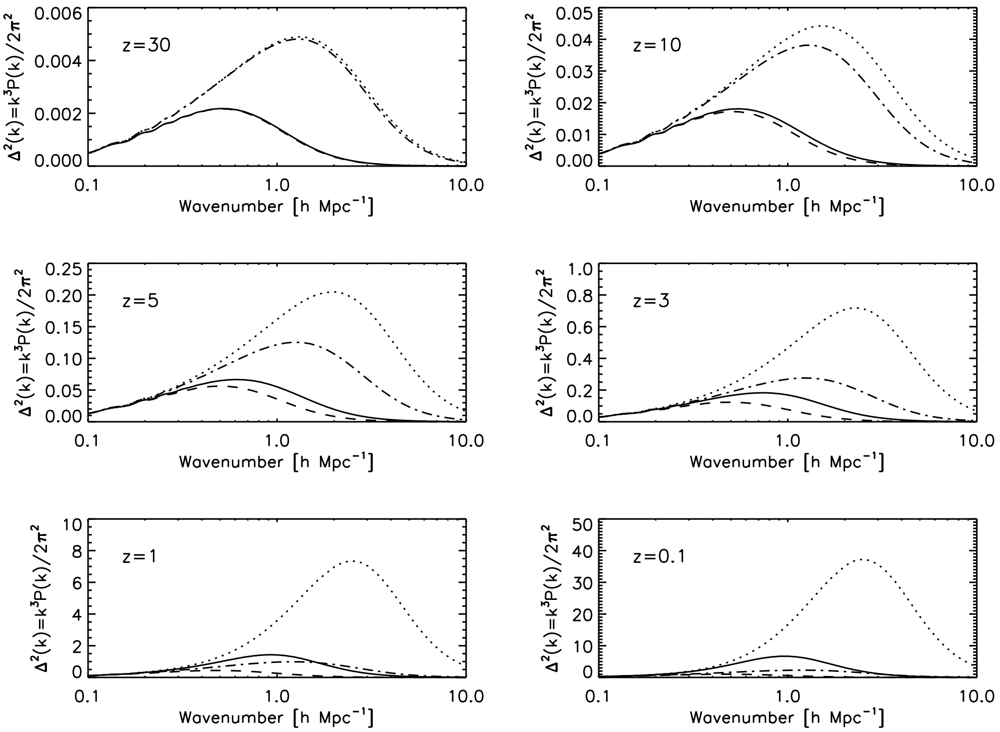

Figure B.1: The dimensionless power spectra, $\Delta^2(k) \equiv k^3P(k)/(2\pi^2)$, for a matter component with pressure (i.e., baryon, neutrino, etc) are shown for several redshifts ($z = 0.1$, 1.0, 3.0, 5.0, 10 and 30). We show the non-linear calculations with 3PT in the solid and dotted lines for $k_J = 1.0$ and 3.0 h Mpc^{-1}, respectively. We also show the linear calculations in the dashed and dot-dashed lines for $k_J = 1.0$ and 3.0 h Mpc^{-1}, respectively.

Appendix C

Free-Streaming Neutrino

C.1 Sound speed versus Velocity Dispersion

The wavenumber corresponding to the free-streaming scale, $k_{\rm FS}$, is defined by the single-fluid continuity and Euler equations:

$$\dot{\delta}(\mathbf{k},\tau) + \theta(\mathbf{k},\tau) = 0 \tag{C.1}$$

$$\dot{\theta}(\mathbf{k},\tau) + \mathcal{H}(\tau)\theta(\mathbf{k},\tau) + c_{\rm s}^2(\tau)\left[k_{\rm FS}^2(\tau) - k^2(\tau)\right]\delta(\mathbf{k},\tau) = 0, \tag{C.2}$$

where

$$k_{\rm FS}(\tau) \equiv \sqrt{\frac{3}{2}}\frac{\mathcal{H}(\tau)}{c_{\rm s}(\tau)}, \tag{C.3}$$

is the scale that divides the characteristics of the solution, $\delta(\mathbf{k},\tau)$. For $k < k_{\rm FS}$, $\delta(\mathbf{k},\tau)$ grows, while for $k > k_{\rm FS}$, $\delta(\mathbf{k},\tau)$ oscillates.

In the literature, however, the sound speed, $c_{\rm s}(\tau)$, has often been replaced, or crudely approximated, by the velocity dispersion, σ_ν, such that $c_{\rm s} \simeq \sigma_{\nu,\rm i}$ without any justification. Strictly speaking, the velocity dispersion should not be used to define the free-streaming scale, $k_{\rm FS}$, as the Euler equation contains sound horizon, $c_{\rm s}^2 \equiv \frac{\delta P}{\delta\rho}$, not the velocity dispersion. In this Appendix, we shall clarify this issue.

The sound speed is given by

$$c_s^2(k,\tau) \equiv \frac{\delta P(k,\tau)}{\delta\rho(k,\tau)} = \frac{1}{3}\frac{\int q^2 dq \frac{q^2}{\epsilon(q,\tau)} f_0(q)\Psi_0(k,q,\tau)}{\int q^2 dq \epsilon(q,\tau) f_0(q)\Psi_0(k,q,\tau)}, \tag{C.4}$$

and the velocity dispersion is given by

$$\sigma_\nu^2(\tau) \equiv \frac{\int q^2 dq \left[\frac{q}{\epsilon(q,\tau)}\right]^2 f_0(q)}{\int q^2 dq f_0(q)}. \tag{C.5}$$

Note that the sound speed can depend on k in general, while velocity dispersion is, by definition, independent of k.

As we see from Eq.(4.46), in the non-relativistic limit, where the phase-space distribution of the particles is dominated by non-relativistic particles ($q \ll a(x)m$), the k dependence of $\Psi_0(k,q,\tau) \equiv \tilde{\Psi}_0(k,\tau)\frac{d\ln f_0(q)}{d\ln q}$ will be canceled both in the denominator and numerator of Eq.(C.4). If perturbations are adiabatic, i.e., $\frac{\delta P}{\delta\rho} = \frac{\dot{\bar{P}}(\tau)}{\dot{\bar{\rho}}(\tau)}$, we have

$$c_s^2(\tau) = \frac{\dot{\bar{P}}(\tau)}{\dot{\bar{\rho}}(\tau)} = w(\tau) - \frac{\dot{w}(\tau)}{3\mathcal{H}(\tau)[1+w(\tau)]}, \tag{C.6}$$

where $w(\tau) \equiv \frac{\bar{P}(\tau)}{\bar{\rho}(\tau)}$ is an equation of state. Since the velocity dispersion *in the non-relativistic* limit is given as

$$\sigma_\nu^2(\tau) \to \frac{1}{a^2(\tau)m^2}\frac{\int q^2 dq\ q^2 f_0(q)\Psi_0(k,q,\tau)}{\int q^2 dq f_0(q)\Psi_0(k,q,\tau)} = 3w(\tau), \tag{C.7}$$

we have

$$c_s^2(\tau) \to \frac{1}{3}\sigma_\nu^2(\tau) + \frac{2}{9}\frac{\sigma_\nu^2(\tau)}{1+\frac{1}{3}\sigma_\nu^2(\tau)} \simeq \frac{5}{9}\sigma_\nu^2(\tau). \tag{C.8}$$

Here, we have used $\sigma_\nu^2(\tau) \ll 1$. Therefore, in the non-relativistic limit, we have $c_s = \frac{\sqrt{5}}{3}\sigma_{\nu,\mathrm{i}} \simeq 0.745\sigma_{\nu,\mathrm{i}}$.

C.2 Exact Analytic Solution of $\tilde{\Psi}_l(k, q, x)$

We derive the analytic solutions of the Boltzmann equation. We start from Eq.(4.16),

$$\frac{\partial \tilde{\Psi}(k, q, \mu, x)}{\partial x} + i\frac{q}{\epsilon(q, x)}\mu\tilde{\Psi}(k, q, \mu, x) = S(k, q, \mu, x), \tag{C.9}$$

where

$$S(k, q, \mu, x) \equiv i\frac{\epsilon(q, x)}{q}\mu\psi(k, x) - \frac{\partial \phi(k, x)}{\partial x}. \tag{C.10}$$

The solution of the first order linear differential equation with the source term $S(k, q, \mu, x)$ is

$$\begin{aligned}
&\tilde{\Psi}(k, q, \mu, x) \\
&= \tilde{\Psi}(k, q, \mu, x_i) \exp\left[-i\mu \int_{x_i}^{x} \frac{q}{\epsilon(q, x)} dx'\right] + \exp\left[-i\mu \int_{x_i}^{x} \frac{q}{\epsilon(q, x')} dx'\right] \\
&\times \int_{x_i}^{x} dx' \exp\left[i\mu \int_{x_i}^{x'} \frac{q}{\epsilon(q, x'')} dx''\right] S(k, q, \mu, x') \\
&= \tilde{\Psi}(k, q, \mu, x_i) e^{-i\mu[z(x) - z(x_i)]} + \int_{x_i}^{x} dx' e^{-i\mu[z(x) - z(x')]} S(k, q, \mu, x'),
\end{aligned} \tag{C.11}$$

where we define

$$z(x) \equiv \int_{C}^{x} \frac{q}{\epsilon(q, x')} dx', \tag{C.12}$$

for arbitrary constant, $C \in \Re$.

C.2.1 massless case with constant ϕ and ψ

For massless neutrinos, $\epsilon(q, x) = q$, with constant gravitational potential, $\dot{\phi} = \dot{\psi} = 0$, we can avoid the complexity in the time dependent source term, $S(q,x)$, and the form of Eq.(C.11) is simplified to

$$\begin{aligned}\tilde{\Psi}(k,q,\mu,x) &= \tilde{\Psi}(k,q,\mu,x_i)e^{-i\mu(x-x_i)} + i\mu\psi(k)\int_{x_i}^{x} dx' e^{-i\mu(x-x')} \\ &= \left[\tilde{\Psi}(k,q,\mu,x_i) - \psi(k)\right] e^{-i\mu(x-x_i)} + \psi(k). \qquad \text{(C.13)}\end{aligned}$$

Now, we expand Eq.(C.13) by Legendre polynomials, using the following identities and orthogonality condition,

$$\tilde{\Psi}(k,q,\mu,x) = \sum_l (-i)^l(2l+1)\tilde{\Psi}_l(k,q,x)P_l(\mu), \qquad \text{(C.14)}$$

$$e^{-i\mu(x-x')} = \sum_l (-i)^l(2l+1)j_l(x-x')P_l(\mu), \qquad \text{(C.15)}$$

$$\int_{-1}^{1} d\mu P_l(\mu)P_{l'}(\mu) = \frac{2}{2l+1}\delta_{ll'}. \qquad \text{(C.16)}$$

We find

$$\begin{aligned}&\sum_{l'}(-i)^{l'}(2l'+1)\tilde{\Psi}_{l'}(k,q,x)P_{l'}(\mu) \\ &= \sum_{l'}\sum_{l''}(-i)^{l'+l''}(2l'+1)(2l''+1)\tilde{\Psi}_{l'}(k,q,x_i)j_{l''}(x-x_i)P_{l'}(\mu)P_{l''}(\mu) \\ &+\psi(k)\left[1-\sum_{l'}(-i)^{l'}(2l'+1)j_{l'}(x-x_i)P_{l'}(\mu)\right]. \qquad \text{(C.17)}\end{aligned}$$

Multiplying the both sides by $P_l(\mu)$ and integrating over μ, we find,

$$\begin{aligned}&\sum_{l}(-i)^{l}\tilde{\Psi}_{l}(k,q,x) \\ &= \sum_{l'}\sum_{l''}(-i)^{l'+l''}(2l'+1)(2l''+1)\tilde{\Psi}_{l'}(k,q,x_i)j_{l''}(x-x_i)\begin{pmatrix} l & l' & l'' \\ 0 & 0 & 0\end{pmatrix}^2 \\ &+\psi(k)\left[\delta_{l0}-\sum_{l}(-i)^{l}j_{l}(x-x_i)\right], \qquad \text{(C.18)}\end{aligned}$$

where we have used the Wigner 3-j symbols to write

$$\int_{-1}^{1} \frac{d\mu}{2} P_l(\mu) P_{l'}(\mu) P_{l''}(\mu) = \begin{pmatrix} l & l' & l'' \\ 0 & 0 & 0 \end{pmatrix}^2 . \tag{C.19}$$

Therefore, for a given l, we have

$$\begin{aligned} \tilde{\Psi}_l(k,q,x) &= \sum_{l'} \sum_{l''} (-i)^{l'+l''-l} (2l'+1)(2l''+1) \tilde{\Psi}_{l'}(k,q,x_i) j_{l''}(x-x_i) \\ &\times \begin{pmatrix} l & l' & l'' \\ 0 & 0 & 0 \end{pmatrix}^2 + \psi(k) \left[\delta_{l0} - j_l(x-x_i) \right] . \end{aligned} \tag{C.20}$$

Here, non-zero Wigner 3-j symbols must satisfy the triangular inequalities such that

$$|l - l'| \leq l'' \leq l + l', \tag{C.21}$$

and from the initial conditions, we have $\tilde{\Psi}_{l' \geq 3}(x_i) = 0$.

The exact solutions for $l = 0$ and 1 are

$$\begin{aligned} \tilde{\Psi}_0(k,q,x) &= \tilde{\Psi}_0(k,q,x_i) j_0(x-x_i) - 3\tilde{\Psi}_1(k,q,x_i) j_1(x-x_i) \\ &+ 5\tilde{\Psi}_2(k,q,x_i) j_2(x-x_i) + \psi(k) \left[1 - j_0(x-x_i) \right] , \end{aligned} \tag{C.22}$$

$$\begin{aligned} \tilde{\Psi}_1(k,q,x) &= \tilde{\Psi}_0(k,q,x_i) j_1(x-x_i) + \tilde{\Psi}_1(k,q,x_i) j_0(x-x_i) \\ &- 2\tilde{\Psi}_2(k,q,x_i) j_1(x-x_i) - 2\tilde{\Psi}_1(k,q,x_i) j_2(x-x_i) \\ &+ 3\tilde{\Psi}_2(k,q,x_i) j_3(x-x_i) - \psi(k) j_1(x-x_i). \end{aligned} \tag{C.23}$$

C.2.2 massive case with constant ϕ and ψ

For massive neutrinos, $\epsilon(q,x)\neq q$, with constant gravitational potential, $\dot{\phi}=\dot{\psi}=0$, we have

$$\begin{aligned}&\sum_{l'}(-i)^{l'}(2l'+1)\tilde{\Psi}_{l'}(k,q,x)P_{l'}(\mu)\\&=\sum_{l'}\sum_{l''}(-i)^{l'+l''}(2l'+1)(2l''+1)\tilde{\Psi}_{l'}(k,q,x_i)j_{l''}(z-z_i)P_{l'}(\mu)P_{l''}(\mu)\\&+i\psi(k)\mu\sum_{l'}(-i)^{l'}(2l'+1)P_{l'}(\mu)\int_{x_i}^{x}dx'\frac{\epsilon(x')}{q}j_{l'}(z-z'),\end{aligned}\qquad\text{(C.24)}$$

where we have used Eqs.(C.14)∼(C.16) and $z-z'=z(x)-z(x')\equiv\int_{x'}^{x}dx'\frac{q}{\epsilon(q,x')}$ as defined in Eq.(C.12).

Multiplying the both sides by $P_l(\mu)$ and integrating over μ, we find

$$\begin{aligned}&\sum_{l}(-i)^{l}\tilde{\Psi}_{l}(k,q,x)\\&=\sum_{l'}\sum_{l''}(-i)^{l'+l''}(2l'+1)(2l''+1)\tilde{\Psi}_{l'}(k,q,x_i)j_{l''}(z-z_i)\begin{pmatrix}l&l'&l''\\0&0&0\end{pmatrix}^2\\&-\psi(k)\sum_{l}(-i)^{l}\int_{x_i}^{x}dx'\frac{\epsilon(q,x')}{q}\left[\frac{l}{2l+1}j_{l-1}(z-z')-\frac{l+1}{2l+1}j_{l+1}(z-z')\right].\end{aligned}\qquad\text{(C.25)}$$

Therefore, for a given l, we have

$$\begin{aligned}&\tilde{\Psi}_{l}(k,q,x)\\&=\sum_{l'}\sum_{l''}(-i)^{l'+l''-l}(2l'+1)(2l''+1)\tilde{\Psi}_{l'}(k,q,x_i)j_{l''}(z-z_i)\begin{pmatrix}l&l'&l''\\0&0&0\end{pmatrix}^2\\&-\psi(k)\int_{x_i}^{x}dx'\frac{\epsilon(q,x')}{q}\left[\frac{l}{2l+1}j_{l-1}(z-z')-\frac{l+1}{2l+1}j_{l+1}(z-z')\right].\end{aligned}\qquad\text{(C.26)}$$

The exact solutions for $l = 0$ and 1 are

$$\begin{aligned}
&\tilde{\Psi}_0(k,q,x) = \tilde{\Psi}_0(k,q,x_i)j_0(z-z_i) - 3\tilde{\Psi}_1(k,q,x_i)j_1(z-z_i) \\
&+5\tilde{\Psi}_2(k,q,x_i)j_2(z-z_i) + \psi(k)\int_{x_i}^{x} dx' \frac{\epsilon(q,x')}{q} j_1(z-z'), \qquad \text{(C.27)} \\
&\tilde{\Psi}_1(k,q,x) = \tilde{\Psi}_0(k,q,x_i)j_1(z-z_i) + \tilde{\Psi}_1(k,q,x_i)j_0(z-z_i) \\
&-2\tilde{\Psi}_2(k,q,x_i)j_1(z-z_i) - 2\tilde{\Psi}_1(k,q,x_i)j_2(z-z_i) + 3\tilde{\Psi}_2(k,q,x_i)j_3(z-z_i) \\
&-\psi(k)\int_{x_i}^{x} dx' \frac{\epsilon(q,x')}{q}\left[\frac{1}{3}j_0(z-z') - \frac{2}{3}j_2(z-z')\right]. \qquad \text{(C.28)}
\end{aligned}$$

C.2.3 general case

For more general cases, where neutrinos are either massless or massive, and $\dot{\phi} \neq 0$ and $\dot{\psi} \neq 0$. In this case, we use the full expression of the source term, $S(k,q,\mu,x) \equiv i\frac{\epsilon(q,x)}{q}\mu\psi(k,x) - \frac{\partial\phi(k,x)}{\partial x}$.

Again, we expand Eq.(C.11) with the series of Legendre polynomials with the time dependent source term, and find

$$\begin{aligned}
&\sum_{l'}(-i)^{l'}(2l'+1)\tilde{\Psi}_{l'}(k,q,x)P_{l'}(\mu) \\
&= \sum_{l'}\sum_{l''}(-i)^{l'+l''}(2l'+1)(2l''+1)\tilde{\Psi}_{l'}(k,q,x_i)j_{l''}(z-z_i)P_{l'}(\mu)P_{l''}(\mu) \\
&+i\mu\sum_{l'}(-i)^{l'}(2l'+1)P_{l'}(\mu)\int_{x_i}^{x} dx' \frac{\epsilon(x')}{q}\psi(k,x')j_{l'}(z-z') \\
&-\sum_{l'}(-i)^{l'}(2l'+1)P_{l'}(\mu)\int_{x_i}^{x} dx' \frac{\partial\phi(k,x')}{\partial x'} j_{l'}(z-z'). \qquad \text{(C.29)}
\end{aligned}$$

Multiplying the both sides by $P_l(\mu)$ and integrating over μ, we find

$$\begin{aligned}
&\sum_l (-i)^l \tilde{\Psi}_l(k,q,x) \\
&= \sum_{l'} \sum_{l''} (-i)^{l'+l''} (2l'+1)(2l''+1) \tilde{\Psi}_{l'}(k,q,x_i) j_{l''}(z-z_i) \begin{pmatrix} l & l' & l'' \\ 0 & 0 & 0 \end{pmatrix}^2 \\
&- \sum_l (-i)^l \int_{x_i}^{x} dx' \frac{\epsilon(q,x')}{q} \psi(k,x') \left[\frac{l}{2l+1} j_{l-1}(z-z') - \frac{l+1}{2l+1} j_{l+1}(z-z') \right] \\
&- \sum_l (-i)^l \int_{x_i}^{x} dx' \frac{\partial \phi(k,x')}{\partial x'} j_l(z-z'). \qquad \text{(C.30)}
\end{aligned}$$

With the recursion relation,

$$\frac{d}{dx} j_l(x) = \frac{l}{2l+1} j_{l-1}(x) - \frac{l+1}{2l+1} j_{l+1}(x), \qquad \text{(C.31)}$$

we have

$$\begin{aligned}
&\tilde{\Psi}_l(k,q,x) \\
&= \sum_{l'} \sum_{l''} (-i)^{l'+l''-l} (2l'+1)(2l''+1) \tilde{\Psi}_{l'}(k,q,x_i) j_{l''}(z-z_i) \begin{pmatrix} l & l' & l'' \\ 0 & 0 & 0 \end{pmatrix}^2 \\
&- \int_{x_i}^{x} dx' \left[\frac{\epsilon(q,x')}{q} \psi(k,x') - \frac{q}{\epsilon(q,x')} \phi(k,x') \right] \\
&\times \left[\frac{l}{2l+1} j_{l-1}(z-z') - \frac{l+1}{2l+1} j_{l+1}(z-z') \right] \\
&+ \phi(k,x_i) j_l(z-z_i) - \phi(k,x) \delta_{l0}, \qquad \text{(C.32)}
\end{aligned}$$

for a fixed l. We can easily recover the massless and massive case solutions Eq.(C.20) and (C.26) from Eq.(C.32) with approximations such as $\dot{\psi}(k,x) = \dot{\phi}(k,x) = 0$ and/or $\epsilon(q,x) = q$.

Appendix D

HETDEX: Combined Mass of Neutrinos

In order to measure (or place a firm upper limit) on the combined mass of neutrinos, we need to measure power spectrum on small scales accurately enough, including non-linear corrections, in order to constrain suppression of growth of structure due to the free-streaming massive neutrinos. The suppression of a linear matter power spectrum due to massive neutrinos at small scale is roughly given as:

$$\frac{P^L_{m,f_\nu\neq 0}(k)}{P^L_{m,f_\nu=0}(k)} \sim 1 - 8f_\nu, \tag{D.1}$$

where $P^L_{m,f_\nu\neq 0}(k)$ and $P^L_{m,f_\nu=0}(k)$ are linear matter power spectra with and without massive neutrinos respectively, and f_ν is a fraction of the massive neutrino energy density today to the matter energy density today, $f_\nu \equiv \Omega_\nu/\Omega_m$ (Lesgourgues & Pastor, 2006). Figure D.1 shows the suppression of the linear matter power spectra due to massive neutrinos ranging from few % to 40%. With the nominal accuracy of HETDEX in constraining the amplitude of a power spectrum, we will measure (or at least place a firm upper limit) on the combined mass of neutrinos.

With the nominal HETDEX survey parameters with three redshift bins (see table D.1) combined with the Planck prior, we measure the total mass of neutrinos to the accuracy of $\sigma_{\Sigma m_\nu} = 0.041$ and 0.052 eV assuming the total mass of neutrinos of $\Sigma m_{\nu,i} = 0.13$ eV and the number of massive neutrinos of $N_\nu = 1$ and 3 respectively (with $k_{\max} \sim 0.3\,\mathrm{hMpc}^{-1}$). With different assumption on the total mass of massive neutrinos, $\Sigma m_{\nu,i} = 0.64$ eV, we have $\sigma_{\Sigma m_\nu} = 0.046$ and 0.048 eV for $N_\nu = 1$ and 3 respectively. Those numbers are close to the current lower limit from experiments ($\Sigma m_{\nu,i} \sim 0.05$ eV), and therefore, HETDEX potentially makes a positive detection of the total mass of neutrinos depending on the actual total mass of neutrinos.

In figure D.2, we plot the marginalized 1-σ error of the total mass of neutrinos, $\sigma_{\Sigma m_\nu}$, as a function of the maximum wavenumber used for our parameter search, $k_{\max}$, with and without the hypothetical Planck prior on the total mass of neutrinos. The model parameters we consider are

$$p_\alpha = \{\Omega_m, \Omega_m h^2, \Omega_b h^2, f_\nu, n_s, \alpha_s, \delta_R, \tau, b_1(z)\}, \tag{D.2}$$

where $f_\nu \equiv \Omega_\nu/\Omega_m$ is the fraction of the massive neutrino, and related to the total mass of neutrinos such that

$$\Sigma m_\nu = 0.128 \left(\frac{f_\nu}{0.01}\right) \left(\frac{\Omega_m h^2}{0.136}\right) \text{ eV} \tag{D.3}$$

Note that the current survey specification of the HETDEX is shot-noise limited at small scale ($k \gtrsim 0.2\ \mathrm{hMp}^{-1}$), so that increasing $k_{\max}$ hardly adds any further information about the total mass of neutrinos. It is also worth mentioning that the effect of the non-linear clustering of neutrinos on the matter power spectrum is negligible as long as the total mass of neutrinos is less than the current upper limit drawn by WMAP5yr ($\Sigma m_\nu < 0.67$ eV) (Komatsu et al., 2009; Shoji & Komatsu, 2009). As a case study, we calculate the marginalized 1-σ error of the total mass of neutrinos for the future extended ground based survey, HETDEX-extension, which carries roughly ~ 10 times larger area and number of Ly-α emitters. At this level, together with the Planck prior we measure the total mass of neutrinos to the accuracy of $\sigma_{\Sigma m_\nu} = 0.021$ and 0.028 eV assuming the total mass of neutrinos of $\Sigma m_{\nu,i} = 0.13$ eV, and the number of massive neutrinos of $N_\nu = 1$ and 3 respectively (with $k_{\rm max} \sim 0.3$ hMpc^{-1}).

Since we are working on small scales, understanding the small scale window function is more important than for HETDEX. Issues include understanding the effects of the gaps between IFUs, gaps between pointings, and gaps due to the other instruments. A detailed simulation is required, including weather effects, in order to understand the effects on the small scale power due to the window function.

	Ω_{survey} (deg^2)	V_{survey} (h^{-3} Gpc^3)	N_g (10^6)	$\bar{n}_g$ (h^3 Mpc^{-3})	b_1
Bin1 ($1.9 < z < 2.4$)	420	0.93	0.5	0.00054	2.0
Bin2 ($2.4 < z < 3.0$)	420	1.12	0.3	0.00027	2.5
Bin3 ($3.0 < z < 3.5$)	420	0.91	0.1	0.00011	2.8

Table D.1: HETDEX survey parameters that we assume. We divide the survey into three redshift bins, where the median redshifts are $z_{center} = 2.15$, 2.70 and 3.25, and Ω_{survey} is the sky coverage of the survey. "b_1" denotes the assumed linear bias of Ly-α emitters at given redshift. We calculate the survey volume and number density based on the flat-ΛCDM model with the maximum likelihood parameters from Table 1 of the Komatsu et al. (2009) ("WMAP+BAO+SN ML"). The HETDEX-extension covers $\Omega_{survey} = 4000$ deg^2 over the same redshift bins as HETDEX, and the number of Ly-α emitters is 10 times of HETDEX survey. For all the surveys and bins, we assume the measurement errors in redshifts of $\Delta z = 180$ km/s.

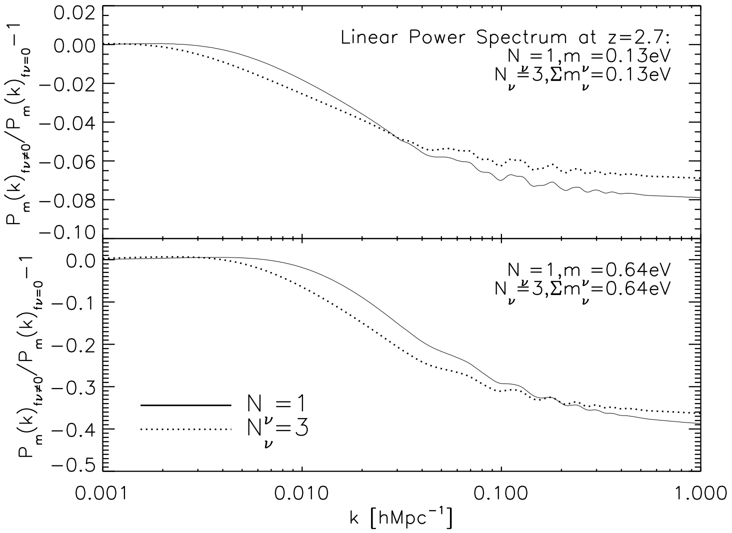

Figure D.1: A fractional suppression of a linear matter power spectrum at z=2.7 (median redshift of the HETDEX). We compare the linear matter power spectra with massive neutrino of different total masses against the linear matter power spectrum with massless neutrino (top: $\Sigma m_{\nu,i} = 0.13$ eV and $f_\nu = 0.01$, bottom: $\Sigma m_{\nu,i} = 0.64$ eV and $f_\nu = 0.05$). We fix the number of massive neutrinos to be $N_\nu = 1$ (solid) and $N_\nu = 3$ (dotted). We see that the asymptotic ratio of the power spectra, $P_{m,f_\nu \neq 0}(k)/P_{m,f_\nu=0}(k) \sim 1 - 8f_\nu$, holds approximately well at small scale.

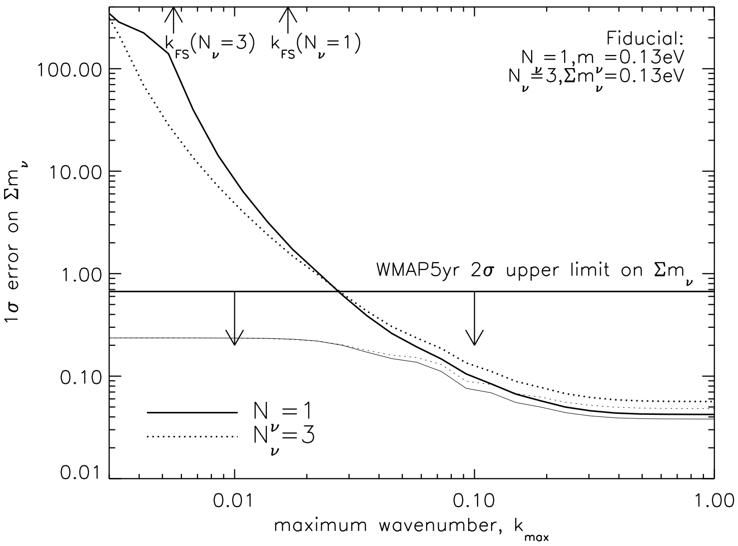

Figure D.2: The Fisher matrix forecast on marginalized 1-σ errors of the total mass of neutrinos, $\sigma_{\Sigma m_\nu}$, as a function of the maximum wavenumber to be used for our parameter search, $k_{\rm max}$. We use fiducial cosmological parameters from Table 1 of the Komatsu et al. (2009) ("WMAP+BAO+SN ML") assuming flat-ΛCDM model with $p_i = \{\Omega_m, \Omega_m h^2, \Omega_b h^2, f_\nu, n_s, \alpha_s, \delta_R, \tau, b_1(z)\}$ being our model parameters. We add hypothetical Planck prior to the HETDEX survey such that $\mathbf{F}_{ij} = \mathbf{F}_{ij}^{\rm HETDEX} + \mathbf{F}_{ij}^{\rm Planck}$. We fix the number of massive neutrinos to be $N_\nu = 1$ (solid) and $N_\nu = 3$ (dotted). Thick lines do not include the Planck prior on the total mass of neutrinos (i.e., $\mathbf{F}_{f_\nu i}^{\rm Planck} = \mathbf{F}_{i f_\nu}^{\rm Planck} = 0$), and thin lines include the Planck prior on f_ν. We also show the current upper limit on the total mass of neutrinos from WMAP5yr as a reference.

Appendix E

Void in the Redshift Space

E.1 Calculation of $\kappa(\mathbf{x})$

A mapping between the real-space to the redshift space is

$$x_1^s = x_1^r \tag{E.1}$$

$$x_2^s = x_2^r \tag{E.2}$$

$$x_3^s = x_3^r - f\mathbf{u}\cdot\hat{\mathbf{x}}_3^r, \tag{E.3}$$

where $f \equiv \frac{d\ln\delta(a)}{d\ln a}$ is the growth rate, and we set the unit vector, $\hat{\mathbf{x}}_3^r$, to be along the line of sight direction. Here, $\mathbf{u} \equiv \frac{-\mathbf{v}}{\mathcal{H}f}$, where $\mathbf{v}$ is the peculiar velocity of a void galaxy, and $\mathcal{H}(z)$ is a comoving Hubble rate.

We define $\kappa(\mathbf{x}^r)$ to quantify the strength of the redshift space distortion as follows

$$\kappa(\mathbf{x}^r) \equiv -\frac{f\hat{\mathbf{x}_3^r}\cdot\mathbf{u}(\mathbf{x}^r)}{x_3^r}, \tag{E.4}$$

and we re-write Eq.(E.3) as

$$x_3^s = x_3^r(1+\kappa(\mathbf{x}^r)). \tag{E.5}$$

Here, we use a spherical coordinate such that

$$x_1 = x \sin\theta_x \cos\phi_x \tag{E.6}$$

$$x_2 = x \sin\theta_x \sin\phi_x \tag{E.7}$$

$$x_3 = x \cos\theta_x \tag{E.8}$$

and

$$k_1 = k \sin\theta_k \cos\phi_k \tag{E.9}$$

$$k_2 = k \sin\theta_k \sin\phi_k \tag{E.10}$$

$$k_3 = k \cos\theta_k, \tag{E.11}$$

where $x \equiv |\mathbf{x}| = \sqrt{x_1^2 + x_2^2 + x_3^2}$, $k \equiv |\mathbf{k}| = \sqrt{k_1^2 + k_2^2 + k_3^2}$, and θ and ϕ are the azimuthal and inclination angles respectively.

$$\begin{aligned} \kappa(\mathbf{x}^r) &\equiv -\frac{f\widehat{\mathbf{x}_3^r} \cdot \mathbf{u}(\mathbf{x}^r)}{x_3^r} = -\frac{f\widehat{\mathbf{x}_3^r} \cdot \nabla\Phi(\mathbf{x}^r)}{4\pi G a^2 \bar{\rho} x_3^r} \\ &= -\frac{f}{4\pi G a^2 \bar{\rho} x_3^r} \int \frac{d^3k}{(2\pi)^3} i\mathbf{k} \cdot \hat{\mathbf{x}}_3^r \tilde{\Phi}(\mathbf{k}) e^{i\mathbf{k}\cdot\mathbf{x}^r} \\ &= \frac{f}{x_3^r} \int \frac{d^3k}{(2\pi)^3} i\mathbf{k} \cdot \hat{\mathbf{x}}_3^r \frac{\tilde{\delta}(\mathbf{k})}{k^2} e^{i\mathbf{k}\cdot\mathbf{x}^r} \\ &= \frac{f}{x_3^r} \int_0^\infty \frac{dk}{(2\pi)^3} ik \int_0^{2\pi} d\phi_k \int_{-1}^{1} d\mu_k \mu_k \tilde{\delta}(\mathbf{k}) e^{i\mathbf{k}\cdot\mathbf{x}^r}, \end{aligned} \tag{E.12}$$

where $\mu_k \equiv \cos\theta_k$. Here, $\mathbf{k} \cdot \mathbf{x} = kx\cos\gamma$, where

$$\cos\gamma \equiv \cos\theta_k \cos\theta_x + \cos(\phi_k - \phi_x) \sin\theta_k \sin\theta_x. \tag{E.13}$$

E.1.1 Spherical Void

As for the spherical void of radius R with homogeneous top-hat density contrast, $\delta(\mathbf{x})$, we have

$$\tilde{\delta}(\mathbf{k}) = \bar{\delta}\int d^3x' e^{-i\mathbf{k}\cdot\mathbf{x}'} = 4\pi\bar{\delta}\int_0^R dx\ x^2 e^{-ikx} = 4\pi R^3\bar{\delta}\frac{j_1(kR)}{kR}. \tag{E.14}$$

Therefore, Eq.(E.12) becomes

$$\kappa(\mathbf{x}^r) = \frac{4\pi R^3 f\bar{\delta}}{x_3^r}\int_0^\infty \frac{dk}{(2\pi)^3} ik\frac{j_1(kR)}{kR}\int_0^{2\pi} d\phi\int_{-1}^1 d\mu_k\mu_k e^{i\mathbf{k}\cdot\mathbf{x}^r}. \tag{E.15}$$

We first integrate the angular portion of the integration, $\int d\Omega_k\mu_k e^{i\mathbf{k}\cdot\mathbf{x}^r}$, expanding the exponent into Legendre polynomials,

$$e^{i\mathbf{k}\cdot\mathbf{x}^r} = \sum_l^\infty (-i)^l(2l+1)j_l(-kx)P_l(\cos\gamma), \tag{E.16}$$

and using the Spherical harmonics addition theorem (a.k.a., Legendre addition theorem),

$$\begin{aligned} P_l(\cos\gamma) &= \frac{4\pi}{2l+1}\sum_{m=-l}^{l}(-1)^m Y_l^m(\theta_k,\phi_k)Y_l^{-m}(\theta_x,\phi_x) \\ &= \frac{4\pi}{2l+1}\sum_{m=-l}^{l} Y_l^m(\theta_k,\phi_k)\bar{Y}_l^m(\theta_x,\phi_x) \\ &= P_l(\cos\theta_k)P_l(\cos\theta_x) \\ &+ 2\sum_{m=1}^{l}\frac{(l-m)!}{(l+m)!}P_l^m(\cos\theta_k)P_l^m(\cos\theta_x)\cos[m(\phi_k-\phi_x)], \end{aligned} \tag{E.17}$$

where $P_l^m(x)$ is an associated Legendre polynomial, and it is related to the unassociated Legendre polynomial such that

$$\begin{aligned} P_l^m(x) &= (-1)^m(1-x^2)^{m/2}\frac{d^m}{dx^m}P_l(x) \\ &= \frac{(-1)^m}{2^l l!}(1-x^2)^{m/2}\frac{d^{l+m}}{dx^{l+m}}(x^2-1)^l. \end{aligned} \tag{E.18}$$

Therefore,

$$\begin{aligned} &\int d\Omega_k \mu_k e^{i\mathbf{k}\cdot\mathbf{x}^r} = \sum_l^\infty (-i)^l(2l+1)j_l(-kx)\int d\Omega_k \mu_k P_l(\cos\gamma) \\ =& \sum_l^\infty \sum_{m=-l}^{l} (-i)^l(2l+1)j_l(-kx)\left(\frac{4\pi}{2l+1}\right)^{3/2} \\ \times& \ Y_l^{-m}(\theta_x,\phi_x)\int d\Omega_k Y_1^0(\theta_k,\phi_k)\bar{Y}_l^{-m}(\theta_k,\phi_k) \\ =& \sum_l^\infty \sum_{m=-l}^{l} (-i)^l(2l+1)j_l(-kx)\left(\frac{4\pi}{2l+1}\right)^{3/2} Y_l^{-m}(\theta_x,\phi_x)\delta_{m0}\delta_{l1} \\ =& -3ij_1(-kx)\left(\frac{4\pi}{3}\right)^{3/2} Y_1^0(\theta_x,\phi_x) = 4\pi i j_1(kx)\cos\theta_x, \end{aligned} \tag{E.19}$$

where we used $Y_1^0(\theta,\phi) = \sqrt{\frac{3}{4\pi}}\cos\theta$ and $j_l(-x) = (-1)^l j_l(x)$.

Finally, we obtain κ for a spherical void as

$$\begin{aligned} \kappa(\mathbf{x}^r) &= \frac{4\pi R^3 f\bar{\delta}}{x_3^r}\int_0^\infty \frac{dk}{(2\pi)^3} ik\frac{j_1(kR)}{kR}[4\pi i j_1(kx)\cos\theta_x] \\ &= -\frac{2R^2 f\bar{\delta}\cos\theta_x}{\pi x_3^r}\int_0^\infty dk j_1(kR)j_1(kx) \\ &= -\frac{2R^2 f\bar{\delta}\cos\theta_x}{\pi x_3^r}\left(\frac{\pi x}{6R^2}\right) = -\frac{f\bar{\delta}}{3}. \end{aligned} \tag{E.20}$$

E.1.2 Spheroidal Void with azimuthal symmetry

Here, we consider a spheroidal void with an azimuthal symmetry (i.e., an ellipsoid with two of the three principal axes have the same length, $a = b \neq c$). We again choose a spherical coordinate, but with the ellipsoidal volume element being projected on to spherical volume element such that

$$\begin{aligned} x_1 &= a\ r \sin\theta \cos\phi \qquad &\text{(E.21)} \\ x_2 &= a\ r \sin\theta \sin\phi \qquad &\text{(E.22)} \\ x_3 &= c\ r \cos\theta, \qquad &\text{(E.23)} \end{aligned}$$

where $0 \leq r \leq 1$ and $d^3x = a^2c\ r^2dr\ d\phi\ d\cos\theta$.

First, let us derive the Fourier transform of the spheroidal void with a homogeneous top-hat density contrast, $\delta(\mathbf{x})$ as follows,

$$\tilde{\delta}(\mathbf{k}) = \bar{\delta}\int d^3x e^{-i\mathbf{k}\cdot\mathbf{x}} = a^2c\bar{\delta}\int_0^1 r^2dr \int d\Omega e^{-i\mathbf{k}\cdot\mathbf{x}}, \tag{E.24}$$

where

$$\mathbf{k}\cdot\mathbf{x} = kr[a\sin\theta_k \sin\theta_x \cos(\phi_k - \phi_x) + c\cos\theta_k\cos\theta_x]. \tag{E.25}$$

Here, we define

$$\begin{aligned} \cos\gamma_a &\equiv \sin\theta_k \sin\theta_x \cos(\phi_k - \phi_x) \qquad &\text{(E.26)} \\ \cos\gamma_c &\equiv \cos\theta_k \cos\theta_x, \qquad &\text{(E.27)} \end{aligned}$$

and

$$\begin{aligned} \cos\gamma &\equiv \cos\gamma_a + \cos\gamma_c \qquad &\text{(E.28)} \\ \cos\eta &\equiv -\cos\gamma_a + \cos\gamma_c, \qquad &\text{(E.29)} \end{aligned}$$

where $\cos\eta$ is obtained by changing a sign of θ_x. In terms of $\cos\gamma$ and $\cos\eta$, we have

$$\mathbf{k}\cdot\mathbf{x} = \frac{1}{2}kr[(c+a)\cos\gamma + (c-a)\cos\eta]. \tag{E.30}$$

Again, we use the spherical harmonics addition theorem (Eq.(E.17)). Note that due to the definition of Eq.(E.29) and from Eq.(E.17), we see that $P_l(\cos\eta) = P_l(\cos\gamma)$, and therefore,

$$\begin{aligned}
e^{-i\mathbf{k}\cdot\mathbf{x}} &= \exp[-\frac{1}{2}ikr(c+a)\cos\gamma]\exp[-\frac{1}{2}ikr(c-a)\cos\eta] \\
&= \left[\sum_{l=0}^{\infty}(-i)^l(2l+1)j_l\left(\frac{1}{2}kr(c+a)\right)P_l(\cos\gamma)\right] \\
&\times \left[\sum_{l'=0}^{\infty}(-i)^{l'}(2l'+1)j_{l'}\left(\frac{1}{2}kr(c-a)\right)P_{l'}(\cos\gamma)\right] \\
&= \sum_{l=0}^{\infty}\sum_{l'=0}^{\infty}(-i)^{l+l'}(2l+1)(2l'+1)j_l\left(\frac{1}{2}kr(c+a)\right) \\
&\times j_{l'}\left(\frac{1}{2}kr(c-a)\right)P_l(\cos\gamma)P_{l'}(\cos\gamma).
\end{aligned} \tag{E.31}$$

From the Legendre addition theorem, we have

$$\begin{aligned}
&\int d\Omega_x P_l(\cos\gamma)P_{l'}(\cos\gamma) \\
= \;& \frac{(4\pi)^2}{(2l+1)(2l'+1)}\sum_{m=-l}^{l}\sum_{m'=-l'}^{l'}(-1)^m Y_l^m(\theta_k,\phi_k)Y_{l'}^{m'}(\theta_k,\phi_k) \\
\times \;& \int_0^{2\pi}d\phi_x\int_{-1}^{1}d\cos\theta_x Y_l^{-m}(\theta_x,\phi_x)\bar{Y}_{l'}^{m'}(\theta_x,\phi_x) \\
= \;& \frac{(4\pi)^2}{(2l+1)(2l'+1)}\sum_{m=-l}^{l}\sum_{m'=-l'}^{l'}(-1)^m Y_l^m(\theta_k,\phi_k)Y_{l'}^{m'}(\theta_k,\phi_k)\delta_{ll'}\delta_{-mm'},
\end{aligned} \tag{E.32}$$

then we have

$$\begin{aligned}
\int d\Omega_x\ e^{-i\mathbf{k}\cdot\mathbf{x}} &= \sum_{l=0}^{\infty}\sum_{l'=0}^{\infty}(-i)^{l+l'}(2l+1)(2l'+1)j_l\left(\frac{1}{2}kr(c+a)\right) \\
&\times\ j_{l'}\left(\frac{1}{2}kr(c-a)\right)\int d\Omega_x P_l(\cos\gamma)P_{l'}(\cos\gamma) \\
&= 16\pi^2\sum_{l=0}^{\infty}\sum_{m=-l}^{l}(-1)^{l+m}j_l\left(\frac{1}{2}kr(c+a)\right)j_l\left(\frac{1}{2}kr(c-a)\right) \\
&\times\ Y_l^m(\theta_k,\phi_k)Y_l^{-m}(\theta_k,\phi_k). \qquad \text{(E.33)}
\end{aligned}$$

Therefore,

$$\begin{aligned}
\tilde{\delta}(\mathbf{k}) &= a^2c\bar{\delta}\int_0^1 r^2dr\int d\Omega e^{-i\mathbf{k}\cdot\mathbf{x}} \\
&= 16\pi^2a^2c\bar{\delta}\sum_{l=0}^{\infty}\sum_{m=-l}^{l}(-1)^{l+m}Y_l^m(\theta_k,\phi_k)Y_l^{-m}(\theta_k,\phi_k) \\
&\times\ \int_0^1 r^2dr j_l\left(\frac{1}{2}kr(c+a)\right)j_l\left(\frac{1}{2}kr(c-a)\right), \qquad \text{(E.34)}
\end{aligned}$$

and integrating over $r \in [0,1]$, we have

$$\begin{aligned}
\tilde{\delta}(\mathbf{k}) &= -\frac{8\pi^3a\bar{\delta}}{\sqrt{c^2-a^2}k^2}\sum_{l=0}^{\infty}\sum_{m=-l}^{l}(-1)^{l+m}Y_l^m(\theta_k,\phi_k)Y_l^{-m}(\theta_k,\phi_k) \\
&\times\ \left[(c+a)J_{l-\frac{1}{2}}\left(\frac{1}{2}k(c+a)\right)J_{l+\frac{1}{2}}\left(\frac{1}{2}k(c-a)\right)\right. \\
&-\ \left.(c-a)J_{l-\frac{1}{2}}\left(\frac{1}{2}k(c-a)\right)J_{l+\frac{1}{2}}\left(\frac{1}{2}k(c+a)\right)\right]. \qquad \text{(E.35)}
\end{aligned}$$

We Taylor expand the above equation for $\tilde{\delta}(\mathbf{k})$ about $\epsilon \simeq 0$ up to a linear order.

$$\begin{aligned}
\tilde{\delta}(\mathbf{k}) &\simeq \frac{a\pi^3\bar{\delta}}{k^2}\sum_{l=0}^{\infty}\frac{(ka)^{l+1/2}}{2^{2l-3/2}\Gamma(l+3/2)}\epsilon^l\left[ka\epsilon J_{l+\frac{1}{2}}(ka)+\{2+(l-1)\epsilon\}J_{l+\frac{3}{2}}(ka)\right] \\
&\times\ \sum_{m=-l}^{l}(-1)^{l+m}Y_l^m(\theta_k,\phi_k)Y_l^{-m}(\theta_k,\phi_k) \qquad \text{(E.36)}
\end{aligned}$$

For a prolate ellipsoid, where $a < c$ and $\epsilon \equiv 1 - \frac{a}{c}$,

$$\tilde{\delta}(\mathbf{k}) \simeq 4\pi\bar{\delta}a^3 \left[\frac{j_1(ka)}{ka} + \epsilon\left(\frac{j_1(ka)}{ka} - j_2(ka)\right)\right] + \mathcal{O}(\epsilon^2). \tag{E.37}$$

For an oblate ellipsoid, where $a > c$ and $\epsilon \equiv 1 - \frac{c}{a}$,

$$\tilde{\delta}(\mathbf{k}) \simeq 4\pi\bar{\delta}a^3 \left[\frac{j_1(ka)}{ka} - \epsilon\left(\frac{j_1(ka)}{ka} - j_2(ka)\right)\right] + \mathcal{O}(\epsilon^2). \tag{E.38}$$

Therefore, Eq.(E.12) becomes

$$\begin{aligned}\kappa(\mathbf{x}) &= \frac{4\pi a^3 f\bar{\delta}}{x_3}\int_0^\infty \frac{dk}{(2\pi)^3} ik\left[\frac{j_1(ka)}{ka} \pm \epsilon\left(\frac{j_1(ka)}{ka} - j_2(ka)\right)\right] \\ &\quad \int d\Omega_k \cos\theta_k e^{i\mathbf{k}\cdot\mathbf{x}},\end{aligned} \tag{E.39}$$

where

$$\begin{aligned}\int d\Omega_k \cos\theta_k e^{i\mathbf{k}\cdot\mathbf{x}} &= \sum_{l=0}^{\infty}\sum_{l'=0}^{\infty}\sqrt{\frac{4\pi}{3}}(-i)^{l+l'}(2l+1)(2l'+1)j_l\left(-\frac{1}{2}kr(c+a)\right) \\ &\times\ j_{l'}\left(-\frac{1}{2}kr(c-a)\right)\int d\Omega_k Y_1^0(\theta_k,\phi_k)P_l(\cos\gamma)P_{l'}(\cos\gamma).\end{aligned} \tag{E.40}$$

Using the addition theorem given in Eq.(E.17), we rewrite the above equation,

$$\begin{aligned}\int d\Omega_k \cos\theta_k e^{i\mathbf{k}\cdot\mathbf{x}} &= \sum_{l=0}^{\infty}\sum_{l'=0}^{\infty}\sum_{m=-l}^{l}\sum_{m'=-l'}^{l'}(4\pi)^2\sqrt{\frac{4\pi}{3}}(-i)^{l+l'}j_l\left(-\frac{1}{2}kr(c+a)\right) \\ &\times\ j_{l'}\left(-\frac{1}{2}kr(c-a)\right)(-1)^{m+m'}Y_l^{-m}(\theta_x,\phi_x)Y_{l'}^{-m'}(\theta_x,\phi_x) \\ &\times\ \int d\Omega_k Y_1^0(\theta_k,\phi_k)Y_l^m(\theta_k,\phi_k)Y_{l'}^{m'}(\theta_k,\phi_k).\end{aligned} \tag{E.41}$$

Here,

$$
\begin{aligned}
& j_l\left(-\frac{1}{2}kr(c+a)\right) j_{l'}\left(-\frac{1}{2}kr(c-a)\right) \\
& \simeq 2^{-2l'-\frac{5}{2}}\pi\frac{(-1)^{l+l'}}{\Gamma(l'+\frac{3}{2})}(kra)^{l'-\frac{1}{2}}\epsilon^{l'} \\
\times \quad & \left[\{2+(l+2l')\epsilon\}J_{l+\frac{1}{2}}(kra) - kra\epsilon J_{l+\frac{3}{2}}(kra)\right] \\
& = 2^{-2(l'+1)}\frac{\sqrt{\pi}(-1)^{l+l'}}{\Gamma(l'+\frac{3}{2})}(kra)^{l'}\epsilon^{l'}\left[\{2+(l+2l')\epsilon\}j_l(kra) - kra\epsilon j_{l+1}(kra)\right]
\end{aligned}
\tag{E.42}
$$

for a prolate ellipsoid ($c > a$), and

$$
\begin{aligned}
& j_l\left(-\frac{1}{2}kr(c+a)\right) j_{l'}\left(-\frac{1}{2}kr(c-a)\right) \\
& \simeq 2^{-2l'-\frac{5}{2}}\pi\frac{(-1)^{l}}{\Gamma(l'+\frac{3}{2})}(kra)^{l'-\frac{1}{2}}\epsilon^{l'}\left[(2-l\epsilon)J_{l+\frac{1}{2}}(kra) + kra\epsilon J_{l+\frac{3}{2}}(kra)\right] \\
& = 2^{-2(l'+1)}\frac{\sqrt{\pi}(-1)^{l}}{\Gamma(l'+\frac{3}{2})}(kra)^{l'}\epsilon^{l'}\left[(2-l\epsilon)j_l(kra) + kra\epsilon j_{l+1}(kra)\right]
\end{aligned}
\tag{E.43}
$$

for an oblate ellipsoid ($c < a$). In order to truncate the equation at linear order in ϵ, we have $l' \leq 1$, such that

$$
\begin{aligned}
& j_l\left(-\frac{1}{2}kr(c+a)\right) j_{l'}\left(-\frac{1}{2}kr(c-a)\right) \\
& \simeq \begin{cases} \frac{1}{2}(-1)^l\left[(2+l\epsilon)j_l(kra) - kra\epsilon j_{l+1}(kra)\right] & \text{for } l'=0 \\ -\frac{1}{6}(-1)^l kra\epsilon j_l(kra) & \text{for } l'=1 \\ \mathcal{O}(\epsilon^2) & \text{otherwise} \end{cases}
\end{aligned}
\tag{E.44}
$$

for a prolate ellipsoid, and

$$
\begin{aligned}
& j_l\left(-\frac{1}{2}kr(c+a)\right) j_{l'}\left(-\frac{1}{2}kr(c-a)\right) \\
& \simeq \begin{cases} \frac{1}{2}(-1)^l\left[(2-l\epsilon)j_l(kra) + kra\epsilon j_{l+1}(kra)\right] & \text{for } l'=0 \\ \frac{1}{6}(-1)^l kra\epsilon j_l(kra) & \text{for } l'=1 \\ \mathcal{O}(\epsilon^2) & \text{otherwise} \end{cases}
\end{aligned}
\tag{E.45}
$$

for an oblate ellipsoid.

As for the integration over the solid angle, Ω_k, we have

$$\int d\Omega_k Y_1^0(\theta_k,\phi_k)Y_l^m(\theta_k,\phi_k)Y_{l'}^{m'}(\theta_k,\phi_k) \\ = \sqrt{\frac{3(2l+1)(2l'+1)}{4\pi}} \begin{pmatrix} 1 & l & l' \\ 0 & 0 & 0 \end{pmatrix} \begin{pmatrix} 1 & l & l' \\ 0 & m & m' \end{pmatrix}, \tag{E.46}$$

where the Wigner-3J symbol must satisfy the triangular inequality such that $|1-l| \leq l' \leq 1+l$, and $0+m=-m'$ in order to have a non-zero value.

As for Eq.(E.41), since $l' \leq 1$, we have a limited number of non-zero terms. We have $(l,l',m,m') = (0,1,0,0)$, $(1,0,0,0)$, $(2,1,-1,1)$, $(2,1,0,0)$ and $(2,1,1,-1)$ as the non-zero terms. We rewrite Eq.(E.41) with a finite number of terms truncating $\mathcal{O}(\epsilon^2)$ and higher as follows,

$$\begin{aligned} \int d\Omega_k \cos\theta_k e^{i\mathbf{k}\cdot\mathbf{x}} \simeq & \frac{(4\pi)^2}{\sqrt{3}} i \Bigg[\pm\frac{1}{6}kra\epsilon j_0(kra)Y_0^0(\theta_x,\phi_x)Y_1^0(\theta_x,\phi_x) \\ & + \frac{1}{2}\left\{(2\pm\epsilon)j_1(kra) \mp kra\epsilon j_2(kra)\right\} Y_0^0(\theta_x,\phi_x)Y_1^0(\theta_x,\phi_x) \\ & \pm \frac{1}{6}kra\epsilon j_2(kra)\Bigg\{\sqrt{\frac{3}{5}}Y_1^{-1}(\theta_x,\phi_x)Y_2^1(\theta_x,\phi_x) \\ & + \sqrt{\frac{3}{5}}Y_1^1(\theta_x,\phi_x)Y_2^{-1}(\theta_x,\phi_x) - \frac{2}{\sqrt{5}}Y_1^0(\theta_x,\phi_x)Y_2^0(\theta_x,\phi_x)\Bigg\}\Bigg] \end{aligned} \tag{E.47}$$

Here, in the limit of $\epsilon \to 0$, we recover

$$\int d\Omega_k \cos\theta_k e^{i\mathbf{k}\cdot\mathbf{x}} = \frac{(4\pi)^2}{\sqrt{3}} i j_1(kra)Y_0^0(\theta_x,\phi_x)Y_1^0(\theta_x,\phi_x) = 4\pi i j_1(kra)\cos\theta_x, \tag{E.48}$$

as in Eq.(E.19).

Finally, from Eq.(E.39) and (E.47), and truncating $\mathcal{O}(\epsilon^2)$ and higher terms, we have

$$
\begin{aligned}
\kappa(\mathbf{x}) &= \frac{4\pi a^3 f\bar{\delta}}{x_3}\int_0^\infty \frac{dk}{(2\pi)^3} ik\left[\frac{j_1(ka)}{ka} + \epsilon\left(\frac{j_1(ka)}{ka} - j_2(ka)\right)\right] \\
&\times \int d\Omega_k \cos\theta_k e^{i\mathbf{k}\cdot\mathbf{x}} \\
&\simeq -\frac{8f\bar{\delta}a^3}{\sqrt{3}x_3}\left[\frac{r}{6}\epsilon Y_0^0(\theta_x,\phi_x)Y_1^0(\theta_x,\phi_x)\int_0^\infty dk\ kj_1(ka)j_0(kra)\right. \\
&+ \frac{2+\epsilon}{2a}Y_0^0(\theta_x,\phi_x)Y_1^0(\theta_x,\phi_x)\int_0^\infty dk\ j_1(ka)j_1(kra) \\
&- \frac{r}{2}\epsilon Y_0^0(\theta_x,\phi_x)Y_1^0(\theta_x,\phi_x)\int_0^\infty dk\ kj_1(ka)j_2(kra) \\
&+ \frac{r}{6}\epsilon\left\{\sqrt{\frac{3}{5}}Y_1^{-1}(\theta_x,\phi_x)Y_2^1(\theta_x,\phi_x) + \sqrt{\frac{3}{5}}Y_1^1(\theta_x,\phi_x)Y_2^{-1}(\theta_x,\phi_x)\right. \\
&- \left.\frac{2}{\sqrt{5}}Y_1^0(\theta_x,\phi_x)Y_2^0(\theta_x,\phi_x)\right\}\int_0^\infty dk\ kj_1(ka)j_2(kra) \\
&+ \frac{\epsilon}{a}Y_0^0(\theta_x,\phi_x)Y_1^0(\theta_x,\phi_x)\int_0^\infty dk\ j_1(ka)j_1(kra) \\
&- \left.\epsilon Y_0^0(\theta_x,\phi_x)Y_1^0(\theta_x,\phi_x)\int_0^\infty dk\ kj_2(ka)j_1(kra)\right].
\end{aligned}
\tag{E.49}
$$

Taking integrations over k (see appendix §E.2),

$$
\begin{aligned}
\kappa(\mathbf{x}) &\simeq -\frac{f\bar{\delta}}{3}\frac{ar\cos\theta_x}{x_3}(1-\epsilon) \\
&= -\frac{f\bar{\delta}}{3}\frac{a}{c}(1-\epsilon) \\
&= -\frac{f\bar{\delta}}{3}(1-\epsilon)^2 \\
&\simeq -\frac{f\bar{\delta}}{3}(1-2\epsilon)
\end{aligned}
\tag{E.50}
$$

Similarly, for an oblate spheroid,

$$\kappa(\mathbf{x}) \simeq -\frac{f\bar{\delta}}{3}(1+2\epsilon) \tag{E.51}$$

As we compare against numerical calculations of $\kappa(\mathbf{x})$, we see $\kappa(\mathbf{x}) \simeq -\frac{f\bar{\delta}}{3}(1\mp\epsilon)$ fits the result better for both prolate and oblate spheroids.

We see how real space geometry of a given void affects the peculiar velocity field within the void by comparing Eqs.(E.20) and (E.50). As for a prolate spherical void, we set the longest principal axis, $a < c \equiv a/(1-\epsilon)$, to lie along the line of sight. As discussed by Icke (1984), originally aspherical voids tend to become a sphere with a slower expansion speed along the longest principal axis, and vice versa. For a given prolate spheroidal void with its longest principal axis along the line of sight, peculiar velocity along the largest axis become smaller as we increase ellipticity. Since the deformation of the void shape in the redshift space, $\kappa(\mathbf{x})$, is proportional to the peculiar velocity, an aspherical void in real space with the longest axis being along the line of sight experiences less deformation compared to an originally spherical void.

Also, we see that the degree of deformation of an aspherical void in the redshift space, $\kappa(\mathbf{x})$, is independent of the size of the void, but dependent only on the linear growth factor, $f \equiv \frac{d\ln D}{d\ln a}$, the mean density contrast of the void, $\bar{\delta}$, and the ellipticity of the void in the real space.

E.2 List of Y_l^m, j_l and Wigner-3J symbol

$$
\begin{aligned}
Y_0^0(\theta,\phi) &= \frac{1}{2\sqrt{\pi}} && \text{(E.52)}\\
Y_1^{-1}(\theta,\phi) &= \frac{1}{2}\sqrt{\frac{3}{2\pi}}\sin\theta e^{-i\phi} && \text{(E.53)}\\
Y_1^0(\theta,\phi) &= \frac{1}{2}\sqrt{\frac{3}{\pi}}\cos\theta && \text{(E.54)}\\
Y_1^1(\theta,\phi) &= -\frac{1}{2}\sqrt{\frac{3}{2\pi}}\sin\theta e^{i\phi} && \text{(E.55)}
\end{aligned}
$$

$$J_{l+\frac{1}{2}}(z) = \sqrt{\frac{2z}{\pi}}j_l(z) \tag{E.56}$$

$$
\begin{aligned}
j_0(z) &= \frac{\sin z}{z} && \text{(E.57)}\\
j_1(z) &= \frac{\sin z}{z^2} - \frac{\cos z}{z} && \text{(E.58)}\\
j_2(z) &= \left(\frac{3}{z^3} - \frac{1}{z}\right)\sin z - \frac{3}{z^2}\cos z && \text{(E.59)}\\
j_3(z) &= \left(\frac{15}{z^4} - \frac{6}{z^2}\right)\sin z - \left(\frac{15}{z^3} - \frac{1}{z}\right)\cos z && \text{(E.60)}
\end{aligned}
$$

$$\begin{aligned} \Gamma(1/2) &= \sqrt{\pi} && \text{(E.61)} \\ \Gamma(3/2) &= \frac{\sqrt{\pi}}{2} && \text{(E.62)} \\ \Gamma(5/2) &= \frac{3\sqrt{\pi}}{4} && \text{(E.63)} \\ \Gamma(7/2) &= \frac{15\sqrt{\pi}}{8} && \text{(E.64)} \\ \Gamma(9/2) &= \frac{105\sqrt{\pi}}{16} && \text{(E.65)} \end{aligned}$$

$$\begin{aligned} \begin{pmatrix} 1 & 0 & 1 \\ 0 & 0 & 0 \end{pmatrix} &= -\frac{1}{\sqrt{3}} && \text{(E.66)} \\ \begin{pmatrix} 1 & 1 & 0 \\ 0 & 0 & 0 \end{pmatrix} &= -\frac{1}{\sqrt{3}} && \text{(E.67)} \\ \begin{pmatrix} 1 & 2 & 1 \\ 0 & 0 & 0 \end{pmatrix} &= \sqrt{\frac{2}{15}} && \text{(E.68)} \\ \begin{pmatrix} 1 & 2 & 1 \\ 0 & -1 & 1 \end{pmatrix} &= -\frac{1}{\sqrt{10}} && \text{(E.69)} \\ \begin{pmatrix} 1 & 2 & 1 \\ 0 & 1 & -1 \end{pmatrix} &= -\frac{1}{\sqrt{10}} && \text{(E.70)} \end{aligned}$$

For $0 < r < 1$ and $a > 0$,

$$\begin{aligned} \int_0^\infty dk\; j_1(ka)j_1(kra) &= \frac{\pi r}{6a} && \text{(E.71)} \\ \int_0^\infty dk\; k\; j_2(ka)j_1(kra) &= \frac{\pi r}{2a^2} && \text{(E.72)} \\ \int_0^\infty dk\; k\; j_1(ka)j_0(kra) &= \frac{\pi}{2a^2} && \text{(E.73)} \\ \int_0^\infty dk\; k\; j_1(ka)j_2(kra) &= 0 && \text{(E.74)} \end{aligned}$$

Bibliography

Abdurashitov, J. N. et al. 1999, Phys. Rev., C60, 055801

Abdurashitov, J. N., et al. 2002, Soviet Journal of Experimental and Theoretical Physics, 95, 181

Acquaviva, V. & Gawiser, E. 2010, Phys. Rev. D, 82, 082001

Afshordi, N., Loh, Y.-S., & Strauss, M. A. 2004, Phys. Rev., D69, 083524

Ahmad, Q. R., et al. 2002a, Physical Review Letters, 89, 011301

—. 2002b, Physical Review Letters, 89, 011302

Ahmed, S. N. et al. 2004, Phys. Rev. Lett., 92, 181301

Alcock, C. & Paczynski, B. 1979, Nature, 281, 358

Altmann, M., et al. 2000, Physics Letters B, 490, 16

Angulo, R. E., Baugh, C. M., Frenk, C. S., & Lacey, C. G. 2008, Mon. Not. R. Astron. Soc., 383, 755

Ashie, Y. et al. 2005, Phys. Rev., D71, 112005

Ballinger, W. E., Peacock, J. A., & Heavens, A. F. 1996, Mon. Not. R. Astron. Soc., 282, 877

Bardeen, J. M. 1980, Phys. Rev. D, 22, 1882

Benson, A. J., Bower, R. G., Frenk, C. S., Lacey, C. G., Baugh, C. M., & Cole, S. 2003, Astrophys. J., 599, 38

Bernardeau, F., Colombi, S., Gaztañaga, E., & Scoccimarro, R. 2002, Phys. Rep., 367, 1

Blake, C. & Glazebrook, K. 2003, Astrophys. J., 594, 665

Bond, J. R., Efstathiou, G., & Silk, J. 1980, Physical Review Letters, 45, 1980

Boughn, S. & Crittenden, R. 2004, Nature, 427, 45

Bower, R. G., Benson, A. J., Malbon, R., Helly, J. C., Frenk, C. S., Baugh, C. M., Cole, S., & Lacey, C. G. 2006, Mon. Not. R. Astron. Soc., 370, 645

Carlson, J., White, M., & Padmanabhan, N. 2009, Phys. Rev. D, 80, 043531

Chevallier, M. & Polarski, D. 2001, Int. J. Mod. Phys., D10, 213

Cleveland, B. T. et al. 1998, Astrophys. J., 496, 505

Colberg, J. M., Sheth, R. K., Diaferio, A., Gao, L., & Yoshida, N. 2005, Mon. Not. R. Astron. Soc., 360, 216

Colberg, J. M., et al. 2008, Mon. Not. R. Astron. Soc., 387, 933

Cole, S., Lacey, C. G., Baugh, C. M., & Frenk, C. S. 2000, Mon. Not. R. Astron. Soc., 319, 168

Cole, S., et al. 2005, Mon. Not. R. Astron. Soc., 362, 505

Copeland, E. J., Sami, M., & Tsujikawa, S. 2006, Int. J. Mod. Phys., D15, 1753

Crocce, M. & Scoccimarro, R. 2008, Phys. Rev. D, 77, 023533

Croton, D. J., et al. 2006, Mon. Not. R. Astron. Soc., 365, 11

Davis, M. & Peebles, P. J. E. 1983, Astrophys. J., 267, 465

Davis, R. 1994, Progress in Particle and Nuclear Physics, 32, 13

De Lucia, G. & Blaizot, J. 2007, Mon. Not. R. Astron. Soc., 375, 2

Doroshkevich, A. G. 1970, Astrophysics, 6, 320

Doroshkevich, A. G., Khlopov, M. I., Sunyaev, R. A., Szalay, A. S., & Zeldovich, I. B. 1981, New York Academy Sciences Annals, 375, 32

Doroshkevich, A. G. & Khlopov, M. Y. 1981, Soviet Astronomy, 25, 521

Doroshkevich, A. G., Zeldovich, Y. B., Syunyaev, R. A., & Khlopov, M. Y. 1980a, Soviet Astronomy Letters, 6, 257

—. 1980b, Soviet Astronomy Letters, 6, 252

Dunkley, J., et al. 2009a, Astrophys. J., submitted arXiv:0811.4280v1

—. 2009b, Astrophys. J. Suppl., 180, 306

Eisenstein, D. J. & Hu, W. 1999, Astrophys. J., 511, 5

Eisenstein, D. J., Hu, W., & Tegmark, M. 1999, Astrophys. J., 518, 2

Eisenstein, D. J., Seo, H.-J., & White, M. 2007, Astrophys. J., 664, 660

Eisenstein, D. J., et al. 2005, Astrophys. J., 633, 560

Evrard, A. E., et al. 2002, Astrophys. J., 573, 7

Foster, C. & Nelson, L. A. 2009, Astrophys. J., 699, 1252

Franx, M., Illingworth, G., & de Zeeuw, T. 1991, Astrophys. J., 383, 112

Fry, J. N. & Gaztanaga, E. 1993, Astrophys. J., 413, 447

Fukuda, S., et al. 2002, Physics Letters B, 539, 179

Fukuda, Y. et al. 1998, Phys. Rev. Lett., 81, 1562

Gnedin, N. Y. & Hui, L. 1998, Mon. Not. R. Astron. Soc., 296, 44

Gno Collaboration, et al. 2005, Physics Letters B, 616, 174

Gonzalez-Garcia, M. C. & Maltoni, M. 2008, Phys. Rep., 460, 1

Guzzo, L., et al. 2008, Nature, 451, 541

Hamilton, A. J. S. 2001, Mon. Not. R. Astron. Soc., 322, 419

Hampel, W. et al. 1999, Phys. Lett., B447, 127

Hannestad, S., Mirizzi, A., Raffelt, G. G., & Wong, Y. Y. Y. 2010, ArXiv e-prints

Heavens, A. F., Matarrese, S., & Verde, L. 1998, Mon. Not. R. Astron. Soc., 301, 797

Hill, G. J., Gebhardt, K., Komatsu, E., & MacQueen, P. J. 2004, in American Institute of Physics Conference Series, Vol. 743, The New Cosmology: Conference on Strings and Cosmology, ed. R. E. Allen, D. V. Nanopoulos, & C. N. Pope, 224–233

Hinshaw, G., et al. 2009, Astrophys. J. Suppl., 180, 225

Hoeft, M., Yepes, G., Gottlöber, S., & Springel, V. 2006, Mon. Not. R. Astron. Soc., 371, 401

Hosaka, J., et al. 2006a, Phys. Rev. D, 73, 112001

—. 2006b, Phys. Rev. D, 74, 032002

Hoyle, F. & Vogeley, M. S. 2002, Astrophys. J., 566, 641

Hu, W. 1998, Astrophys. J., 506, 485

Hu, W. & Eisenstein, D. J. 1998, Astrophys. J., 498, 497

Hu, W., Eisenstein, D. J., & Tegmark, M. 1998, Physical Review Letters, 80, 5255

Hu, W. & Haiman, Z. 2003, Phys. Rev. D, 68, 063004

Hui, L. & Bertschinger, E. 1996, Astrophys. J., 471, 1

Hütsi, G. 2006, Astron. Astrophys., 449, 891

Icke, V. 1984, Mon. Not. R. Astron. Soc., 206, 1P

Itoh, N., Hayashi, H., Nishikawa, A., & Kohyama, Y. 1996, Astrophys. J. Suppl., 102, 411

Jang-Condell, H. & Hernquist, L. 2001, Astrophys. J., 548, 68

Jeong, D. & Komatsu, E. 2006, Astrophys. J., 651, 619

—. 2009, Astrophys. J., 691, 569

Kaiser, N. 1987, Mon. Not. R. Astron. Soc., 227, 1

Kodama, H. & Sasaki, M. 1984, Prog. Theor. Phys. Suppl., 78, 1

Koehler, R. S., Schuecker, P., & Gebhardt, K. 2007, Astron. Astrophys., 462, 7

Komatsu, E., et al. 2009, Astrophys. J.Suppl., 180, 330

Komatsu, E. et al. 2010a, in preparation

Komatsu, E., et al. 2010b, ArXiv e-prints

Kowalski, M., et al. 2008, ArXiv e-prints, 804

Lavaux, G. & Wandelt, B. D. 2010, Mon. Not. R. Astron. Soc., 403, 1392

—. 2011, ArXiv e-prints

Lee, J. & Park, D. 2009, Astrophys. J. Lett., 696, L10

Lesgourgues, J., Matarrese, S., Pietroni, M., & Riotto, A. 2009, Journal of Cosmology and Astro-Particle Physics, 6, 17

Lesgourgues, J. & Pastor, S. 2006, Phys. Rept., 429, 307

Lewis, A. & Challinor, A. 2002, Phys. Rev. D, 66, 023531

Lewis, A., Challinor, A., & Lasenby, A. 2000, Astrophys. J., 538, 473

Lightman, A. P. & Schechter, P. L. 1990, Astrophys. J. Suppl., 74, 831

Linder, E. V. 2003, Phys. Rev. Lett., 90, 091301

Linder, E. V. & Jenkins, A. 2003, Mon. Not. R. Astron. Soc., 346, 573

Ma, C.-P. & Bertschinger, E. 1995, Astrophys. J., 455, 7

Maeda, K.-i., Sakai, N., & Triay, R. 2011, Journal of Cosmology and Astroparticle Physics, 8, 26

Makino, N., Sasaki, M., & Suto, Y. 1992, Phys. Rev. D, 46, 585

Maltoni, M., Schwetz, T., Tórtola, M., & Valle, J. W. F. 2004, New Journal of Physics, 6, 122

Mantz, A., Allen, S. W., & Rapetti, D. 2009, ArXiv e-prints

Matarrese, S. & Pietroni, M. 2007, Journal of Cosmology and Astro-Particle Physics, 6, 26

Matsubara, T. 2008, Phys. Rev. D, 77, 063530

McDonald, P. 2006, Phys. Rev. D, 74, 103512

—. 2007, Phys. Rev. D, 75, 043514

—. 2009, ArXiv e-prints

Naoz, S. & Barkana, R. 2005, Mon. Not. R. Astron. Soc., 362, 1047

Nishimichi, T., et al. 2007, Publ. Astron. Soc. Jap., 59, 1049

Nolta, M. R., et al. 2004, Astrophys. J., 608, 10

Nusser, A. 2000, Mon. Not. R. Astron. Soc., 317, 902

Okamoto, T., Gao, L., & Theuns, T. 2008, Mon. Not. R. Astron. Soc., 390, 920

Okumura, T., Matsubara, T., Eisenstein, D. J., Kayo, I., Hikage, C., Szalay, A. S., & Schneider, D. P. 2008, Astrophys. J., 676, 889

Padmanabhan, N. & White, M. 2008, ArXiv e-prints, 804

Pan, D. C., Vogeley, M. S., Hoyle, F., Choi, Y.-Y., & Park, C. 2011, ArXiv e-prints

Park, D. & Lee, J. 2007, Physical Review Letters, 98, 081301

Patiri, S. G., Prada, F., Holtzman, J., Klypin, A., & Betancort-Rijo, J. 2006, Mon. Not. R. Astron. Soc., 372, 1710

Peebles, P. J. E. 1976, Astrophys. Space. Sci., 45, 3

—. 1980, The large-scale structure of the universe (Research supported by the National Science Foundation. Princeton, N.J., Princeton University Press, 1980. 435 p.)

Percival, W. J., Cole, S., Eisenstein, D. J., Nichol, R. C., Peacock, J. A., Pope, A. C., & Szalay, A. S. 2007, Mon. Not. R. Astron. Soc., 381, 1053

Perlmutter, S., et al. 1999, Astrophys. J., 517, 565

Platen, E., van de Weygaert, R., & Jones, B. J. T. 2008, Mon. Not. R. Astron. Soc., 387, 128

Rassat, A., et al. 2008, ArXiv e-prints

Reid, B. A., et al. 2010, Mon. Not. R. Astron. Soc., 404, 60

Riess, A. G., et al. 1998, Astron. J., 116, 1009

Ryden, B. S. 1995, Astrophys. J., 452, 25

Ryden, B. S. & Melott, A. L. 1996, Astrophys. J., 470, 160

Saito, S., Takada, M., & Taruya, A. 2008, Physical Review Letters, 100, 191301

Sanchez, A. G., Baugh, C. M., & Angulo, R. 2008, ArXiv e-prints, 804

Sanchez, M., et al. 2003, Phys. Rev. D, 68, 113004

Schmidt, J. D., Ryden, B. S., & Melott, A. L. 2001, Astrophys. J., 546, 609

Schwetz, T., Tórtola, M., & Valle, J. W. F. 2008, New Journal of Physics, 10, 113011

Scoccimarro, R. 2004, Phys. Rev. D, 70, 083007

Sefusatti, E. & Komatsu, E. 2007, Phys. Rev. D, 76, 083004

Sekiguchi, T., Ichikawa, K., Takahashi, T., & Greenhill, L. 2010, Journal of Cosmology and Astro-Particle Physics, 3, 15

Seljak, U. & Zaldarriaga, M. 1996, Astrophys. J., 469, 437

Seo, H., Siegel, E. R., Eisenstein, D. J., & White, M. 2008, Astrophys. J., 686, 13

Seo, H.-J. & Eisenstein, D. J. 2003, Astrophys. J., 598, 720

Seo, H.-J. & Eisenstein, D. J. 2005, Astrophys. J., 633, 575

Seo, H.-J. & Eisenstein, D. J. 2007, Astrophys. J., 665, 14

Sheth, R. K. & van de Weygaert, R. 2004, Mon. Not. R. Astron. Soc., 350, 517

Shoji, M., Jeong, D., & Komatsu, E. 2009, Astrophys. J., 693, 1404

Shoji, M. & Komatsu, E. 2009, Astrophys. J., 700, 705

Simpson, F. & Peacock, J. A. 2010, Phys. Rev. D, 81, 043512

Smith, R. E., Scoccimarro, R., & Sheth, R. K. 2008, Phys. Rev. D, 77, 043525

Springel, V., et al. 2005, Nature, 435, 629

Surdo, A. 2002, Nuclear Physics B Proceedings Supplements, 110, 342

Takada, M., Komatsu, E., & Futamase, T. 2006, Phys. Rev. D, 73, 083520

Takahashi, R. 2008, Progress of Theoretical Physics, 120, 549

Taruya, A. & Hiramatsu, T. 2008, Astrophys. J., 674, 617

Thomas, S. A., Abdalla, F. B., & Lahav, O. 2009, ArXiv e-prints

Valageas, P. 2007, Astron. Astrophys., 465, 725

Valdarnini, R., Kahniashvili, T., & Novosyadlyj, B. 1998, Astron. Astrophys., 336, 11

Vikhlinin, A., et al. 2009, Astrophys. J., 692, 1060

Wagner, C., Müller, V., & Steinmetz, M. 2008, Astron. Astrophys., 487, 63

Wang, L. & Steinhardt, P. J. 1998, Astrophys. J., 508, 483

Weinberg, S. 2008, Cosmology (Oxford, UK: Oxford University Press)

White, S. D. M. 1979, Mon. Not. R. Astron. Soc., 186, 145

Wong, Y. Y. Y. 2008, Journal of Cosmology and Astro-Particle Physics, 10, 35

Yamamoto, K., Bassett, B. A., & Nishioka, H. 2005, Physical Review Letters, 94, 051301

Zaldarriaga, M., Hui, L., & Tegmark, M. 2001, Astrophys. J., 557, 519

Vita

Masatoshi Shoji was born in Sendai, Japan on 27 November 1983, the son of Akira Shoji and Kazuko Shoji. He attended Sendai Daini High School, Sendai, Japan. In 2002, he entered the University of Nebraska at Lincoln, where he received the Bachelor of Science degree in both Physics and Mathematics in 2006. He started graduate studies in the Astronomy Department at the University of Texas at Austin from the Fall of 2006, where he searved as a teaching assistant and a research assistant for Dr. Eiichiro Komatsu.

Permanent address: 6-15-10 Nagamachi Taihaku-ku, Sendai
Miyagi, Japan 982-0011

This dissertation was typeset with LaTeX[†] by the author.

[†] LaTeX is a document preparation system developed by Leslie Lamport as a special version of Donald Knuth's TeX Program.